EFFECTS OF ENVIRONMENT ON GALAXY FORMATION AND EVOLUTION

A Dissertation

by

LALITWADEE KAWINWANICHAKIJ

Submitted to the Office of Graduate and Professional Studies of
Texas A&M University
in partial fulfillment of the requirements for the degree of

DOCTOR OF PHILOSOPHY

Chair of Committee,	Casey J. Papovich
Committee Members,	Kim-Vy H. Tran
	Darren DePoy
	Mark Lemmon
Head of Department,	Grigory Rogachev

August 2018

Major Subject: Physics

ABSTRACT

In this dissertation, I seek to advance our understanding of environment effects on galaxy formation and evolution. First, I use the deep near-infrared (IR) observation from the FourStar Galaxy Evolution Survey (ZFOURGE) and the Cosmic Assembly Near-IR Deep Extragalactic Legacy Survey (CANDELS) to derive the distribution of satellites ($\log(M/\mathrm{M}_{\odot}) > 9$) around massive galaxies at $1 < z < 3$ to provide constraints on the dark matter halo mass of massive galaxies with different star-formation activity (quiescent versus star-forming), and demonstrate that while halo mass may be an important mechanism for star formation suppression ("quenching"), it is unlikely to be the only factor.

Second, to gain further understanding in star formation suppression in galaxies, I combine imaging from three deep near-infrared-selected surveys (ZFOURGE/CANDELS, UDS, and UltraVISTA) to study the correlation between star formation activity of massive central galaxies and their satellites out to $z \sim 2.5$. Satellites around quiescent centrals are more likely to be quenched compared to the satellites around star-forming centrals, demonstrating that satellite quenching is connected to the star formation properties of the central galaxy as well as to the mass of the halo.

Third, I utilize the robust photometric redshift ($\sigma_z/(1+z) \lesssim 0.02$) of ZFOURGE to accurately recover galaxies in low- and high-density environments and study of galactic star formation activity as a function of environmental density and stellar mass over 0.5<z<2.0. The strength of environmental quenching depends on galaxy stellar mass, indicating that the effects of quenching related to (stellar) mass and environment are not separable. The evolution of the environmental quenching favors models that combine gas starvation (as galaxies become satellites) with gas exhaustion through star-formation and outflows ("overconsumption"), and additional processes to account for the morphological differences between the quiescent and star-forming galaxy populations.

Fourth, I apply *The Tractor* image modeling code to the *Spitzer*/HETDEX Exploratory Large-Area (SHELA) survey, covering $\sim 24\ \mathrm{deg}^2$ of the Sloan Digital Sky Survey (SDSS) "Stripe82" region with spanning optical to mid-infrared wavelength. The new multi-band forced photomet-

ric catalogs provide several advantages over traditional position-matched catalog, including (1) consistent source cross-identification between bands, (2) deblending of sources that are clearly resolved in the higher resolution bands but blended in the lower resolution *Spitzer*/IRAC bands, (3) detecting extremely faint sources that fall below the IRAC detection threshold, and (4) an improvement in the photometric redshift accuracy as evidenced by decreasing in bias and outlier fraction compared to spectroscopic redshifts.

Finally, I demonstrate the utility of the multi-wavelength forced photometric catalogs constructed for SHELA survey. The large area ($\sim 17.5\ \mathrm{deg}^2$) and moderate depth of SHELA survey drastically reduces the statistical uncertainties. After accounting for a number of potential systematic errors, I measure galaxy stellar mass functions (SMF) over $0.3 < z < 1.0$ down to $\log(M_*/M_\odot) = 10.5$ and find no evolution in the typical stellar mass over this redshift and stellar mass range with an uncertainty of 12%. This confidence interval is dominated by uncertainties in the assumed star formation history and stellar population synthesis models for stellar mass estimations. Similarly, I do not detect evolution ($\lesssim 0.1$ dex) in the typical stellar mass for massive quiescent galaxies ($\log(M_*/M_\odot) > 11.0$). Because quiescent galaxies are expected to loose mass through processes of stellar evolution, this implies massive galaxies continue to build up by merging at a rate that offsets the stellar mass loss. Lastly, the lack of evolution in the observed SMF provide the upper limit of mass growth by merging to be $\sim 48\%$ over $0.3 < z < 1.0$.

DEDICATION

To my beloved parents.

ACKNOWLEDGMENTS

Foremost, I extend my sincere gratitude to my graduate advisor, Casey Papovich, for his careful attention and guidance over these many years. You have taught me invaluable lessons in advising, teaching, writing, and research, and helped me transform from an inexperienced post-undergraduate student into a capable independent researcher. I also thank my committee members Kim-Vy Tran, Darren DePoy, Mark Lemmon for their diverse guidance throughout graduate school and for their contributions, time, and efforts through serving on my dissertation committee.

I thank the postdocs at Texas A&M, Vithal Tilvi, Nicola Mehrtens for providing practical advice during my first years of graduate school. I especially thank to Ryan Quadri for being a dedicated mentor throughout much of my work.

My thanks go out to the ZFOURGE Collaboration for all their support and guidance through the majority of the work that this dissertation entails. Special thanks to Caroline Straatman for creating the data catalogs on which most of this dissertation is based. Other ZFOURGE team members I would like to recognize: Ivo Labbé, Lee Spitler, Glenn Kacprzak, Michael Cowley, Karl Glazebrook, Pieter van Dokkum, Rebecca Allen, Themiya Nanayakkara, Adam Tomczak, Ben Forrest, and Glen Rees.

I also appreciate the SHELA/HETDEX Collaboration for all of their hard work to provide a robust and valuable dataset: Steven Finkelstein, Robin Ciardullo, Caryl Gronwall, Sharda Jogee, Matthew Stevans, Sydney Sherman, and Jonathan Florez. Special thanks also to Isak Wold for his work on the data reduction and catalogs. In addition, I also acknowledge the CANDELS Collaboration. Without their dedication and assistance, my work would not have been possible.

I also thank the LSSTC Data Science Fellowship Program, especially to Lucianne Walkowicz and Adam Miller.

I own deep gratitude to my undergraduate advisor, Professor David Ruffolo and Dr. Alejandro Sáiz Rivera, for their investment time, thoughts, and energy in mentoring me throughout undergraduate school.

Special thanks go to the following figures whose support is pivotal to my career as an astronomer: Khun Thagoon Kirdkao, Dr. Wiphu Rujopakarn, and Ajarn Pannee Prayung, for getting me started in astronomical research and provide me with valuable advice. My research experience under their guidance proved to be extremely influential to my training as a scientist later on.

Thanks to current and former grad students of the Department of Physics and Astronomy at Texas A&M University, especially Brett Salmon, Adam Tomczak, Ryan Oelkers, Steven Boada, Jimmy, Michael Smitka, Heath Shipley, Ting Li, Ben Forrest, Daniel Nagasawa, Leo Alcorn, Andrew Quick, Wenlong Yuan, Yi Yang, Katelyn Stringer, Vince Estrada-Carpenter, Taylor Hutchison, Alex Riley, Jacqueline Antwi-Danso, Jonathan Cohn, Peter Chi, Peter Ferguson, Sarah Cantu, Tarini Konchady, Jiawen Yang and Sijie Chen, along with my friends and colleagues in Thailand. I also thank the Mitchell family and the late George P. Mitchell for starting a worldclass astronomy department through their commitment to science and philanthropy.

Lastly, I thank my parents, whom this dissertation is dedicated to, for more than I can ever say.

CONTRIBUTORS AND FUNDING SOURCES

Contributors

This work was supported by a dissertation committee consisting of Professor Casey Papovich [advisor], Professor Darren DePoy, and Professor Kim-Vy Tran of the Department of Physics and Astronomy, and Professor Mark Lemmon of the Department of Atmospheric Sciences.

The data analyzed for Chapter 2, Chapter 3, and Chapter 4 was provided by the FourStar Galaxy Evolution Survey (ZFOURGE) and the Cosmic Assembly Near-IR Deep Extragalactic Legacy Survey (CANDELS) teams.

All other works in Chapter 2 Chapter 3, and Chapter 4 were completed by the student, in collaboration with both ZFOURGE and CANDELS teams, and were published in 2014, 2016, and 2017 in the Astrophysical Journal.

For Chapter 2, valuable comments and feedback were kindly provided by Professor James Bullock of the Department of Physics and Astronomy, University of California, Irvine and Professor Simon White of the Max Planck Institute for Astrophysics. For Chapter 3, valuable comments and feedback were kindly provided by Professor Andrew Wetzel of the Department of Physics , University of California, Davis and Dr. Duncan Campbel of the Department of Astronomy, Yale University.

A very helpful and constructive report for all publications which Chapter 2, Chapter 3, and Chapter 4 are based on were provided by the anonymous referees.

The data analyzed in Chapter 5 and Chapter 6 were completed by the student, in collaboration with the *Spitzer*/HETDEX Exploratory Large-Area (SHELA) survey team.

All other works in Chapter 5 and Chapter 6, were completed by the student, in collaboration with the SHELA/HETDEX team.

The catalog of candidate redMaPPer clusters in the SHELA survey for preliminary analysis presented in Chapter 7 was calibrated and provided by Dr. Eli Rykoff of the Kavli Institute for

Particle Astrophysics and Cosmology. All other preliminary analysis in Chapter 7 is completed by the student, under the advisement of Professor Casey Papovich of the Department of Physics and Astronomy.

Funding Sources

The work for Chapter 2 is supported by the National Science Foundation through grants AST-1009707 and AST-0808133. This work is based on observations taken by the CANDELS Multi-Cycle Treasury Program with the NASA/ESA HST, which is operated by the Association of Universities for Research in Astronomy, Inc., under NASA contract NAS5- 26555. This work is supported by HST program number GO-12060. Support for Program number GO-12060 was provided by NASA through a grant from the Space Telescope Science Institute, which is operated by the Association of Universities for Research in Astronomy, Inc., under NASA contract NAS5-26555. Australian access to the Magellan Telescopes was supported through the National Collaborative Research Infrastructure Strategy of the Australian Federal Government.

The work for Chapter 3 is supported by the National Science Foundation through grants AST 1009707 and AST 1413317. This work is based on observations taken by the CANDELS Multi-Cycle Treasury Program with the NASA/ ESA HST, which is operated by the Association of Universities for Research in Astronomy, Inc., under NASA contract NAS5-26555. This work is supported by HST program number GO-12060. Support for Program number GO-12060 was provided by NASA through a grant from the Space Telescope Science Institute, which is operated by the Association of Universities for Research in Astronomy, Incorporated, under NASA contract NAS5-26555. Australian access to the Magellan Telescopes was supported through the National Collaborative Research Infrastructure Strategy of the Australian Federal Government. Professor Glenn G. Kacprzak acknowledges the support of the Australian Research Council through the award of a Future Fellowship (FT140100933). Professor Ivo Labbé and Dr. Caroline M.S. Straatman acknowledge support from NL-NWO.

The work for Chapter 4 is supported by the National Science Foundation through grants AST14 13317 and 1614668. This work is based on observations taken by the CANDELS Multi-Cycle

Treasury Program with the NASA/ESA HST, which is operated by the Association of Universities for Research in Astronomy, Inc., under NASA contract NAS5-26555. This work is supported by HST program number GO-12060. Support for Program number GO-12060 was provided by NASA through a grant from the Space Telescope Science Institute, which is operated by the Association of Universities for Research in Astronomy, Incorporated, under NASA contract NAS5-26555. Australian access to the Magellan Telescopes was supported through the National Collaborative Research Infrastructure Strategy of the Australian Federal Government. As members of ZFOURGE collaboration, Professor Glenn G. Kacprzak acknowledges the support of the Australian Research Council through the award of a Future Fellowship (FT140100933). Prof. Kim-Vy Tran acknowledges support by the National Science Foundation under grant 1410728.

The works for both Chapter 5 and Chapter 6 are supported by the National Science Foundation through grants AST1413317 and 1614668. These work are based on observations made with the Spitzer Space Telescope, which is operated by the Jet Propulsion Laboratory, California Institute of Technology under a contract with NASA.

NOMENCLATURE

Å	Angstrom
Ω_Λ	Energy Density of the Universe
$\Omega_{\rm m}$	Matter Density of the Universe
λ	Wavelength
τ	e-folding Time of Star Formation History
$\sigma_{\rm MAD}$	Median Absolute Deviation
μm	Micron/Micrometer
AB	Absolute Bolometric
AGN	Active Galactic Nuclei
A_V	Total Extinction/Attenuation at the V band
CANDELS	Cosmic Assembly Near-IR Deep Extragalactic Legacy Survey
CDF-S	Chandra Deep Field - South
CMD	Color-Magnitude Diagram
COSMOS	Cosmic Evolution Survey
EAZY	Easy and Accurate Redshifts from Yale
FAST	Fitting and Assessment of Synthetic Templates
GOODS-S	Great Observatories Origins Deep Survey - South
Gyr	Gigayear
HETDEX	Hobby-Eberly Telescope Dark Energy Experiment
HST	Hubble Space Telescope
IMF	Initial Mass Function

IR	Infrared
IRAC	Infrared Array Camera
JWST	James Webb Space Telescope
kpc	Kiloparsec
$L_\odot$	Solar Luminosity
$M_\odot$	Solar Mass
M_*	Stellar Mass
M_h	Halo Mass
mag	magnitude
Mpc	Megaparsec
NEWFIRM	NOAO Extremely Wide-Field Infrared Imager
NFW	Navarro-Frenk-White
pc	pacsec
PRF	Point Response Function
PSF	Point Spread Function
S/N	Signal-to-Noise
SAM	Semi-Analytic Model
SDSS	Sloan Digital Sky Survey
SED	Spectral Energy Distribution
SExtractor	Source Extractor
SFH	Star Formation History
SFR	Star Formation Rate
SHELA	Spitzer/HETDEX Exploratory Large-Area
SMF	Stellar Mass Function
sSFR	Specific Star Formation Rate

SSP	Single Stellar Population
UDS	Ultra Deep Survey
UV	Ultraviolet
VISTA	Visible and Infrared Survey Telescope
WFC3	Wide Field Camera 3
WMAP	Wilkinson Microwave Anisotropy Probe
Z	Metallicity
z	Redshift
z_{phot}	Photometric Redshift
z_{spec}	Spectroscopic Redshift
ZFOURGE	FourStar Galaxy Evolution Survey

TABLE OF CONTENTS

Page

LIST OF FIGURES

FIGURE Page

LIST OF TABLES

TABLE Page

1. INTRODUCTION

One of the most important requirements to understand galaxy evolution is to measure accurately galaxy distances and determine which galaxies are in the process of influencing one-another's evolution. Particularly for extragalactic astronomy, this means that one requires an accurate measurement of redshift to derive physical properties of galaxies, such as stellar mass, age, or star formation rate, and ultimately, to understand the formation and evolution of galaxies across the cosmic time.

The best approach is to determine redshift by observing galaxy spectra and identifying emission and absorption lines in those spectra. These spectral features of distant galaxies systematically shift along the scale in wavelength, while the relative distance between each spectral features do not. We can compare the wavelengths of these spectral features observed from distant galaxies to those which are precisely known based on the atomic physics. The redshift determined with this method is referred to as spectroscopic redshift. However, the disadvantages of this approach are the following. First, the spectroscopic redshift is limited to bright sources or sources with strong emission lines, such as star forming galaxies. These galaxies are not necessary the representative of galaxy population. Second, spectroscopic observation is time-consuming, and is therefore observationally prohibitive for large galaxy sample.

Another approach for determining, or at least estimating, redshift for large galaxy sample is to rely on an imaging of sources observed through different filters, construct a spectral energy distribution (SED) of a galaxy, and estimate a galaxy redshift by fitting a set of standard galaxy spectra to this SED. The redshift determined with this method is referred to as photometric redshift. Basically, the observed galaxy SED is low-resolution spectra. Therefore, the higher the number of filters spreading over a broad spectral range is used, the more accurate the photometric redshift is.

Furthermore, for distant galaxies at $z \gtrsim 1$, the important rest-frame optical spectral features related to aging stellar populations are shifted to the near-infrared. Therefore, if one uses only optical filters, the estimated redshift of these type of galaxies could be extremely wrong.

In this dissertation, I use accurate photometric redshift surveys to study the build-up of galaxies based on their mass and their environment. One of these surveys is the FourStar Galaxy Evolution Survey (ZFOURGE), which was developed in response to the need for accurate redshift for galaxy sample at $1 < z < 3$. ZFOURGE survey is carried out using the FourStar instrument with a set of six near-infrared medium-bandwidth filters equipped on the 6.5m Magellan Baade Telescope at Las Campanas Observatory in Chile. These six near-infrared medium-band filters provide an excellent sampling of spectral features, enabling accurate and robust redshift with $1-2\%$ accuracy for $\sim 60,000$ galaxies at $1 < z < 3$ relative to employing the broad-band filters alone. The goal of ZFOURGE is to establish an observational benchmark of galaxy properties at $z > 1$.

In addition to studying environmental effect on galaxies with the ZFOURGE survey, I exploit a large sample of galaxies from a homogeneous survey covering sufficient volume to make headway in studying differences in the galaxy population in the full range of environments (from rich clusters to groups and to the field). One of these surveys is the *Spitzer*/HETDEX Exploratory Large-Area (SHELA) survey. SHELA survey covers $\sim 24 \text{ deg}^2$ of the Sloan Digital Sky Survey (SDSS) "Stripe82" region and spans an optical to mid-infrared wavelength range. All of these will provide accurate photometric redshift and stellar mass measurements and enable a broad range of scientific studies, including the relationship between structure formation, galaxy stellar mass, halo mass, and environmental effects over $0.5 < z < 3.5$. The basis of the scientific success of surveys such as SHELA lies in the construction of robust multi-band source catalogs. As part of my dissertation, I also worked on developing a multi-band photometric catalog of the $ugriz$-band plus 3.6 and 4.5 μm from *Spitzer*/IRAC for SHELA survey.

In the following sections, I describe several areas of galaxy formation and evolution that can be explored with data from the ZFOURGE and SHELA surveys.

1.1 Galaxies and their host dark matter halo

In the standard theory of galaxy formation in the Lambda Cold Dark Matter (ΛCDM) universe, galaxies form and evolve in massive dark matters halos. A larger halo forms from accretion of smaller clumps of dark matter, gradually building up a massive halo with nearby smaller sub-halos. As a consequence, we expect that satellite galaxies in those sub-halos are tracers of the overall mass distribution of the "unseen" parent dark matter halos, and they provide constraints on the halo mass.

As dark matter halos grow and merge overtime, galaxies within these halos evolve, involving multiple physical mechanisms to regulate galaxy star-formation. In this picture, the formation and evolution of host dark matter halos influences the galaxy properties in those halos (for a recent review see Somerville & Davé, 2015). We can therefore connect properties of galaxies (such as stellar mass and star formation activity) to those of their host dark matter halo (such dark matter halo mass) by studying the distribution of satellite galaxies, i.e., those small galaxies orbiting around larger ("central") galaxy.

The distribution of satellites provides an independent constraint to other techniques such as galaxy correlation function, galaxy-galaxy weak lensing, satellite kinematics, and abundance matching (e.g., Vader & Sandage, 1991; Zehavi et al., 2002; Madore et al., 2004; Mandelbaum et al., 2006; Wake et al., 2008; Conroy & Wechsler, 2009; Behroozi et al., 2010; Hartley et al., 2010; More et al., 2011). Tal et al. (2012) used a statistical background subtraction technique to measure the distribution of satellites around local luminous red galaxies, and demonstrated that the derived ratio of dark matter halo mass to baryonic matter consistent with those from galaxy-galaxy weak lensing measurement (Mandelbaum et al., 2006).

The statistical background subtraction technique for measuring distribution of satellite requires accurate redshift estimates of satellites, which are typically too faint for spectroscopic observation. Therefore, the deep near-infrared imaging with accurate photometric redshift from ZFOURGE provides unique opportunity to probe the connection between galaxies and dark matter halo through the distribution of satellites even at $z < 3$.

Additionally, studying the distribution of satellite galaxies provides particular insight into the evolution of massive galaxies. Under the ΛCDM cosmological model, we expect these massive galaxies inside dark matter halos to undergo hierarchical mergers with other galaxies. Indeed, a growing number of observations have revealed that massive ($10^{11}\ M_{\odot}$) quiescent galaxies (those lacking substantial star formation) have grown primarily in their outer regions through the accretion of small satellite galaxies since $z \sim 2$ (e.g., van Dokkum et al., 2010; Greene et al., 2012; Huang et al., 2013; Buitrago et al., 2017; Huang et al., 2018). The growth of these massive galaxies should be reflected in the evolution of stellar mass functions. The SHELA survey covers large area of 17.5 deg^2. Therefore, SHELA survey is excellently suited to measure the stellar mass functions for galaxies more massive than $10^{10.5}\ M_\odot$ over $0.3 < z < 1.0$ and hence provides tighter constraints on the mass assembly of those galaxies.

1.2 Star formation Regulation

The population of galaxies can be broadly classified into two distinct types: quiescent galaxies with relatively red colors, spheroid-dominated morphologies, and little to no on-going star-formation activity (with star-formation rates (SFRs) much less than their past averages); and star-forming galaxies with relatively blue colors, disk-dominated morphologies, and SFRs comparable to (or above) their past average. This *bimodality* in the color distribution of galaxies has long been observed in the local universe (e.g., Strateva et al., 2001; Kauffmann et al., 2003; Baldry et al., 2004, 2006; Bell, 2008; van Dokkum et al., 2011; Schawinski et al., 2014). The advent of deep galaxy surveys show that these two populations (star forming and quiescent) have been clearly identified at least up to $z \sim 2$, and up to higher redshifts at $z \sim 3 - 4$ (e.g., Whitaker et al., 2011; Tomczak et al., 2014; Spitler et al., 2014; Straatman et al., 2014).

The processes that inhibit star formation activity ("quenching") and result in the observed bimodality in galaxy population are of great interest in understanding galaxy evolution. The proposed mechanisms for this can be broadly classify into: (1) those processes internal to galaxy and closely tie to mass (dark matter halo mass, supermassive blackhole mass, or galaxy stellar mass) and (2) those processes external to galaxy (i.e., environment).

For low mass galaxies, the efficiency of star formation is mostly regulated by supernovae and stellar winds. Due the low escape velocity, gas for star formation in these low mass galaxies can be easily expelled. As galaxies grow, their escape velocity is large enough so that the gas is no longer expelled by supernovae, and therefore the star formation can proceed.

Second, a galaxy's host dark halo mass provides a natural quenching mechanism related to mass (e.g., Rees & Ostriker, 1977; White & Rees, 1978; Birnboim & Dekel, 2003; Dekel & Birnboim, 2006; Gabor & Davé, 2012, 2015). When the mass of galaxy's host dark matter halo exceeds a critical value, the gas is heated by shocks. This prevents infalling gas from cooling to form new stars, and therefore star formation is halted. Galaxies in these massive halos gradually become quiescent. Based on this quenching mechanism, one could expect that quiescent galaxies live in more massive dark matter halos relative to the counterpart star forming galaxies at the equal stellar mass. Indeed, this prediction is consistent the observational results (e.g., Hartley et al., 2010, 2013; Phillips et al., 2014). The deep near-IR dataset of ZFOURGE provides a complete sample of faint and low mass galaxies to study the distribution of satellite around massive galaxies with different star formation activity and provide means to trace dark matter halo mass and gain additional clue regarding the how halo mass and galaxy star formation is related.

1.3 Environmental Effects on Galaxy Properties

In addition to physical mechanisms internal to galaxy itself, the environmental density in which a galaxy resides strongly affects the evolution of a galaxy. For instance, galaxies in denser environmental density (i.e., cluster) evolve much more rapidly, and their star formation cease and eventually become red, spheroid-dominated morphologies relative to their counterparts of equal stellar mass in lower environmental density (i.e., "field"). In the local universe, this morphological segregation of galaxies in different environment has long been observed (e.g., Oemler, 1974; Davis & Geller, 1976; Dressler, 1980; Balogh et al., 2004b; Hogg et al., 2004; Kauffmann et al., 2004; Blanton & Moustakas, 2009; Peng et al., 2010; Woo et al., 2013).

Many dynamical effects in dense environments are able to transform galaxies into more evolved morphologies. In such environment, like clusters, the high density of galaxies encourages: (1) relatively slow encounters between galaxies leading to merging and (2) high-speed, multiple collisions, which is referred to as "galaxy harassment". Furthermore, clusters are not just a collection of galaxies, they largely contain hot gas. This hot gas exerts pressure force on galaxies orbiting in cluster: galaxies experience "wind", capable of removing cold gas from galaxies. Overtime, this effect, referred to as ram-pressure stripping, leads to exhaustion of cold gas reservoir for supplying star formation, and then galaxies turn to red and quiescent (Gunn & Gott, 1972; Abadi et al., 1999). On the other hand, if only the outer, more loosely bound gas is lost, a galaxy can still continue forming stars with the existing cold gas in the inner part until all of available gas is exhaust due to the lack of gas cooling or accretion. This effect is called strangulation (Larson et al., 1980; Balogh et al., 1997).

The different environmental effects operate with different strength and over different timescales depending on stellar mass and host dark matter halo mass. Therefore, significant efforts have been devoted to study environmental effects of galaxy evolution at local universe and out to $z \sim 3$ (e.g., Cooper et al., 2007, 2010; Peng et al., 2010; Kovač et al., 2010; Quadri et al., 2012; Kovač et al., 2014; Darvish et al., 2016; Nantais et al., 2017; Papovich et al., 2018).

Here, the deep near-infrared imaging survey with accurate photometric redshifts from ZFOURGE survey provides unique opportunity to robustly quantify environmental density of faint and low mass galaxies ($K_s \simeq 25.5 - 26$ AB mag) than possible with either ground-based spectroscopy ($K_s < 24$ AB mag, Nanayakkara et al. 2016) or spaced-based spectroscopy ($JH_{140} < 24$ AB mag, Fossati et al. 2017). As a result, ZFOURGE dataset provides insight into the effect of stellar mass and environment on quenching of galaxies with low stellar mass out to high redshift ($M_* \sim 3 \times 10^9\ M_\odot$ at $z = 2$).

In addition to using the deep near-infrared imaging survey like ZFOURGE, SHELA survey is excellently suited for studying galaxy environment from rich clusters to the field (region with relatively low environmental density compared to groups/clusters) due to its large cosmological volume. To identify clusters of galaxies, the cluster finding algorithms based on cluster red-sequence (e.g., Koester et al., 2007; Oguri, 2014; Rykoff et al., 2014) have been widely employed. This is based on the observations that (1) clusters are mostly dominated by massive, red, quiescent galaxies (the cluster red sequence; e.g., Eisenhardt et al., 2008) and (2) colors of galaxies in these clusters evolve with their redshift (Muzzin et al., 2013; Papovich, 2008). Among several red-sequence cluster finders, the redMaPPer (Rykoff et al., 2014) has been extensively studied and applied to large photometric surveys such as the Sloan Digital Sky Survey (SDSS) and the Dark Energy Survey (DES) for calibrating the relation between its mass proxy, the richness (λ), to the total mass of groups/clusters (Rozo et al., 2009a,b, 2011; Rykoff et al., 2016). Here, we apply redMaPPer to find candidate clusters in SHELA survey and explore the effect of environments on galaxy quenching by estimating quiescent fraction of galaxies in field and in redMaPPer clusters $z \sim 1$, where environmental processes are become dominant (e.g., Peng et al., 2010; Kovač et al., 2014; Balogh et al., 2016; Nantais et al., 2017).

The outline of this dissertation is as follows. In Chapter 2 I present a study of the statistical distribution of satellites around massive galaxies at $1 < z < 3$. With the deep near-infrared dataset, I use the statistical background subtraction technique to select satellite galaxies down to $\log(M/\mathrm{M}_{\odot}) > 9$ at $z < 3$, and explore the dependence of the galaxy distribution on the star formation activity of the massive centrals. In Chapter 3 I use a new set of near-infrared (IR)-selected datasets, spanning multiple wide and deep fields to explore the correlation between the star-formation activity of central galaxies and their satellites over a large range of stellar mass at $0.3 < z < 2.5$. In Chapter 4 I estimate the galaxy environment using a Bayesian-motivated measure of the distance to the third nearest neighbor for galaxies to the stellar mass completeness of our survey, $\log(M/M_{\odot}) > 9$ (9.5) at z=1.3 (2.0). Then I study how quenching of galaxies correlates with galaxy stellar mass and environment, and how these evolve with cosmic time. In Chapter 5 I apply *The Tractor* image modeling code to improve upon existing multi-band photometry for the *Spitzer*/HETDEX Exploratory Large-Area (SHELA) survey, spanning optical to mid infrared wavelength. In Chapter 6, I demonstrate the utility of the multi-band catalog constructed by forced photometry technique in Chapter 5. I study the number density evolution for massive galaxies by accounting for systematic uncertainties due to the assumptions in modeling a galaxy spectral energy distribution and random error in stellar mass measurement. Finally, in Chapter 7 I present the conclusions of these studies and discuss the direction of future work.

2. THE DISTRIBUTION OF SATELLITES AROUND MASSIVE GALAXIES AT $1 < z < 3$ IN ZFOURGE/CANDELS: DEPENDENCE ON STAR FORMATION ACTIVITY [1]

2.1 Synopsis

We study the statistical distribution of satellites around star-forming and quiescent central galaxies at $1 < z < 3$ using imaging from the FourStar Galaxy Evolution Survey (ZFOURGE) and the Cosmic Assembly Near-IR Deep Extragalactic Legacy Survey (CANDELS). The deep near-IR data allow us to select satellites down to $\log(M/\mathrm{M}_{\odot}) > 9$ at $z < 3$. The projected radial number density of satellites around centrals with stellar masses of $\log(M/\mathrm{M}_{\odot}) > 10.48$ is consistent with a projected NFW profile. For the most massive galaxies, $\log(M/\mathrm{M}_{\odot}) > 10.78$, quiescent centrals have ~ 2 times the number of satellites compared to star-forming centrals. This excess persists at 2.7 sigma significance even after accounting for differences in the centrals' stellar mass distributions. In contrast, we find no statistical difference in the satellite distributions of less-massive quiescent and star-forming centrals, $10.48 < \log(M/\mathrm{M}_{\odot}) < 10.78$. Comparing to the Guo et al. (2011) semi-analytic model, the excess number of satellites indicates that quiescent centrals have dark-matter halo masses 0.3 dex larger than star-forming centrals, even when the stellar-mass distributions are fixed. We interpret these results using a simple model that investigates the relationship between halo mass and quenching, and which roughly reproduces the observed quenched fractions and the differences in halo mass between star-forming and quenched galaxies in our two stellar mass bins. A model with a single, fixed halo mass quenching threshold is unable to reproduce the quiescent fraction and satellite distribution of centrals. Rather, we find that the data favor a scenario where galaxies have a probability of being quenched that increases with halo mass from ~ 0 for $\log(M_h/\mathrm{M}_{\odot}) \sim 11$ to ~ 1 for $\log(M_h/\mathrm{M}_{\odot}) \sim 13.5$. Therefore, while halo quenching may be an important mechanism, it remains unclear why a high fraction of centrals remain star-forming even in relatively massive halos. This suggests that halo mass may not be the

---

[1] Reprinted with permission from "The Distribution of Satellites around Massive Galaxies at $1 < z < 3$ in ZFOURGE/CANDELS: Dependence on Star Formation Activity" by Kawinwanichakij et al., 2014. The Astrophysical Journal, Volume 792, Issue 2, article id. 103 pp. 19, Copyright 2014.

only factor driving quenching.

2.2 Background Information

One of the fundamental goals in studying galaxy formation and evolution is to understand the relationship between galaxies and their host dark matter halos. In ΛCDM models galaxies grow hierarchically, and we expect to see the signatures of such growth in satellite galaxies, which trace the accreted dark-matter sub-halos. The distribution of satellite galaxies can be used as a tracer of the overall mass distribution of the parent halo and provides constraints on the halo mass. Therefore, investigating the distribution of satellites provides a means to study how properties of host galaxies (such as stellar mass and star formation activity) are related to the mass of their dark matter halos.

The distribution of satellite galaxies provides constraints that are independent of other techniques that use correlation functions, galaxy-galaxy lensing, adundance matching, and kinematics to study how the dark matter masses relate to galaxy observables (e.g. Vader & Sandage, 1991; Zehavi et al., 2002; Madore et al., 2004; Mandelbaum et al., 2006; Masjedi et al., 2006; Gavazzi et al., 2007; Wake et al., 2008; Conroy & Wechsler, 2009; Drory et al., 2009; Behroozi et al., 2010; Hartley et al., 2010, 2013; More et al., 2011). Several studies show that the distribution of satellite galaxies follows a Navarro, Frenk, & White (1996) profile (NFW-profile), and this can be used to measure the mass distribution and scale size of the dark matter halo (Nierenberg et al., 2011, 2012; Tal et al., 2012, 2013; Wang & White, 2012; Watson et al., 2012; Wang et al., 2014).

Studying the distribution of satellite galaxies is expected to provide particular insight into galaxy evolution for massive galaxies. Growing observational evidence suggests that massive ($> 10^{11}$ $\mathrm{M}_{\odot}$), quiescent galaxies (those lacking substantial star-formation) have grown primarily in their outer regions through the accretion of small satellites since $z \sim 2$ (e.g. van Dokkum et al., 2010; McLure et al., 2013; Greene et al., 2012, 2013). This is consistent with the results from hydrodynamical simulations, which have reproduced the observed size and mass growth of massive elliptical galaxies by stellar accretion from minor mergers (Naab et al., 2007, 2009; Oser et al., 2010, 2012; Hilz et al., 2013).

Recently, Tal et al. (2012) use a statistical background subtraction to measure the radial number-density profiles of satellites around local luminous red galaxies (LRGs). They show that the best fit NFW+Sérsic model of the derived satellites profile results in a total dark-to-baryonic mass ratio in agreement with the weak-lensing result from Mandelbaum et al. (2006) for massive early type galaxies. Tal et al. (2013) extend this technique to massive galaxies out to $z \sim 2$ and show that the radial number density profile of satellite galaxies has not evolved significantly since $z = 1.6$, suggesting a balance between mergers and accretion of new satellites.

The technique used by Tal et al. (2012, 2013) requires statistically isolating satellites from unassociated galaxies along the line of sight. Surveys with homogeneous multiwavelength photometry provide photometric redshift information on faint galaxies, which is useful to identify satellites around more distant galaxies as shown by Tal et al. 2013. This statistical technique has an advantage over methods using spectroscopic redshifts, as the latter are observationally prohibitive for all but the brightest satellites and very costly in telescope time.

At $z > 1$, growing evidence shows that massive galaxies are a mix of quiescent and star-forming populations (e.g., Papovich et al., 2006). This is an extension of the well-known bimodality in their color and star-formation activity. At fixed stellar mass, galaxies divide into star-forming galaxies with bluer UV–optical colors and active star formation (forming a "main sequence",e.g., Noeske et al., 2007; Martin et al., 2007), and quiescent galaxies with red colors and low star formation rates compared to their past average (forming a "red sequence", e.g. Bell et al., 2004; Blanton, 2006). This bimodality in the galaxy color-mass distribution extends at least out to $z \sim 3$ (Whitaker et al., 2011; Tomczak et al., 2014) and perhaps beyond (Spitler et al. 2014, Straatman et al., 2014). Recent studies of the evolution of the progenitors of local ultra-massive galaxies ($\log{(M/\mathrm{M}_\odot)} \approx 11.8$) at $1 < z < 3$ shows that the contribution of star-forming galaxies increases at $z > 1$. Understanding why some massive galaxies are quiescent and some are star-forming has important implications for galaxy formation models (e.g. Croton et al., 2006; Martig et al., 2009; Dekel & Birnboim, 2006). This may be tied to differences in the galaxies' dark matter halo growth. For this reason, it is of interest to study differences in the satellite distribution of quiescent and star-forming centrals at $1 < z < 3$ because it allows us to trace the dark-matter halos of such objects when the dichotomy in star-formation activity (quiescent versus star-forming) is at its peak for massive galaxies (e.g. Marchesini et al., 2014)

In this work, we use the most recent data from the FourStar Galaxy Evolution Survey (ZFOURGE) and the Cosmic Assembly Near-IR Deep Extragalactic Legacy Survey (CANDELS) to derive the distribution of satellites around massive galaxies at $1 < z < 3$. We study the dependence of the galaxy distribution on the star formation activity of the massive centrals. The outline of this chapter is as follows. In Section 2.3 we describe our ZFOURGE/CANDELS dataset and our galaxy sample selection criteria. In Section 2.4 we describe the method for identifying satellites and for measuring the satellite number density profile. In Section 2.5 we discuss how the satellite distribution depends on the stellar mass and star-formation activity of central galaxy. In Section 2.6, we explore why quiescent and star-forming galaxies have differences in their satellite distributions, including a comparison between galaxies in our dataset and those in a semi-analytical model (Guo et al., 2011). In Chapter 7, we present our summary. Throughout, we adopt the following cosmological parameters where appropriate, $H_0 = 70\,\mathrm{km\,s^{-1}\,Mpc^{-1}}$, $\Omega_m = 0.3$, and $\Omega_\Lambda = 0.7$. For this cosmology, the angular diameter conversion is $\approx$ 8 kpc arcsec^{-1} and constant within 5% for $1 < z < 3$.

2.3 Data and Sample Selection

We use the deep near-IR imaging from ZFOURGE (Straatman et al. in prep), which is composed of three $11' \times 11'$ pointings with coverage in the CDFS (Giacconi et al., 2002), COSMOS (Capak et al., 2007), and UDS (Lawrence et al., 2007). The imaging reaches depths of $\sim 26\,\mathrm{mag}$ in J_1, J_2, J_3 and $\sim 25\,\mathrm{mag}$ in H_s, H_l, K_s. A brief description of the filter set is described in detail by Spitler et al. (2012); Tilvi et al. (2013). The medium-band filters from ZFOURGE provide an advantage by sampling the Balmer break at $1 < z < 4$ better than broadband filters alone. We combine the ZFOURGE data with public HST/WFC3 F160W and F125W imaging from CANDELS (Grogin et al., 2011; Koekemoer et al., 2011) in the three fields. As described in Tomczak et al. (2014), we make use of the CANDELS F160W as a detection image to preselect a sample of galaxies at $z < 3$ to low masses (10^9 $\mathrm{M}_\odot$).

Photometry is performed in dual-image mode with SExtractor (Bertin & Arnouts, 1996) on PSF-matched images. The colors are measured in 0.8" apertures, and total magnitudes are measured using the AUTO magnitude and applying an aperture correction for the flux falling outside the AUTO aperture.

As described by Tomczak et al. (2014), we estimate the photometric redshifts and rest-frame colors of galaxies with EAZY (Brammer et al., 2008). By using the default set of spectral templates derived from the PEGASE models (Fioc & Rocca-Volmerange, 1997) and a dust reddened template derived from the Maraston (2005) model to fit the $0.3-8\,\mu\,\mathrm{m}$ photometry for each galaxy to obtain its photometric redshift. Similarly, we derive stellar masses using Bruzual & Charlot (2003) stellar population models with FAST code (Kriek et al., 2009), assuming exponentially declining star formation histories, solar metallicity, and a Chabrier (2003) initial mass function.

We estimate relative uncertainties in photometric redshifts using the technique described by Quadri & Williams (2010). For our study, the relative errors between the centrals and satellites are paramount, and traditional photometric redshift testing (comparing photometric redshifts to spectroscopic) is infeasible as the satellite galaxies in our sample are typically much fainter than spectroscopic magnitude limits. The underlying principle of the Quadri & Williams technique is that close pairs of galaxies have some probability of being physically associated. In this case, each galaxy provides an independent estimate of the true redshift. Therefore, the distribution of the differences in the photometric redshifts of galaxy pairs can be used to estimate the photometric redshift uncertainties.

We apply this method to derive the distribution of differences between the photometric redshifts of centrals and satellites using the samples defined below (Section 2.3.1 and Section 2.3.2). From these we find that the typical photometric redshift uncertainty between the centrals and satellites in the COSMOS, CDFS, and UDS fields are σ_z= 0.06, 0.05, and 0.08, respectively (where $\sigma_z = \sigma/\sqrt{2}$, and where σ is the width measured from a Gaussian fit to the distribution of pair redshift differences in each field, and the $\sqrt{2}$ accounts for the fact that we take the difference between two independent measurements). These uncertainties translate to $\sigma_z/(1+z) < 2\%$ and 4% for galaxies at $1 < z < 3$ down to 10^9 $\mathrm{M}_\odot$.

Throughout, we consider two samples of galaxies, the central galaxies and their satellite galaxies, which are defined in Section 2.3.1 and Section 2.3.2. We denote the stellar masses of the centrals as M_c and the stellar masses of the satellites as M_sat. We use N_sat throughout to denote the radial number density of satellites around the central galaxies, and correct this quantity for projected field galaxies (Section 2.4).

2.3.1 Selection of Centrals

Our goal is to measure the distribution of satellites around massive galaxies at $1 < z < 3$. We therefore select all galaxies in ZFOURGE with $\log(M_\mathrm{c}/\mathrm{M}_\odot) > 10.48$ (i.e., $M_\mathrm{c} > 3 \times 10^{10}$ $\mathrm{M}_\odot$) and photometric redshift $1 < z < 3$ as our sample of central galaxies. We will further consider the subsamples of central galaxies in bins of stellar mass, $10.48 < \log(M_\mathrm{c}/\mathrm{M}_\odot) < 10.78$ (i.e., $M_\mathrm{c} = (3-6) \times 10^{10}$ $\mathrm{M}_\odot$) and $\log(M_\mathrm{c}/\mathrm{M}_\odot) > 10.78$ (i.e., $M_\mathrm{c} > 6 \times 10^{10}$ $\mathrm{M}_\odot$). A summary of number and mean stellar mass of centrals in each of the ZFOURGE field and in each subsample is given in Table 2.1.

According to the central galaxies selection criteria used by Tal et al. (2013), they consider galaxies as “central” if no other, more massive galaxies are found within a projected radius of 500 kpc. Otherwise, they are counted as “satellites" of their more massive neighbor. We have tested if the projected radial distribution changes if we exclude galaxies from our sample of central galaxies if there are other more massive galaxies within 10 arcsec (about 80 kpc, projected), which is $\sim 2\times$ our derived halo scale radius (described in Section 2.4.2, below). We find that our derived projected radial distribution is not significantly changed. Therefore, we do not apply the above selection criteria to select our central sample.

We further consider the subsamples of central galaxies divided by star-formation activity. Williams et al. (2009) show that the $U-V$ and $V-J$ rest-frame colors are able to distinguish reliably between quiescent galaxies with low specific SFRs (sSFR) and star-forming galaxies with high specific SFRs; see also discussion in Whitaker et al. (2011). Galaxies are classified as quies-

Table 2.1: Number and mean stellar masses of quiescent centrals and star-forming centrals in ZFOURGE survey at $1 < z < 3$. Reprinted with permission from “The Distribution of Satellites around Massive Galaxies at $1 < z < 3$ in ZFOURGE/CANDELS: Dependence on Star Formation Activity" by Kawinwanichakij et al., 2014. The Astrophysical Journal, Volume 792, Issue 2, article id. 103 pp. 19, Copyright 2014.

Field	$\log(M_{\rm c}/{\rm M}_{\odot})$	$N_{\rm c}$	$\log(M_{\rm c,mean}/{\rm M}_{\odot}$
Quiescent centrals			
COSMOS	10.48–10.78	63	10.61
	> 10.78	67	11.01
CDFS	10.48–10.78	46	10.61
	> 10.78	53	11.02
UDS	10.48–10.78	96	10.61
	> 10.78	70	11.04
Star-forming centrals			
COSMOS	10.48–10.78	85	10.62
	> 10.78	71	11.08
CDFS	10.48–10.78	83	10.62
	> 10.78	52	11.03
UDS	10.48–10.78	87	10.62
	> 10.78	68	10.97

cent if their rest-frame colors satisfy these criteria:

$$\begin{array}{rcl} U-V & > & 0.88 \times (V-J) + 0.49 \\ U-V & > & 1.3 \\ V-J & < & 1.6 \end{array} \tag{2.1}$$

Figure 2.1 shows the $U-V$ vs. $V-J$ diagram (hereafter UVJ diagram) for the centrals in our ZFOURGE samples. We find that between $1 < z < 3$ the massive centrals (841 in total with $M_{\rm c} > 3 \times 10^{10}$ ${\rm M}_{\odot}$) are roughly evenly divided into quiescent galaxies (47%) and star-forming galaxies (53%) based on their UVJ colors. The numbers of the quiescent and star-forming centrals in each ZFOURGE field and mass subsample are shown in Table 2.1.

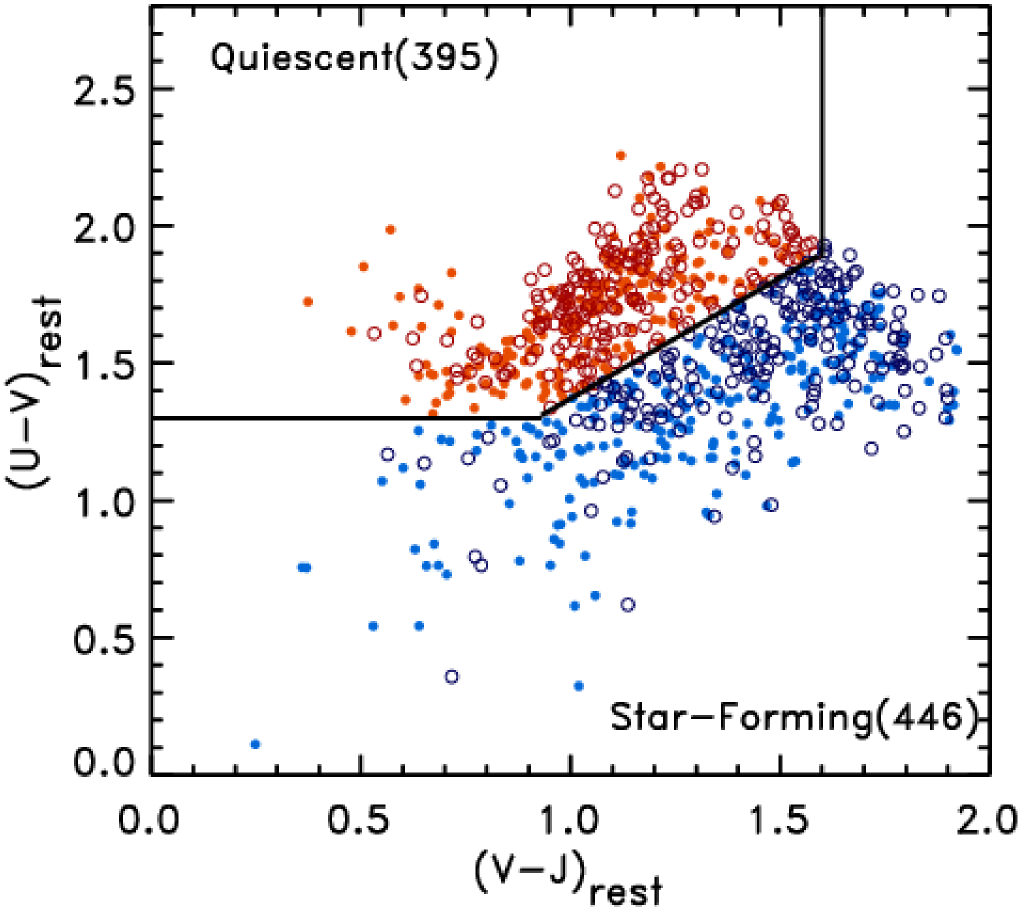

Figure 2.1: Rest-frame $U - V$ versus $V - J$ color for massive central galaxies

Rest-frame $U - V$ versus $V - J$ color for massive central galaxies in our sample from all three ZFOURGE pointings (COSMOS, CDFS, and UDS) at $1 < z < 3$. The data points show centrals with stellar masses of $10.48 < \log(M_{\rm c}/{\rm M}_{\odot}) < 10.78$ (small filled circles) and $\log(M_{\rm c}/{\rm M}_{\odot}) > 10.78$ (large open circles). The galaxies in the upper left region of the plot (separated by the solid line) are quiescent (red open and filled circles); galaxies outside this region are star forming (blue open and filled circles), using the definition of Williams et al. (2009) and Equation 2.2. The numbers of quiescent and star-forming centrals are indicated in parentheses in the plot legend. Quiescent and star-forming galaxies each account for approximately half of galaxies population at these masses and redshifts. Reprinted with permission from “The Distribution of Satellites around Massive Galaxies at $1 < z < 3$ in ZFOURGE/CANDELS: Dependence on Star Formation Activity" by Kawinwanichakij et al., 2014. The Astrophysical Journal, Volume 792, Issue 2, article id. 103 pp. 19, Copyright 2014.

2.3.2 Selection of Satellites

To identify satellites of the central galaxies in our sample, we build on the statistical background subtraction technique, as discussed in Tal et al. (2012, 2013). We first select all galaxies around each central from our ZFOURGE catalogs that satisfy the following conditions

$$\begin{aligned} |z_{\rm c} - z_{\rm sat}| &\leq 0.2 \\ 10^9\ {\rm M}_\odot \leq M_{\rm sat} &< M_{\rm c} \end{aligned} \tag{2.2}$$

where $z_{\rm c}$ and $z_{\rm sat}$ are the photometric redshift of the central and satellite, respectively. Similarly, $M_{\rm c}$ and $M_{\rm sat}$ are the stellar mass of the central and satellite, respectively. Our requirement that $\Delta z = |z_{\rm c} - z_{\rm sat}| \leq 0.2$ is motivated by our relative photometric uncertainty (σ_z) between centrals and satellites derived above. In each case, the σ_z values for galaxies in each ZFOURGE field are less than about half the $\Delta z \leq 0.2$ requirement in Equation 2.2, which argues that this selection criterion is appropriate.

The mass-completeness limits for all galaxies in the ZFOURGE sample at $z = 3$ are $\log(M/{\rm M}_\odot) = 9.3$ (Tomczak et al., 2014). Below these mass limits, we are incomplete for quiescent galaxies, while our sample remains complete for star-forming galaxies down to $\log(M/{\rm M}_\odot) = 9$. However, in this study, we are comparing the relative number of satellites between quiescent and star-forming galaxies, so they have the same relative bias due to incompleteness in satellite detection.

We consider the possibility that our samples of quiescent and star-forming centrals have different redshift distributions. For example, it is possible that the quiescent galaxies are all at low redshift, while star-forming galaxies have higher redshift. Then we might have more satellites around quiescent galaxies because we can see them to lower mass. We have tested that the redshift distributions for quiescent and star-forming centrals are the same (described in Section 2.6.1). We have also repeated our analysis over $1 < z < 2$, where incompleteness is less of an issue, and our primary conclusions are unchanged. Therefore, the redshift distributions of central galaxies do not affect the relative number of satellites between the star-forming and quiescent samples.

2.4 Radial Number Density Profiles

2.4.1 Profile derivation

The method to extract a radial distribution of satellites is illustrated in Figure 2.2, expanding from the method outlined in Tal et al. 2012. For a given projected distance from each central, we measure the number of all galaxies satisfying our definition of satellite in Equation 2.2. This includes both physically associated galaxies, as well as chance alignments of foreground and background galaxies. We measure the projected radial distribution by binning the distance from those galaxies to central galaxies in logarithmic bins.

We remove the contamination from foreground and background galaxies statistically by repeating the measurements in randomly selected positions within the entire area of the ZFOURGE fields. We require that random fields are not centered within 6 arcsec (about 50 kpc, projected) of any central. However, we have not required that the random fields have zero overlap with areas around our centrals, as the surface density of our centrals is $\sim 2\,\mathrm{arcmin}^{-2}$, and such a constraint would be too prohibitive. This is a tradeoff between our requirement to subtract off statistically the foreground and background galaxies, and having a sufficiently high number of the random fields to measure the background accurately in each ZFOURGE field. We then subtract the number density of satellites in the random pointings from the number density of satellites of each central. In practice, we measure the number density of galaxies in > 500 random pointings and take the average to estimate the number density of foreground and background galaxies for each central in each ZFOURGE field.

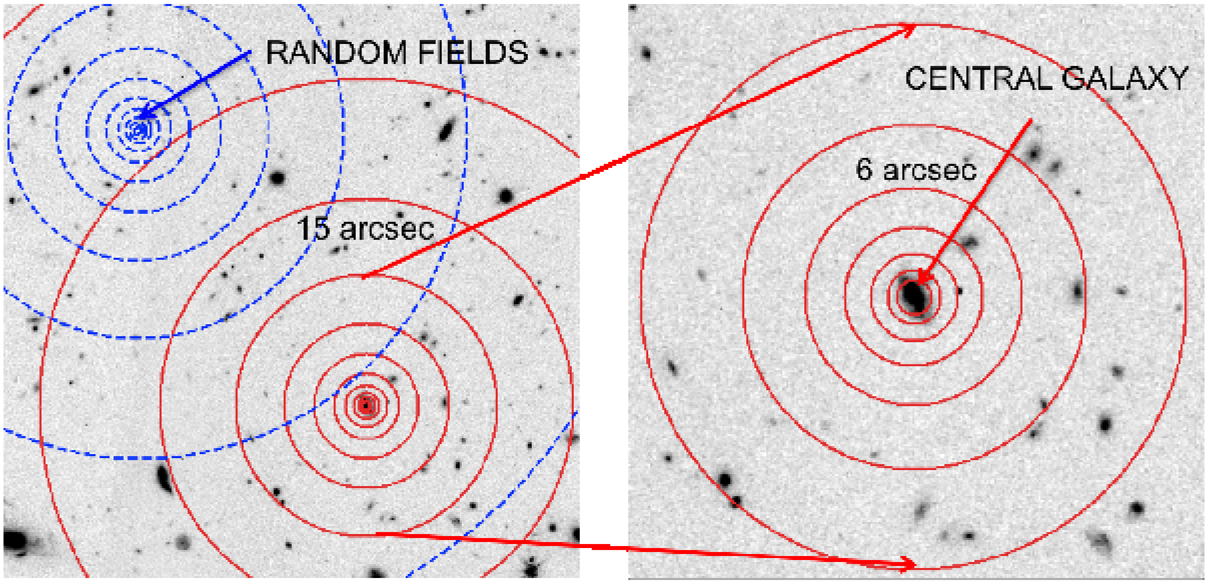

Figure 2.2: Background subtraction technique for measuring radial profile of satellite galaxies.

Demonstration of the statistical technique to measure the radial number density profile of satellite galaxies. All galaxies that satisfy the definition of "satellite" in Equation 2.2 are divided into $\log(r)$ bins around each central (red solid circles) and also around randomly selected positions in the field (blue dashed circles). The number density profile of satellites is then measured from the difference between the satellites measured around the central and those measured in the field. In practice, we use many random fields per each central and calculate the average to infer the statistical distribution of foreground and background galaxies. In this figure we show one random field for illustration only. Reprinted with permission from "The Distribution of Satellites around Massive Galaxies at $1 < z < 3$ in ZFOURGE/CANDELS: Dependence on Star Formation Activity" by Kawinwanichakij et al., 2014. The Astrophysical Journal, Volume 792, Issue 2, article id. 103 pp. 19, Copyright 2014.

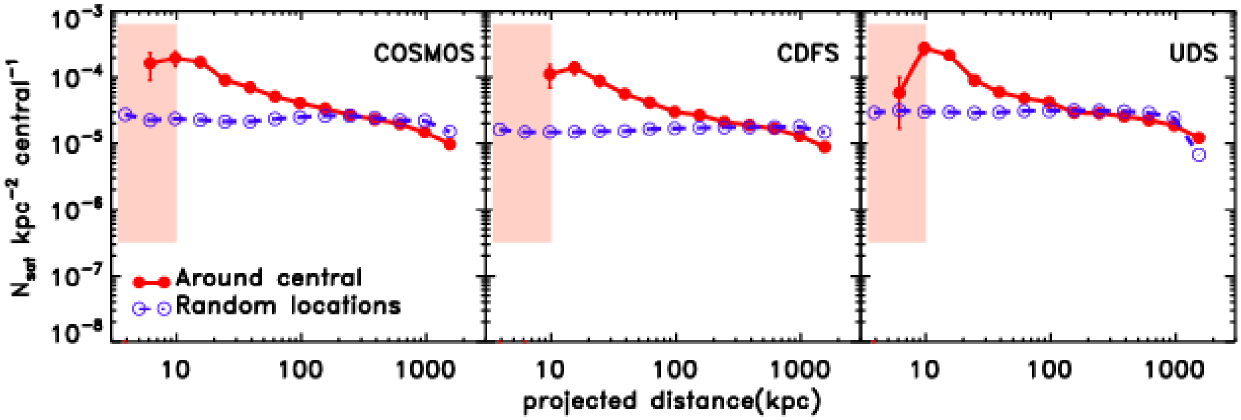

Figure 2.3: Average projected radial profile of galaxies around centrals and in random fields.

The average projected radial profile of satellites around central galaxies at $1 < z < 3$ with stellar masses of $\log(M_c/M_\odot) > 10.48$ and the field in each pointing of ZFOURGE (COSMOS, CDFS, and UDS). The measured projected distribution of satellites is calculated by subtracting the average random profile (blue lines with open circles) from that measured around the central galaxy profile (red lines with filled circles). The shaded areas show the range of projected distance where satellites are blended with centrals; these we exclude from our analysis. Reprinted with permission from "The Distribution of Satellites around Massive Galaxies at $1 < z < 3$ in ZFOURGE/CANDELS: Dependence on Star Formation Activity" by Kawinwanichakij et al., 2014. The Astrophysical Journal, Volume 792, Issue 2, article id. 103 pp. 19, Copyright 2014.

Figure 2.3 shows the raw number density of galaxies measured around both the centrals and measured in random pointings. In each field there is a strong statistical excess of galaxies around our centrals extending from 10 kpc to $\sim$ 100–200 kpc ($\sim$12–25 arcsec), which we attribute to physically associated satellites. There are slight variations in the $N_{\rm sat}$ distribution inferred from the background, as we would expect from natural field-to-field variations. We see no substantial variation in the $N_{\rm sat}$ projected distributions between the three separate fields.

We have tested if this signal changes if we require that no random background aperture is centered within 12 arcsec of a central (compared to the 6 arcsec requirement above), but we find that this does not change significantly the number density of galaxies in the random pointings, and therefore this does not affect our measurement.

At smaller projected distances (< 10 kpc), we are unable to measure reliably the number density of satellites, as such objects are blended with the isophotes of the central galaxies. For example, we cross-match our central galaxy catalog from ZFOURGE to the morphology parameter catalog for the CANDELS WFC3/F160W imaging from van der Wel et al. (2012). From this, the typical effective radii of our centrals at $1 < z < 3$ is $\sim 3.2\,\mathrm{kpc}$, consistent with measurements of massive galaxies at $z \sim 2$ from van Dokkum et al. (2010). Furthermore, van Dokkum et al. show that such galaxies have $\sim 1\%$ of their stellar mass at a distance of $10\,\mathrm{kpc}$. Therefore, it seems likely that satellites around these galaxies would be indistinguishable from substructure in the centrals for projected distances $r < 10$ kpc. Indeed, doing a careful analysis by subtracting the light from the central, Tal et al. (2012) find that the number density of satellites around centrals follows a $r^{1/4}$-law, consistent with the surface-brightness profile of the central galaxies. This suggests that radial density profile of satellites at small scales is strongly influenced by the baryonic content of the central galaxy, rather than the dark matter halo.

Figure 2.4 shows the number density of satellites measured for the centrals in each ZFOURGE field, and for the combined sample. The satellite distribution in each field is consistent with that measured in the combined sample for $10 < r/\,\mathrm{kpc} < 100$, and we observe differences at larger and smaller radii. ZFOURGE contains three largely separated fields on the sky, and we interpret the differences at larger radii as a result of field-to-field variations in the number density of background/foreground galaxies in each field.

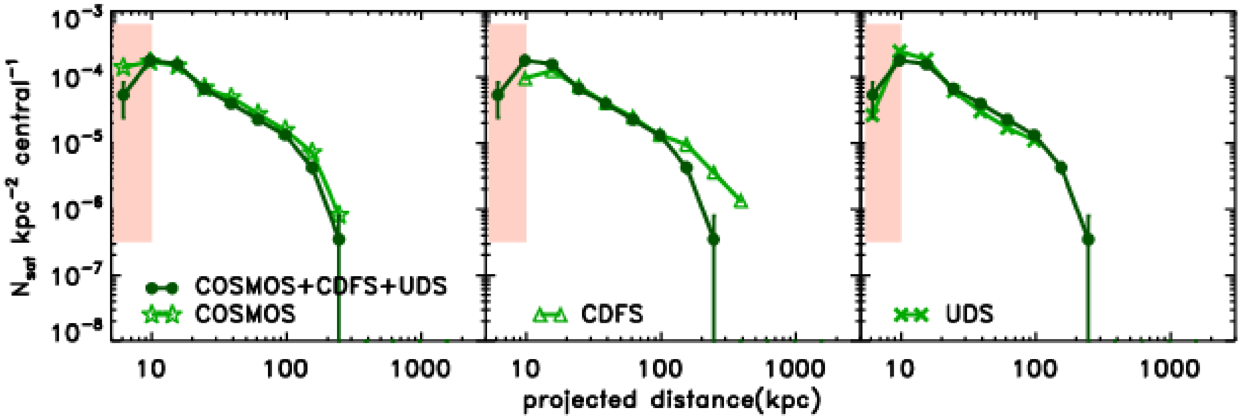

Figure 2.4: Projected radial profile of satellites around central galaxies in each ZFOURGE field.

The projected radial profile for central galaxies at $1 < z < 3$ with stellar masses of $\log(M_c/\mathrm{M}_\odot) > 10.48$ combined from all ZFOURGE fields (dark green solid line), compared to the profiles of each field separately (light green). In each panel, the combined measurement is the same, where each field shows the result from COSMOS (left panel), CDFS (middle panel), and UDS (right panel). The profile of each field separately is consistent with the combined one at $10 < r/\,\mathrm{kpc} < 100$, but differences exist at larger projected radii, which we attribute to variations in the background of field galaxies. Reprinted with permission from “The Distribution of Satellites around Massive Galaxies at $1 < z < 3$ in ZFOURGE/CANDELS: Dependence on Star Formation Activity" by Kawinwanichakij et al., 2014. The Astrophysical Journal, Volume 792, Issue 2, article id. 103 pp. 19, Copyright 2014.

2.4.2 Model Fitting

We fit the combined projected number-density profile of satellites using a simple powerlaw model, where $N_{\mathrm{sat}} \propto r^{\gamma}$. Figure 2.5 shows that in the range $10 < r/\,\mathrm{kpc} < 100$ the profile is well described by the power-law with $\gamma = -1.28 \pm 0.08$. The power-law slope of the projected radial profile of satellites around luminous red galaxies at $z = 0.34$ is -1.1 (Tal et al., 2012), which is marginally consistent with our measurement here.

We also compare our measured projected radial profile of satellites with a projected NFW profile, which Bartelmann (1996) show is

$$\Sigma(x) = \begin{cases} (x^2-1)^{-1}\left(1 - \frac{2}{\sqrt{x^2-1}}\arctan\sqrt{\frac{x-1}{x+1}}\right) & (x > 1) \\ 1/3 & (x = 1) \\ (x^2-1)^{-1}\left(1 - \frac{2}{\sqrt{1-x^2}}\mathrm{arctanh}\sqrt{\frac{1-x}{1+x}}\right) & (x < 1) \end{cases}$$

where $x \equiv r/r_s$ and r_s is the NFW-profile scale radius. We utilize the nonlinear least-squares curve fitting program MPFIT (Markwardt, 2009) to fit the projected NFW model to the measured projected radial profile of satellites around centrals at $10 < r/\,\mathrm{kpc} < 100$, where we fit for both the normalization factor and scale radius.

Figure 2.5 shows that our derived projected radial density of satellites at $1 < z < 3$ is well fitted by the projected NFW model with $r_s = 32.8 \pm 7.1\,\mathrm{kpc}$. Assuming the scale radius is independent of redshift and only scales with a halo mass as $r_s \sim M_h^{0.45}$ (e.g., Bullock et al., 2001), this would predict $r_s \simeq 100$ kpc at $z = 0$ (assuming a factor ∼10 growth in halo mass, see e.g.,Moster et al. (2013)). This is smaller than that found by Tal et al. (2012), who find $r_s \sim 270$ kpc for galaxies at $z = 0.02$ in SDSS, but the results are probably consistent as the galaxies in their sample correspond to progenitors with higher stellar masses by factors of ∼3–5 compared to our sample here (e.g., Tal et al., 2013). Furthermore, this provides us with confidence that our measured satellite distribution is tracing the dark-matter halo of the centrals in our ZFOURGE samples.

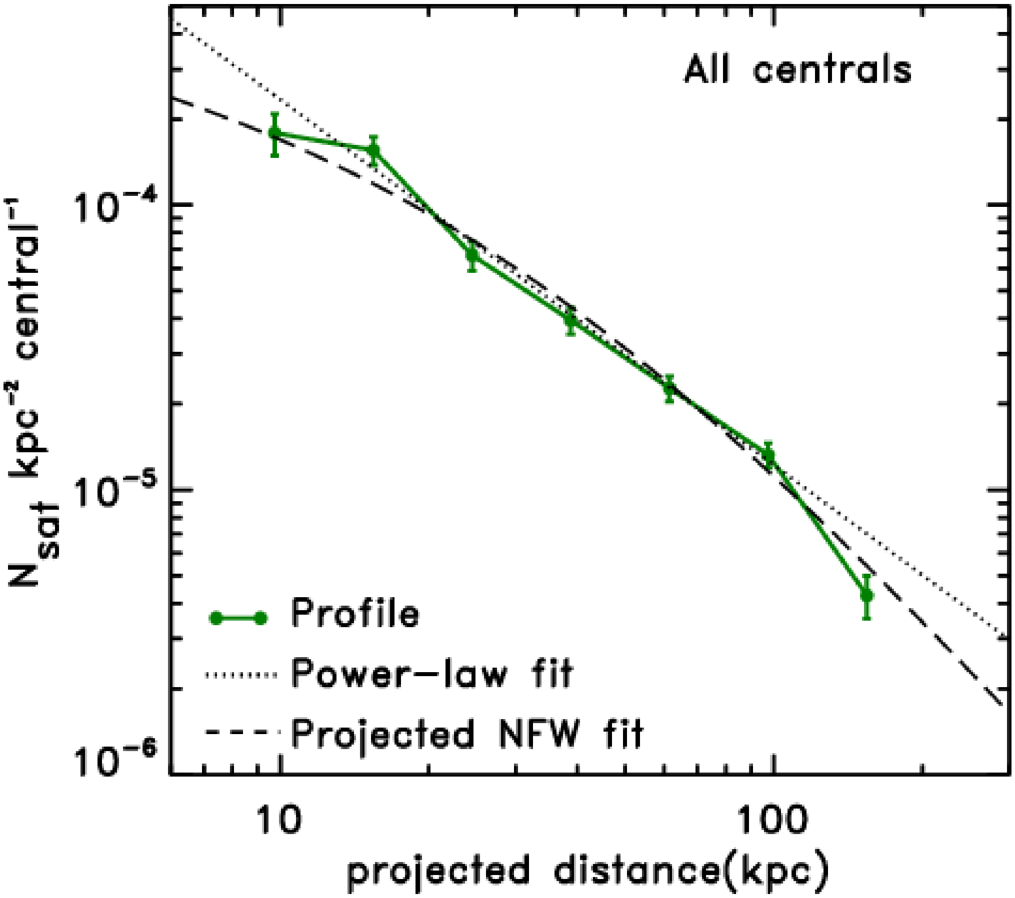

Figure 2.5: Projected radial profile of satellites around central galaxies in combined ZFOURGE fields.

The average projected radial profile of satellites around all central galaxies at $1 < z < 3$ with stellar masses of $\log(M_{\rm c}/{\rm M}_{\odot}) > 10.48$ (green solid line) combined from all ZFOURGE fields. The radial profile is fitted well with a power-law model with $r^{-1.3}$ (dotted line) and a projected NFW model with $r_s = 32.8 \pm 7.1$ kpc (dashed line) over the range $10 < r/{\rm kpc} < 100$. Reprinted with permission from “The Distribution of Satellites around Massive Galaxies at $1 < z < 3$ in ZFOURGE/CANDELS: Dependence on Star Formation Activity" by Kawinwanichakij et al., 2014. The Astrophysical Journal, Volume 792, Issue 2, article id. 103 pp. 19, Copyright 2014.

2.5 The Satellite Distribution Dependence on Galaxy Property

2.5.1 Significance estimation

It is desirable to assign a significance statistic (p-value) when comparing the differences between the satellite number densities for different subsamples. The uncertainties of each datum of our projected radial distribution of satellites ($N_{\rm sat}$ in the figures above) are derived using simple Poisson statistics. When comparing the satellite number density distributions for difference subsamples, we use two methods, a direct rank-sum test and a Monte Carlo simulation. In practice, for reasons described below we find that the Monte Carlo simulation provides more physical probabilities, and we will use those to estimate the significance in our results.

We first apply a one-sided Wilcoxon-Mann-Whitney rank-sum (WMW) test (Mann & Whitney, 1947) to quantify a probability that the number density of satellites around quiescent and star-forming centrals have the same parent population. The WMW test measures a probability (p-value) using the data and Poisson errors on the satellite distributions between two subsamples (e.g., the quiescent and star-forming centrals). However, the WMW test is not strictly appropriate for our analysis because we are applying it to heavily binned data: each datum is binned (logarithmically) in radius over $10 < r/\mathrm{kpc} < 200$. In particular, the WMW test is insensitive to the fact that our sample includes hundreds of central galaxies and thousands of satellite galaxies.

To estimate meaningful p-values, we use a Monte Carlo approach. We create 10,000 simulations for each subsample of central galaxies. For a given stellar mass range of the central subsample, we randomly select new samples of centrals from the subsample (allowing replacement). We then randomly assign each galaxy to be either quiescent or star-forming. In each simulated subsample, the number of the quiescent and star-forming centrals are equal to the actual number of each in the real subsamples. We then recalculate the radial number density of satellites for each set of random samples and calculate the $p_{\rm WMW}$–value using the WMW test for each iteration. The likelihood from the Monte Carlo simulations $(p_{\rm MC})$ are calculated by determining the fraction of the number of simulations when we have the $p_{\rm WMW}$ less than the $p_{\rm WMW}$ value we derive from the real data. A summary of these likelihoods is given in Table 2.2.

Table 2.2: Summary of the probabilities p-values comparing the number density of satellites around quiescent and star-forming centrals at $1 < z < 3$ in the ZFOURGE survey. Reprinted with permission from “The Distribution of Satellites around Massive Galaxies at $1 < z < 3$ in ZFOURGE/CANDELS: Dependence on Star Formation Activity" by Kawinwanichakij et al., 2014. The Astrophysical Journal, Volume 792, Issue 2, article id. 103 pp. 19, Copyright 2014.

Sample	$\log(M_{\rm c}/{\rm M}_\odot)$	$N_{\rm c}$(Quiescent)	$N_{\rm c}$(Star − forming)	$p_{\rm MC}$
All centrals	> 10.48	395	446	0.081
	10.48-10.78	205	255	0.478
	> 10.78	190	191	0.002
Fixed in stellar mass	> 10.48	337	337	0.550
	10.48-10.78	195	195	0.985
	> 10.78	142	142	0.004

(1) Description of samples used, (2) stellar mass of the sample, (3) number of quiescent centrals, (4) number of star-forming centrals, and (5) The probability we derive from our Monte Carlo simulations that we would have obtain a difference between the satellite distributions of the quiescent and star-forming centrals by chance. Low probabilities (p-value) indicate more significant differences in the distributions.

2.5.2 Dependence on Central Stellar Mass

We study how the number density of satellites depends on the stellar mass of centrals by dividing our central galaxy sample into two mass bins: $10.48 < \log(M_{\rm c}/{\rm M}_\odot) < 10.78$ and $\log(M_{\rm c}/{\rm M}_\odot) > 10.78$. We then recompute the number density of satellites for each of these subsamples using the method above. Figure 2.6 shows that the more massive centrals have a higher number density of satellites compared to the lower mass centrals. Using our Monte Carlo simulations (see Section 2.5.1), we find that the significance of this result is $p_{\rm MC} = 0.026$ ($\simeq 1.9\sigma$). Therefore, there is suggestive evidence that the number of satellites increases with the stellar mass of the central galaxy.

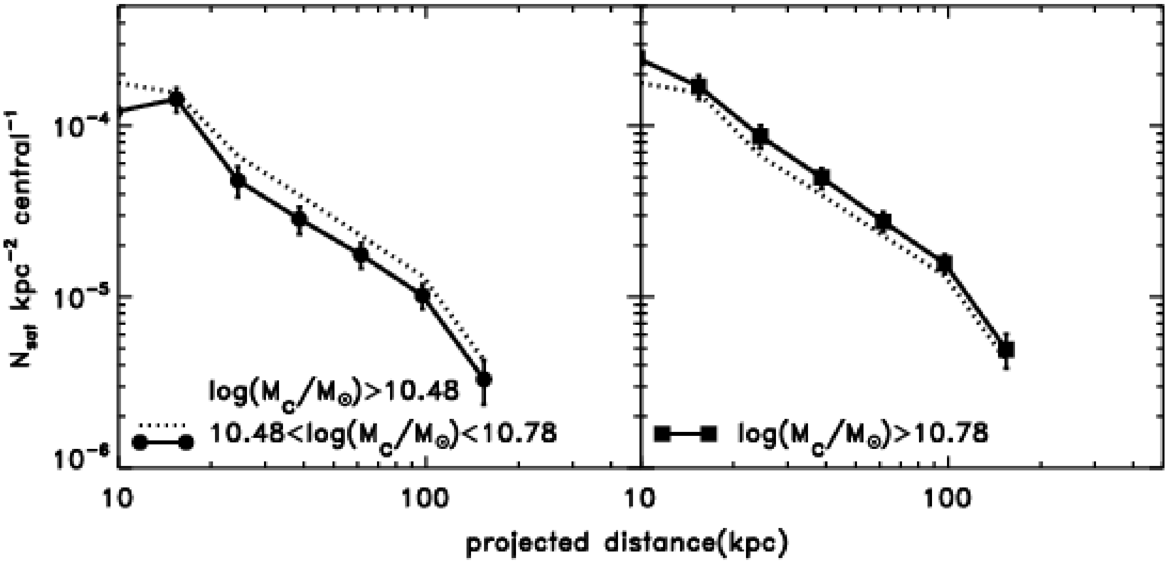

Figure 2.6: The dependence of the number density of satellites on stellar mass of the central.

Left: the projected radial profile around all ZFOURGE centrals at $1 < z < 3$ with stellar masses of $10.48 < \log(M_{\rm c}/{\rm M_\odot}) < 10.78$ (solid line with circles) compared with that of all samples with stellar masses of $\log(M_{\rm c}/{\rm M_\odot}) > 10.48$ (dotted line), ***Right:*** same as the left panel but for the comparison between the profile of satellites around centrals with stellar masses of $\log(M_{\rm c}/{\rm M_\odot}) > 10.78$ (solid line with boxes) and the profile of total centrals. The number of satellites around centrals with stellar masses of $\log(M_{\rm c}/{\rm M_\odot}) > 10.78$ is higher on average than that around centrals with stellar masses of $10.48 < \log(M_{\rm c}/{\rm M_\odot}) < 10.78$ at 1.9σ. Reprinted with permission from “The Distribution of Satellites around Massive Galaxies at $1 < z < 3$ in ZFOURGE/CANDELS: Dependence on Star Formation Activity" by Kawinwanichakij et al., 2014. The Astrophysical Journal, Volume 792, Issue 2, article id. 103 pp. 19, Copyright 2014.

2.5.3 Dependence on Star Formation Activity of Central Galaxy

We investigate how the satellite distribution depends on the star-formation activity of the central galaxies by dividing our sample of central galaxies into subsamples that are star-forming and quiescent (where these labels correspond to galaxies with high and low sSFRs) using their rest-frame $U - V$ and $V - J$ colors as illustrated in Figure 2.1 and discussed in Section 2.3.1. We then recompute the satellite distribution for each subsample.

Figure 2.7 shows the projected radial distribution of satellites around the star-forming and quiescent centrals with $\log(M_{\rm c}/{\rm M}_{\odot}) > 10.48$. We find that quiescent centrals host more satellites than their star-forming counterparts. Using our Monte Carlo simulation the likelihood we would obtain this result by chance has a probability of $p_{\rm MC} = 0.081$, corresponding to 1.4σ significance.

We further investigate how the number density of satellites depends on both star-formation activity and stellar mass of the central. Figure 2.8 shows for centrals with moderate stellar mass $10.48 < \log(M_{\rm c}/{\rm M}_{\odot}) < 10.78$. There is no significant evidence that the number density depends on star-formation activity (with a p-value $p_{\rm MC} = 0.478$): both quiescent and star-forming moderate mass centrals have the same number of satellites. In contrast, all the difference in the number density of satellites occurs for centrals at the high stellar-mass end. For the high mass centrals, $\log(M_{\rm c}/{\rm M}_{\odot}) > 10.78$, the quiescent central galaxies have a significant excess of satellites compared to the star-forming centrals, with a p-value of $p_{\rm MC} = 0.002$ (significant at about $\simeq 3.1\sigma$). We discuss the implications of these results in Section 2.6.

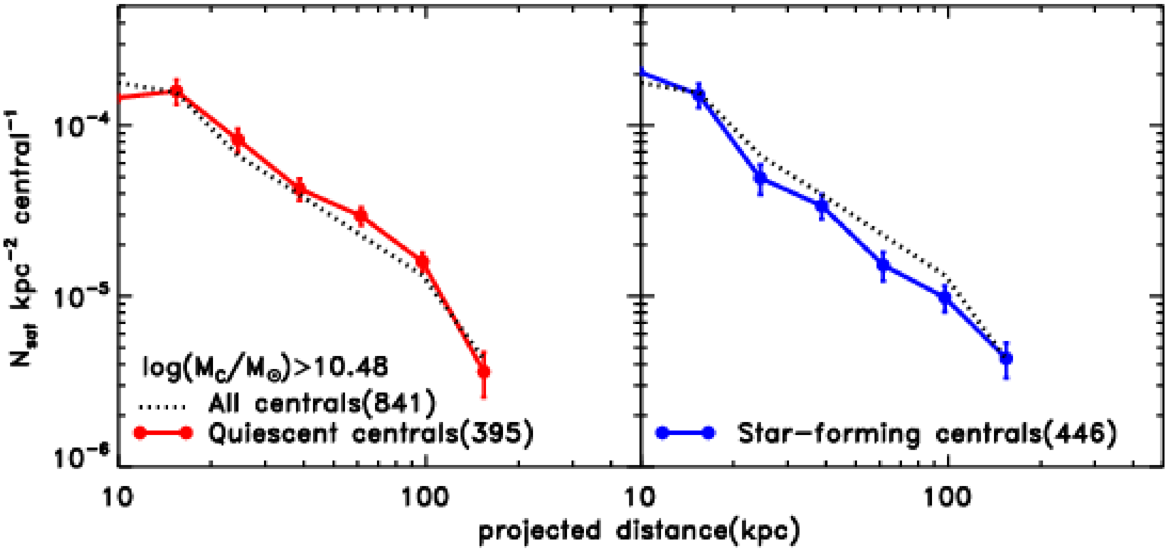

Figure 2.7: The dependence of the number density of satellites on star-formation activity of the central.

Left: the projected radial profile around all centrals (black dotted line) at $1 < z < 3$ with stellar masses of $\log(M_c/\mathrm{M}_\odot) > 10.48$ compared with the profile of quiescent centrals (red solid line). ***Right:*** the projected radial profile around all centrals (black dotted line) at $1 < z < 3$ with stellar masses of $\log(M_c/\mathrm{M}_\odot) > 10.48$ compared with the profile of star-forming centrals (blue solid line). In each panel, the number in parentheses gives the number of centrals in each subsample. The number of satellites around quiescent centrals is higher on average than that around star-forming centrals at 1.4σ. Reprinted with permission from “The Distribution of Satellites around Massive Galaxies at $1 < z < 3$ in ZFOURGE/CANDELS: Dependence on Star Formation Activity" by Kawinwanichakij et al., 2014. The Astrophysical Journal, Volume 792, Issue 2, article id. 103 pp. 19, Copyright 2014.

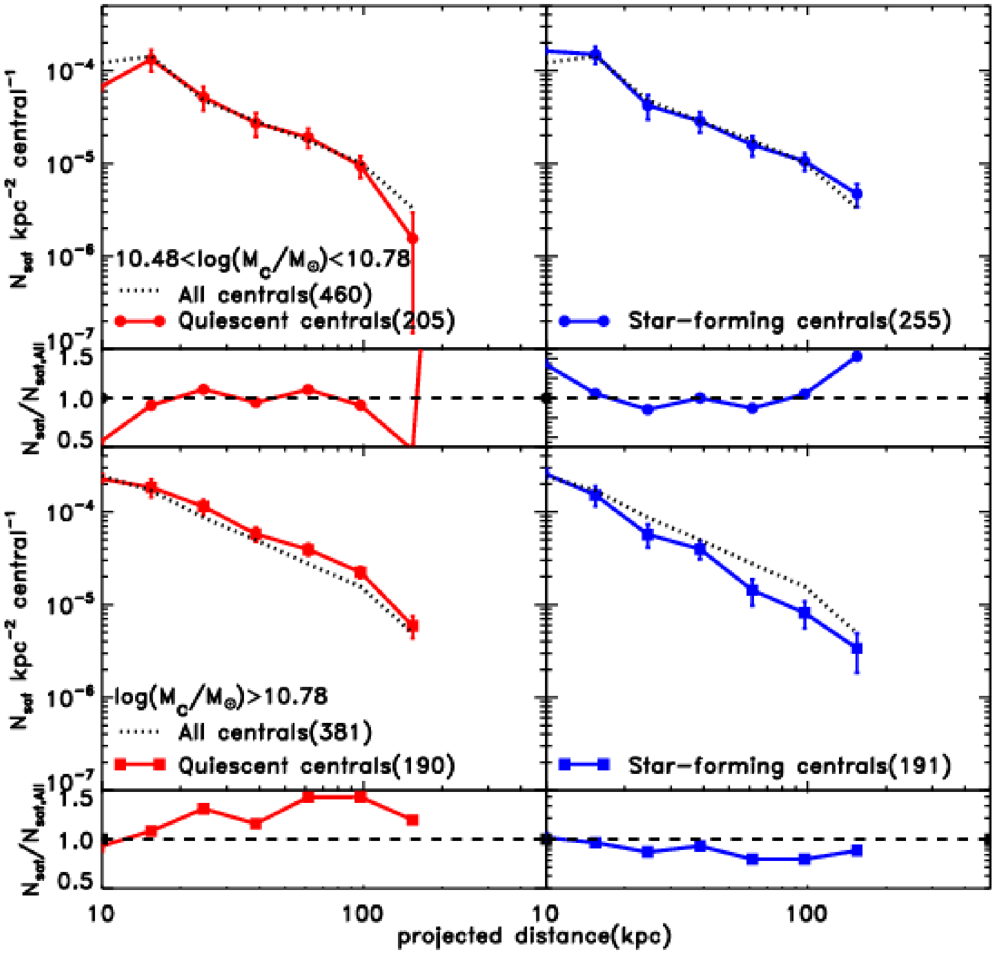

Figure 2.8: The dependence of the number density of satellites on star-formation activity and stellar mass.

Top: the projected radial profile around all centrals (black dotted line) at $1 < z < 3$ with stellar masses of $10.48 < \log(M_{\rm c}/{\rm M}_{\odot}) < 10.78$ compared with quiescent centrals (red solid line with circles, left panel) and star-forming centrals (blue solid line with circles, right panel). ***Bottom:*** the projected radial profile around all centrals (black dotted line) at $1 < z < 3$ with stellar masses of $\log(M_{\rm c}/{\rm M}_{\odot}) > 10.78$ compared with quiescent centrals (red solid line with boxes, left panel) and star-forming galaxies (blue solid line with boxes, right panel). The number in parentheses is the number of centrals in each subsample. Below each $N_{\rm sat}$ plot the ratio of $N_{\rm sat}$ around quiescent (star-forming) centrals to the $N_{\rm sat}$ around all centrals is shown to illustrate the difference between $N_{\rm sat}$ around quiescent and star-forming centrals. The uncertainty on the ratio is derived assuming that the uncertainties on the number of quiescent galaxies and star-forming galaxies both are given by Poisson statistics, and they are uncorrelated. However, the derived error bars of the ratios are very small compared to the size of the data points. For the centrals with stellar masses of $\log(M_{\rm c}/{\rm M}_{\odot}) > 10.78$, the quiescent central galaxies have $\sim 2\times$ the number of satellites compared to star-forming centrals, and this difference is significant at 3.1σ. Reprinted with permission from “The Distribution of Satellites around Massive Galaxies at $1 < z < 3$ in ZFOURGE/CANDELS: Dependence on Star Formation Activity" by Kawinwanichakij et al., 2014. The Astrophysical Journal, Volume 792, Issue 2, article id. 103 pp. 19, Copyright 2014.

2.5.4 Cumulative Number Density of Satellite Galaxies

We integrate the satellite number densities to measure the total (cumulative) number of satellites within a projected distance of the centrals in our samples down to our mass limit for the satellites, $\log(M/\mathrm{M}_{\odot}) > 9$. Figure 2.9 compares the cumulative number density of satellites around quiescent centrals and star-forming centrals with $10.48 < \log(M_{\mathrm{c}}/\mathrm{M}_{\odot}) < 10.78$ and $\log(M_{\mathrm{c}}/\mathrm{M}_{\odot}) > 10.78$. On average the intermediate mass centrals have $\approx$1 satellite more massive than $\log(M_{\mathrm{sat}}/\mathrm{M}_{\odot}) > 9$ within 100 kpc. This is true for both the star-forming and quiescent centrals. The intermediate mass star-forming galaxies have an excess of satellites at larger projected radii than the quiescent centrals, but this has $<2\sigma$ significance.

Figure 2.9 also shows that the massive quiescent centrals ($\log(M_{\mathrm{c}}/\mathrm{M}_{\odot}) > 10.78$) have nearly double the number of satellites more massive than $\log(M_{\mathrm{sat}}/\mathrm{M}_{\odot}) > 9$ within 100–200 kpc compared to the massive star-forming centrals. On average a massive star-forming central has $\approx$1 such satellite, whereas a massive quiescent central has $\approx$2. These results are comparable with the number of satellites found around massive centrals by Tal et al. (2013), who find that on average the total number of galaxies with the mass ratio of 1:10 and within 400 kpc around the massive centrals between $z = 0.04$ to $z = 1.6$ is 2 to 3.

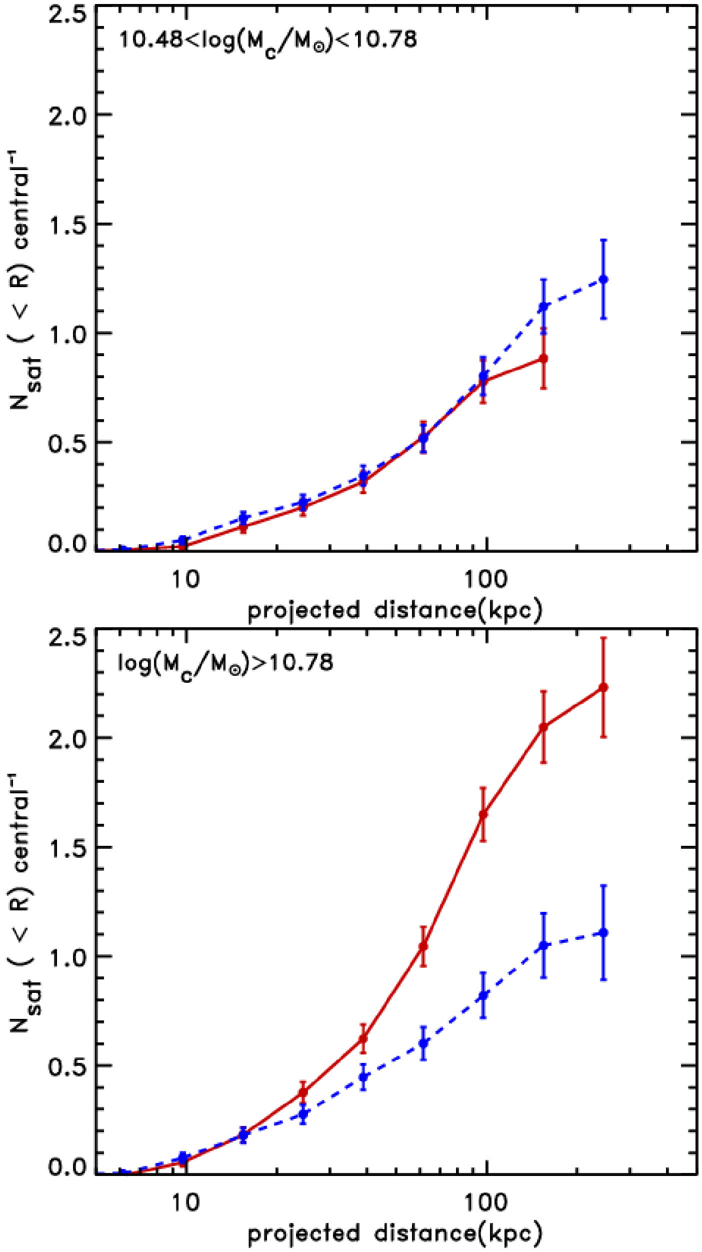

Figure 2.9: Cumulative number of satellites as a function of projected distance for quiescent central galaxies and star-forming central galaxies.

Cumulative number of satellites as a function of projected distance for quiescent central galaxies (red solid lines) and star-forming central galaxies (blue dashed line). *Top:* Quiescent centrals (red solid lines) and star-forming central galaxies (blue dashed line) with $10.48 < \log(M_{\rm c}/{\rm M}_{\odot}) < 10.78$. *Bottom:* the cumulative number of satellites for centrals with stellar mass of $\log(M_{\rm c}/{\rm M}_{\odot}) > 10.78$. At $1 < z < 3$ centrals with these stellar masses have between 1 and 2.5 satellites within 200 kpc depending on mass and star-formation activity. Reprinted with permission from "The Distribution of Satellites around Massive Galaxies at $1 < z < 3$ in ZFOURGE/CANDELS: Dependence on Star Formation Activity" by Kawinwanichakij et al., 2014. The Astrophysical Journal, Volume 792, Issue 2, article id. 103 pp. 19, Copyright 2014.

2.6 Discussion

2.6.1 Why do Quiescent and Star-forming Centrals have Different Satellite Distributions?: the Effects of Stellar Mass and Redshift

There is significant evidence that at high stellar mass ($\log(M_{\rm c}/{\rm M}_{\odot}) > 10.78$) quiescent galaxies have more satellites than star-forming galaxies. There are two interpretations. One is that there is something intrinsic to a galaxy being quiescent that also causes the galaxy to have more satellites. The second is that the higher number of satellites is related to stellar mass. If the quiescent centrals have higher stellar masses than the star-forming galaxies—even though the stellar mass *limit* is the same—then they may also be expected to have more satellites.

We test the second of these possibilities by looking at the cumulative stellar mass distribution of the quiescent and star-forming centrals. As shown in Figure 2.10, indeed the quiescent centrals have a slightly higher median stellar mass, which is higher than the median for the star-forming centrals by 0.05 dex.

Although this difference in stellar mass between the quiescent and star-forming centrals is small, it could affect the number of satellites. Therefore, we make a new sample of quiescent centrals from our real sample. First, we divide the sample of centrals into narrow stellar mass bins. In each stellar mass bin we randomly select equal numbers of quiescent and star-forming galaxies, therefore creating a new sample matched in stellar mass. The numbers of the quiescent and star-forming centrals in the matched stellar mass samples are shown in Table 2.2. The right panel of Figure 2.10 shows that the stellar mass distributions of the matched samples agree very well.

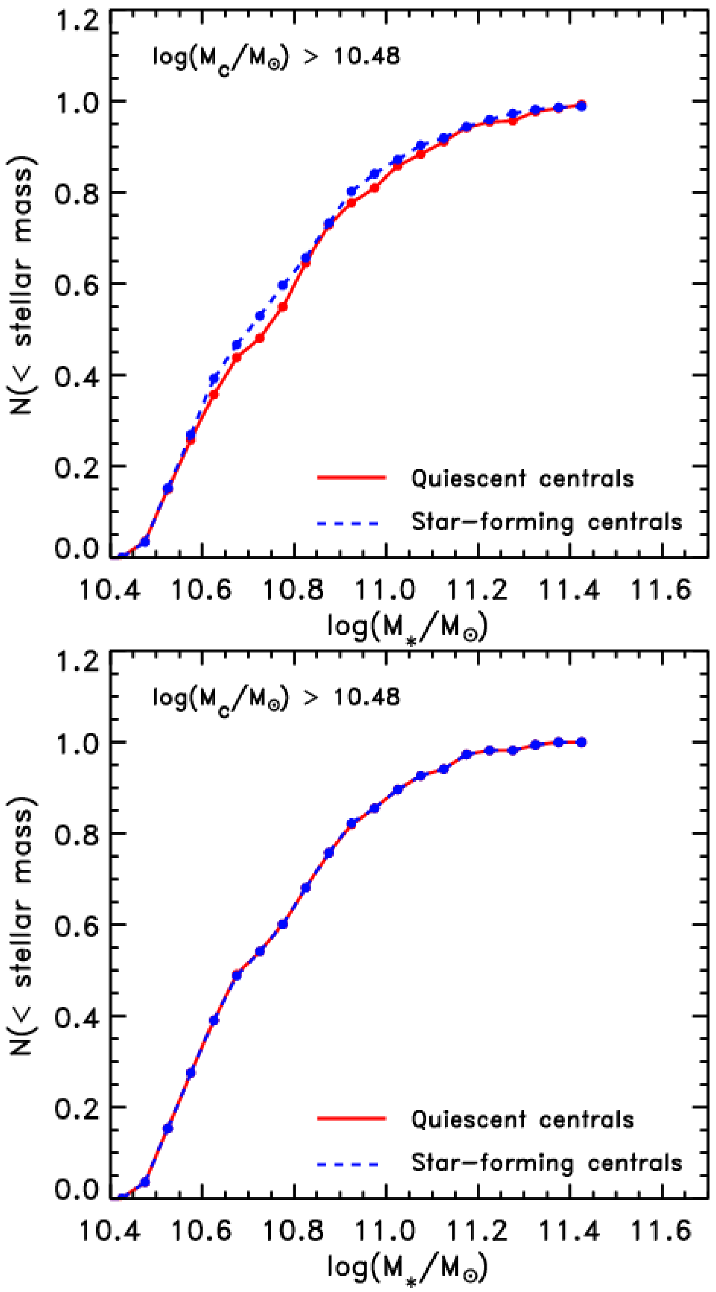

Figure 2.10: Cumulative distribution in stellar mass for the quiescent centrals and star-forming centrals.

Top: the stellar mass distribution of the full samples in our ZFOURGE data for centrals $\log(M_{\rm c}/{\rm M}_\odot) > 10.48$. The quiescent centrals (red curve) have a slightly higher median stellar mass, and this could be related to those galaxies having more satellites than the star-forming galaxies (blue curves). ***Bottom:*** the same distribution after we have matched the stellar mass distributions. This allows us to test if the quiescent centrals have more satellites even when they are matched in stellar mass to the star-forming centrals. Reprinted with permission from “The Distribution of Satellites around Massive Galaxies at $1 < z < 3$ in ZFOURGE/CANDELS: Dependence on Star Formation Activity" by Kawinwanichakij et al., 2014. The Astrophysical Journal, Volume 792, Issue 2, article id. 103 pp. 19, Copyright 2014.

After we match the mass distributions of quiescent and star-forming centrals, we then recalculate the number density profiles of satellites around the centrals for each subsample. Figure 2.11 shows that the number densities of satellites of moderate mass quiescent and star-forming centrals with $10.48 < \log(M_{\rm c}/{\rm M}_{\odot}) < 10.78$ are nearly identical with no evidence for any difference. Our Monte Carlo tests (Section 2.5.1) give 98.5% likelihood ($p_{\rm MC} = 0.985$) that the distributions are identical.

However, the excess of satellites around the massive quiescent centrals with $\log(M_{\rm c}/{\rm M}_{\odot}) > 10.78$ compared to the massive star-forming centrals is still significant, where our Monte Carlo tests give a likelihood that we would have obtained this result by chance as 0.4% (i.e., the difference is significant at $\simeq 2.7\sigma$ ($p_{\rm MC} = 0.004$)). Therefore, while the offset in the stellar mass accounts for some of the increase in the number of satellites around the massive centrals, it is unable to account for all of it. Even though the stellar masses are matched, the massive quiescent centrals have more satellites than star-forming centrals.

As another check, one could expect that quiescent and star-forming galaxies may have different redshift distributions, i.e., if at fixed stellar mass the star-forming galaxies lie at higher redshift, then this could possibly affect our results, as the number of satellites (and dark matter halo mass) could build up with time. For example, Moster et al. (2013) show that at fixed stellar mass the halo mass of massive galaxies increases with decreasing redshift.

However, using the WMW statistic we find no statistically significant difference between the quiescent/star-forming redshift distributions for either moderate ($p_{\rm WMW} = 0.166$) or high-mass centrals ($p_{\rm WMW} = 0.358$).

As a final check, we recalculate the number density of satellites for our samples of centrals, restricting the redshift range of centrals to $1 < z < 2$. The results are consistent with the satellite distribution measured for the full $1 < z < 3$ samples. This also implies that the number of satellites does not change very much over this redshift range. Tal et al. (2013) find that the radial number density of satellites has not evolved much over $z = 0.04 - 1.6$. Therefore, our results show that the trend observed by Tal et al. extends to $z \sim 3$.

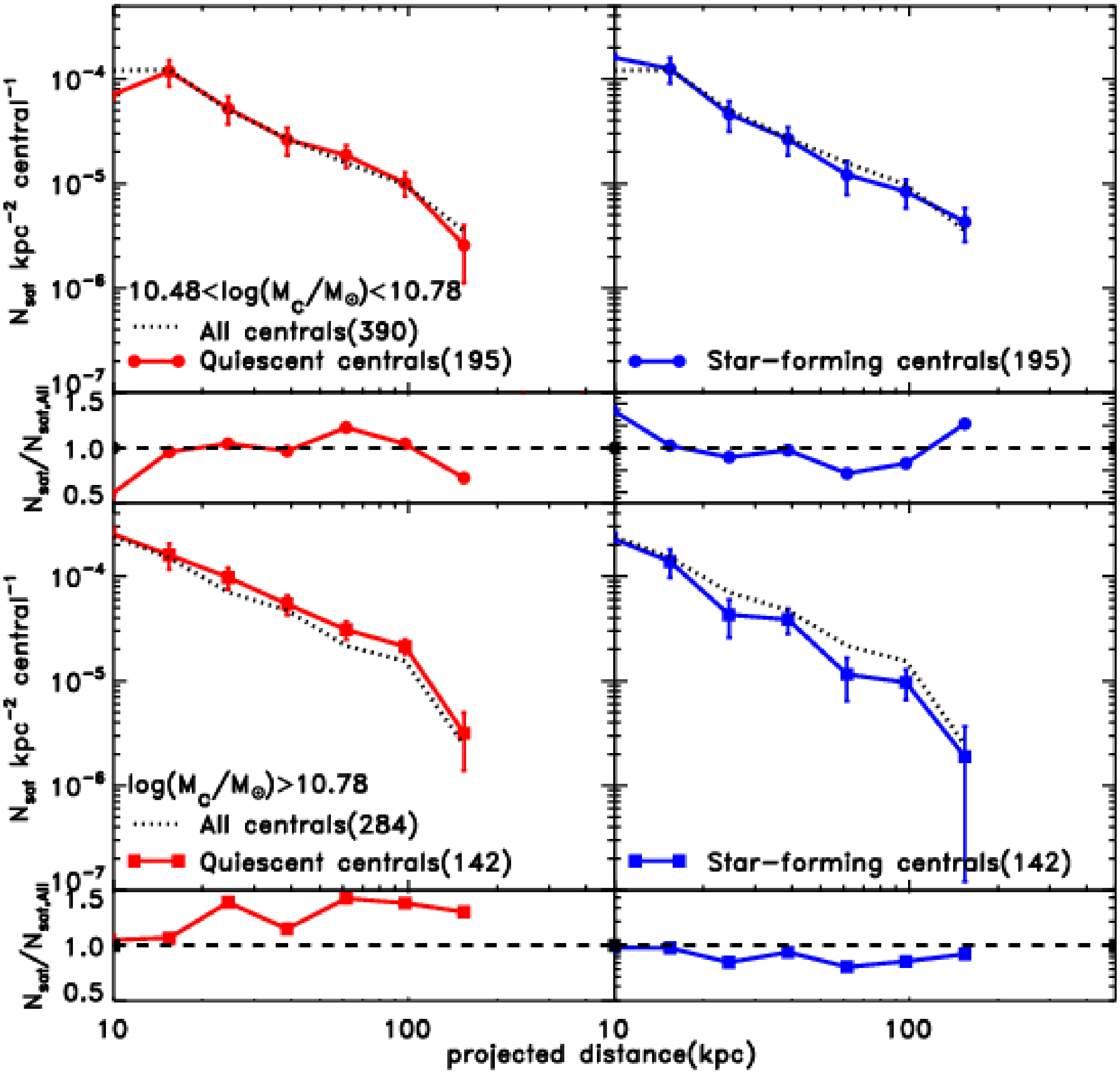

Figure 2.11: Cumulative distribution in stellar mass for the mass-matched quiescent centrals and star-forming centrals.

Same as Figure 2.8 but for the subsamples in which the cumulative stellar mass density of quiescent and star-forming centrals have been matched (see Figure 2.10). In the high mass subsample $\log(M_c/M_\odot) > 10.78$, quiescent centrals have a higher number density of satellites compared to star-forming counterparts at 2.7σ even when the stellar mass distributions of the quiescent and star-forming galaxies are fixed. Reprinted with permission from “The Distribution of Satellites around Massive Galaxies at $1 < z < 3$ in ZFOURGE/CANDELS: Dependence on Star Formation Activity" by Kawinwanichakij et al., 2014. The Astrophysical Journal, Volume 792, Issue 2, article id. 103 pp. 19, Copyright 2014.

To summarize, there appears to be some physical connection between the quenching of star-formation and the presence of an increased number of satellites, at least for massive galaxies. One likely explanation is that the higher number of satellites corresponds to larger dark-matter halo masses, and that at fixed stellar mass the quiescent galaxies have higher halo mass. Because we have no direct measures of the halo masses of the galaxies in our sample, we test this conclusion using semi-analytical models of galaxy formation in the next section.

2.6.2 Comparison to the Guo et al. Semi-Analytic Model: the Role of Halo Mass

To further explore the physical reasons that the massive ($\log(M_{\rm c}/{\rm M}_\odot) > 10.78$) quiescent centrals have more satellites than star-forming counterparts at $1 < z < 3$, we use predictions from the semi-analytic model (SAM) of Guo et al. (2011). The Guo et al. SAM is derived using the Millennium-I simulation (Springel et al., 2001). Henriques et al. (2012) provide mock "lightcone" catalogs from the Guo et al. models, and these lightcones include galaxies at redshifts and to (low) stellar masses comparable to our ZFOURGE dataset.

We select central galaxies from the mock catalogs using the same redshift and stellar mass limits as for our ZFOURGE samples. We further split the mock centrals by sSFR into quiescent ($\log({\rm sSFR}/{\rm yr}^{-1}) < -10$) and star-forming ($\log({\rm sSFR}/{\rm yr}^{-1}) > -10$) subsamples. We use the sSFRs for this classification because currently the Henriques et al. (2012) light cones do not include rest-frame magnitudes (e.g., we are unable to classify them using the UVJ colors as done for the ZFOURGE galaxies). However, this makes little difference as Papovich et al. (2012) show that at $z \sim 1.6$ the sSFR threshold of $\log({\rm sSFR}/{\rm yr}^{-1}) = -10$ effectively separates galaxies classified as quiescent or star-forming by a UVJ-type color-color selection. Therefore, the sSFR selection here is equivalent to our UVJ color-color selection above.

We identify centrals and measure the number density of satellites at $1 < z < 2$ in the SAM lightcone using the same methods as applied to the data. We restrict ourselves to comparisons between the SAM and our data to $1 < z < 2$ and $\log(M/{\rm M}_\odot) > 9.33$ because this is the adopted stellar mass-completeness limit for red satellites at $z = 2$ in the ZFOURGE data (Tomczak et al., 2014). We note that the SAM is also complete to this mass limit. We then measure the projected radial number density of satellites around centrals in the SAM and in the data using this mass limit and redshift range.

Figure 2.12 compares the satellite number density profiles in the SAM for the different central samples in our ZFOURGE data. The shape of the distributions is similar between the SAM and the data, but the SAM has $\sim 3\times$ the satellites than the data at nearly all projected radii. For our comparison here, we are interested in the relative difference between the quiescent and star-forming centrals in the data and the simulation, so this offset is less important. The reason for this offset is an interesting problem (this is similar to the well-known "missing satellite problem" (Bullock, 2010)), and may indicate a mistreatment of important physics in the models. For example, the stellar mass functions in the SAM show a higher number density of lower mass galaxies at $1.3 < z < 3.0$ compared to observations (see Guo et al. 2011, their Figure 23), and it may be expected that such a disagreement would carry over to the satellite population. We do note that Wang & White (2012); Wang et al. (2014) find the good agreement in the abundance of satellites in the low-redshift SDSS data and in the Guo et al. (2011) SAM. The origin of our observed offset in the number of satellites in the SAM and our data is not clear.

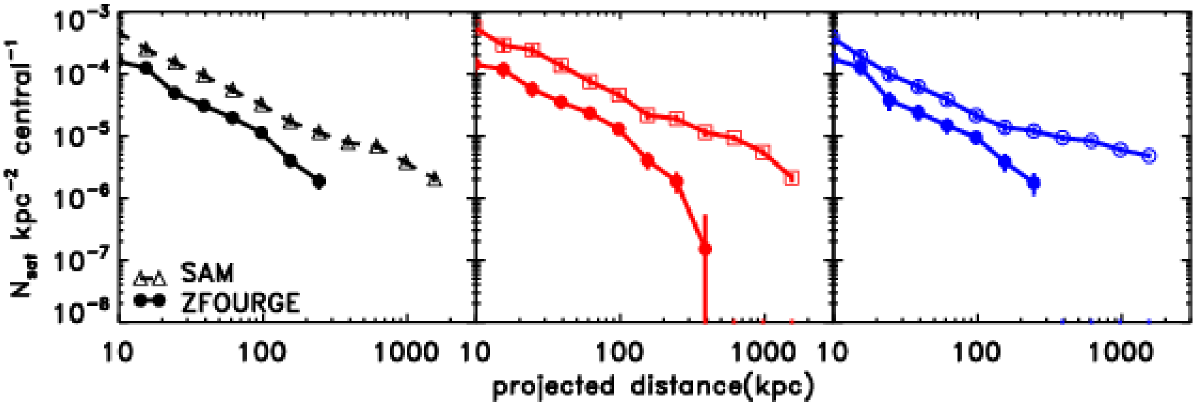

Figure 2.12: The comparison of satellites radial profile from ZFOURGE and SAM.

The projected radial profile of satellites around each type of central at $1 < z < 2$ with stellar masses of $\log(M_c/M_\odot) > 10.48$ for centrals selected from the semi-analytic model (SAM; open circles) compared to the satellites around the centrals in our ZFOURGE dataset (filled circles). The left panel shows the satellites for all centrals, the middle panel shows the results for quiescent centrals, and the right panel shows the results for star-forming centrals. In all cases the shape of the satellite distribution is similar for the centrals in the SAM and data, but the normalization is higher for the centrals in the SAM. Reprinted with permission from “The Distribution of Satellites around Massive Galaxies at $1 < z < 3$ in ZFOURGE/CANDELS: Dependence on Star Formation Activity" by Kawinwanichakij et al., 2014. The Astrophysical Journal, Volume 792, Issue 2, article id. 103 pp. 19, Copyright 2014.

We fit the projected NFW profiles to the satellite distributions of the centrals in the SAM and the data (using the restricted redshift range, $1 < z < 2$, and higher stellar mass-completeness limit for the satellites). The fit to the projected NFW profile for the satellite distribution in the SAM gives $r_s = 73.92 \pm 9.40\,\mathrm{kpc}$. This is larger than the one we measure for the comparable sample in the ZFOURGE data, where the fit gives $r_s = 43.93 \pm 11.67\,\mathrm{kpc}$. This difference may point to shortcomings in the treatment of sub-halos (and, therefore, satellite galaxies) in the N-body simulations, but further discussion of this point is beyond the scope of this work.

To compare with the data, we investigate how the number density of satellites around centrals in the SAM depends on stellar mass and star-formation activity. Figure 2.13 shows the number density of satellites for all the SAM centrals with $\log(M_c/M_\odot) > 10.48$, and for the quiescent and star-forming centrals separately. As with the data, there is an excess of satellites around quiescent galaxies and most of the signal comes from the most massive centrals, with $\log(M_{\rm c}/{\rm M_{\odot}}) > 10.78$: the p-values are $p_{\rm MC} = 0.032$ ($\simeq 1.9\sigma$) and $p_{\rm MC} = 0.001$ ($\simeq 3.7\sigma$) for the centrals with $10.48 < \log(M_{\rm c}/{\rm M_{\odot}}) < 10.78$ and $\log(M_{\rm c}/{\rm M_{\odot}}) > 10.78$, respectively. As with the data, we investigate if the excess of the satellites around the quiescent galaxies is a result of a higher average stellar mass. We therefore match the stellar mass distributions between the star-forming and quiescent centrals in the SAM (see Section 2.6.1). Figure 2.14 shows the cumulative stellar mass distribution of the SAM centrals after the stellar mass distributions are matched. Figure 2.13 shows that quiescent centrals in the SAM have a higher number density of satellites compared to the star-forming centrals, even after the stellar mass distributions have been matched. The p-values are $p_{\rm MC} = 0.050$ ($\simeq 1.7\sigma$) and $p_{\rm MC} = 0.016$ ($\simeq 2.1\sigma$) for the centrals with $10.48 < \log(M_{\rm c}/{\rm M_{\odot}}) < 10.78$ and $\log(M_{\rm c}/{\rm M_{\odot}}) > 10.78$, respectively.

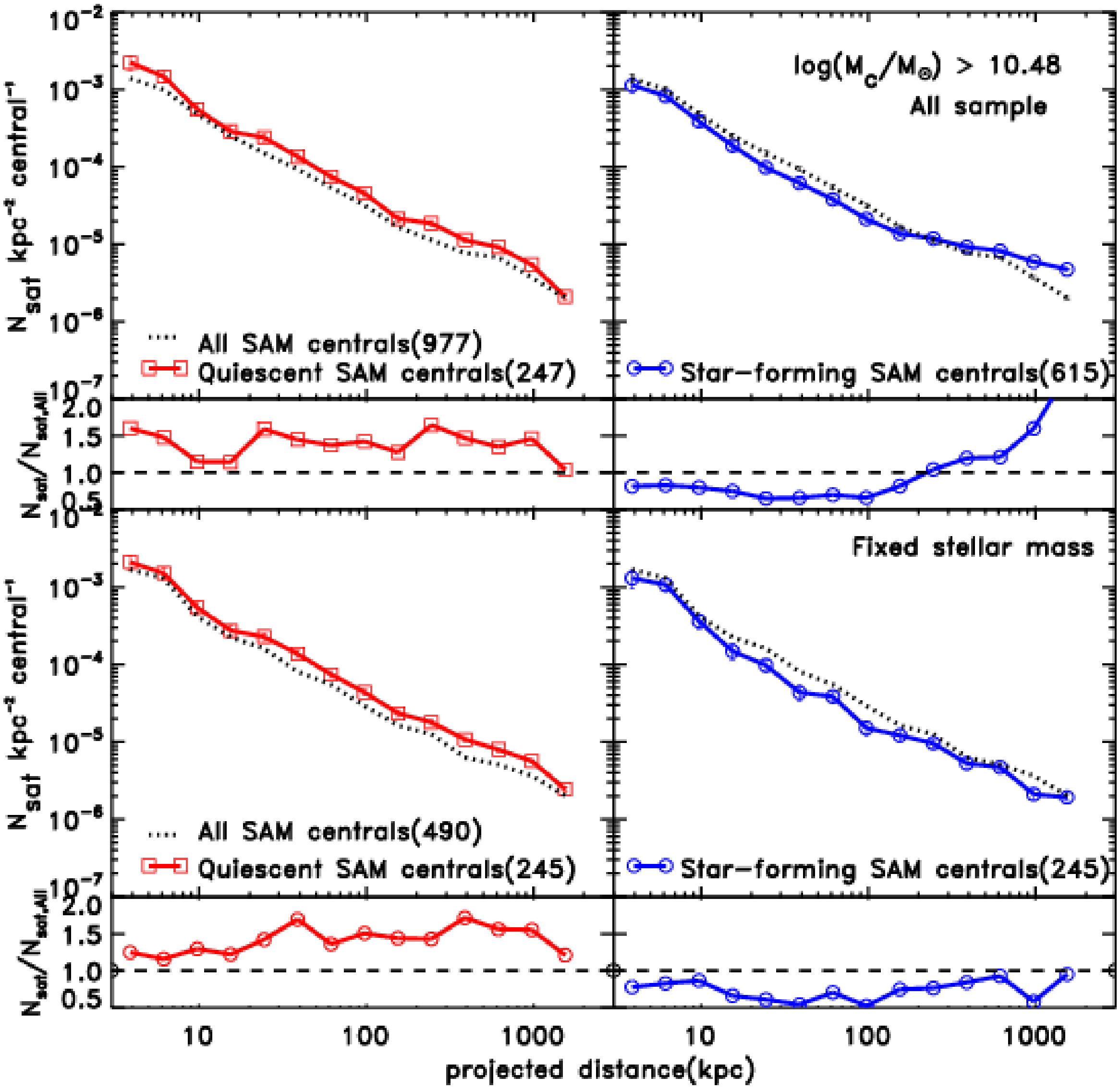

Figure 2.13: The projected radial profile of satellites around each type of centrals from SAM.

Top: the projected radial profile of satellites around all centrals in the SAM (black dotted line), quiescent centrals (red solid line with boxes in the left panel), and star-forming centrals (blue solid line with filled circles in the right panel) at $1 < z < 2$ with stellar masses of $\log(M_{\rm c}/{\rm M}_\odot) > 10.48$. ***Bottom:*** same plot as the top panels but where we have matched the stellar mass distributions of the quiescent and star-forming centrals. In each panel, the number in parentheses indicates the number of centrals in each subsample. There is a significant excess of satellites around quiescent central even when we match the stellar mass distributions of the centrals. Reprinted with permission from “The Distribution of Satellites around Massive Galaxies at $1 < z < 3$ in ZFOURGE/CANDELS: Dependence on Star Formation Activity" by Kawinwanichakij et al., 2014. The Astrophysical Journal, Volume 792, Issue 2, article id. 103 pp. 19, Copyright 2014.

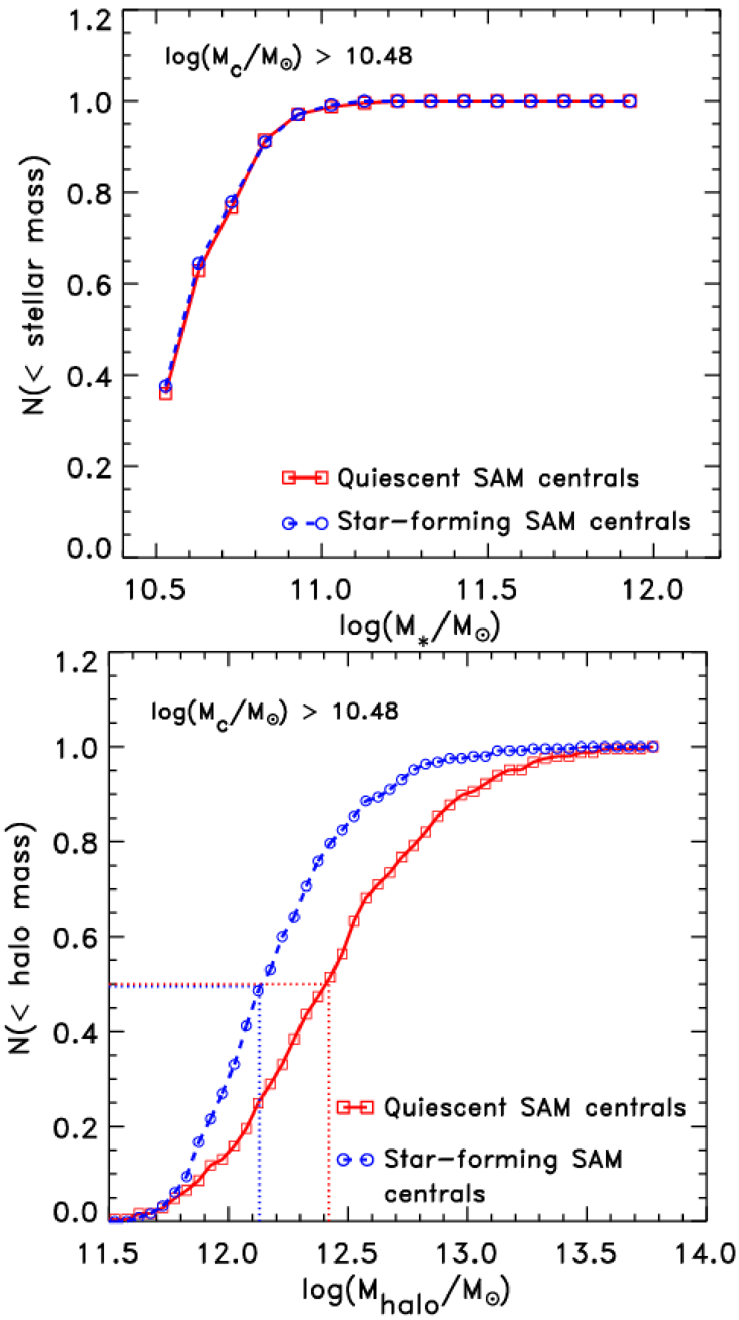

Figure 2.14: The cumulative stellar mass distribution for centrals in the SAM.

Top: the cumulative stellar mass distribution for all quiescent centrals and star-forming centrals in the SAM after matching their stellar mass distributions. ***Bottom:*** the cumulative distributions of the halo masses of quiescent (red solid curve) and star-forming (blue dashed curve) centrals after matching their stellar mass distributions (as shown in the left panel). Even when the centrals are matched in stellar mass, the quiescent galaxies have higher halo masses. The dotted lines show that the median halo mass is higher by ≈0.3 dex. Reprinted with permission from "The Distribution of Satellites around Massive Galaxies at $1 < z < 3$ in ZFOURGE/CANDELS: Dependence on Star Formation Activity" by Kawinwanichakij et al., 2014. The Astrophysical Journal, Volume 792, Issue 2, article id. 103 pp. 19, Copyright 2014.

The difference in number density of satellites between quiescent and star-forming centrals in the SAM is similar to that observed in our centrals in the ZFOURGE data. The massive quiescent centrals ($\log(M/\mathrm{M}_{\odot}) > 10.78$) have about twice the number of satellites relative to massive star-forming centrals. This is still the case in a stellar mass-matched sample. However, we do note that the difference in satellite content can still be found in the SAM at intermediate masses ($10.48 < \log(M_{\mathrm{c}}/\mathrm{M}_{\odot}) < 10.78$), whereas we do not see a significant difference in the data.

Therefore, we explore in the SAM the underlying reason for the excess satellites around quiescent galaxies to interpret the physical reason we observe this feature in our data.

The main reason appears to be that in the SAM the quiescent centrals have higher halo masses compared to the star-forming centrals at fixed stellar mass. Figure 2.14 shows that after we have matched the stellar mass distributions of the centrals in the SAM, the quiescent centrals have a higher median halo mass by a factor of ≈ 0.3 dex (factor of order 2).

To test if halo mass is the driving cause, we match the halo mass distributions between the quiescent and star-forming centrals in the SAM using the method to match the stellar mass distributions (see Section 2.6.1). Figure 2.15 shows the number density of satellites around quiescent and star-forming centrals after matching their halo mass distributions. The difference in the number density of satellites has almost entirely disappeared. Using our p-values from Monte Carlo simulations (see Section 2.5.3), we derive a likelihood of $p_{\mathrm{MC}} = 0.176$ ($\simeq 0.9\sigma$) that there is a difference between the satellite distributions for the centrals with $\log(M_{\mathrm{c}}/\mathrm{M}_{\odot}) > 10.48$. Therefore, in the SAM most of the excess in the number density satellites around quiescent galaxies can be attributed to those galaxies having higher halo masses compared to star-forming centrals.

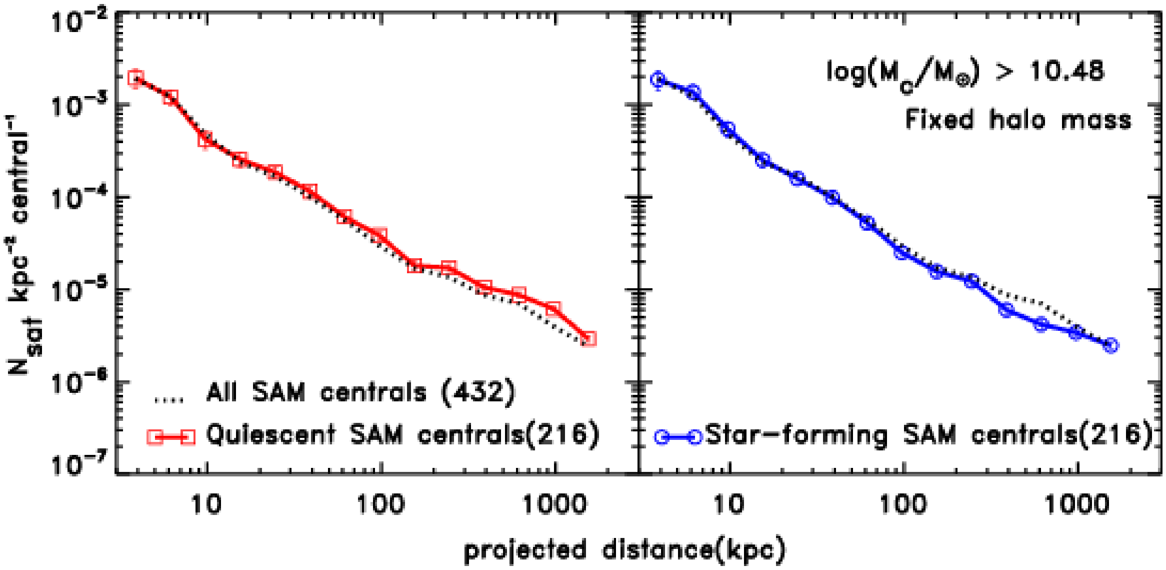

Figure 2.15: Satellite radial profile for halo mass-matched centrals in SAM.

Same as Figure 2.13 but for the subsamples in which the cumulative halo mass density of quiescent and star-forming centrals in the SAM at $1 < z < 2$ with stellar masses of $\log(M_c/M_\odot) > 10.48$ have been matched. As indicated in the plot, fixing the halo mass makes the number density of satellites at $10 < r/\mathrm{kpc} < 100$ equal between the star-forming and quiescent centrals. Therefore the excess number density of satellites is an indication that the latter systems have higher halo mass. Reprinted with permission from “The Distribution of Satellites around Massive Galaxies at $1 < z < 3$ in ZFOURGE/CANDELS: Dependence on Star Formation Activity" by Kawinwanichakij et al., 2014. The Astrophysical Journal, Volume 792, Issue 2, article id. 103 pp. 19, Copyright 2014.

In ΛCDM, the dark matter halos grow through accretion and mergers. Clearly, this will involve the accretion and merging of smaller halos that contain the satellite galaxies. Our analysis of the SAM suggests that the observed difference in satellite content between different types of galaxies is driven by differences in halo mass (see also Cattaneo et al., 2006), with the number of satellites roughly proportional to the halo mass. Therefore, a plausible interpretation of our results is that, at $\log(M_c/M_\odot) > 10.78$, quiescent centrals have a median halo mass that is about a factor of 2 larger than comparable star-forming galaxies, and that this difference becomes significantly smaller at lower masses.

2.6.3 Comparison to Results at Lower Redshift

Based on our analysis of the simulations in Section 2.6.2, we interpret the excess of satellites around quiescent galaxies as evidence that—even at fixed mass—quiescent centrals have more massive dark matter halos than their star-forming counterparts. Our results are derived from galaxies from the three fields in ZFOURGE (COSMOS, UDS, CDFS), which are well separated on the sky. We see no evidence for strong field-to-field variance (see Section 2.4), and therefore our results seem robust against cosmic variance and/or systematics that vary between the dataset in each field.

Our interpretation that quiescent galaxies have higher dark-matter halos masses compared to star-forming galaxies agrees with findings from analyses of galaxy clustering. These studies also find that quiescent galaxies have stronger clustering amplitudes, and presumably higher dark mass halo masses, compared to their star-forming counterparts (e.g., Hartley et al., 2013; Li et al., 2006). It is perhaps unsurprising that our results agree because our measurement of the number distribution of satellite galaxies is similar to the "one-halo" term of the galaxy correlation function, but here we measure this to much lower masses and because of our methodology, we are able to track the number of satellites and the mass contained within them on average for each central galaxy.

Our results extend trends from the local Universe to higher redshifts. For example, More et al. (2011) study the kinematics of satellite galaxies from SDSS to infer the relation between the properties of central galaxies and their halo masses. Similar to our findings, More et al. find that central galaxies with the lower stellar masses ($\log(M/\,\mathrm{M}_{\odot}) < 10.8$) have no significant difference in halo mass regardless of being quiescent vs. star-forming. Also similar to our findings, More et al. find that the more massive quiescent centrals have larger halo masses compared to star-forming centrals even when the stellar mass is fixed. They find that the difference between halo mass of quiescent and star-forming centrals increases from 0.2 to 0.4 dex as the stellar mass of the central increased from $\log(M/\,\mathrm{M}_{\odot}) = 10.8$ to $\log(M/\,\mathrm{M}_{\odot}) = 11.1$.

These similar results also have been found by other studies using the data from SDSS.Wang & White (2012) study the abundance of satellite galaxies in the stellar mass range $9.0 <$

$\log(M/\,\mathrm{M}_{\odot}) < 10.0$. They find that red centrals (what they call "primaries") with the stellar masses of $\log(M/\,\mathrm{M}_{\odot}) > 10.8$, have significantly more satellites than blue centrals of the same stellar mass. For the centrals with stellar masses of $\log(M/\,\mathrm{M}_{\odot}) \sim 11.2$, red centrals have more satellites about a factor of 2 relative to the star-forming counterparts. They also compare the observation with the Guo et al. (2011) SAMs and find that the red centrals have more satellites because they reside in more massive halos. Recently, Phillips et al. (2014) study the satellites around bright host galaxies with $\log(M/\,\mathrm{M}_{\odot}) = 10.5$. The distribution of velocity offset for satellites and their hosts show that at fixed stellar mass the halo mass of passive host galaxies are $\sim 45\%$ more massive than the those of star-forming galaxies.

These results are in agreement with our findings. Therefore, it seems as if there is little redshift evolution in the conclusion that quiescent galaxies have higher halo masses than star-forming galaxies at fixed stellar mass, at least for the more massive centrals.

2.6.4 Constraints on Models of Mass Quenching

Qualitatively, it may not be surprising that quenched central galaxies occupy more massive halos than star-forming galaxies at fixed stellar mass, regardless of the particular quenching mechanism. Even after a galaxy stops forming new stars, its halo will continue to grow at a rate comparable to the past average (e.g. Conroy & Wechsler, 2009; Moster et al., 2013), meaning that the ratio of dark matter mass to stellar mass will begin increasing relative to galaxies that continue to form stars. This is consistent with the results we derive from the Guo et al. (2011) SAM, where the quiescent galaxies have higher median dark-matter masses compared to the star-forming galaxies, even when we match the stellar mass distributions.

In this respect it is notable that we find a difference in the number of satellites only in our high-mass sample (~ 0.3 dex), and no significant difference at intermediate masses (upper limit ~ 0.1 dex). Using the reasoning given above, this could be explained if high-mass galaxies quench first, and thus their halos have had the most time to grow relative to their stellar mass. Indeed, such mass–dependent quenching has been clearly demonstrated by Tomczak et al. (2014, see their Figure 11).

However, our observations may have interesting implications for the mechanisms that *cause* quenching. It has long been recognized that star formation in high-mass halos may be suppressed due to the shock-heating, and the subsequent inefficient cooling, of infalling gas (e.g. White & Rees, 1978; Birnboim & Dekel, 2003; Kereš et al., 2005; Dekel & Birnboim, 2006). Here we wish to interpret our results using a simple model in order to test how halo mass and quenching are related. We first use the redshift-dependent parametrization of the stellar-to-halo mass relation from Moster et al. (2013) to populate halos at $1 < z < 3$ in the Millennium simulation with galaxies, and add in 0.30 dex scatter in stellar mass. We label the galaxies as star-forming if their halo masses fall below a fixed threshold mass (a few times $10^{12}\mathrm{M}_{\odot}$) and quiescent if their halo masses fall above this threshold (Figure 2.16, top-left panel). We then calculate the quenched fraction and the average halo mass of star-forming and quiescent galaxies in our two mass bins (Figure 2.16, top-center and top-right panels, respectively). This fixed halo-mass threshold for quenching results in a quenched fraction that differs significantly between the mass bins, which we do not observe. It also predicts a mean halo mass of quiescent galaxies that is significantly larger than the star-forming galaxies in both stellar mass bins, which we also do not observe.

Because we cannot reproduce the observations for any single value of quenching halo mass and scatter in stellar mass, rather than using the model with a single halo mass quenching, we assign each galaxy a probability for being quenched based on the halo mass. We set the probability to be a steplike function with a soft cutoff profile, $P_{\mathrm{quench}} = 0.5(1 + \mathrm{erf}(\log(M_h/\mathrm{M}_{\odot}) - \log(M_{0.5}/\mathrm{M}_{\odot}))/\sigma)$, where erf is the error function[2]. We adjust the parameter $M_{0.5}$, which is defined such that $P_{\mathrm{quench}}(\log(M_{0.5}/\mathrm{M}_{\odot})) = 0.5$, and the parameter σ, as well as the scatter in stellar mass to roughly reproduce the observed quenched fraction and the difference in mean halo mass. We find that a $\log(M_{0.5}/\mathrm{M}_{\odot})$ of $12.3-12.5$, a standard deviation of $0.7-0.9$, which corresponds to $P_{\mathrm{quench}} = 0$ for $\log(M_h/\mathrm{M}_{\odot}) \sim 11 - 11.5$ and $P_{\mathrm{quench}} = 1$ for $\log(M_h/\mathrm{M}_{\odot}) \sim 13.5$, and a scatter in stellar mass of $0.15 - 0.2$ dex, is able to roughly reproduce the observed quiescent fractions and the difference in the average halo mass of centrals at both stellar mass bins (Figure 2.16, bottom

---

[2] Our choice of functional form for P_{quench} here is arbitrary except that it obeys our requirement that P_{quench} increase with mass. We expect other parameterizations with a mass-dependent P_{quench} can reproduce the data as well.

row). We find that the differences in mean halo mass of quiescent and star-forming galaxies are ~ 0.1 dex and ~ 0.2 dex for intermediate and high stellar mass bins, respectively (Figure 2.16, bottom right panel), in better agreement with the observations. The small scatter favored by the model in the stellar-to-halo mass relation is due to the fact that we see significant differences in $N_{\rm sat}$ over a relatively small range in stellar mass: the mean mass in the intermediate-mass sample is $\log(M_*/{\rm M}_\odot) \sim 10.6$, while in the high mass sample it is $\log(M_*/{\rm M}_\odot) \sim 11.0$, and so a large amount of scatter would wash out differences in halo mass over this relatively limited range in stellar mass. We do note that the scatter in our modeling represents intrinsic scatter in the stellar-to-halo mass relation *combined with* the random errors in our stellar mass estimates, suggesting that the *intrinsic* scatter must be small indeed.

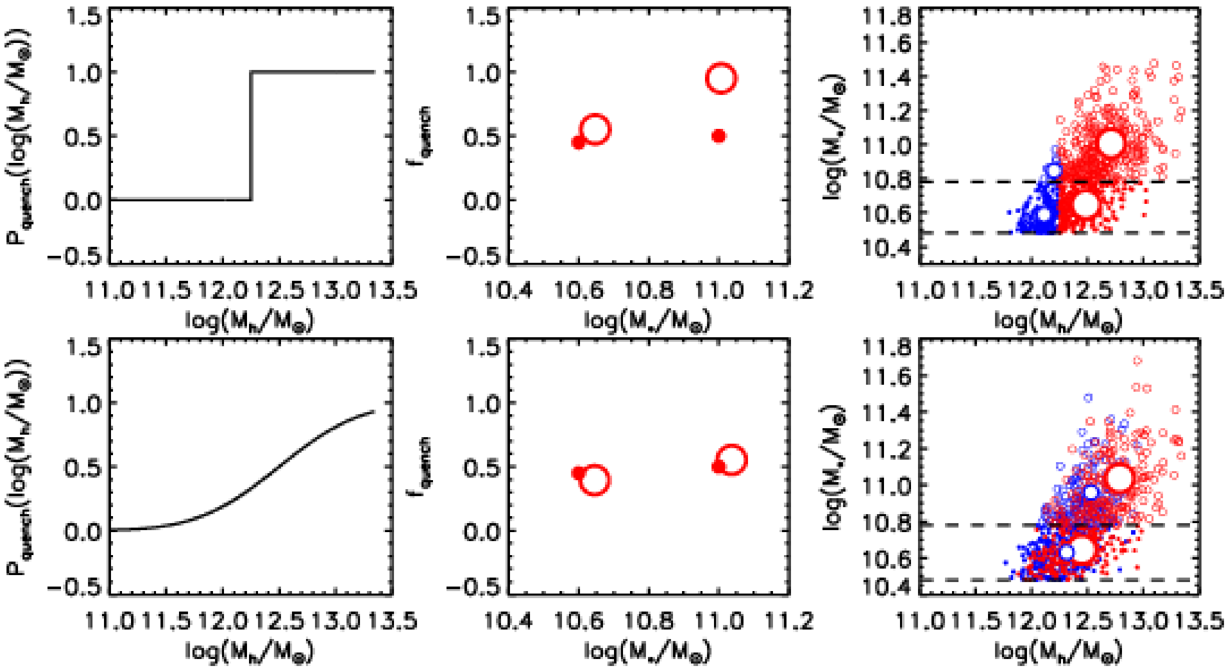

Figure 2.16: A toy model for exploring possible models of mass quenching.

A toy model that explores scenarios in which the quenching of star formation is related to halo mass, and which attempts to explain the large inferred difference in halo mass between star-forming and quiescent galaxies at high stellar masses, while maintaining a smaller difference at intermediate stellar masses. We use the redshift-dependent stellar-to-halo mass relation from Moster et al. (2013) to populate halos from an N-body simulation with galaxies, and add in additional scatter to the stellar masses. We then quench some subset of the galaxies based on their halo mass. ***Top:*** A scenario where the quenching probability is a step function in halo mass, with a threshold of $\log(M_h/\mathrm{M}_\odot) = 12.25$, as shown on the left. The center panel shows that the predicted quenched fraction in our two stellar mass bins (large open circles) does not agree with the observations (small filled circles). The right panel shows the stellar and halo masses of the simulated galaxies, color-coded according to whether the galaxies have been quenched. The small and large open circles show the mean stellar and halo masses for star-forming galaxies and quiescent galaxies, respectively. The mean halo masses differ by 0.3 dex in the intermediate mass bin and 0.5 dex in the high-mass bin, in contrast with the differences inferred from the data, which are ~ 0.08 and ~ 0.3 dex, respectively. ***Bottom:*** same as the top panels for for a scenario where the probability of each galaxy being quenched is modeled as a steplike function with a softened profile. The predicted quenched fractions, and the predicted differences in halo masses between star-forming and quiescent galaxies in our two mass bins, are in significantly better agreement with the data. Reprinted with permission from “The Distribution of Satellites around Massive Galaxies at $1 < z < 3$ in ZFOURGE/CANDELS: Dependence on Star Formation Activity" by Kawinwanichakij et al., 2014. The Astrophysical Journal, Volume 792, Issue 2, article id. 103 pp. 19, Copyright 2014.

It would be possible to develop this model further. For instance, we note that adding a mass-dependent scatter in the stellar masses — where the scatter increases from 0.15 dex at lower masses to 0.3 dex at the higher masses — further improves the agreement between the toy model and the data. However, given the uncertainties involved in the current data, particularly with regard to the incompleteness in satellite detection at low masses and the (limited) expected misclassification between centrals and satellites (see Section 2.3.2), our modeling results can only be regarded as indicative, and we do not push the modeling any further.

If our observation that intermediate mass quiescent and star-forming centrals have the same $N_{\rm sat}$ is correct, then our toy model strongly favors a scenario where there is no single quenching halo mass threshold: even at relatively high halo masses $(\log(M/h^{-1}{\rm M}_{\odot})\sim 12$ based on the SAM), only about 50% of the galaxies are quiescent while the rest remain star-forming, and galaxies have some likelihood of being quenched over a very wide range in halo masses $(\log(M_h/{\rm M}_{\odot})\sim 11-13.5)$. One remaining question is that if halo mass quenching is an important mechanism, *why* do some galaxies remain star-forming while others quench? Our result implies that halo mass can only be a contributing factor. Other factors may include environmental processes (assembly bias and environmental effects on the gas-accretion process), stochastic processes such as mergers, and galaxy structure (e.g Gao et al., 2005; Wechsler et al., 2006; Croton et al., 2007; Cooper et al., 2010; Papovich et al., 2012; Rudnick et al., 2012; Bassett et al., 2013; Lotz et al., 2013).

This result may be expected on theoretical grounds, as some variation in the quenching mass is expected due to variations in metallicity and perhaps also due to the enhanced ability of cold flows to penetrate halos at the higher redshifts in our sample (Dekel & Birnboim, 2006; Dekel et al., 2009). A variation in halo mass is also expected based on the results of Gabor & Davé (2012). In their model galaxy quenching is based on the hot gas content of halos, which is correlated with, but not directly tied to halo mass. Recently, Lu et al. (2014) also show that galaxy models require a quenching probability that increases with mass to explain the color-mass distributions of galaxies in the CANDELS survey.

The mergers that grow massive quiescent galaxies are supposed to be primarily dissipationless, and devoid of cold gas available for star-formation (e.g., so-called “dry” mergers, van Dokkum et al., 2010; Oser et al., 2010, 2012; Hopkins et al., 2010). If this is the case, it is expected that satellites around the quiescent centrals in our sample, which will eventually merge with their central galaxies, should be largely devoid of gas (or some process must cause them to expel or consume their gas prior to merging with the central). Therefore it may be expected that the satellites should show signs of passive colors. A discussion of the color and stellar mass distributions of the satellites is beyond the scope of the present work, but we will study these distributions in a future work.

3. SATELLITE QUENCHING AND GALACTIC CONFORMITY AT $0.3 < z < 2.5$[1]

3.1 Synopsis

We measure the evolution of the quiescent fraction and quenching efficiency of satellites around star-forming and quiescent central galaxies with stellar mass $\log(M_{\rm cen}/{\rm M}_{\odot}) > 10.5$ at $0.3 < z < 2.5$. We combine imaging from three deep near-infrared-selected surveys (ZFOURGE/CANDELS, UDS, and UltraVISTA), which allows us to select a stellar-mass complete sample of satellites with $\log(M_{\rm sat}/{\rm M}_{\odot}) > 9.3$. Satellites for both star-forming and quiescent central galaxies have higher quiescent fractions compared to field galaxies matched in stellar mass at all redshifts. We also observe "galactic conformity": satellites around quiescent centrals are more likely to be quenched compared to the satellites around star-forming centrals. In our sample, this conformity signal is significant at $\gtrsim 3\sigma$ for $0.6 < z < 1.6$, whereas it is only weakly significant at $0.3 < z < 0.6$ and $1.6 < z < 2.5$. Therefore, conformity (and therefore satellite quenching) has been present for a significant fraction of the age of the universe. The satellite quenching efficiency increases with increasing stellar mass of the central, but does not appear to depend on the stellar mass of the satellite to the mass limit of our sample. When we compare the satellite quenching efficiency of star-forming centrals with stellar masses 0.2 dex higher than quiescent centrals (which should account for any difference in halo mass), the conformity signal decreases, but remains statistically significant at $0.6 < z < 0.9$. This is evidence that satellite quenching is connected to the star-formation properties of the central as well as to the mass of the halo. We discuss physical effects that may contribute to galactic conformity, and emphasize that they must allow for continued star-formation in the central galaxy even as the satellites are quenched.

---

[1] Reprinted with permission from "Satellite Quenching and Galactic Conformity at $0.3 < z < 2.5$" by Kawinwanichakij et al., 2016. The Astrophysical Journal, Volume 817, Issue 1, article id. 9 pp. 19, Copyright 2016.

3.2 Background Information

Galaxies can be broadly classified as either quiescent or star-forming. As deep multiwavelength galaxy surveys have allowed us to obtain complete samples to higher and higher redshifts, it has become clear that a substantial population of quiescent galaxies exists out to at least $z \sim 4$ (e.g., Cimatti et al., 2002; Bell et al., 2004; Papovich et al., 2006; Williams et al., 2009; Whitaker et al., 2011; Straatman et al., 2014). However, the processes that are responsible for the quenching of star formation remain one of the central mysteries in the field of galaxy evolution.

It has long been known that environmental processes act to inhibit star formation (e.g., Dressler, 1980; Balogh et al., 1999; Kauffmann et al., 2004; Peng et al., 2010; Quadri et al., 2012; Kovač et al., 2014; Tal et al., 2014). Although the exact mechanisms are not well-understood, it is generally expected that galaxies in dense environments (or more specifically, satellite galaxies) should lose their gas supply (Gunn & Gott, 1972; Larson et al., 1980). But quiescent galaxies are also found in low-density environments (Kauffmann et al., 2004) and are often the central galaxy in their halo, in which case they will not be affected by satellite-specific processes. Thus there must be other ways to quench galaxies, and there has not been a shortage of proposed mechanisms: these include the shock-heating of infalling gas (White & Rees, 1978; Dekel & Birnboim, 2006), gas heating caused by minor mergers (Johansson et al., 2009), low-level AGN feedback (Croton et al., 2006), explosive AGN feedback (Hopkins et al., 2006), and the stabilization of gas disks (Martig et al., 2009). Finding clear observational evidence that either supports or rules out any one specific process has been notoriously difficult.

A new clue regarding galaxy quenching was presented by Weinmann et al. (2006), who found that the star-formation activities of satellite and central galaxies at $z < 0.2$ are correlated. The correlation is such that the quiescent fraction of satellites is higher around quiescent central galaxies than around star-forming centrals. This phenomenon, which they refer to as “galactic conformity", suggests that whatever process or processes cause the quenching of central galaxies also operate on their satellites.

Since the original Weinmann et al. (2006) result, a number of other studies have analyzed the correlation between the properties of satellites (i.e., specific star-formation rate, colors, and gas fraction) and their more massive centrals in the local universe using data from the Sloan Digital Sky Survey (SDSS). While Weinmann et al. (2006) refer to “galactic conformity" as a correlation in the properties of central and satellite galaxies at fixed *halo* mass, other studies have investigated conformity at fixed *stellar* mass. These studies have generally confirmed that the quiescent fraction of satellites around quiescent centrals must be higher than those of star-forming centrals (see Ross & Brunner, 2009; Kauffmann et al., 2010; Wang & White, 2012; Kauffmann et al., 2013; Knobel et al., 2015; Phillips et al., 2014, 2015).

However, there are a number of important questions that are raised by studies of galactic conformity at low redshift. One is, whether the satellites of star-forming centrals are quenched in excess of field galaxies at the same mass, or whether it is only the satellites of quiescent centrals that experience excess quenching. A second question is whether conformity exists only at fixed stellar mass, or whether residual signal is seen when the halo masses of the star-forming and quiescent centrals have been matched.

Wang & White (2012) showed that the color distribution of satellites is different for star-forming centrals than for quiescent centrals, consistent with galactic conformity. They also found that the satellites of intermediate-mass star-forming centrals are not quenched at higher rates than mass-matched field galaxies, but that the satellites of higher mass star-forming centrals (with stellar masses $\log(M_{\rm stellar}/{\rm M}_{\odot}) > 11.1$) do show excess quenching.

Phillips et al. (2014) studied bright ($\sim 0.1L^{*}$) satellites around isolated $\sim L^{*}$ galaxies in SDSS at low redshift, $z < 0.032$. In order to narrow the range of halo masses probed by their sample, these authors required that central galaxies have exactly one bright satellite. They found that satellites of quiescent centrals are more likely to be quenched than stellar mass-matched field galaxies, but that satellites of star-forming centrals are similar to field galaxies (echoing the observational results of Wang & White 2012). These authors also use the pairwise velocities between the centrals and satellites to show that the quiescent centrals occupy more massive halos than star-forming centrals.

In a follow-up study, Phillips et al. (2015) also considered central galaxies with exactly two bright satellites. In this case the quenched fraction of satellites is nearly the same for star-forming and quiescent centrals, thereby reducing or eliminating the conformity signal. They also use the pairwise velocities to show that, for the systems with two satellites, the the halo masses of star-forming and quiescent centrals are consistent with each other.

Taken together, the Phillips et al. (2014, 2015) results suggest that conformity in the local Universe could be driven largely, or entirely, by a difference in halo mass between star forming and quiescent centrals. This contrasts with conclusions based on SDSS group catalogs (e.g., Weinmann et al., 2006; Knobel et al., 2015). It is possible that studies based on group catalogs are affected by inaccurate halo mass estimates and by the misidentification of centrals and satellites, which can introduce a weak conformity signal at fixed halo mass even when none is present (Campbell et al., 2015; Paranjape et al., 2015; Bray et al., 2016). This leaves open the possibility that differences in the halo masses of quiescent and star-forming centrals are responsible for galactic conformity.

To study the physical cause of conformity, Wang & White (2012) inspected mock catalogs from the Guo et al. (2011) semi-analytic model. They showed that within the model, the conformity effect can be partially explained by the fact that quiescent centrals occupy more massive halos than star-forming centrals. But even at fixed halo mass, the satellites of quiescent centrals were accreted at earlier (corresponding to the earlier overall assembly times of the parent halos) and were exposed to more hot halo gas, which also contributes to conformity.

The findings of Kauffmann et al. (2013) point to an interesting addition to the idea of conformity as applying to central galaxies and their satellites. Using SDSS, they studied the correlation in star-formation activity between galaxies as a function of separation, including galaxies separated by small (intra-halo) and large (inter-halo) scales. They found that the correlation depends on the stellar mass of the central: for high-mass centrals, there is a correlation on small scales, within the dark-matter halo, consistent with previous observations of galactic conformity. For lower-mass centrals, Kauffmann et al. found that a correlation in the star-formation properties of galaxies extends over many Mpc, beyond the putative virial radii of the individual galaxies. Kauffmann

(2015) also found that low-mass galaxies with low star formation rates have an excess of massive radio-loud neighbors extending to several Mpc. These results may be an indication that there are different processes at play, with a conformity effect present amongst the galaxies within a single parent dark matter halo and a separate effect acting on galaxies in neighboring halos (but see Paranjape et al., 2015); these intra-halo and inter-halo effects have been dubbed “1-halo" and “2-halo" conformity, respectively.

Some insight into the physical cause of conformity may come from studying the evolution in the conformity signal with redshift, as this evolution depends on the underlying physics. For example, there is some expectation that 1-halo conformity at low redshifts may be a result of 2-halo conformity at higher redshifts, because galaxies that are currently satellites were previously centrals in nearby halos. The 2-halo conformity in galaxy properties could be expected because of correlations in the recent or past assembly history of those halos, i.e. “assembly bias" (e.g., Gao et al., 2005; Croton et al., 2007; Tinker et al., 2008). Recently Hearin et al. (2016) used the Bolshoi N-body simulation (Klypin et al., 2011) to analyze the correlation between the mass-accretion rates of nearby halos. As the accretion rates of halos are correlated out to many times the halo virial radius, they argue that this effect may provide a physical basis for 2-halo conformity. Hearin et al. (2016) also predict that 2-halo conformity should be much weaker at higher redshifts ($z > 1$). If 1-halo conformity is entirely due to 2-halo conformity, this would suggest that 1-halo conformity should also disappear at $z > 1$.

In addition, there should be an evolutionary trend with redshift if conformity effects are associated with inter-halo effects. Tinker & Wetzel (2010) used clustering measurements with a halo-occupation distribution analysis to conclude that the evolution of the quenched fraction of satellites requires a quenching timescale that evolves with redshift as $T_Q \sim (1 + z)^{-1.5}$, in the same way as the dynamical time, implying that the physical mechanism for satellite quenching should depend on the time that galaxies spend as satellites. Wetzel et al. (2013) use N-body simulations combined with SDSS data to study satellite quenching as a function of both satellite and halo mass, and show that that SFRs for satellites are mostly unaffected for several Gyr after infall, but then they experience rapid quenching. They further find that quenching timescales are shorter for more massive satellites, but do not depend on host halo mass because many satellites quench in lower-mass halos prior to infall. Therefore, key physical insight can be gained by studying the redshift evolution of satellite quenching.

In this work we study the redshift evolution of galactic conformity on scales comparable to halo virial radii out to $z \sim 2.5$ (i.e., “1-halo" conformity between centrals and satellites). Our study is primarily concerned with galactic conformity at fixed stellar mass, but we also investigate the effects of halo mass. Previous studies have looked at the evolution of the correlation in star-formation activity of galaxies with environment (including within galaxy clusters) out to $z \sim 2$ (see, e.g., Quadri et al., 2012; Bassett et al., 2013; Lee et al., 2015, and references therein), but have not generally studied conformity effects. To the best of our knowledge, the only comparable exploration of galactic conformity beyond the low-redshift universe was performed by Hartley et al. (2015). They studied a sample of massive satellites (down to $M_* > 10^{9.7}$ $\mathrm{M}_\odot$) around $\sim M^*$ central galaxies over $0.4 < z < 1.9$. They found evidence that galactic conformity persists over this redshift range, with higher quenched fractions of satellites around quiescent centrals compared to mass-matched samples of star-forming centrals. Furthermore, they found that star-forming centrals have satellites with quenched fractions indistinguishable from field galaxies. Hartley et al. (2015) also argue that conformity is not simply due to a difference in halo mass between star-forming and quiescent centrals. This study was limited to a single field and to a smaller (and shallower) range in stellar mass.

Here, we use a new set of near-infrared (IR)-selected datasets, spanning multiple wide and deep fields to explore the correlation between the star-formation activity of central galaxies and their satellites over a large range of stellar mass and $0.3 < z < 2.5$. The outline of this chapter is as follows. In Section 3.3 we describe our datasets and galaxy sample selection criteria. In Section 3.4 we describe the method for identifying satellites and for measuring the satellite quiescent fractions and quenching efficiencies. In Section 3.5 we explore how satellite quenching depends on the star-formation activity of the central galaxies, finding that conformity is present over our entire redshift range, although the statistical significance becomes weak beyond $z \sim 1.6$. We also investigate satellite quenching as a function of the stellar mass of both centrals and satellites. In Section 3.6 we discuss these results, including the possible physical causes of conformity, and whether conformity persists at fixed halo mass. In Chapter 7 we present our summary. Throughout, we define the process of “galactic conformity" to be the correlation in star-formation activity between centrals and their satellites on scales comparable to the virial radius of the centrals’ halos. With this definition our galactic conformity is akin to 1-halo conformity rather than 2-halo conformity. We adopt the following cosmological parameters where appropriate, $H_0 = 70\,\mathrm{km\ s^{-1}\ Mpc^{-1}}$, $\Omega_m = 0.3$, and $\Omega_\Lambda = 0.7$.

3.3 Data and Sample Selection

We select galaxies at $0.3 < z < 2.5$ from three datasets: the FourStar Galaxy Evolution Survey (ZFOURGE; PI Labbé), the UKIRT Infrared Deep Sky Survey (UKIDSS, Lawrence et al. 2007) Ultra Deep Survey (UDS, Almaini et. al., in prep.), and the Ultra Deep Survey with the VISTA Telescope (UltraVISTA; McCracken et al. 2012).

We include galaxies at $0.3 < z < 1.6$ from a public K_s-selected catalog (Muzzin et al. 2013b) based on the first data release of UltraVISTA. The catalog covers a total area of 1.62 deg^2 in the COSMOS field (Capak et al., 2007). We construct our galaxy sample from the UltraVISTA by selecting galaxies with $K_s < 23$ mag, where the catalog is highly-complete.

In addition to UltraVISTA, at $0.3 < z < 1.6$, we also use the dataset which is based on UKIDSS UDS data release 8 (Williams et al., 2009; Quadri et al., 2012), the deepest degree-scale near-IR survey. The catalog covers an area of 0.65 deg^2, and the K-band reaches 24.6 mag (5σ AB). To ensure a high level of completeness, we select a galaxy sample from this dataset with $K < 24$ mag.

At higher redshift, we draw our galaxy sample at $0.6 < z < 2.5$ from ZFOURGE (Straatman et al. 2015). This survey is composed of three $11' \times 11'$ pointings with coverage in the CDFS (Giacconi et al., 2002), COSMOS, and UDS. The imaging reaches depths of $\sim 26\,\mathrm{mag}$ in J_1, J_2, J_3 and $\sim 25\,\mathrm{mag}$ in H_s, H_l, K_s (see Spitler et al., 2012; Tilvi et al., 2013; Papovich et al., 2015, Straatman et al. 2015). The medium-band filters from ZFOURGE provide an advantage by sampling the Balmer break at $1 < z < 4$ better than broadband filters alone. As in Kawinwanichakij et al. (2014), we combine the ZFOURGE data with public HST/WFC3 F160W and F125W imaging from CANDELS (Grogin et al., 2011; Koekemoer et al., 2011) in the three fields. As described by Tomczak et al. (2014), we make use of the CANDELS F160W image as the detection band to select a sample of galaxies at $z < 2.5$ to low masses ($10^{9.3}$ $\mathrm{M}_{\odot}$).

We rederive photometric redshifts, rest-frame colors and stellar masses for the public UDS and UltraVista catalogs using the same method as for our ZFOURGE catalogs to ensure as homogeneous a dataset as possible. Photometric redshifts and rest-frame colors are derived using EAZY (Brammer et al., 2008). We use the default set of spectral templates derived from the PEGASE models (Fioc & Rocca-Volmerange, 1997) and a dust reddened template derived from the Maraston (2005) model to fit the $0.3-8$ μm photometry for each galaxy to obtain its photometric redshift, but note that the templates are iteratively tweaked during the fitting process. Similarly, we derive stellar masses using Bruzual & Charlot (2003) stellar population models with FAST code (Kriek et al., 2009), assuming exponentially declining star formation histories, solar metallicity, and a Chabrier (2003) initial mass function.

For our study, the relative redshift errors between the centrals and satellites are paramount, and traditional photometric redshift testing (comparing photometric to spectroscopic redshifts) is infeasible as the satellite galaxies in our sample are typically much fainter than spectroscopic magnitude limits. We estimate the relative uncertainties in photometric redshifts between the centrals and satellites using the technique described by Quadri & Williams (2010), in which the photometric redshift differences in close galaxy pairs are measured. Since many close galaxy pairs are physically-associated, each galaxy provides an independent estimate of the true redshift. Therefore, the distribution of the differences in the photometric redshifts of galaxy pairs can be used to estimate the photometric redshift uncertainties. For ZFOURGE, the typical photometric redshift uncertainties at $1 < z < 2.5$ in the COSMOS, CDFS, and UDS fields are σ_z= 0.06, 0.07, and 0.08, respectively (where $\sigma_z = \sigma/\sqrt{2}$, and where σ is the width measured from a Gaussian fit to the distribution of pair redshift differences in each field, and the $\sqrt{2}$ accounts for the fact that we take the difference between two independent measurements). For the UDS we derive $\sigma_z = 0.05$ and 0.04 for galaxies at $0.5 < z < 1.0$ and $1.0 < z < 1.5$, respectively. For UltraVISTA, we derive $\sigma_z = 0.01$ and 0.05 for the same redshift ranges.

We explore the evolution of satellite quenching over $0.3 < z < 2.5$ by dividing our galaxy sample into four redshift bins, each spanning roughly the same interval of cosmic time ($1.4 - 2.3$ Gyr): $0.3 < z < 0.6$, $0.6 < z < 0.9$, $0.9 < z < 1.6$, and $1.6 < z < 2.5$. To guard against possible survey-to-survey systematic biases, we select galaxy samples from at least two surveys depending on the stellar mass-completeness limit, as explained below. But for the highest redshift bin we can only use ZFOURGE because the UDS and UltraVISTA datasets are not deep enough to identify satellites to our desired mass range.

In this study we consider central galaxies and their satellites, which are defined in Section 3.3.2 and Section 3.3.3. We denote the stellar masses of the centrals as $M_{\rm cen}$ and the stellar masses of the satellites as $M_{\rm sat}$. We use $f_{q,sat}$ and $\epsilon_{q,sat}$ to denote the quiescent fraction and quenching efficiency of satellite galaxies. Those quantities have been corrected for projected background galaxies using the same method as in Kawinwanichakij et al. (2014, and see below).

3.3.1 Stellar Mass-Completeness

Understanding the stellar mass-completeness limit for each dataset is crucial for our analysis. Because we are concerned with the galaxy quiescent fractions, it is important that we are highly-complete for both star-forming and quiescent galaxies. Quiescent galaxies have higher mass-to-light ratios, and therefore we adopt 95% mass-completeness limits for galaxies with quiescent stellar populations. In Figure 3.1, we plot the adopted stellar mass-completeness limits for galaxies from ZFOURGE, UDS, and UltraVISTA at $0.3 < z < 2.5$. For UDS and UltraVISTA, we employ an updated version of the technique described by Quadri et al. (2012) to estimate the 95% mass-completeness limit that corresponds to the magnitude limit as a function of redshift. We select quiescent galaxies in narrow redshift bins, scale their fluxes and masses downward until they have the same magnitude as our adopted limit $K = 24.0$ for UDS and $K_s = 23.0$ for UltraVISTA. Then we define the mass-completeness limit as the stellar mass at which we detect 95% of the dimmed

Table 3.1: Stellar mass completeness limits for three datasets at $0.3 < z < 2.5$. Reprinted with permission from “Satellite Quenching and Galactic Conformity at $0.3 < z < 2.5$" by Kawinwanichakij et al., 2016. The Astrophysical Journal, Volume 817, Issue 1, article id. 9 pp. 19, Copyright 2016.

Redshift	UDS $\log(M(z))$ $\log(M_*/\mathrm{M}_\odot)$	UltraVISTA $\log(M(z))$ $\log(M_*/\mathrm{M}_\odot)$	ZFOURGE $\log(M(z))$ $\log(M_*/\mathrm{M}_\odot)$
0.3	8.3	8.7	7.7
0.4	8.5	8.9	7.9
0.5	8.7	9.1	8.1
0.6	8.9	9.3	8.3
0.7	9.0	9.4	8.4
0.8	9.2	9.6	8.6
0.9	9.3	9.7	8.7
1.0	9.4	9.8	8.8
1.1	9.5	9.9	8.8
1.2	9.6	10.0	8.9
1.3	9.7	10.1	9.0
1.4	9.7	10.1	9.0
1.5	9.8	10.2	9.1
1.6	9.9	10.3	9.2
1.7	10.0	10.4	9.2
1.8	10.0	10.4	9.3
1.9	10.1	10.5	9.3
2.0	10.2	10.6	9.3
2.1	10.2	10.6	9.4
2.2	10.3	10.7	9.4
2.3	10.3	10.7	9.4
2.4	10.4	10.8	9.5
2.5	10.4	10.8	9.5

galaxies at each redshift.

The empirical technique to derive stellar mass completeness (used for UltraVISTA and UDS) may be inaccuate for ZFOURGE. The ZFOURGE catalogs were selected using a different bandpass (WFC3/H_{160} for ZFOURGE compared to K for the other fields), so we are unable to scale directly the mass limits determined from those surveys to ZFOURGE. Additionally, the estimates of the 95% mass completeness limits in ZFOURGE may be inaccurate using the empirical method because the smaller ZFOURGE fields do not allow for a precise determination of the mass-to-flux ratio distributions of quiescent galaxies in narrow redshift bins.

Therefore, for ZFOURGE we determined the stellar mass-completeness limits using a stellar population synthesis model (using EzGal, Mancone & Gonzalez, 2012) for a passively evolving single stellar population with a Chabrier (2003) IMF, solar metallicity, a formation redshift $z_f = 5$, and $H_{160} < 26.5$ mag. This gives a slightly higher (i.e., more conservative) stellar mass completeness limit than what we would have derived using the empirical method (which we used for UltraVISTA and UDS). Moreover, it could be argued that one should use a lower formation redshift for lower mass galaxies because observationally lower mass galaxies have lower mass-to-light ratios (see, e.g., Speagle et al., 2014). However, we use the conservative assumption of $z_f = 5$ in order to ensure that our sample of low-mass quiescent galaxies is highly complete even for galaxies with the highest stellar-mass–to–light ratios.

We provide the adopted completeness limits for UDS, UltraVISTA, and ZFOURGE at $0.3 < z < 2.5$ in Table 3.1.

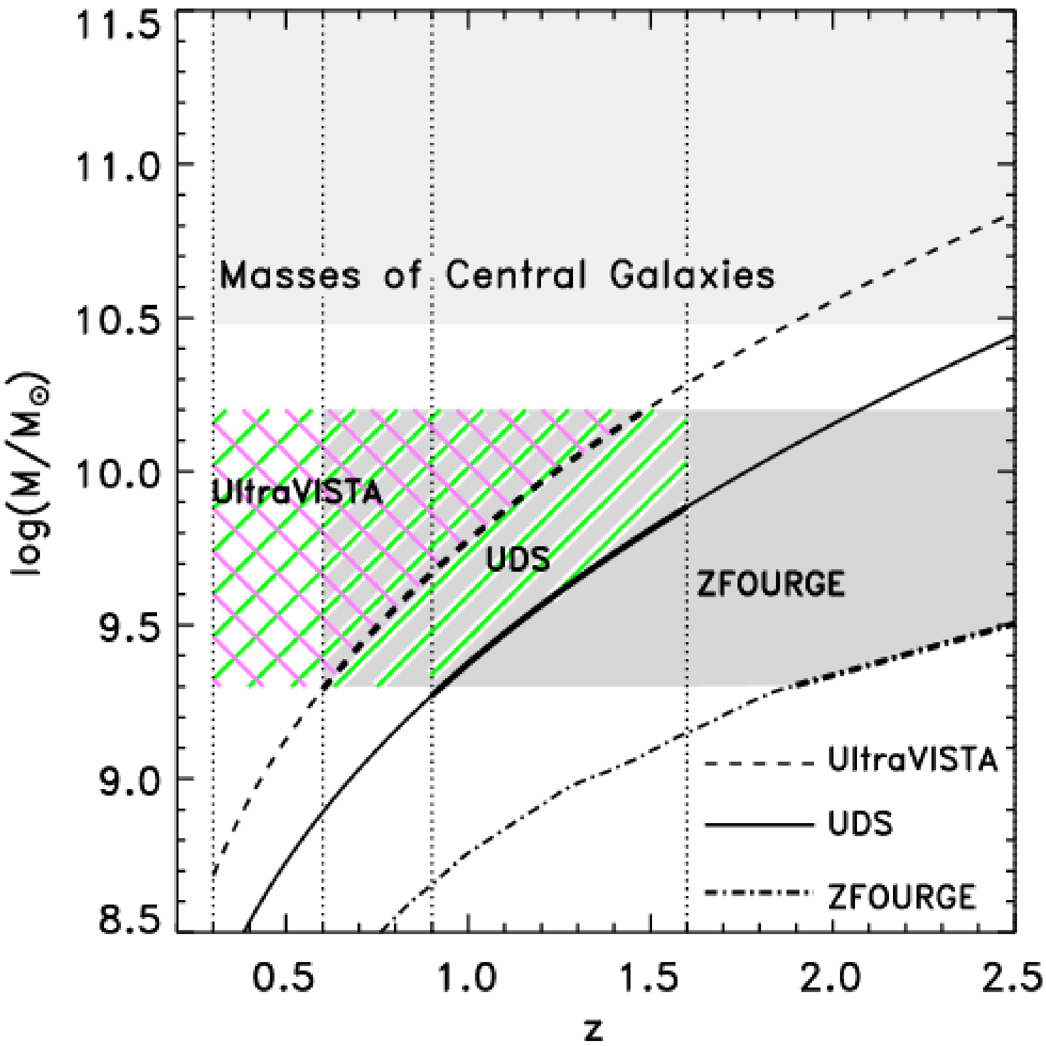

Figure 3.1: Stellar mass-completeness limit vs. redshift for quiescent galaxies.

95% Stellar mass-completeness limit vs. redshift computed for quiescent galaxies in three datasets: UltraVISTA ($K_s < 23$ mag; dash curve), UKIDSS UDS ($K < 24$ mag; solid curve), and ZFOURGE ($H_{160} < 26.5$ mag; dot dash curve). The mass-completeness limits for UDS and UltraVISTA are derived using the technique described by Quadri et al. (2012), whereas the mass-completeness limits for ZFOURGE is determined from passively evolving a SSP with a formation redshift $z_f = 5$. The light grey shaded region shows the stellar mass ranges of our samples centrals. The dotted vertical lines indicate our redshift bins used in this study. The thicker curves show the redshift and stellar mass ranges where we count neighboring galaxies using lower mass limit that evolves with redshift. The green and magenta diagonal hatched regions show the stellar mass ranges of satellites from UDS and UltraVISTA, whereas the gray shaded region is for ZFOURGE. Reprinted with permission from “Satellite Quenching and Galactic Conformity at $0.3 < z < 2.5$" by Kawinwanichakij et al., 2016. The Astrophysical Journal, Volume 817, Issue 1, article id. 9 pp. 19, Copyright 2016.

Table 3.2: Number of quiescent centrals and star-forming centrals in three datasets at $0.3 < z < 2.5$. Reprinted with permission from “Satellite Quenching and Galactic Conformity at $0.3 < z < 2.5$" by Kawinwanichakij et al., 2016. The Astrophysical Journal, Volume 817, Issue 1, article id. 9 pp. 19, Copyright 2016.

Stellar mass range	Redshift	Dataset	$N_{\rm c}$(Quiescent)	$N_{\rm c}$(Star − forming)
Central mass: $\log(M_{\rm cen}/{\rm M}_{\odot}) > 10.5$				
Satellite mass: $\log(M_{\rm sat}/{\rm M}_{\odot}) = 9.3 - 9.8$	$0.3 < z < 0.6$	UDS	263	134
		UltraVISTA	846	701
	$0.6 < z < 0.9$	UDS	468	317
		UltraVISTA	1494	1375
		ZFOURGE	92	91
	$0.9 < z < 1.6$	UDS	1207	1486
		UltraVISTA	2770	3924
		ZFOURGE	156	219
	$1.6 < z < 2.5$	ZFOURGE	140	199
Satellite mass: $\log(M_{\rm sat}/{\rm M}_{\odot}) = 9.8 - 10.2$	$0.3 < z < 0.6$	UDS	263	134
		UltraVISTA	846	701
	$0.6 < z < 0.9$	UDS	468	317
		UltraVISTA	1494	1375
		ZFOURGE	92	91
	$0.9 < z < 1.6$	UDS	1207	1486

		UltraVISTA	2770	3924
		ZFOURGE	156	219
	$1.6 < z < 2.5$	ZFOURGE	140	199
Central mass: $10.5 < \log(M_{\rm cen}/{\rm M}_{\odot}) < 10.8$				
Satellite Mass: $\log(M_{\rm sat}/{\rm M}_{\odot}) = 9.3 - 10.2$	$0.3 < z < 0.6$	UDS	161	108
		UltraVISTA	369	479
	$0.6 < z < 0.9$	UDS	288	240
		UltraVISTA	762	951
		ZFOURGE	38	53
	$0.9 < z < 1.6$	UDS	656	977
		UltraVISTA	1461	2652
		ZFOURGE	79	120
	$1.6 < z < 2.5$	ZFOURGE	71	95
Central mass: $\log(M_{\rm cen}/{\rm M}_{\odot}) > 10.8$				
Satellite mass: $\log(M_{\rm sat}/{\rm M}_{\odot}) = 9.3 - 10.2$	$0.3 < z < 0.6$	UDS	102	26
		UltraVISTA	477	222
	$0.6 < z < 0.9$	UDS	180	77
		UltraVISTA	732	424
		ZFOURGE	53	38

$0.9 < z < 1.6$	UDS	551	509
	UltraVISTA	1309	1272
	ZFOURGE	77	96
$1.6 < z < 2.5$	ZFOURGE	65	100

3.3.2 Selection of Centrals and UVJ Classification

Our goal is to measure the fraction of quiescent satellites ($f_{q,sat}$) around massive galaxies at $0.3 < z < 2.5$. We select central galaxies from the three datasets with $\log(M_{\rm cen}/{\rm M}_{\odot}) > 10.5$ (i.e., $M_{\rm cen} > 3 \times 10^{10}$ ${\rm M}_{\odot}$). We also study the dependence of satellite quenching on the stellar mass of central galaxies, and will consider subsamples of central galaxies with $10.5 < \log(M_{\rm cen}/{\rm M}_{\odot}) < 10.8$ and $\log(M_{\rm cen}/{\rm M}_{\odot}) > 10.8$ (i.e., $> 6 \times 10^{10}$ ${\rm M}_{\odot}$). A summary of number of centrals from each galaxy sample is given in Table 3.2.

Similar works by Tal et al. (2013) and Hartley et al. (2015) applied isolation criteria for the selection of central galaxies. They considered galaxies as "central" if no other, more massive galaxies are found within a projected radius of 500 pkpc (proper kpc). Otherwise, galaxies are counted as satellites of their more massive neighbors. Phillips et al. (2014) applied a similar isolation criteria for galaxies with $\log(M_{\rm cen}/{\rm M}_{\odot}) > 10.5$ by allowing no other galaxies with similar stellar mass within a projected distance of 350 pkpc. In addition to this isolation criterion, they allow no more than one galaxy with $\log(M_{\rm cen}/{\rm M}_{\odot}) > 10.5$ within an inner (outer) radius of 350 pkpc (1 pMpc).

We apply a similar rejection criterion for our central galaxy sample selection, as contamination in our sample of centrals can potentially introduce a spurious conformity signal (Campbell et al., 2015). We exclude galaxies from our sample of centrals if there is a more massive galaxy within a projected radius of 300 ckpc (comoving kpc). We opt to use this comoving aperture size as it is approximately the virial radius of a halo with mass of $\log(M/{\rm M}_{\odot}) \sim 12.0$ over our redshift range, which is near the halo mass of our intermediate-mass galaxy sample ($10.5 < \log(M_{\rm cen}/{\rm M}_{\odot}) < 10.8$). Because the virial radius increases weakly with halo mass, we also test an isolation criteria of 500 ckpc. We find that the conformity signals described in Section 3.5 persist, but the significance decreases because the sample size drops by $20 - 50\%$, so we adopt 300 ckpc isolation criteria.

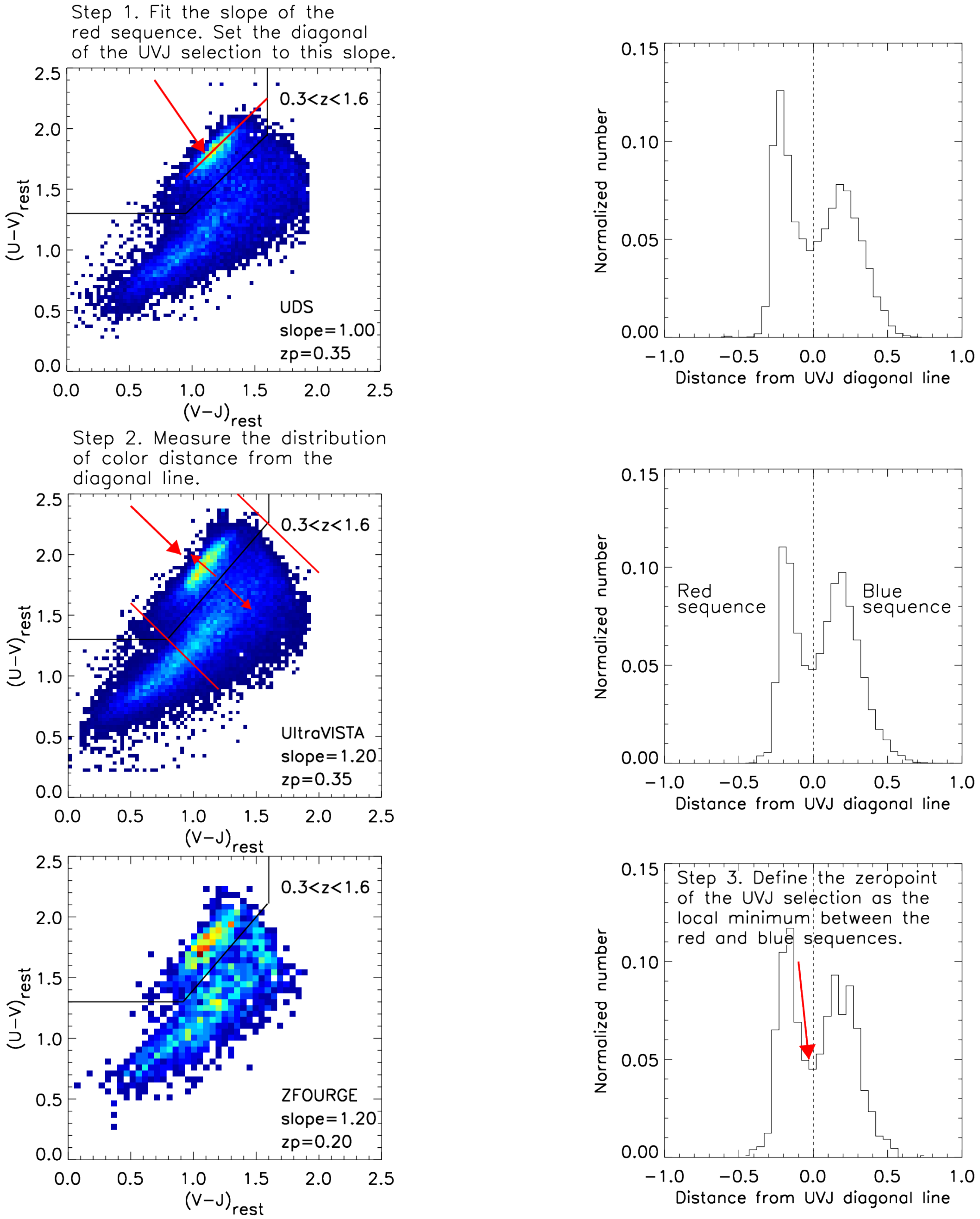

Figure 3.2: Rest-frame $U-V$ versus $V-J$ color of galaxies in ZFOURGE, UDS, and UltraVISTA.

Left: Rest-frame $U-V$ versus $V-J$ color for galaxy sample with $\log(M_*/\mathrm{M}_\odot) > 9.8$ at $0.3 < z < 1.6$. The galaxies in the upper left region of the plot (separated by the solid line) are quiescent; galaxies outside this region are star forming. ***Right***: Distribution of the distance (in color) from the diagonal line in UVJ color (the slope A, see Equation 3.1) that separates the quiescent and star-forming sequences in the UVJ color space. We define the zeropoint of the UVJ quiescent region as the local minimum in this distribution, indicated by the vertical dashed line. Reprinted with permission from "Satellite Quenching and Galactic Conformity at $0.3 < z < 2.5$" by Kawinwanichakij et al., 2016. The Astrophysical Journal, Volume 817, Issue 1, article id. 9 pp. 19, Copyright 2016.

We classify galaxies as either star-forming or quiescent based on the rest-frame $U - V$ versus $V - J$ color-color diagram (UVJ diagram; e.g., Williams et al., 2009; Whitaker et al., 2011). Our early tests of the different catalogs showed that there exist (small) systematic variations in the rest-frame colors of galaxies at fixed mass and redshift in different surveys. To remove the effect of these systematic variations on our analysis, we implement a method to self-calibrate the region delineating the colors of star-forming and quiescent in the color-color space (Figure 3.2).We start by defining a generic region of the UVJ diagram for quiescent galaxies as,

$$\begin{aligned} U - V &> A \times (V - J) + zp \\ U - V &> 1.3 \\ V - J &< 1.6 \end{aligned} \tag{3.1}$$

where A and zp are variables we derive as follows. We fit for A as the slope of the red sequence in the UVJ plane, finding slopes of $A = 1.2, 1.0$, and 1.2 for ZFOURGE, UDS, and UltraVISTA, respectively. Next, we measure the distribution of the distance in UVJ color from the diagonal line defined by the slope A in Equation 3.1 (where the "color distance" is the distance in UVJ color from the line). We measure the zeropoint zp as the local minimum between the two peaks in the UVJ color distribution. Figure 3.2 shows a demonstration. We find zeropoints of $zp = 0.2, 0.35$, and 0.35 for ZFOURGE, UDS, and UltraVISTA. Our method therefore removes any systematics between the data and/or in the analysis of the survey catalogs and minimizes any differences in the definition of the quiescent region for the UVJ diagram. Table 3.2 gives the numbers of quiescent and star-forming galaxies in the UDS, UltraVISTA, and ZFOURGE fields.

3.3.3 Selection of Satellites

To identify satellites of the central galaxies in our sample, we first select all neighboring galaxies around each central from our sample that satisfy the following satellite conditions

$$\begin{aligned} |z_{\rm cen} - z_{\rm sat}| &\leq 0.2 \\ M_{\rm lim} \leq M_{\rm sat} &< 10^{10.2}\,{\rm M}_\odot \end{aligned} \tag{3.2}$$

where $z_{\rm cen}$ and $z_{\rm sat}$ are the photometric redshift of the central and satellite, respectively. $M_{\rm sat}$ is the stellar mass of the satellite, and $M_{\rm lim}$ is the lower-mass limit, which is shown in Figure 3.1. Our requirement that $\Delta z = |z_{\rm cen} - z_{\rm sat}| \leq 0.2$ is motivated by our relative photometric uncertainty (σ_z) between centrals and satellites as mentioned in Section 3.3. In each case, the σ_z values for galaxies are less than half the $\Delta z \leq 0.2$ requirement in Equation 3.2, which argues that this selection criterion is appropriate. The stellar mass limits for satellites we study is $9.3 < \log(M_{\rm sat}/{\rm M}_\odot) < 10.2$, and later we subdivide this into bins of $9.3 < \log(M_{\rm sat}/{\rm M}_\odot) < 9.8$ and $9.8 < \log(M_{\rm sat}/{\rm M}_\odot) < 10.2$ in order to test for variations in the quenching efficiency as a function of satellite mass.

Our primary results in this study are determined using an evolving stellar-mass limit, in which we only select satellites in each field that are above the mass-completeness limits (See Section 3.3.1 and Figure 3.1). This maximizes our sample size and boosts the significance of our results. For example, at $0.6 < z < 0.9$ and $0.9 < z < 1.6$, where the UltraVISTA galaxy sample starts to become incomplete, we then only use satellites from that survey lying above the mass completeness curve (shown as the hatched region above the thick dash curve in Figure 3.1). In principle this may affect our results, since in some of the redshift/mass bins the mean redshift and the mean satellite stellar mass will differ slightly between our fields. However this is a small effect as the satellite quenching efficiency does not depend strongly on satellite mass (Section 3.5.3), and moreover we have verified that none of our main results change if we use fixed lower mass limit at all redshifts ($\log(M_{\rm sat}/{\rm M}_\odot) > 9.3$).

3.4 Environmental quenching of satellite galaxies

3.4.1 Identifying Satellites using Statistical Background Subtraction

To perform a statistical analysis of the average quiescent fraction of satellites around our sample of massive galaxies, we use a statistical background subtraction technique (e.g., Kauffmann et al., 2010; Tal et al., 2012; Wang & White, 2012; Kawinwanichakij et al., 2014). We detect objects within fixed apertures centered on our central galaxies and satisfying Equation 3.2. These apertures include both physically-associated galaxies as well as chance alignments of foreground and background galaxies. We estimate and correct for the contamination due to chance alignments by placing random apertures across the field. We adapt this procedure by restricting the placement of the random apertures to regions near to the centrals, as demonstrated by Chen et al. (2006). This accounts for the bias due to contaminating galaxies that are physically-associated with the centrals, but are not satellites (i.e., the two-halo term of the correlation function; see Chen et al. 2006)[2]. We therefore place the random apertures within annuli with inner and outer radii equal to 1 and 3 cMpc from each central galaxy for the UDS and UltraVISTA. Parenthetically, our tests showed that the restriction on the location of the background apertures has only a small effect on the conformity signal. Relative to apertures that are placed randomly through the field, this correction increases the quiescent fractions of background galaxies by 0.4%–10%. For the smaller ZFOURGE fields, placing the random apertures within annuli is too restrictive, and for this survey we randomly place the apertures across the fields. We do note that the ZFOURGE fields are small enough that even these randomly-placed apertures trace the same large-scale environment as the centrals. Additionally, we find that when we restrict the background apertures to be > 3 cMpc from the centrals, it changes the measured quenching efficiencies (see Section 3.5 below) by 10%, and none of our conclusions would be changed.

Both the random and real apertures have a radius of 300 ckpc. We experimented using 300

---

[2] The contaminating galaxies that are physically-associated with the central galaxies in our sample are expected to have marginally different properties than truly random field galaxies due to the fact that they exist in biased regions of the Universe. There may be an additional effect due to large-scale 2-halo conformity. If 2-halo conformity exists, our procedure effectively corrects for it.

pkpc apertures (i.e., apertures with a fixed physical size rather than fixed comoving size), and find that our main conclusions are not appreciably affected by the choice of aperture. We therefore adopt the measurement of quiescent fraction within a circular aperture of 300 ckpc for the rest of this chapter. We also tested a plausible range of aperture sizes, and found they do not appreciably change the results. In the Appendix A we show the effect on the quenching efficiencies of satellites around quiescent and star-forming centrals using these different-sized apertures (both comoving and physical aperture radii).

3.4.2 Matching the Stellar Mass Distribution of Star-Forming and Quiescent Central Galaxies

Quiescent galaxies have a stellar mass distribution that is shifted to higher stellar masses compared to star-forming galaxies. Therefore, any observation that satellites around quiescent central galaxies may be preferentially quenched may be caused by a difference in the stellar mass of the centrals. Therefore we match the stellar mass distributions of the quiescent and star-forming central galaxies. Following the method of Hartley et al. (2015) we construct a histogram of stellar masses of central galaxies in bins of $\Delta \log(M_{\text{cen}}) = 0.1$ and use this to calculate a weighting factor for each stellar mass bin of quiescent centrals (w_i^q) using

$$w_i^q = \frac{N_{\text{cen},i}}{N^q_{\text{cen},i}} \tag{3.3}$$

Similarly, we calculate the weighting factor for each stellar mass bin of star-forming centrals (w_i^{sf}) using

$$w_i^{sf} = \frac{N_{\text{cen},i}}{N^{sf}_{\text{cen},i}} \tag{3.4}$$

where $N_{cen,i}$ is the total number of central galaxies in stellar mass bin i and $N^{q(sf)}_{\text{cen},i}$ is the number of quiescent (star-forming) centrals in stellar mass bin i.

In each bin of central stellar mass, we weight the number of satellites by w_i^q for quiescent centrals and by w_i^{sf} for star-forming centrals. This effectively matches the stellar mass distributions of both the quiescent and star-forming centrals to the stellar mass distribution of all central galaxies (this is similar to the method used to match the stellar mass distributions of centrals in Kawinwanichakij et al., 2014).

In addition to the difference in the stellar mass distributions, there are slight differences in the redshift distributions of quiescent and star-forming centrals within each redshift bin. For example, if, at fixed stellar mass, the star-forming galaxies tend to lie at higher redshift, then this could possibly affect our results. However, we argue this is not the case. In each redshift bin, the difference in mean redshift between the star-forming and quiescent centrals is small, and comparable to the photometric redshift uncertainty, $\Delta z \lesssim 0.02(1+z)$. Furthermore, if differences in the redshift distributions of the star-forming and quiescent centrals were important, we would expect the quenching efficiency of star-forming galaxies to be more similar to the quenching efficiency of quiescent galaxies in adjacent redshift bins. As we show below (Section 3.5.1), this is not the case: the quenching efficiency of satellites around quiescent galaxies is consistently higher than that for star-forming centrals in any of the other redshift bins at $0.6 < z < 0.9$, $0.9 < z < 1.6$, and $1.6 < z < 2.5$. Therefore, it seems unlikely that the (small) differences in the redshift distributions of the quiescent and star-forming centrals within each redshift bin contribute significantly to the observed galactic conformity signal.

3.4.3 Average Quiescent Fraction

We count the number of quiescent and star-forming neighboring galaxies in apertures around central galaxies in redshift bins. We define "neighboring galaxies" as those in the vicinity of the centrals that satisfy the Equation 3.2 (neighboring galaxies include both satellites and foreground or background objects along the line of sight). The quiescent fractions of neighboring galaxies ($f_{q,nei}$) are shown in the left panel of Figure 3.3. We then perform the same measurement with the random apertures. As shown in the right panel of Figure 3.3, the quiescent fractions of galaxies measured in random apertures ($f_{q,bg}$) tend to be lower than for the neighboring galaxies, and are quite consistent among the surveys, with $\langle f_{q,bg} \rangle \sim 0.2$.

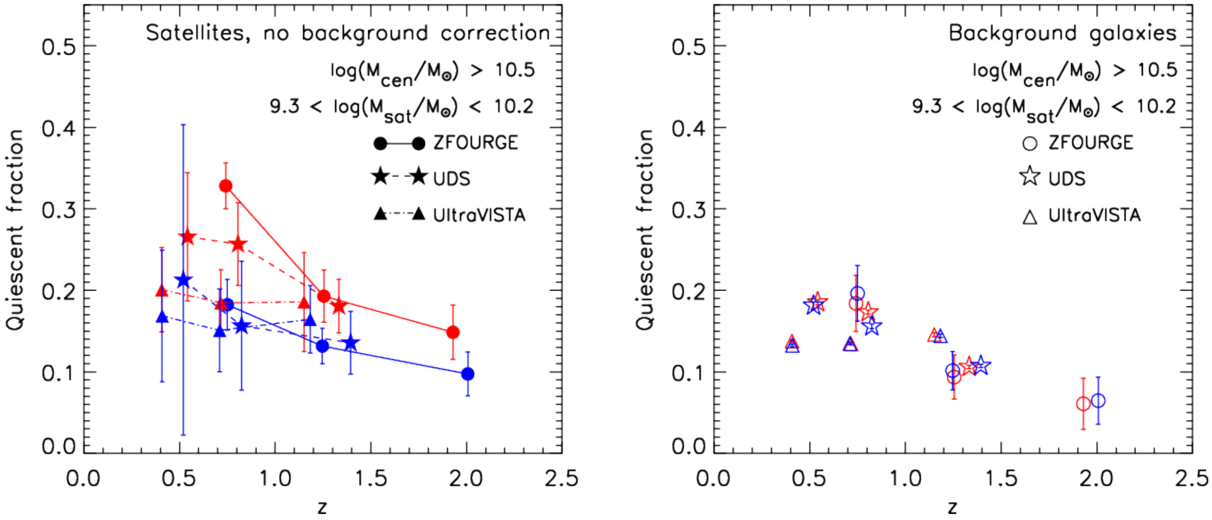

Figure 3.3: The evolution of the average quiescent fraction of neighboring galaxies.

Left: The evolution of the average quiescent fraction of neighboring quiescent galaxies ($f_{q,nei}$) with stellar mass of $9.3 < \log(M_{\rm sat}/{\rm M}_\odot) < 10.2$ around the quiescent centrals (red) and the star-forming centrals (blue) ($\log(M_{\rm cen}/{\rm M}_\odot) > 10.5$) from three datasets: ZFOURGE (circles), UKIDSS UDS (stars), and UltraVISTA (triangles). ***Right:*** Same as the left panel but for the average quiescent fraction of neighboring background ($f_{q,bg}$) measured in random apertures. We use the measurement in random apertures to account for physically associated galaxies as well as chance alignment of foreground and background galaxies (Section 3.4). The error bars are based on the 68 percentile of the distribution of the quiescent fraction of satellites from a bootstrap resampling technique (Section 3.4.5). The UltraVISTA and UDS points have been offset to lower and higher redshift slightly for clarity. Reprinted with permission from “Satellite Quenching and Galactic Conformity at $0.3 < z < 2.5$" by Kawinwanichakij et al., 2016. The Astrophysical Journal, Volume 817, Issue 1, article id. 9 pp. 19, Copyright 2016.

We estimate the average quiescent fraction of satellites ($f_{q,sat}$) using

$$f_{q,sat} = \frac{\Sigma(N^{q}_{nei} - N^{q}_{bg})}{\Sigma(N^{tot}_{nei} - N^{tot}_{bg})} \tag{3.5}$$

where N^{q}_{nei} and N^{tot}_{nei} are the number of neighboring quiescent galaxies and the total neighboring galaxies, respectively, around a central. Similarly, N^{q}_{bg} and N^{tot}_{bg} are the number of neighboring quiescent galaxies and the total neighboring galaxies, respectively, measured in the random aperture. The summation is for all central galaxies in a given subsample of stellar mass and/or redshift. The resulting fraction ($f_{q,sat}$) represents the average fraction of quiescent satellites around that sample of central galaxies.

3.4.4 Average Quenching Efficiency

In this work we are concerned with the difference in quiescent fractions of satellites and background galaxies. This difference, normalized by the star-forming fraction of the background galaxies, gives a direct estimate of the fraction of satellites that have been quenched in excess of the quenched field galaxy population,

$$\epsilon_{q,sat} = \frac{f_{q,sat} - f_{q,bg}}{1 - f_{q,bg}} \tag{3.6}$$

where $f_{q,sat}$ is the quiescent fraction of satellites measured around centrals, and $f_{q,bg}$ is the quiescent fraction of satellites measured in random apertures. We refer to $\epsilon_{q,sat}$ as the quenching efficiency.

3.4.5 Error estimation

We estimate the uncertainty on the quiescent fraction ($f_{q,sat}$) and the quenching efficiency ($\epsilon_{q,sat}$) measurements using a bootstrap resampling technique. We generate 100,000 bootstrap samples for each subsample of quiescent and star-forming centrals. We then measure the satellite quiescent fractions and the quenching efficiencies for each set of bootstrap samples. We calculate the uncertainty as the 68 percentile of the distribution of the quiescent fraction (or quenching efficiency) of satellites from the bootstrap samples. The error bars estimated from these bootstrap resamplings are up to 3 times larger than the Poisson uncertainties.

We also use the uncertainties from a bootstrap technique of each field and survey (the three ZFOURGE fields, UDS, and UltraVISTA) to calculate weights for combining the results from the fields. We use this combined dataset for our analysis, but we also discuss survey-to-survey variations.

3.4.6 Significance estimation

It is desirable to assign a significance statistic (p–value) when comparing the differences between the quiescent fraction of satellites (or the quenching efficiency of satellites) for different subsamples. We estimate the significance as the fraction of bootstrap samples (Section 3.4.5) in which the quiescent fraction (or the quenching efficiency) of satellites around star-forming centrals is equal or greater than that of quiescent centrals. We denote the p–value derived from the bootstrap resampling technique as p.

3.5 Dependence of Satellite Quenching on Galaxy Properties

3.5.1 The Detection of Satellite Quenching and Galactic Conformity to $z \sim 2$

We investigate how satellite quenching depends on the star-formation activity of central galaxies by dividing our sample of central galaxies into subsamples that are star-forming and quiescent, where these labels correspond to galaxies with high and low sSFRs (Williams et al., 2009; Papovich et al., 2012), using their rest-frame $U-V$ and $V-J$ colors as illustrated in Figure 3.2 and discussed in Section 3.3.2. We then compute the quiescent fraction (Equation 3.5) and quenching efficiency of satellites (Equation 3.6) for each subsample. We use the evolving stellar-mass selection limit for satellites (Section 3.3.3), and we apply the weighting factors to match the stellar-mass distributions of star-forming and quiescent central galaxies (Section 3.4.2). Error bars are estimated from a bootstrap resampling technique as described in Section 3.4.5.

Figure 3.4 shows the satellite quiescent fraction for both quiescent and star-forming centrals from each dataset and each redshift bin. At all redshifts, satellites of quiescent centrals have higher quiescent fractions compared to satellites of star-forming centrals. Thus the phenomenon of galactic conformity can be seen in each of our datasets and in every redshift bin – out to the highest redshifts probed by each dataset. This is one of the main conclusions of this study.

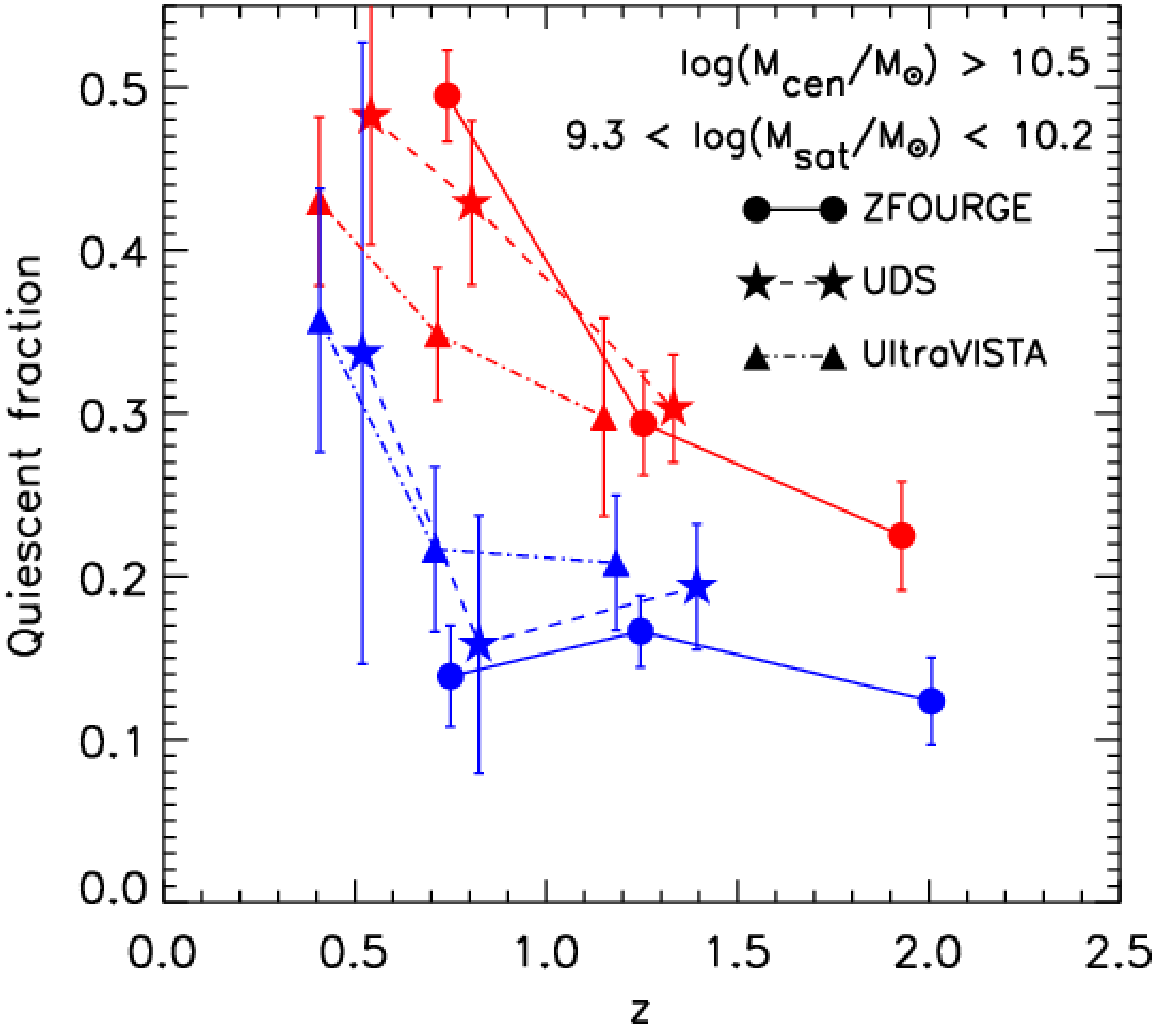

Figure 3.4: The evolution of the average quiescent fraction of satellites.

The evolution of the average quiescent fraction ($f_{q,sat}$) of satellites with stellar mass of $9.3 < \log(M_{\rm sat}/{\rm M}_{\odot}) < 10.2$ around quiescent centrals (red) and star-forming centrals (blue) ($\log(M_{\rm cen}/{\rm M}_{\odot}) > 10.5$) from three datasets: ZFOURGE (circles), UKIDSS UDS (stars), and UltraVISTA (triangles). The error bars are based on the 68 percentile of the distribution of the quiescent fraction of satellites from the bootstrap samples. For all fields and redshift ranges, we see evidence for higher quiescent fractions for satellites around quiescent centrals compared to satellites around star-forming centrals at fixed stellar mass. The UltraVISTA and UDS points have been offset to lower and higher redshift slightly for clarity. Reprinted with permission from “Satellite Quenching and Galactic Conformity at $0.3 < z < 2.5$" by Kawinwanichakij et al., 2016. The Astrophysical Journal, Volume 817, Issue 1, article id. 9 pp. 19, Copyright 2016.

Figure 3.5 shows the satellite quenching efficiency, which quantifies the excess quiescent fraction of satellites compared to mass-matched field samples (see Equation 3.6). This figure shows that satellites of both quiescent and star-forming centrals have excess quenching (i.e., positive quenching efficiency). The effect is most pronounced for quiescent centrals, especially at $0.6 < z < 0.9$. As discussed in Section 3.2, there have been mixed results in the literature regarding whether or not star-forming centrals can quench their satellites; we find that they can. This suggests that the cause of quenching in satellites is not tied directly to quenching in centrals, i.e., that satellites can be quenched even when the central galaxy is not. This is another primary conclusion of this study.

These conclusions can be seen more clearly in Figures 3.6 and 3.7, where we show the quiescent fraction and quenching efficiency of satellites after combining the measurements from the three datasets. Although satellites are quenched over time, we see evidence for galactic conformity at all redshifts for centrals at fixed stellar mass. When the three fields are combined, there is significant, strong evidence that satellites around both star-forming and quiescent centrals have greater than zero quenching efficiencies: satellites have excess quenching above similar galaxies in the field regardless of the activity of their central galaxy.

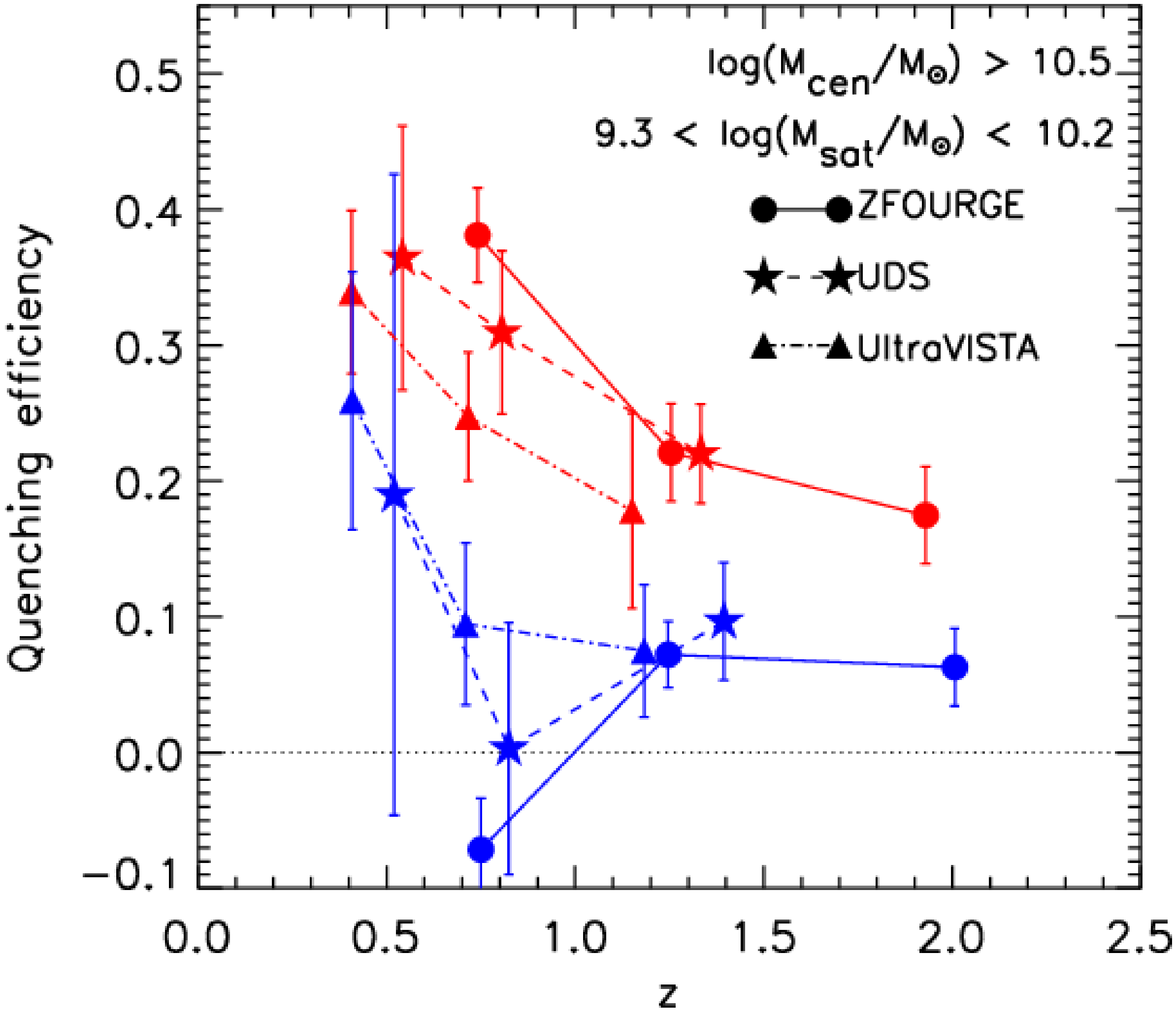

Figure 3.5: The quenching efficiency of satellites as a function of redshifts for galaxies in ZFOURGE, UDS, UltraVISTA .

The average quenching efficiency of satellites ($\epsilon_{q,sat}$) with stellar mass of $9.3 < \log(M_{\rm sat}/{\rm M}_{\odot}) < 10.2$ around central galaxies ($\log(M_{\rm cen}/{\rm M}_{\odot}) > 10.5$) from three datasets: ZFOURGE (circles), UKIDSS UDS (stars), and UltraVISTA (triangles). The horizontal dotted line at $\epsilon_{q,sat} = 0$ indicates where a galaxy is not quenched as it becomes a satellite of a central galaxy. The quenching efficiency of satellites around quiescent centrals is higher compared to those around the star-forming centrals, although the effect is most pronounced at $0.6 < z < 0.9$. The positive quenching efficiency of satellites of star-forming centrals (at least at $z < 0.6$) indicates that satellites of star-forming centrals are more quenched compared to background galaxies at the same stellar mass. The UltraVISTA and UDS points have been offset to lower and higher redshift slightly for clarity. Reprinted with permission from “Satellite Quenching and Galactic Conformity at $0.3 < z < 2.5$" by Kawinwanichakij et al., 2016. The Astrophysical Journal, Volume 817, Issue 1, article id. 9 pp. 19, Copyright 2016.

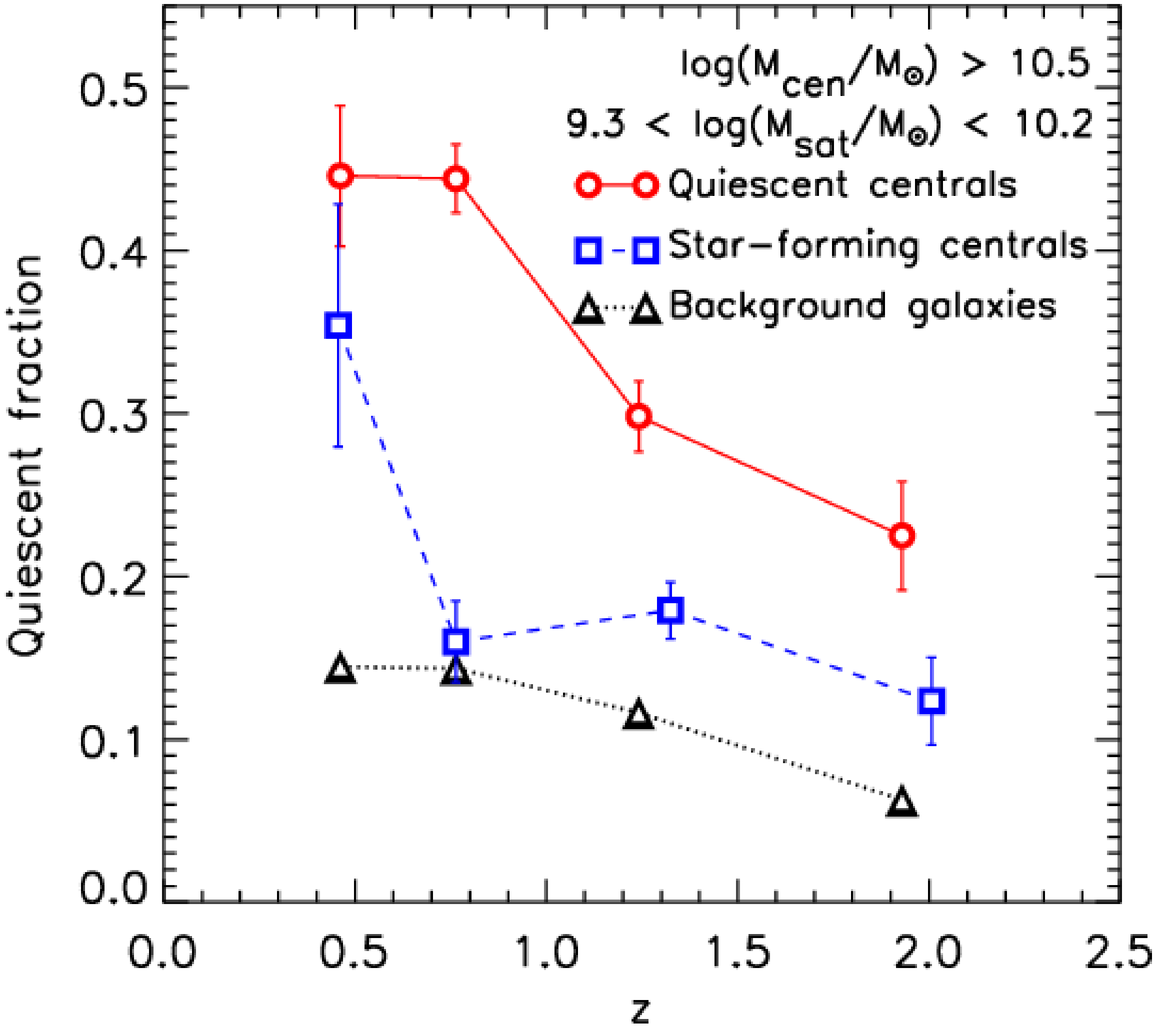

Figure 3.6: The evolution of quiescent fraction of satellites.

The average quiescent fraction of satellites ($f_{q,sat}$) with stellar mass of $9.3 < \log(M_{\rm sat}/{\rm M}_{\odot}) < 10.2$ around quiescent centrals (red circles) and star-forming centrals (blue squares) with stellar mass of $\log(M_{\rm cen}/{\rm M}_{\odot}) > 10.5$ combining from the three datasets. The average quiescent fraction of background galaxies of the same stellar masses are also shown (black triangles). Reprinted with permission from “Satellite Quenching and Galactic Conformity at $0.3 < z < 2.5$" by Kawinwanichakij et al., 2016. The Astrophysical Journal, Volume 817, Issue 1, article id. 9 pp. 19, Copyright 2016.

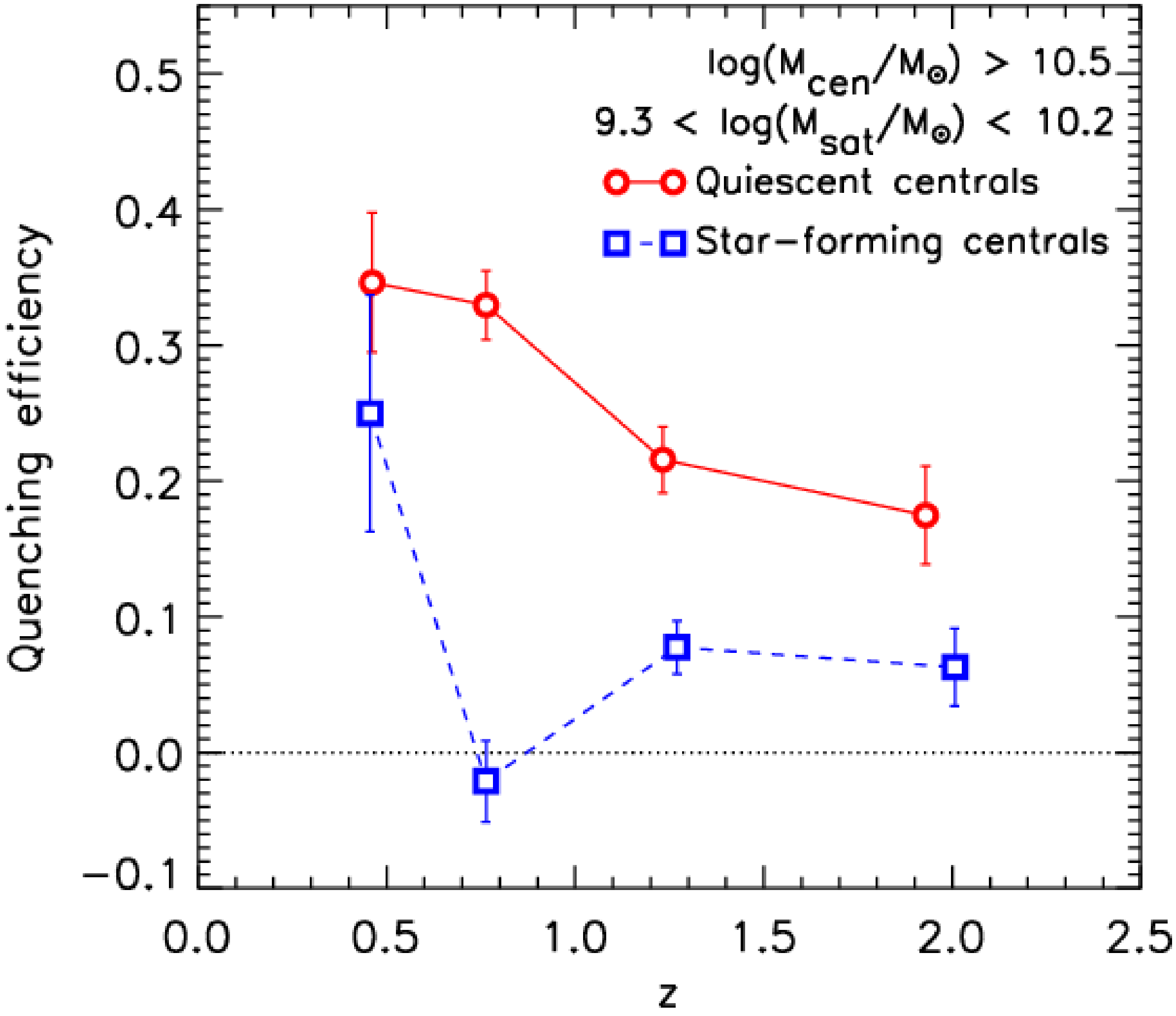

Figure 3.7: The quenching efficiency of satellites as a function of redshift.

The average quenching efficiency of satellites ($\epsilon_{q,sat}$) with stellar mass of $9.3 < \log(M_{\rm sat}/{\rm M}_{\odot}) < 10.2$ around central galaxies ($\log(M_{\rm cen}/{\rm M}_{\odot}) > 10.5$) combining from three datasets. The horizontal dotted line at $\epsilon_{q,sat} = 0$ indicates no excess quenching of a satellite compared to mass-matched field samples. Galactic conformity is evident as the higher quenching efficiency of satellites of quiescent centrals. Satellites of star-forming centrals show low quenching efficiency for $z > 0.6$. For $z < 0.6$ there is evidence for elevated quenching of satellites of star-forming centrals (though still less than that for quiescent centrals). Based on our bootstrap analysis, at $0.6 < z < 1.6$ the galactic conformity is significant at $3-4.5\sigma$, whereas the conformity at lowest and highest redshift is less significant. Reprinted with permission from "Satellite Quenching and Galactic Conformity at $0.3 < z < 2.5$" by Kawinwanichakij et al., 2016. The Astrophysical Journal, Volume 817, Issue 1, article id. 9 pp. 19, Copyright 2016.

At $0.6 < z < 0.9$ and $0.9 < z < 1.6$, there is high statistical significance that satellites of quiescent centrals have a higher quenching efficiency than satellites of star-forming centrals with $p \sim 0.000001$ ($\simeq 4.5\sigma$) and $p = 0.00021$ ($\simeq 3.5\sigma$), respectively. At $0.3 < z < 0.6$ the conformity signal is less significant ($p = 0.088$, 1.4σ) and at $1.6 < z < 2.5$ there is no appreciable signal ($p = 0.42$).

Even though the survey volume is small and the statistical significance of the conformity signal is weak at $0.3 < z < 0.6$ (1.4σ significance; see above and Figure 3.7), the signal is in line with what has been observed at even lower redshifts in SDSS (see Section 3.2). Additionally, in the Appendix A we show that the strength of the conformity signal at $0.3 < z < 0.6$ depends on the size of the aperture used to select satellites, where using different apertures can increase the conformity signal in this redshift bin, making it more in line with the SDSS results.

In the remainder of this chapter we will continue exploring the dependence of satellite quenching by studying the quenching efficiency measured by combining all three datasets.

3.5.2 Does Galactic Conformity Depend on the Central Mass?

We divide our central galaxy sample into two mass bins: $10.5 < \log(M_{\rm cen}/{\rm M}_{\odot}) < 10.8$ and $\log(M_{\rm cen}/{\rm M}_{\odot}) > 10.8$. We then recompute the quenching efficiency of satellites for each of these subsamples to study the dependence of satellite quenching on the stellar mass of centrals using the method described in Section 3.3.3.

As shown in Figure 3.8, there is evidence for a dependence of satellite quenching on central mass for quiescent centrals at $0.3 < z < 0.6$ and $0.9 < z < 1.6$: satellites of more massive quiescent centrals at these redshifts have a higher quenching efficiency. Similarly, for star-forming centrals, satellites of more massive centrals have a higher quenching efficiency at all redshifts, except at $1.6 < z < 2.5$. Figure 3.8 also shows that we observe the conformity of intermediate-mass centrals and high-mass centrals only at $0.6 < z < 0.9$.

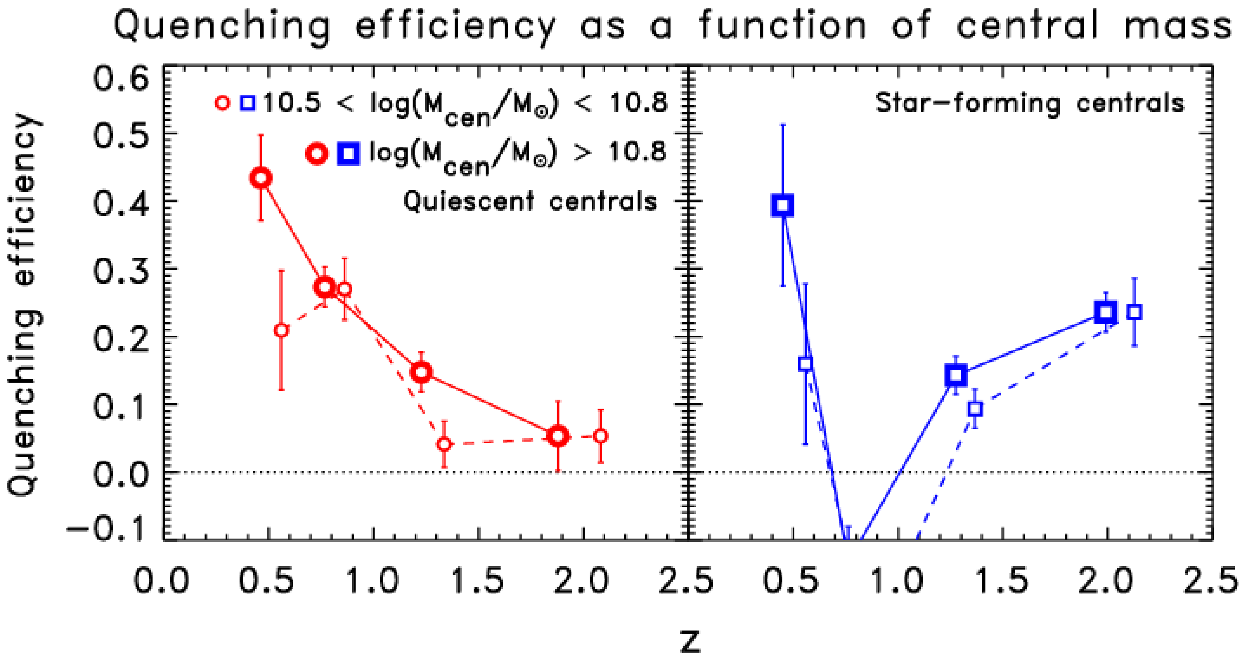

Figure 3.8: Quenching efficiency of satellites as a function of central mass.

Left: Comparison between the average quenching efficiency of satellites ($9.3 < \log(M_{\rm sat}/{\rm M}_\odot) < 10.2$) around intermediate ($10.5 < \log(M_{\rm cen}/{\rm M}_\odot) < 10.8$; red solid line with small open circles, offset slightly for clarity) and high-mass ($\log(M_{\rm cen}/{\rm M}_\odot) > 10.8$; red dash line with large open circles) quiescent centrals. ***Right:*** Same as the left panel but for star-forming centrals. Reprinted with permission from “Satellite Quenching and Galactic Conformity at $0.3 < z < 2.5$" by Kawinwanichakij et al., 2016. The Astrophysical Journal, Volume 817, Issue 1, article id. 9 pp. 19, Copyright 2016.

3.5.3 Does Galactic Conformity Depend on the Satellite Mass?

We divide our satellite galaxy sample with stellar masses in the range $9.3 < \log(M_{\rm sat}/{\rm M}_{\odot}) < 10.2$ into two mass bins: $9.3 < \log(M_{\rm sat}/{\rm M}_{\odot}) < 9.8$ and $9.8 < \log(M_{\rm sat}/{\rm M}_{\odot}) > 10.2$. We then recompute the quenching efficiency of satellites for each of these subsamples following the method described in Section 3.4, and use an evolving stellar-mass limit for satellites (Section 3.3.3).

Figure 3.9 shows that there is no significant evidence that the quenching efficiency depends on satellite mass for quiescent centrals. The lack of a strong dependence of quenching on the mass of satellites is in agreement with the results from several studies (e.g., van den Bosch et al., 2008; Peng et al., 2012; Quadri et al., 2012; Wetzel et al., 2013; Knobel et al., 2015) The galactic conformity signals for both low and high-mass satellites persist, except perhaps for low-mass satellites at $0.3 < z < 0.6$. We discuss the implications of these results in Section 3.6.

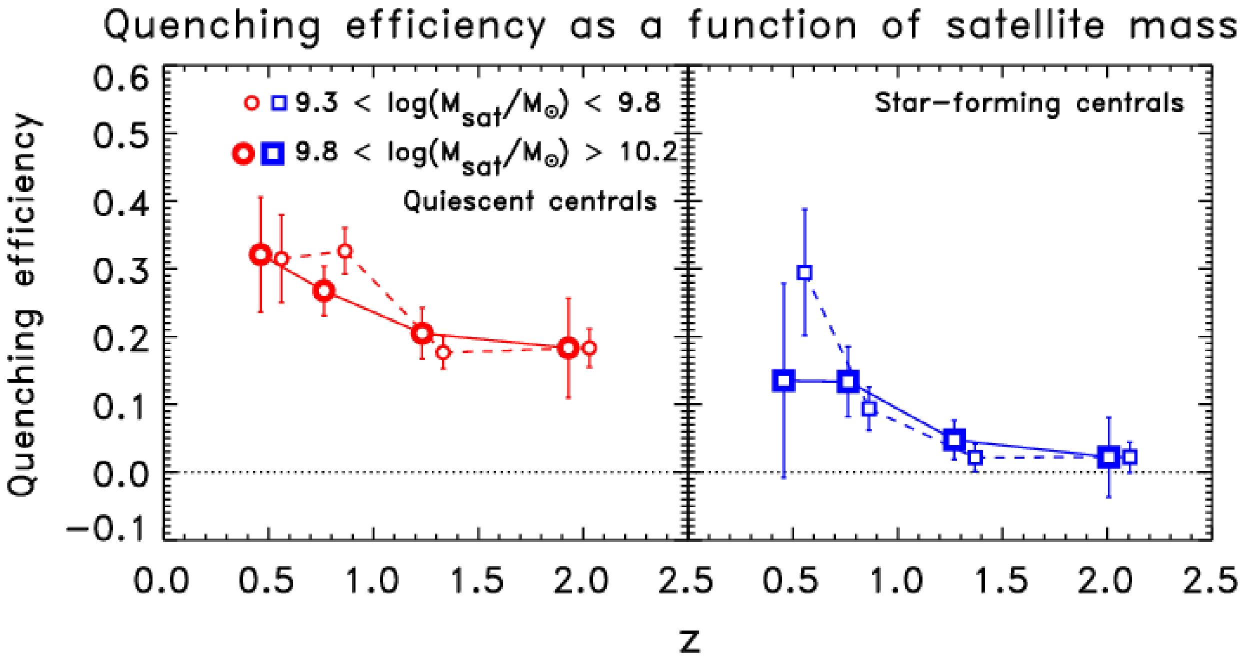

Figure 3.9: Quenching efficiency of satellites as a function of satellite mass.

Left: Comparison between the average quenching efficiency of low-mass satellites ($9.3 < \log(M_{\rm sat}/{\rm M}_\odot) < 9.8$; red dash line with small open circles) and high-mass satellites ($9.8 < \log(M_{\rm sat}/{\rm M}_\odot) < 10.2$; red solid line with large open circles) around all quiescent centrals ($\log(M_{\rm cen}/{\rm M}_\odot) > 10.5$). ***Right:*** Same as the left panel but for satellites around star-forming centrals. Reprinted with permission from "Satellite Quenching and Galactic Conformity at $0.3 < z < 2.5$" by Kawinwanichakij et al., 2016. The Astrophysical Journal, Volume 817, Issue 1, article id. 9 pp. 19, Copyright 2016.

A remaining question is how the conformity signal depends on the mass ratio of the central and satellite galaxies (rather than the absolute central and satellite stellar masses). We attempted to investigate this effect by binning the sample by the stellar mass ratio between the satellites and centrals. However, this procedure severely limited the number of galaxies in the samples, such that we were unable to recover meaningful results. To study this effect we will require larger samples than are currently available.

3.6 Discussion

In § 3.5 we showed that satellites around quiescent centrals have a higher quenching efficiency compared to satellites around star-forming centrals. This is galactic conformity, and it persists with high significance at intermediate redshift ($0.7 < z < 2.0$), and with a low level of significance at lower ($z \sim 0.5$) and higher ($z \sim 2.5$) redshift (Figure 3.6 and 3.7). In addition, the quenching efficiency of satellites around star-forming centrals is greater than zero indicating that satellites of star-forming centrals are more quenched compared to background galaxies. In this section we discuss the origin of the galactic conformity and the origin of the excess quenching of satellites of star-forming centrals.

3.6.1 Does Halo Mass Drive Galactic Conformity?

Thus far we have investigated galactic conformity at fixed stellar mass, i.e., we have compared satellite quenching for samples of star-forming and quiescent centrals that have the same stellar mass distribution. However there is some observational evidence that, at fixed stellar mass, quiescent central galaxies occupy more massive halos than star-forming central galaxies (e.g., Mandelbaum et al., 2006; More et al., 2011; Hartley et al., 2013; Phillips et al., 2014; Kawinwanichakij et al., 2014). This raises the possibility that, if satellite quenching is a function of halo mass, the observed conformity signal is due to a difference in halo mass rather than to a difference in star formation properties of central galaxies. As discussed in §3.2, there is some observational evidence that this is the case, although the results have been mixed. Ideally we would test this by matching the halo masses of our quiescent and star-forming sample rather than matching the stellar masses, but we lack halo mass estimates for the galaxies in our samples.

However, we can approximately match the halo masses of the star-forming and quiescent galaxy samples by matching their average number of satellites. As we showed in a previous study (Kawinwanichakij et al., 2014), the number density of satellites around massive quiescent centrals ($\log(M_{\rm cen}/{\rm M}_{\odot}) > 10.8$) at $1 < z < 3$ from ZFOURGE/CANDELS is approximately twice as high as the number density of satellites around star-forming centrals with the same stellar mass (see also Zheng et al., 2005). We further argued in Kawinwanichakij et al. that the increase in satellites corresponds to a comparable increase in halo mass.

We therefore make the assumption that the mean number of satellites around our centrals is proportional to the halo mass. By selecting samples of star-forming and quiescent centrals with the same average number of satellites, we are able to select samples with approximately the same average halo mass and therefore test if conformity can be explained by differences in halo mass. We define ν to be the average number of satellites per central for our sample. Figure 3.10 shows that we can roughly match the number of satellites per central between star-forming (ν_{sf}) and quiescent centrals (ν_q) over our entire redshift range by selecting quiescent centrals with $10.4 < \log(M_{\rm cen}/{\rm M}_{\odot}) < 10.7$, and star-forming centrals with $10.6 < \log(M_{\rm cen}/{\rm M}_{\odot}) < 10.9$. Therefore, we conclude that at fixed halo mass the quiescent centrals have stellar masses *lower* by $\simeq$0.2 dex compared to the star-forming centrals.[3]

---

[3] If the halos that host quiescent centrals are older than the halos that host star-forming centrals, they may also have less substructure, and therefore will have fewer satellites at fixed halo mass. In this case our satellite-matching scheme would over-correct for differences in halo mass (see also the discussion in Hearin et al., 2016)

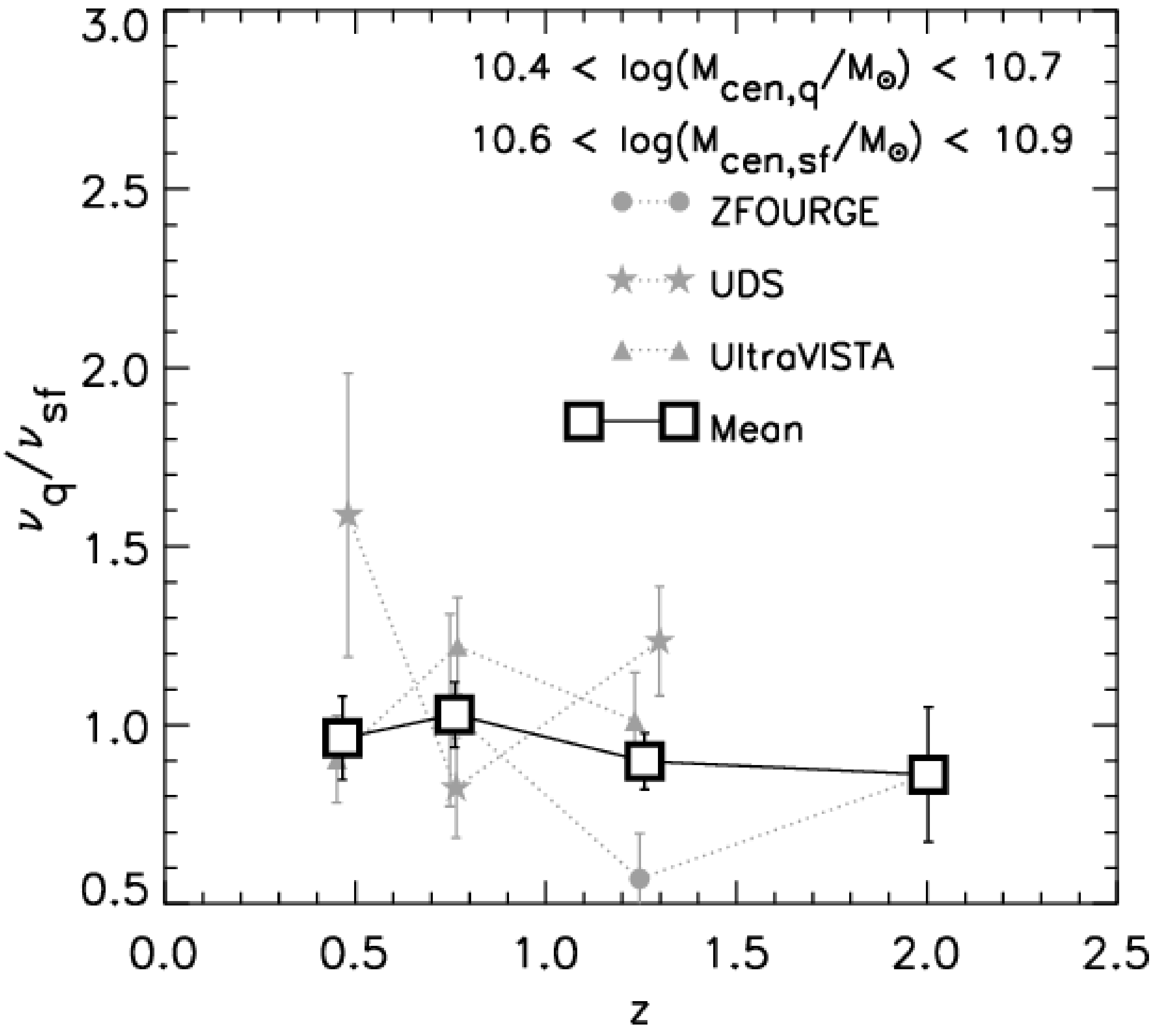

Figure 3.10: Ratio of number of satellites per a quiescent central to those per star-forming central.

Using the mean number of satellites per central galaxy to match approximately the halo masses of the quiescent and star-forming centrals. The figure shows that the number of satellites per quiescent central (ν_q) with $10.4 < \log(M_{\rm cen}/{\rm M}_{\odot}) < 10.7$ is approximately the same as the number of satellites per star-forming central (ν_{sf}) with $10.6 < \log(M_{\rm cen}/{\rm M}_{\odot}) < 10.9$. Assuming that the number of satellite scales with the halo mass of a central galaxy, this ratio implies that halo masses of our quiescent and star-forming here are roughly the same using these stellar mass ranges. Reprinted with permission from “Satellite Quenching and Galactic Conformity at $0.3 < z < 2.5$" by Kawinwanichakij et al., 2016. The Astrophysical Journal, Volume 817, Issue 1, article id. 9 pp. 19, Copyright 2016.

We have also tried estimating halo mass differences using total group stellar mass (i.e., the central mass plus the mass in detected satellites) rather than using the number of satellites (e.g. Yang et al., 2007). This leads to smaller halo mass differences between star-forming and quiescent centrals, and suggests that we are over-correcting for the halo mass by matching the number of satellites. Therefore, if anything our results should be conservative as we may be comparing satellites of star-forming centrals with slightly more massive halos to satellites of quiescent centrals with slightly less massive halos.

If satellite quenching was only a function of halo mass, with no residual correlation with the star-formation activity of the central, then we would expect that the conformity signal would disappear when applying these different mass cuts. Figure 3.11 shows that, at $0.3 < z < 0.6$ and $z > 0.9$, the satellite quenching efficiency around quiescent centrals and star-forming centrals are statistically equivalent when the mean halo mass of the star-forming centrals is about the same as the quiescent centrals. The p-values derived from the bootstrap samples at $0.3 < z < 0.6$, $0.9 < z < 1.6$, and $1.6 < z < 2.5$, are $p = 0.34$, $p = 0.81$, and $p = 0.83$, implying that the satellites of quiescent and star-forming centrals are quenched equally at fixed halo mass. This suggests that, to within our uncertainties, halo-mass alone can account for galactic conformity at these redshifts.

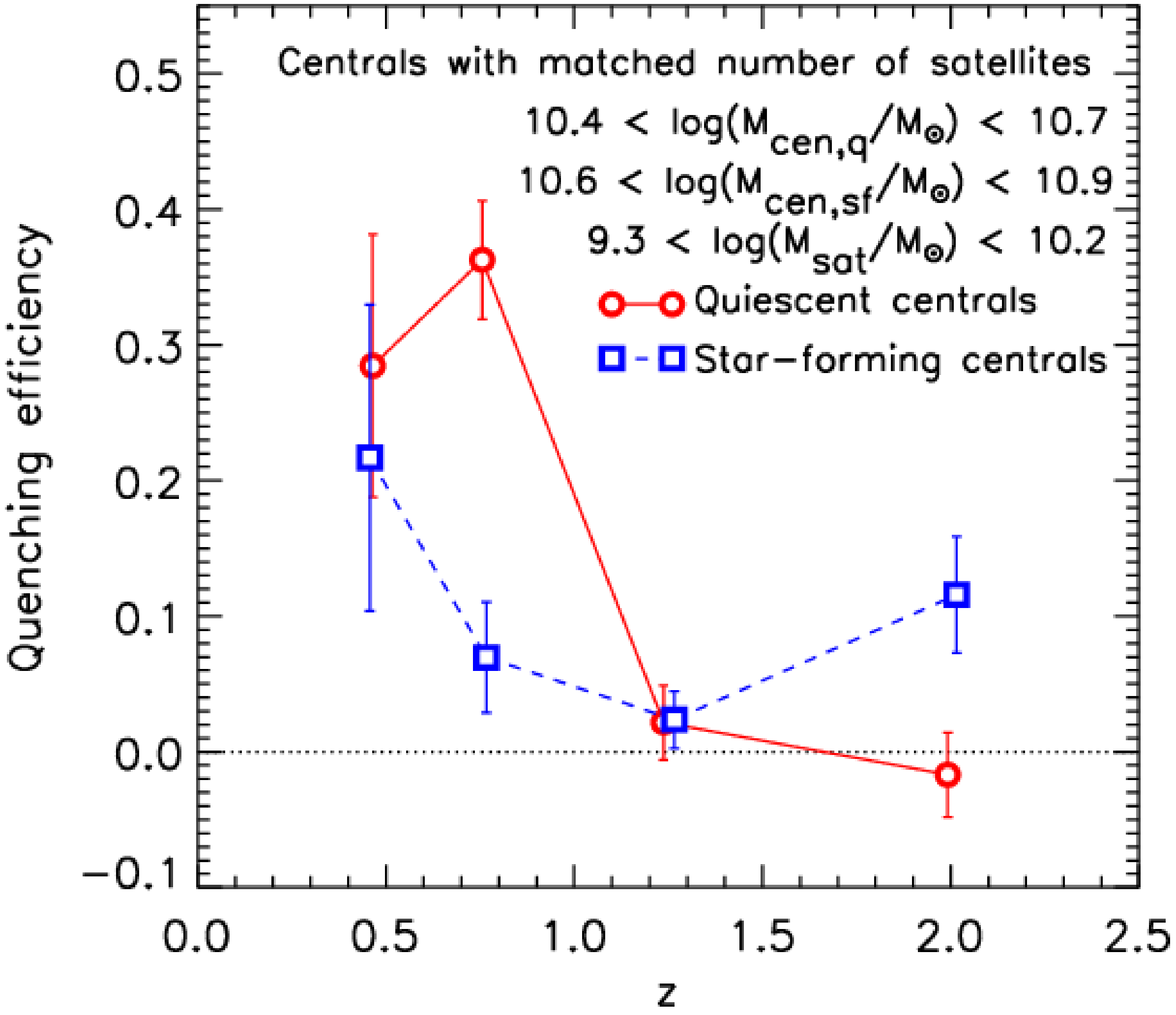

Figure 3.11: The evolution of quenching efficiency of satellites for halo mass-matched centrals.

The average quenching efficiency of satellites after approximately matching the halo masses of the quiescent and star-forming centrals using all three datasets. The mean number of satellites is about equal for quiescent centrals with $10.4 < \log(M_{\rm cen}/{\rm M}_\odot) < 10.7$, and star-forming centrals with $10.6 < \log(M_{\rm cen}/{\rm M}_\odot) < 10.9$, implying they have approximately the same halo mass. Compared with Figure 3.7, the quenching efficiency of satellites of quiescent and star-forming centrals are about the same at all redshift (except at $0.6 < z < 0.9$) after we matched the mean number of satellites of quiescent and star-forming centrals. As discuss in Section 3.6, the galactic conformity observed in our galaxy sample is mainly driven by the halo mass. However, at $0.6 < z < 0.9$, the conformity is due to central galaxies being quiescent rather than just the halo mass of centrals. Reprinted with permission from “Satellite Quenching and Galactic Conformity at $0.3 < z < 2.5$" by Kawinwanichakij et al., 2016. The Astrophysical Journal, Volume 817, Issue 1, article id. 9 pp. 19, Copyright 2016.

However, halo mass appears not to account for all of the conformity signal at $0.6 < z < 0.9$. Figure 3.11 shows that the conformity persists at $0.6 < z < 0.9$ even after we account for differences in the halo masses of the star-forming and quiescent centrals. The significance of conformity at $0.6 < z < 0.9$, based on the bootstrap samples are $p = 0.0004$ ($\simeq 3.4\sigma$). Therefore, the observed galactic conformity at $0.6 < z < 0.9$ even at fixed halo mass implies that satellite quenching at this redshift range is related to the star-formation properties of the centrals in addition to just the halo mass. Furthermore, the conformity signal at this redshift range at fixed halo mass is apparent in each of our datasets (ZFOURGE, UDS, and UltraVISTA), and is not driven by one individual field.

3.6.2 Comparison to Previous Studies

A number of studies analyzed the correlation between properties of satellites and their massive centrals (i.e., specific star-formation rate, colors, gas fraction) and the quiescent fraction of satellites in the local universe by utilizing the data from SDSS (Kauffmann et al., 2010; Wang & White, 2012; Kauffmann et al., 2013; Knobel et al., 2015; Phillips et al., 2014, 2015). These authors have found that the quiescent fraction of satellites around quiescent centrals is higher than those of star-forming centrals.

Phillips et al. (2014) reached the conclusion that massive satellites of isolated star-forming centrals are indistinguishable from a field population, i.e., that satellite quenching does not occur in halos with star-forming centrals. This result, however, appears to be driven by their additional isolation criteria that allow no more than one satellite around their centrals. In a subsequent study, Phillips et al. (2015) demonstrated that star-forming centrals with two satellites have a non-zero satellite quenching efficiency. This is consistent with our result here: the higher quenching efficiency of satellites around star-forming centrals compared to the background galaxies for UDS and UltraVISTA at $0.3 < z < 0.6$, UltraVISTA at $0.6 < z < 0.9$, and all three surveys at higher redshift ranges.

Our results extend trends from the lower-redshift to the higher-redshift Universe. As discussed in Section 3.2, earlier studies (e.g., Weinmann et al., 2006; Knobel et al., 2015), have argued that the phenomenon of galactic conformity exists even after fixing the halo masses of the central galaxies – although this conclusion is somewhat complicated by the results of Phillips et al. (2014, 2015). Wang & White (2012) have demonstrated that conformity at fixed halo mass is present in the Guo et al. (2011) semi-analytic model, and suggest that this is because red centrals live in older halos, where satellite quenching is more efficient. As shown in Section 3.6.1, our result (at least at $z < 0.9$) is consistent with these studies in the sense that quiescent centrals have a higher quiescent fraction compared to star-forming centrals, even after making a rough correction for the difference in halo mass.

The detection of galactic conformity out to $z \sim 2$ was previously reported by Hartley et al. (2015) using an independent analysis of data from the UDS survey. Our analysis, which includes the UDS as well as the ZFOURGE and UltraVISTA surveys, bolsters this conclusion. We also find this conclusion persists to satellites of lower stellar mass ($\log(M/\mathrm{M}_\odot) = 9.3$).

Hartley et al. (2015) also found that the quiescent fraction of satellites around star-forming galaxies is indistinguishable from the field population at all redshifts. When we restrict our analysis to the UDS sample only, we do find excess quenching for the satellites of star-forming galaxies compared to the field in two of our three redshift bins, $0.3 < z < 0.9$ and $0.9 < z < 1.6$, in contrast to Hartley et al., but the significance is weak (Figures 3.4 and 3.5) and likely is a result of different analysis techniques and choice of aperture size. When we combine the UDS sample with our ZFOURGE and UltraVISTA samples, the signal becomes highly significant (Figure 3.7). Hartley et al. also argued that halo mass alone is insufficient to account for all of the galaxy conformity signal by applying different stellar mass cuts to star-forming and quiescent centrals, as we have done here.

To summarize, when we take into account differences in sample selection and analysis, the results from previous studies are consistent with ours in the sense that satellite galaxies are more quenched compared to the background galaxies, and the degree to which satellites have quenched is related to the star-formation activity of their central galaxies. The remaining differences in the quenching of satellites from our analysis and others may be a result of field-to-field (cosmic) variance, small number statistics, or differences associated with the dataset, definition of quiescence, measurement techniques, and isolation criteria. This emphasizes that systematics are still a significant contributor to the absolute measurements and studies of galactic conformity require multiple datasets and analysis techniques to understand the importance of these effects.

3.6.3 Physical Causes of Conformity

In Section 3.6.1 we suggested that the difference in the halo mass of quiescent and star-forming centrals contributes to the observed conformity signal, but there needs to be additional mechanisms (at least at $0.6 < z < 0.9$). In this section, we discuss how halo mass can act as a driver of galactic conformity, and then we discuss additional possible origins of galactic conformity that may operate even at fixed mass.

It is generally argued that at a halo mass $\sim 10^{12}\ \mathrm{M}_{\odot}$, a halo of hot virialized gas is formed near the virial radius (e.g., White & Rees, 1978; Birnboim & Dekel, 2003; Kereš et al., 2005; Dekel & Birnboim, 2006). This hot halo shocks infalling cold gas to the virial temperature. The hot gas cools inefficiently, which may aid in reducing the star formation in the central galaxy, but it is not expected to completely quench star formation because of radiative cooling (Birnboim et al., 2007). Additional heating mechanisms have been proposed to prevent cooling of halo gas, including AGN feedback (Croton et al., 2006) or gravitational heating due to clumpy accretion (Birnboim et al., 2007; Dekel & Birnboim, 2008; Dekel et al., 2009). The hot gaseous halo surrounding quiescent centrals could also create an environment which efficiently quenches satellite galaxies, either by strangulation (Larson et al., 1980) or ram pressure stripping (Gunn & Gott, 1972), thereby causing galactic conformity. As more massive galaxies typically reside in more massive host dark matter halos, the fact that we observe a positive relationship between satellite quenching efficiency and the stellar mass of star-forming centrals (Figure 3.8) may reflect the preference for more massive dark matter halos to harbor hot gas coronas.

However there are several reasons to believe that there is more to the story. Observational (Tumlinson et al., 2011; Churchill et al., 2013) and theoretical (van de Voort et al., 2011; Gabor & Davé, 2015) evidence suggests that the halos of quiescent central galaxies may have a significant cold gas component. In this study we have additionally found that satellites are quenched in the halos of star-forming centrals in excess of mass-matched field populations (Figure 3.7), suggesting that a hot gas halo does not always stifle star formation in the central itself. We also find that conformity persists even when we compare the quenched fractions of satellites of high-mass star-forming centrals to lower-mass quiescent centrals (Figure 3.11), which provides some evidence that quenching is not simply a function of halo mass.

Even at fixed halo mass, there are several ways in which the environment within the halos of quiescent galaxies may be more detrimental to star-formation in satellites. This could be due to a higher fraction of hot gas (even at fixed halo mass; Wang & White, 2012; Gabor & Davé, 2015), which may be related to halo assembly history or to AGN feedback (Croton et al., 2006). It may also be due to tidal stripping or harassment (Farouki & Shapiro, 1981; Moore et al., 1996). These effects could remove gas from the satellite, where it could possibly contribute to the hot halo and/or cool and accumulate on the central.

Even if satellites retain their own disk and (sub-) halo gas, they will eventually exhaust that gas and may not accrete any more gas. At low redshift, it has been argued that environmental processes shut down star formation in satellites over a long timescale of $\sim 2-7$ Gyr in order to explain the distribution of satellite quiescent fractions (e.g., Balogh et al., 2004a; Finn et al., 2008; Weinmann et al., 2009; McGee et al., 2011; De Lucia et al., 2012; Haines et al., 2013; Wetzel et al., 2013). The reduced quenching of satellites at higher redshifts (Figure 3.7) is therefore expected, since satellites will not have had time to quench, however these timescales are still too long to explain the existence of quenched satellites at these higher redshifts. This suggests that satellite quenching must proceed more quickly at higher redshifts, as has been suggested previously (Tinker & Wetzel, 2010; Quadri et al., 2012). Faster gas depletion timescales at higher redshift would also help to alleviate this problem.

In this regard, it is interesting to note that Weinmann et al. (2010) showed that a model in which the diffuse gas is stripped at the same rate that dark matter subhalos lose mass due to tidal stripping can reproduce observations at low redshifts reasonably well. This tidal stripping scenario has the attractive feature that it operates more efficiently at higher redshifts, leading to shorter quenching timescales. It also naturally explains the existence of quenched satellites around star-forming centrals, since tidal stripping takes place independent of the state of the halo gas and the star-formation activity of central galaxies. Further work is required to determine whether tidal stripping can lead to conformity; it could be that the conformity signal reflects earlier assembly time of certain halos, and so the satellites have had more time to be stripped.

Another fast-acting process that has not often been discussed in this context is major merging. The violent dynamical environment of a major merger may affect the sub-halos and satellite galaxies, however future cosmological simulations into the behavior of the gas in centrals and satellites in halos during major mergers would be needed to test this scenario.

Satellite quenching and galactic conformity may also be related to a class of effects due to the assembly history and large-scale environment around dark matter halos, i.e., assembly bias. Because older halos will tend to have accreted their satellites long ago, those satellites will have had more time to lose their gas supply due to stripping and exhaustion. Older halos are also expected to have higher concentration, which may also aid in tidal stripping of satellites. If older halos are *also* more likely to host quiescent central galaxies (Hearin & Watson, 2013; Hearin et al., 2016), then this will naturally lead to conformity. Similar assembly bias effects are also relevant for observations of conformity beyond halo virial radii ("2-halo conformity"). For instance, Kauffmann et al. (2013) discuss the mass- and scale-dependence of conformity in the SDSS. For low mass centrals, ($9.7 < \log(M_{\rm cen}/{\rm M}_{\odot}) < 10.5$), conformity extends out to ~ 4 Mpc around the centrals when they have low star-formation rates or gas content. This could be a result of a correlation in the accretion rates of nearby halos (as discussed by Hearin et al., 2016), but may also be due to large-scale heating of the intergalactic gas ("preheating"; Kauffmann, 2015).[4] Similar large-scale correlations were also suggested by Quadri et al. (2012) as a possible way to explain the existence of a star-formation density relation at $z \sim 2$, and by Quadri et al. (2008) and Tinker & Wetzel (2010) as a way to help explain the strong clustering of red galaxies at similar redshifts.

---

[4] But see Paranjape et al. (2015), who suggest that the apparent large-scale 2-halo conformity may simply be due to the 1-halo conformity within the rare massive halos in the Kauffmann et al. (2013) sample.

Hearin et al. (2016) point out that large-scale 2-halo conformity will naturally lead to 1-halo conformity (which is what we are primarily measuring in this work) after the halos merge. These authors also find that 2-halo conformity due to assembly bias effects should vanish at $z > 1$. If 2-halo conformity were the *only* cause of 1-halo conformity, then 1-halo conformity should decrease with redshift, and also vanish at $z > 1$. Our data show significant 1-halo conformity to at least $z \sim 1.6$, in apparent contradiction with this prediction. It may be that 2-halo conformity extends to higher redshifts than predicted by Hearin et al. (2016), or that 1-halo conformity is not simply caused by the correlated assembly histories of distinct dark matter halos at previous epochs. Additional large and deep datasets would be required to firmly establish or rule out the existence of 1-halo and 2-halo conformity at these and higher redshifts.

Finally we note that, if halo age or recent assembly history are important causes of (either 1-halo or 2-halo) conformity, then this requires that the baryonic physics of star formation and quenching are sensitive to halo assembly history. As mentioned above, this seems obvious in the case of satellite quenching: satellites with early accretion times are more likely to be quenched. However it is less obvious that quenching of central galaxies should be strongly tied to halo accretion rate. If infalling gas is shock-heated and is added to a hot gaseous halo (as is generally expected at $z < 2$; e.g. Dekel & Birnboim, 2006), rather than penetrating to the central regions, then it is not clear that the central star formation should couple strongly to the halo accretion rate. Conversely, even halos with low accretion rates are expected to contain significant hot gas components, which can in principle provide fuel for star formation. Hydrodynamic simulations are necessary to investigate whether low halo accretion rates can be a significant factor in the quenching of central galaxies over the redshift range where conformity is now known to exist; Feldmann & Mayer (2015) have recently demonstrated this at $z > 2$, but their simulations do not extend to lower redshift.

4. EFFECT OF LOCAL ENVIRONMENT AND STELLAR MASS ON GALAXY QUENCHING AND MORPHOLOGY AT $0.5 < z < 2.0$[1]

4.1 Synopsis

We study galactic star-formation activity as a function of environment and stellar mass over 0.5<z<2.0 using the FourStar Galaxy Evolution (ZFOURGE) survey. We estimate the galaxy environment using a Bayesian-motivated measure of the distance to the third nearest neighbor for galaxies to the stellar mass completeness of our survey, $\log(M/M_{\odot}) > 9$ (9.5) at z=1.3 (2.0). This method, when applied to a mock catalog with the photometric-redshift precision ($\sigma_z/(1+z) \lesssim 0.02$) of ZFOURGE, recovers galaxies in low- and high-density environments accurately. We quantify the environmental quenching efficiency, and show that at $z > 0.5$ it depends on galaxy stellar mass, demonstrating that the effects of quenching related to (stellar) mass and environment are not separable. In high-density environments, the mass and environmental quenching efficiencies are comparable for massive galaxies ($\log(M/M_{\odot}) \gtrsim 10.5$) at all redshifts. For lower mass galaxies ($\log(M/M)_{\odot}) \lesssim 10$), the environmental quenching efficiency is very low at $z \gtrsim 1.5$, but increases rapidly with decreasing redshift. Environmental quenching can account for nearly all quiescent lower mass galaxies ($\log(M/M_{\odot}) \sim$ 9–10), which appear primarily at $z \lesssim 1.0$. The morphologies of lower mass quiescent galaxies are inconsistent with those expected of recently quenched star-forming galaxies. Some environmental process must transform the morphologies on similar timescales as the environmental quenching itself. The evolution of the environmental quenching favors models that combine gas starvation (as galaxies become satellites) with gas exhaustion through star-formation and outflows ("overconsumption"), and additional processes such as galaxy interactions, tidal stripping, and disk fading to account for the morphological differences between the quiescent and star-forming galaxy populations.

---

[1] Reprinted with permission from "Effect of local environment and stellar mass on galaxy quenching and morphology at $0.5 < z < 2.0$" by Kawinwanichakij et al. 2017. The Astrophysical Journal, Volume 847, Issue 2, article id. 134 pp. 21, Copyright 2017.

4.2 Introduction

The population of galaxies can be broadly classified into two distinct types: quiescent galaxies with relatively red colors, spheroid-dominated morphologies, and little to no on-going star-formation activity (with star-formation rates [SFRs] much less than their past averages); and star-forming galaxies with relatively blue colors, disk-dominated morphologies, and SFRs comparable to (or above) their past averages (e.g., Strateva et al., 2001; Kauffmann et al., 2003; Baldry et al., 2004, 2006; Bell, 2008; van Dokkum et al., 2011; Schawinski et al., 2014). In the local universe, it is well-known that these types of galaxies are related to the density of galaxies (the galaxy environment). Quiescent, spheroidal galaxies are preferentially found in dense environments rich with galaxies (e.g., Oemler, 1974; Davis & Geller, 1976; Dressler, 1980; Balogh et al., 2004b; Hogg et al., 2004; Kauffmann et al., 2004; Blanton & Moustakas, 2009; Peng et al., 2010; Woo et al., 2013).

How this trend with environment manifests and evolves with redshift is one of the outstanding questions in galaxy evolution. Multiple studies have found a correlation between environmental density and the quenching of star-formation at $z \sim 1$ (e.g., Cooper et al., 2007, 2010; Cucciati et al., 2010; Kovač et al., 2010, 2014; Muzzin et al., 2012; Balogh et al., 2016; Allen et al., 2016; Morishita et al., 2017; Guo et al., 2017). In addition, there is some observational evidence that the environment (or by proxy, the density of galaxies) correlates with other galaxy properties out to $z \sim 2$ (e.g., Cucciati et al., 2006; Tran et al., 2010; Chuter et al., 2011; Papovich et al., 2012; Quadri et al., 2012; Fossati et al., 2017; Nantais et al., 2017), and possibly to at least $z \sim 3$ (Darvish et al., 2016). Developing a further understanding of the physical processes involved in the quenching of star formation clearly requires better observational measurements, and also requires disentangling the observed correlations between SFR, galaxy structure, and environmental density, out to these higher redshifts.

In the low redshift Universe ($z \lesssim 0.1$), it has been shown that the respective relationships between stellar mass and environment on quenching are largely separable (e.g., Baldry et al., 2006; van den Bosch et al., 2008; Peng et al., 2010; Kovač et al., 2014), implying there are two distinct quenching processes at work: one that correlates with stellar mass (independent of environment) and one that correlates with galaxy environment (independent of stellar mass). Peng et al. (2010) show the separability of the effects of stellar mass and environment on the quiescent fraction of galaxies in SDSS (at $z < 0.1$) and zCOSMOS ($0.3 < z < 0.6$). Similarly, Kovač et al. (2014) used mass-matched samples of central and satellite galaxies to show that the quiescent fraction of centrals is primarily related to stellar mass and is almost independent of overdensity (environment), indicating that they are mainly quenched by a process related to stellar mass, at least to the stellar mass limit of their data ($\log M/M_{\odot} > 9.8$ at $z = 0.4$). On the other hand, an additional environmental quenching process is required to explain the observed quiescent fraction of satellite galaxies, which increases with galaxy overdensity.

These separable effects of stellar mass and environment on galaxy properties have been observed out to $z \sim 3$ (e.g., Quadri et al., 2012; Muzzin et al., 2012; Lee et al., 2015; Darvish et al., 2016), but have been limited to more massive galaxies, $\log M/M_{\odot} \gtrsim 10$, due to the depth of the surveys. To this mass limit, these studies also found no evidence that the properties of star-forming galaxies strongly depend on environment: there is no significant change in the median SFR and specific SFR (for star-forming galaxies) with environment at fixed stellar mass, suggesting that the independence of SFR-mass sequence on environment has been in place at $z \sim 3$ (but see Jian et al., 2018). The obvious qualifier is that it has only been possible to study the relatively higher mass galaxies, and it is unknown if these results extend to lower mass galaxies.

Physical explanations for cessation of star-formation in galaxies can also be broadly classified into mechanisms that related to mass (halo mass, supermassive black hole mass, or stellar mass) or to environment. A galaxy's halo mass provides a natural quenching mechanism related to mass (e.g., Rees & Ostriker, 1977; White & Rees, 1978; Gabor et al., 2011; Gabor & Davé, 2015). It is generally argued that the intra-halo gas in halos above $\sim 10^{12}\mathrm{M}_{\odot}$ exists at temperatures high enough (Birnboim & Dekel, 2003; Kereš et al., 2005) to shock-heat infalling gas from the intergalactic medium at the virial radius, preventing the fueling of star-formation in the galaxies (Dekel & Birnboim, 2006; Cattaneo et al., 2006; Birnboim et al., 2007). Another quenching mechanism that may be related to galaxy mass is the feedback from an active galactic nucleus (AGN) (Granato et al., 2004; Springel et al., 2005; Croton et al., 2006; Bower et al., 2006; Cattaneo et al., 2006; Somerville et al., 2008; Knobel et al., 2015; Terrazas et al., 2016). In contrast, star-formation suppression of galaxies in low-mass halos can be driven by energetic feedback from supernova explosions and stellar winds (e.g., Larson, 1974; Dekel & Silk, 1986).

There are also physical processes that operate preferentially in dense environments. One of them is the rapid stripping of cold gas via ram pressure as the galaxy passes through a hot gaseous medium, causing abrupt quenching (Gunn & Gott, 1972; Abadi et al., 1999). In contrast, if only the hot gas in the outer parts of galaxies is stripped, the galaxy may continue forming new stars until all fuel is exhausted. Consequently, this "strangulation" (also called "starvation") results in the gradual decline of star-formation rate (Larson et al., 1980; Balogh et al., 1997). Note, however, that both of these gas-stripping processes will primarily modify the color and SFR of a galaxy, without transforming the galaxy morphology (e.g., Weinmann et al., 2006; van den Bosch et al., 2008)[2]. Satellite galaxies orbiting within dark matter halos may also be subject to tidal stripping as they experience tidal forces due to the central galaxy, due to other satellite galaxies, and due to the potential of the halo itself (e.g., Read et al., 2006). Higher density environments can also lead to enhanced merger rates, which may also affect quenching (Peng et al., 2010). Recently, McGee et al. (2014) pointed out that the gas outflows that are ubiquitous among star-forming galaxies may also affect the quenching of satellites. According to this scenario, which they refer to as "overconsumption," vigorous star formation in recently-accreted satellites may drive outflows that will exhaust the gas supply in the absence of cosmological accretion. These authors also demonstrate that the timescale for satellite quenching due to overconsumption can be much shorter than the time for the gas to be stripped through dynamical processes.

Another clue regarding environmental quenching mechanisms is the observed correlation between the properties of satellites (i.e., specific SFR, colors, and gas fraction) and their more mas-

---

[2] While this is true in morphology as traced by stellar mass, for morphology as traced by light in any passband, even near-IR, the higher luminosity of young stars will make the star-formation disks more prominent and will lead to significant changes in visual appearance of morphology as the star-formation fades (e.g., Fang et al., 2013). We return to this point about "disk fading" in Section 4.6

sive central galaxies. The correlation is such that the satellites of quiescent centrals are more likely to be quenched than the satellites of star-forming centrals, even at fixed stellar mass. This phenomenon was originally presented by Weinmann et al. (2006) and is referred to as “galactic conformity". There is growing observational evidence of galactic conformity in both the local Universe (Kauffmann et al., 2010, 2013; Knobel et al., 2015; Phillips et al., 2014, 2015) and out to $z \sim 2$, even though the signal is weaker at high redshift (Hartley et al., 2015; Kawinwanichakij et al., 2016; Hatfield & Jarvis, 2017). Broadly speaking, the different environmental processes discussed here are expected to act with different strengths and over different timescales as a function of galaxy stellar and halo mass. Therefore, measuring how (stellar) mass and environmental quenching evolve with stellar mass and redshift provides constraints on the quenching processes, particularly at higher redshift ($z \gtrsim 1$), when galaxy specific SFRs are higher.

In this chapter we primarily focus on how the quenching of galaxies correlates with galaxy stellar mass and environment, and how these evolve with redshift. However, we do not attempt to separate our sample into central or satellite galaxies. Rather, we will denote the environmental density, based on the local overdensity of galaxies compared to the mean, as $(1 + \delta)$. We will make use of the deep NIR imaging and high photometric redshift accuracy from the FourStar Galaxy Evolution (ZFOURGE) survey, which allows us to compute accurate estimates of the environment for galaxies to fainter magnitudes and with higher completeness than is possible with either ground-based spectroscopy ($K_s < 24$ AB mag, Nanayakkara et al. 2016, for emission-line galaxies) or space-based spectroscopy ($JH_{140} < 24$ AB mag, Fossati et al. 2017). In contrast, the ZFOURGE data provide precise photometric redshifts for galaxies to $K_s \simeq 25.5 - 26$ AB mag, substantially fainter than what is possible with spectroscopy. As a result, the ZFOURGE data allow us to study environmental impact of quenching for galaxies with low stellar mass out to high redshift ($\log(M/M_{\odot}) \simeq 9.5$ at $z = 2$).

Because we quantify quenching as a function of both stellar mass and local environmental density, throughout this chapter we refer to “mass quenching" and “environmental quenching" processes. This does not imply that stellar mass and environmental density directly cause quenching.

For instance, black hole mass or central stellar mass density may have a more direct relationship to quenching than stellar mass (Terrazas et al., 2016; Woo et al., 2015), but because these quantities correlate with stellar mass, they will result in a measurable "mass quenching" effect. Similarly, the estimator of environmental density that we use may only be correlated with, rather than directly measure, the aspects of a galaxy's location or environment that actually cause quenching.

The outline of this chapter is as follows. In Section 4.3, we describe the ZFOURGE catalog and our galaxy sample selection criteria. In Section 4.4, we describe the method for estimating the environmental densities using photometric redshifts, and we validate our method using simulated catalogs from a semi-analytic model (described further in Appendix B). In Section 4.5, we discuss how the fraction of quiescent galaxies varies with stellar mass and environment, and we compute from these the quenching efficiency for both variables out to $z = 2$. In Section 4.6, we discuss the relative importance of environmental processes in the buildup of red galaxies in dense environments. We investigate whether the cause of environmental quenching is indicated in the morphological distribution of lower-mass quiescent galaxies. In addition, we consider how our results constrain timescales of environmental quenching and therefore the physical processes responsible. In Chapter 7, we present our summary. Throughout, we adopt the following cosmological parameters where appropriate, $H_0 = 70\,\mathrm{km\,s^{-1}\,Mpc^{-1}}$, $\Omega_m = 0.3$, and $\Omega_\Lambda = 0.7$. All magnitudes are expressed in the AB system.

4.3 Data and Sample Selection

We select galaxies at $0.5 < z < 2.0$ from the ZFOURGE survey (Straatman et al., 2016). The survey is composed of three $11' \times 11'$ fields with coverage in regions of the CDFS (Giacconi et al., 2002), COSMOS (Scoville et al., 2007), and UDS (Lawrence et al., 2007) that overlap with the Cosmic Assembly Near-IR Deep Extragalactic Legacy Survey (CANDELS Grogin et al., 2011; Koekemoer et al., 2011), which also provide *Hubble* Space Telescope, high-angular resolution imaging for 0.6–1.6 μm (see, e.g., van der Wel et al., 2012). The ZFOURGE medium–band near-IR imaging reaches depths of $\sim$ 26 AB mag in J_1, J_2, J_3 and $\sim$ 25 AB mag in H_s, H_l and includes the vast amount of deep, multiwavelength imaging available in these legacy fields. The ZFOURGE catalogs are complete for galaxies to $K_s \simeq 25.5 - 26.0$ AB mag (see Straatman et al., 2016).

4.3.1 Photometric Redshifts

The ZFOURGE catalogs include photometric redshifts and rest-frame colors calculated using EAZY (Brammer et al., 2008) from the $0.3 - 8$ μm photometry for each galaxy. Of import here, ZFOURGE uses templates and photometric zeropoints that are iteratively adjusted during the fitting process to improve accuracy of the photometric redshifts.

The precision of photometric redshifts has the ability to potentially introduce spurious signals or wash out structure (Cooper et al., 2005; Quadri et al., 2012). However, our estimates of the quality of the ZFOURGE photometric redshifts show them to be very accurate, and as we demonstrate below, sufficient to recover galaxy environmental densities. By comparing photometric redshifts of galaxy pairs and to spectroscopic subsamples, Straatman et al. (2016) show that the typical photometric redshift uncertainties are $\sigma_z/(1+z)$= 0.01–0.02 to the K_s-band magnitude limit for galaxies between $z = 0.5$ and $z = 2.0$, with negligible dependence on galaxy color, but there is dependence on magnitude and redshift (Straatman et al., 2016, see their section 5.4). Quantitatively, at $K_s < 25.0$ AB mag photometric redshift uncertainties of quiescent galaxies at $z = 2$ are better than that of star-forming galaxies at the same redshift only about 5%. Other studies with ZFOURGE have shown that these redshifts are sufficient to identify protoclusters out to $z \sim 2$ (e.g., Spitler et al., 2012; Yuan et al., 2014; Forrest et al., 2017).

In addition to the photometric redshifts, we also make use of stellar masses for galaxies provided in the ZFOURGE catalogs. The stellar masses were derived by fitting stellar population models to the photometry using FAST (Kriek et al., 2009), assuming exponentially declining star formation histories, solar metallicity, and a Chabrier (2003) initial mass function.

4.3.2 Stellar Mass Completeness

Because we are concerned with the galaxy quiescent fractions, it is important that we use a dataset that is complete in stellar mass for both star-forming and quiescent galaxies. Quiescent galaxies have higher mass-to-light ratios and therefore will have a higher-mass completeness limit

Table 4.1: Stellar mass completeness limits for ZFOURGE galaxies at $0.5 < z < 2.5$. Reprinted with permission from “Effect of local environment and stellar mass on galaxy quenching and morphology at $0.5 < z < 2.0$" by Kawinwanichakij et al., 2017. The Astrophysical Journal, Volume 847, Issue 2, article id. 134 pp. 21, Copyright 2017.

Redshift	$\log(M/\mathrm{M}_{\odot})$	Redshift	$\log(M/\mathrm{M}_{\odot})$
0.5	8.09	1.6	9.24
0.6	8.25	1.7	9.31
0.7	8.40	1.8	9.38
0.8	8.52	1.9	9.44
0.9	8.64	2.0	9.51
1.0	8.74	2.1	9.57
1.1	8.84	2.2	9.62
1.2	8.93	2.3	9.68
1.3	9.01	2.4	9.73
1.4	9.09	2.5	9.79
1.5	9.17		

than star-forming galaxies at fixed magnitude. Here, we adopt 90$\%$ mass-completeness limits for galaxies with a quiescent stellar population using the technique described by Quadri et al. (2012). In a given narrow redshift bin, we select all quiescent galaxies and scale their fluxes (and therefore their stellar masses) downward until they have the same magnitude as the measured magnitude limit, K_s = 25.5 AB mag, for all three ZFOURGE fields. Then we define the mass-completeness limit as the stellar mass at which we recover 90$\%$ of the dimmed galaxies at each redshift. We provide the adopted completeness limits for ZFOURGE at $0.5 < z < 2.5$ in Table 4.1.

4.3.3 Selection of Quiescent and Star-forming Galaxies

Our goal is to measure the fraction of quiescent galaxies as a function of stellar mass, environment, and redshift. From the parent sample of all galaxies in the ZFOURGE catalog, we first select all well-detected galaxies (`USE` flag = 1) and group them into three bins of redshift, $0.5 < z < 1.0$, $1.0 < z < 1.5$, and $1.5 < z < 2.0$. We then further subdivide the samples into bins of galaxy stellar mass, $8.8 < \log(M/\mathrm{M}_{\odot}) < 9.8$, $9.8 < \log(M/\mathrm{M}_{\odot}) < 10.5$, and $10.5 < \log(M/\mathrm{M}_{\odot}) < 11.5$. In each of these bins, we classify galaxies as star-forming or quiescent using their rest-frame $U-V$

and $V-J$ colors, denoted by $(U-V)_0$ and $(V-J)_0$, respectively. This UVJ color–color space is useful to separate galaxies with colors of quiescent and star-forming stellar populations (including the affects of dust attenuation; Williams et al., 2009; Patel et al., 2012). Due to the small systematic variations in the rest-frame colors of galaxies at fixed stellar mass and redshift in different surveys, we follow our previous method (Kawinwanichakij et al., 2016, see their section 2.2) to self-calibrate the region in the UVJ color–color space to delineate star-forming from quiescent galaxies. We then select quiescent galaxies whose rest-frame colors satisfy,

$$\begin{array}{rcl} (U-V)_0 & > & 1.2 \times (V-J)_0 + 0.2 \\ (U-V)_0 & > & 1.3 \\ (V-J)_0 & < & 1.6. \end{array} \tag{4.1}$$

A summary of the number of galaxies from each galaxy mass, redshift, and density subsample is given in Table 4.2.

Figure 4.1 shows the UVJ color–color diagram for galaxies in our ZFOURGE samples at $0.5 < z < 2.0$ split into low stellar mass ($8.8 < \log(M/\mathrm{M}_{\odot}) < 10.2$ and high stellar mass ($10.2 < \log(M/\mathrm{M}_{\odot}) < 11.5$) subsamples, and as a function of environment as defined by local overdensity (see Section 4.4 below). While all panels show a similar range of galaxy colors, differences in the distributions are clearly evident with mass (and also environment). The distribution of lower-mass galaxies is weighted more toward bluer star-forming objects (by number), while the distribution of higher mass star-forming galaxies show higher dust attenuation, consistent with other studies (e.g., Wuyts et al., 2011). All panels also show the existence of a "red sequence" of quiescent galaxies, but this is much more pronounced in the higher density regions (denser environments), which we discuss more below.

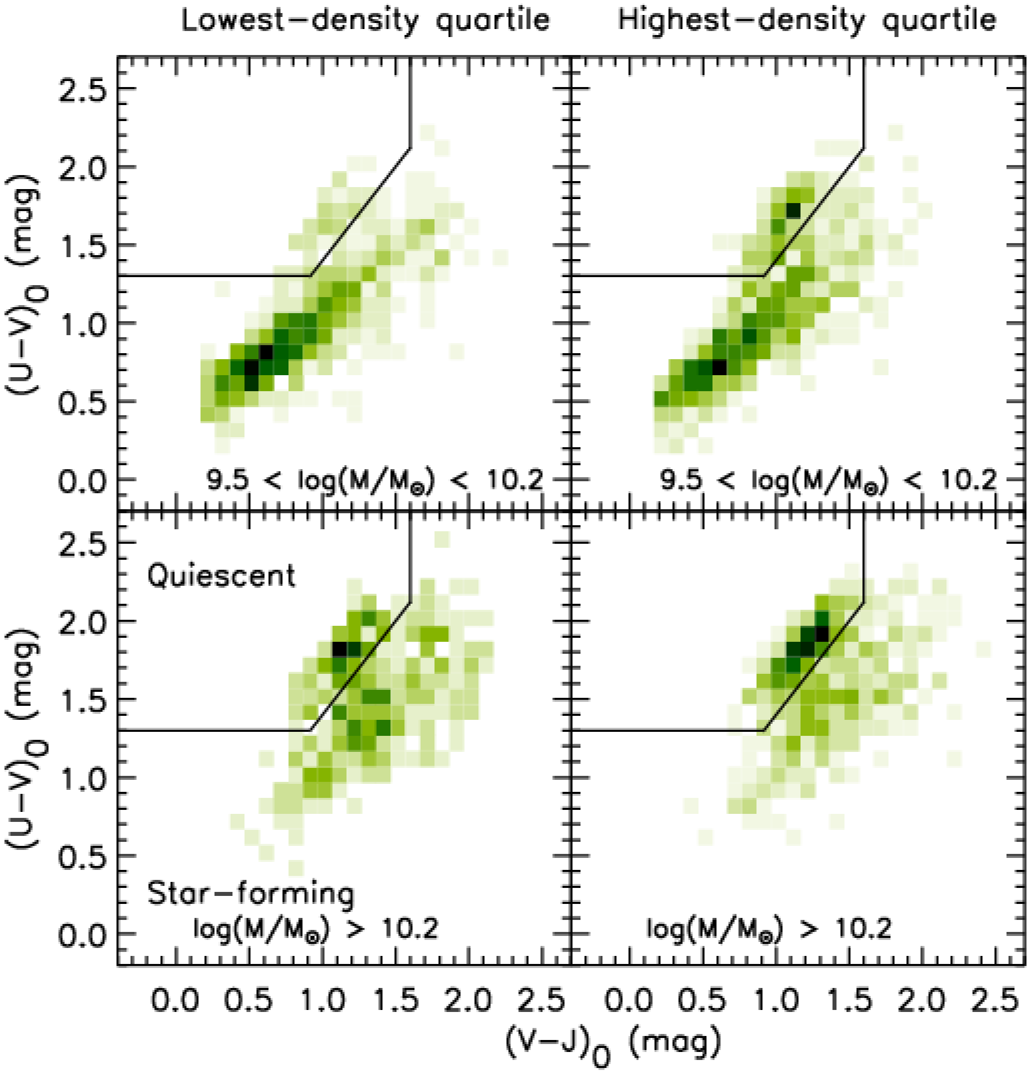

Figure 4.1: Rest-frame $U - V$ versus rest-frame $V - J$ color for galaxies in different stellar mass bins and environments.

Rest-frame $U - V$ versus rest-frame $V - J$ color for galaxies at $0.5 < z < 2.0$ in the lowest-density quartile (left panels) and the highest-density quartile (right panels), with lower stellar masses $9.5 < \log(M/\mathrm{M}_\odot) < 10.2$ (top panels) and higher stellar masses $\log(M/\mathrm{M}_\odot) > 10.2$ (bottom panels). In each panel, the darkness of the shading is proportional to the number of galaxies in that region. Galaxies in the upper left region of each plot (separated by the solid line) have colors of quiescent stellar populations; galaxies outside this region have colors of star-forming populations combined with dust attenuation (see Williams et al., 2009). Reprinted with permission from “Effect of local environment and stellar mass on galaxy quenching and morphology at $0.5 < z < 2.0$" by Kawinwanichakij et al., 2017. The Astrophysical Journal, Volume 847, Issue 2, article id. 134 pp. 21, Copyright 2017.

Table 4.2: Number of quiescent and star-forming galaxies in different stellar mass and density quartile in ZFOURGE at $0.5 < z < 2.0$. Reprinted with permission from "Effect of local environment and stellar mass on galaxy quenching and morphology at $0.5 < z < 2.0$" by Kawinwanichakij et al., 2017. The Astrophysical Journal, Volume 847, Issue 2, article id. 134 pp. 21, Copyright 2017.

Stellar Mass Range	Redshift Range	Lowest-Density Quartile			Highest-Density Quartile		
		$N_{\rm Quiescent}$	$N_{\rm Star-forming}$	$N_{\rm Total}$	$N_{\rm Quiescent}$	$N_{\rm Star-forming}$	$N_{\rm Total}$
$8.8 < \log(M/{\rm M}_\odot) < 9.8$	$0.5 < z < 1.0$	24	662	686	113	427	540
	$1.0 < z < 1.5$	10	491	501	22	406	428
	$1.5 < z < 2.0$	8	259	267	5	212	217
$9.8 < \log(M/{\rm M}_\odot) < 10.5$	$0.5 < z < 1.0$	39	129	168	96	138	234
	$1.0 < z < 1.5$	32	146	178	42	144	186
	$1.5 < z < 2.0$	24	196	220	40	165	205
$10.5 < \log(M/{\rm M}_\odot) < 11.5$	$0.5 < z < 1.0$	30	33	63	87	50	137
	$1.0 < z < 1.5$	15	37	52	51	51	102
	$1.5 < z < 2.0$	19	64	83	54	74	128

4.3.4 Structural Morphological Parameters

In our analysis, we study the morphological differences between quiescent and star-forming galaxies in different environments and as a function of stellar mass. The majority of galaxies in our sample fall within the CANDELS coverage from HST/WFC3, with effective semi-major axis, $a_{\rm eff}$, and Sérsic index, n, measured by van der Wel et al. (2012) using the HST/WFC3 F160W (H_{160})–band imaging. We refer the reader to van der Wel et al. for the measurement of random and systematic uncertainties of the estimated morphological parameters using simulated galaxy images. We cross–matched the sources in our catalog with those of van der Wel et al. The fractions of our galaxy sample with available morphological parameters from van der Wel et al. are 80%, 90%, and 82% for CDFS, COSMOS, UDS, respectively. We note that there are 10%-20% of our galaxy sample that have no morphological information from HST/WFC3 because those galaxies are in the regions around the edges of ZFOURGE fields where there is no HST/WFC3 coverage. We further define the circularized effective radius as $r_{\rm eff} = a_{\rm eff}\sqrt{q}$, where $a_{\rm eff}$ is the effective semi-major axis and $q = b/a$ is the ratio of the semi-minor to semi-major axis. In addition to the morphological parameters from van der Wel et al., we calculate the stellar mass surface density inner 1kpc which we describe the procedure in Appendix B.

4.4 Measurement of Galaxy Density as Estimate of Environment

In this work we estimate the local galaxy (projected) overdensity using the distance to the Nth nearest neighbor, d_N. This distance has often been used as a measure of the overdensity, with N typically varying from 3 to 10 (e.g., Dressler, 1980; Baldry et al., 2006; Muldrew et al., 2012). We then are able to define the environment of a galaxy in terms of the dimensionless overdensity, $1+\delta$, defined as

$$(1+\delta)_N = 1 + \frac{\Sigma_N - \langle\Sigma\rangle}{\langle\Sigma\rangle}, \tag{4.2}$$

where $\Sigma_N = N/(\pi d_N^2)$, is the local surface density of a galaxy based on the distance to the Nth nearest neighbor and $\langle\Sigma\rangle$ is the average surface number density of galaxies over the whole field. We then take $(1+\delta)$ to denote the fractional density of galaxies with respect to the mean (as a function of redshift).

We improve our measurement of overdensity using an estimator for the Nth nearest neighbor introduced by Ivezić et al. (2005). The distances to all N nearest neighbors provide the information about local density (overdensity) of galaxies. Motivated by Bayesian probability framework, we incorporate the projected distance to Nth nearest neighbors into density estimator, and we additionally take into account information from the projected distances to the first $N - 1$ nearest neighbors. Ivezić et al. demonstrate that this increases the accuracy of the overdensity compared to the traditional Nth nearest neighbor metric because it uses the distances to the 1st, 2nd, ... Nth neighbors and is less subject to projection effects (see Appendix B of Ivezic et al. 2005). One of the advantages of this estimator is that it provides a good estimate of the "local density," which corresponds to scales internal to galaxy group halos, provided N is relatively small (see Muldrew et al., 2012). As many of the environmental trends we find appear to correlate with group–sized halos, we adopt N=3 for the analysis here. Specifically, we use the estimator as given by Cowan & Ivezić (2008):

$$\Sigma'_N = C \frac{1}{\Sigma_{i=1}^{N} d_i^2}. \tag{4.3}$$

Here, we take the third nearest neighbor (3NN) distance, where we empirically determine the constant, C, by requiring that $\langle \Sigma'_N \rangle$ be equal to that for a uniform density of galaxies with the same total number and area as in our ZFOURGE dataset.

For this study, we calculate the 3NN distance, Σ'_3, for each galaxy in the ZFOURGE catalog. At each redshift, we consider all galaxies more massive than the mass completeness limits given in Table 4.1. For each galaxy, we measure the density only considering galaxies with a photometric redshift separation that is 2.5 times the estimated redshift uncertainty i.e., $2.5 \times 0.02(1 + z_{\rm phot})$, where we adopt the factor of 0.02 as a conservative redshift uncertainty. We then compute the overdensity of galaxy, $\log(1 + \delta')_3$, using the Bayesian-motivated estimate of the local surface density of galaxies derived from the 3rd nearest neighbor by substituting Σ'_3 into Σ_N of Equation 4.2. In Appendix B, we verify using a mock galaxy catalog that this method recovers well the true projected overdensity for data with the photometric accuracy of ZFOURGE in that it faithfully recovers galaxies in the highest and lowest density quartiles with a minimal amount of contamination. Our tests also showed that N=3 provides a good compromise between the accuracy of measured galaxy overdensity and the ability to probe group-sized environments, which is appropriate for our study here. However, we experimented using Σ'_N with N=2,5,7 and find that our main conclusions are unaffected by the choice of N.

In addition, we have tested for "edge effects" by excluding galaxies from our analysis that are $\sim$ 20 arcseconds (larger than the 3NN distances for the galaxies in the lowest-density quartile) from the survey edges. This does not affect the main results for the differences in the quiescent fractions as a function of stellar mass and environment that are presented in Section 4.5. To be even more conservative, we then tested for edge effects by excluding galaxies that are two times that distance from the survey edges (~ 40 arcseconds), and find no change in our results, although the uncertainties in quiescent fractions increase as the sample size decreases. We therefore apply no correction for the edge effects in this study.

Figure 4.2 shows the projected density, Σ'_3, and overdensity, $\log(1+\delta')$, computed from the 3NN (Σ'_3) of each ZFOURGE galaxy as a function of redshift. We calculated the median, bottom and top quartiles of the distribution (i.e., the bottom and top 25th percentiles) to determine the relative overdensity of each galaxy. We determined these quartiles using a spline linear regression implemented with the COnstrained B-Splines (cobs) package in R (Feigelson & Babu, 2012). We find that, over the redshift range 0.5 – 2.0, the projected density (Σ'_3) at the lower and upper quartiles of overdensity are about 13 and 43 galaxies per arcmin^2, respectively. In the following analysis, we define a galaxy to be in a low (high)-density environment if it has a overdensity $\log(1+\delta')$ less (greater) than the lower (upper) 25th percentile. We will interchangeably use the terms low/high-density environments (hereafter δ_{25}/δ_{75}) with the lowest/the highest-density quartiles.

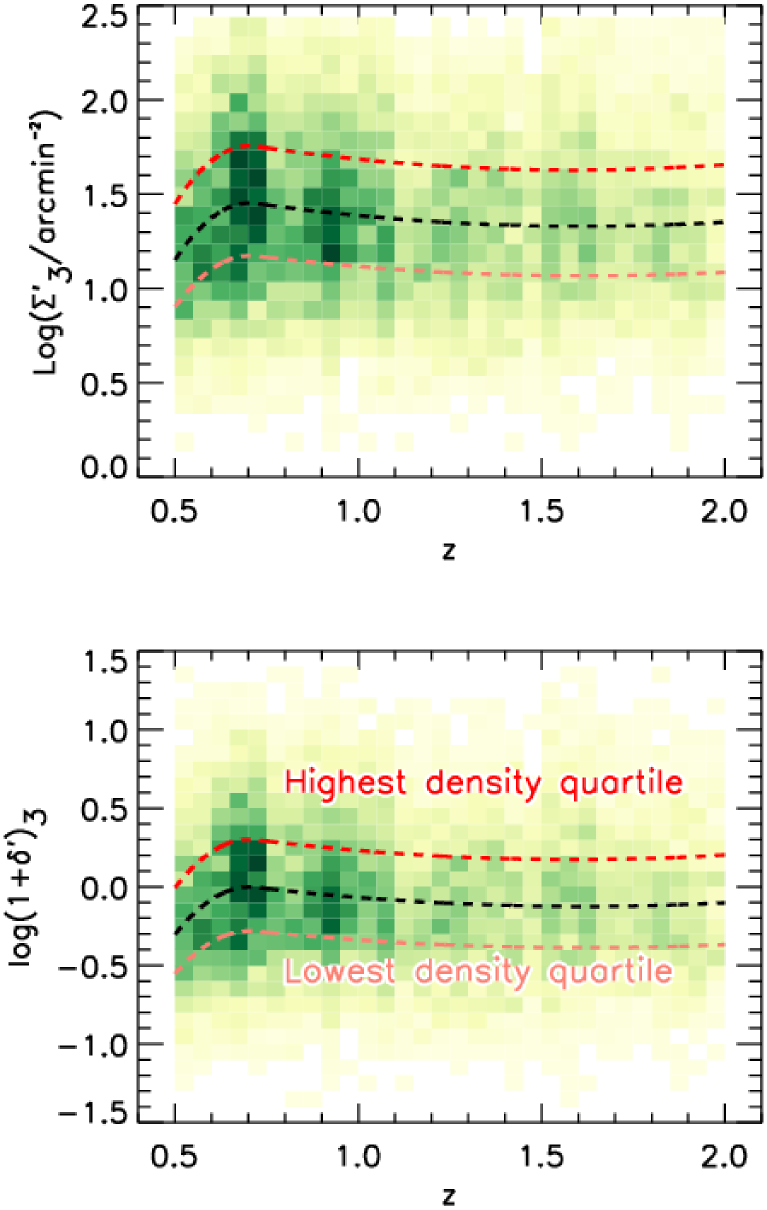

Figure 4.2: The redshift evolution of surface number density and overdensity of ZFOURGE galaxies.

Top: the projected density computed from the Bayesian 3rd nearest neighbor (Σ'_3) of each galaxy in three combined ZFOURGE fields as a function of redshift. The black, light-red, and red dashed lines show the median, bottom, and top quartile (25th percentiles) of the distribution, derived from a spline quartile regression applied to the data (see text). ***Bottom*:** the corresponding overdensity of ZFOURGE galaxies as a function of redshift computed using the same method. We again show the median, bottom, and top quartiles. We define galaxies in the upper and lower quartiles of overdensity to be in "high" and "low" density environments, respectively. In each panel, the darkness of the shading is proportional to the number of galaxies in that region. Reprinted with permission from "Effect of local environment and stellar mass on galaxy quenching and morphology at $0.5 < z < 2.0$" by Kawinwanichakij et al., 2017. The Astrophysical Journal, Volume 847, Issue 2, article id. 134 pp. 21, Copyright 2017.

4.5 Results

In this section we calculate the quiescent fraction as a function of stellar mass and environment, using the overdensities $(1+\delta')$ derived above. We use these fractions to estimate the environmental quenching efficiency and (stellar) mass quenching efficiency as defined below.

4.5.1 Evolution of Quiescent Fraction with Environment and Redshift

We show the quiescent fraction of galaxies as a function of the overdensity in Figure 4.3. We apply a mass limit of $\log(M/\mathrm{M}_{\odot}) > 9.5$ in all three redshift bins, which corresponds to our completeness limit at $z = 2.0$. We also compare our quiescent fraction with those from Quadri et al. (2012) who used the galaxy sample from the UKIDSS Ultra-Deep Survey, so we apply a mass limit of $\log(M/\mathrm{M}_{\odot}) > 10.2$, corresponds to completeness limit at $z = 2.0$ used by Quadri et al. (2012). The error bars indicate the 1σ uncertainty based on Poisson statistics for the number of quiescent galaxies in a bin. At all redshift ranges, we see evidence for a higher quiescent fraction of galaxies at higher densities. This effect is very strong at $z < 1$ (left panel of Figure 4.3), but decreases at higher redshift, $z > 1$ (middle and right hand panels of Figure 4.3). This is in agreement with previous studies of star-formation-density relation (e.g. Quadri et al., 2012), where with the ZFOURGE data we have extended the result to lower masses and higher redshifts (for the recent study of galaxy sample with comparable stellar mass and redshift range to our sample see Guo et al., 2017).

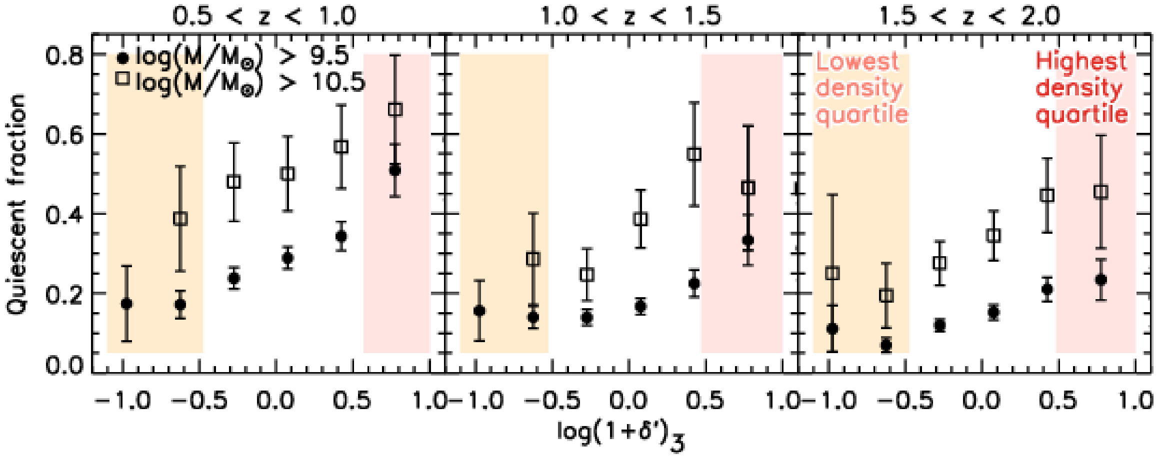

Figure 4.3: Quiescent fraction versus overdensity in three different redshift ranges for two mass-selected samples.

The quiescent fractions of galaxies are determined in bins of 0.4 dex of $\log(1+\delta')$. The error bars indicate 1σ uncertainties based on Poisson statistics. The shaded regions in each panel indicate the lower and upper 25th percentiles of $\log(1+\delta')$, where we define low- and high-density environments. Reprinted with permission from "Effect of local environment and stellar mass on galaxy quenching and morphology at $0.5 < z < 2.0$" by Kawinwanichakij et al., 2017. The Astrophysical Journal, Volume 847, Issue 2, article id. 134 pp. 21, Copyright 2017.

In this section we have shown that the quiescent fraction of galaxies is higher in denser environments over all redshifts probed in this study. In principle it is possible that this result is caused by differences in the stellar mass distribution and/or the redshift distribution of quiescent and star-forming galaxies. To check for this, we create samples of quiescent and star-forming galaxies such that their stellar mass and redshift distributions are matched following the method described by Kawinwanichakij et al. (2016) (see their section 3.2). The left panel of Figure 4.4 shows the differences in overdensity between the quiescent and star-forming galaxies before this matching at $1.5 < z < 2.0$ (a p-value of the differences as measured by a K-S test of $\ll 10^{-3}$) and the right panel shows that the difference persists even after matching the stellar mass and redshift distributions (a p-value of $\ll 10^{-3}$). We obtain even more significant results in our other (lower) redshift bins. We conclude that, at all redshifts studied here, quiescent galaxies are more common in overdense regions compared to star-forming galaxies even taking into account differences in redshift and stellar mass.

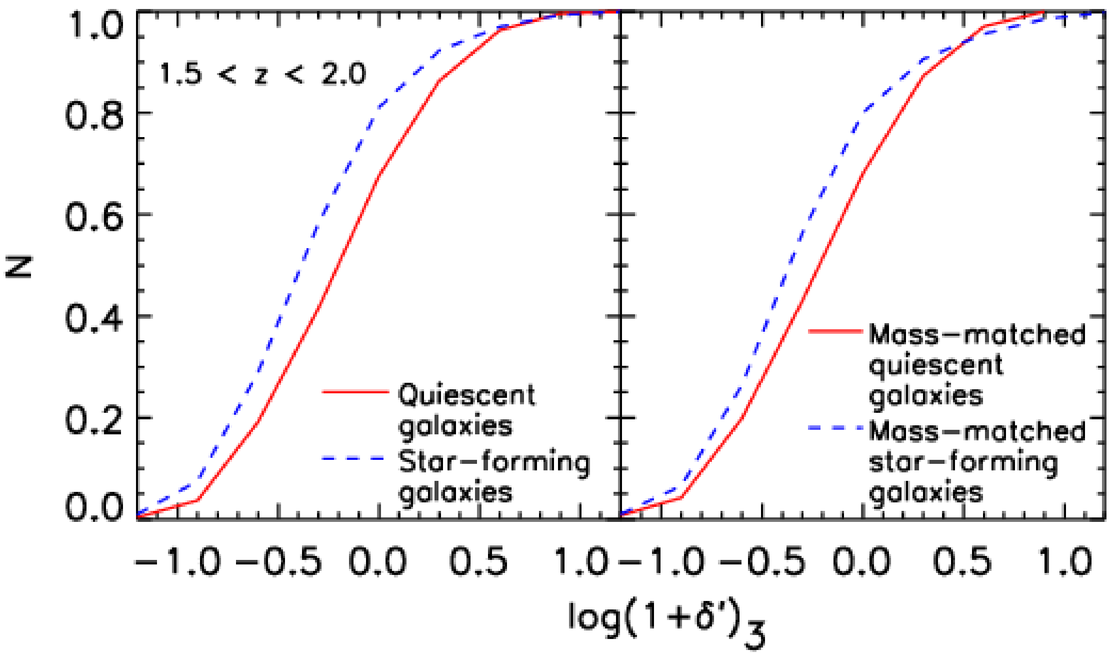

Figure 4.4: Cumulative distributions of overdensity for galaxies with different star-formation activity.

Left: cumulative distribution of overdensities $\log(1+\delta')$ for quiescent galaxies (red solid line) and star-forming galaxies (blue dash lines) with $\log(M/\mathrm{M}_{\odot}) > 9.5$ at $1.5 < z < 2.0$. A K-S test indicates that we can reject the null hypothesis that these two distributions are drawn from the same parent distribution with a p-value of $\ll 10^{-3}$ ***Right:*** same as the left panel but for mass-matched and redshift-matched samples of quiescent and star-forming galaxies. A K-S test indicates the differences in the distributions persists with a p-value of $\ll 10^{-3}$. Reprinted with permission from "Effect of local environment and stellar mass on galaxy quenching and morphology at $0.5 < z < 2.0$" by Kawinwanichakij et al., 2017. The Astrophysical Journal, Volume 847, Issue 2, article id. 134 pp. 21, Copyright 2017.

4.5.2 Evolution of Quiescent Fraction with Stellar Mass and Redshift

Figure 4.5 shows the quiescent fraction as a function of stellar mass in bins of redshift, separating galaxies in the highest (δ_{75}) and lowest (δ_{25}) density quartiles. Qualitatively, at $0.5 < z < 1.5$ galaxies in the highest-density quartile show higher quiescent fractions than galaxies with the same mass in the lowest-density quartile in all stellar mass bins. This is in agreement with Allen et al.

(2016), who show that the fraction of quiescent galaxies with $\log(M/\mathrm{M}_\odot) \gtrsim 9.5$ at $z \sim 0.95$ increases with decreasing distance to the cluster core. At higher redshift, $1.5 < z < 2.0$, this trend persists for more massive galaxies ($\log(M/\mathrm{M}_\odot) \gtrsim 10$).

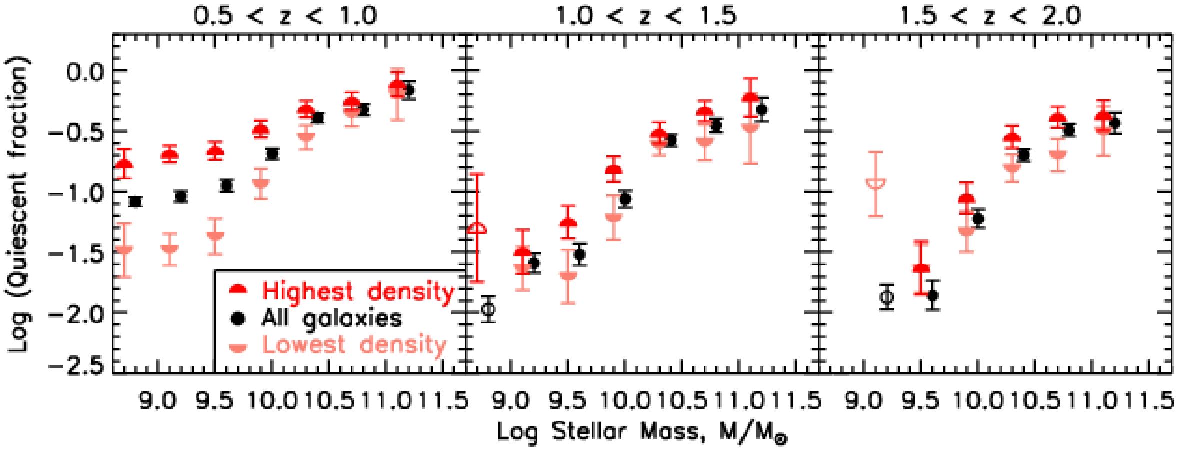

Figure 4.5: Quiescent fraction of galaxies in different environmental densities as a function of galaxy stellar mass.

Quiescent fraction versus stellar mass in three different redshift ranges for all galaxies (black circles), galaxies in the highest-density quartile (red upper-half circles), and galaxies in the lowest-density quartile (light-red lower-half circles). The quiescent fractions are determined in a bin of 0.4 dex in $\log(M/\mathrm{M}_\odot)$. Open symbols correspond to data below each subsample's respective mass-completeness limit. The error bars indicate 1σ uncertainties based on Poisson statistics. The quiescent fraction of all galaxies (black circles) are slightly offset along the abscissa for clarity. Galaxies in denser environments have a higher quiescent fraction in all stellar mass bins out to $z \sim 2.0$, except possibly for the lowest-mass galaxies ($\log(M/\mathrm{M}_\odot) \simeq 9 - 10$) at $1.5 < z < 2.0$. Reprinted with permission from “Effect of local environment and stellar mass on galaxy quenching and morphology at $0.5 < z < 2.0$" by Kawinwanichakij et al., 2017. The Astrophysical Journal, Volume 847, Issue 2, article id. 134 pp. 21, Copyright 2017.

Figure 4.6 shows the quiescent fraction as a function of redshift in bins of stellar mass, separating out the lowest and highest density quartiles. Qualitatively, galaxies have higher quiescent fractions in high-density environments compared to galaxies in low-density environments out to $z \sim 2$ and for galaxies with stellar mass, $\log(M/\mathrm{M}_{\odot}) \gtrsim 9.8$. For lower stellar mass galaxies ($8.8 < \log(M/\mathrm{M}_{\odot}) < 9.8$), the quiescent fractions are higher in the higher density environment at least to $z \lesssim 1.5$, but at higher redshift, $z \gtrsim 1.5$, the quiescent fraction shows less dependence on environment.

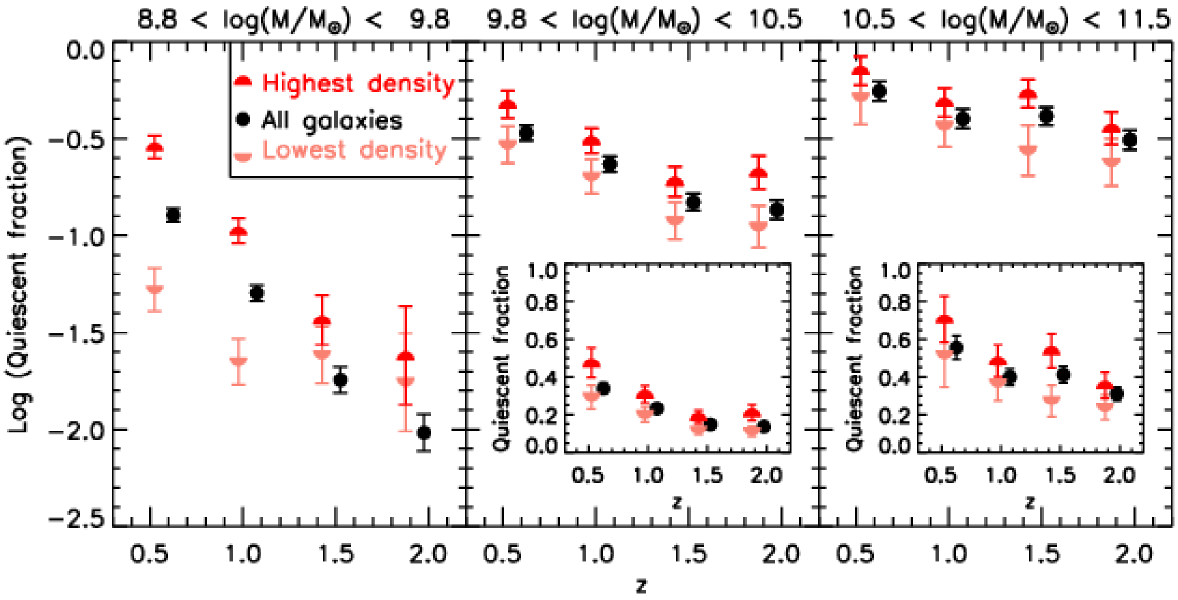

Figure 4.6: The redshift evolution of quiescent fraction of galaxies in different environmental densities.

Quiescent fraction versus redshift in three different stellar mass ranges for all galaxies (black circles), galaxies in the highest-density quartile (red upper-half circles), and galaxies in the lowest-density quartile (light-red lower-half circles). The quiescent fraction of galaxies is determined in bins of $\Delta z = 0.45$, chosen as a balance between redshift sampling and having sufficient statistics in each bin. The error bars indicate 1σ uncertainties based on Poisson statistics. The quiescent fraction of all galaxies (black circles) are slightly offset along the abscissa for clarity. We find a higher quiescent fraction in denser environments for all stellar mass bins out to $z \sim 2.0$, except for lowest-mass galaxies at $z > 1.5$. Quiescent fractions are shown on log scale to present relative quiescent fractions in each stellar mass range. However, the inset plots in the higher redshift panels show a linear scaling for clarity. Reprinted with permission from “Effect of local environment and stellar mass on galaxy quenching and morphology at $0.5 < z < 2.0$" by Kawinwanichakij et al., 2017. The Astrophysical Journal, Volume 847, Issue 2, article id. 134 pp. 21, Copyright 2017.

The range of quiescent fraction as a function of overdensity and stellar mass is large, ranging from nearly 100% to less than 1%. To illustrate this, we show the quiescent fraction in in log scale instead of linear scale in both Figure 4.5 and 4.6. This better presents separation of quiescent fractions of galaxies in different environments, and also the relative quiescent fraction in each stellar mass bins.

Because more massive galaxies tend to exist in higher density environments, it is logical to ask to what extent this drives the trend between mass, redshift, and environment. This is a reasonable question, as the number density of quiescent galaxies, even at high redshift, increases both with stellar mass and environment (e.g. Papovich et al., 2018).

To answer this, we perform a similar procedure as Quadri et al. (2012). We computed the mean overdensity of quiescent and star-forming galaxies in narrow 0.25 dex bins in stellar mass (where we expect such narrow bins to have negligible change in overdensity), which show in Figure 4.7. This figure shows evidence that quiescent galaxies have higher overdensity than mass-matched star-forming galaxies (down to the stellar mass limit of each redshift), and this trend exists to $z \sim 2$. These trends extend correlations found by Quadri et al. (2012) to lower stellar masses. In particular, the density contrast between star-forming and quiescent galaxies is largest for lower mass galaxies, $\log(M/M_{\odot}) \simeq 9 - 10$. As argued by Quadri et al. (2012), this suggests that the environment plays a dominant role in galaxy quenching, and here we show this extends to the lowest stellar masses. Our analysis supports this assertion, which we discuss more below.

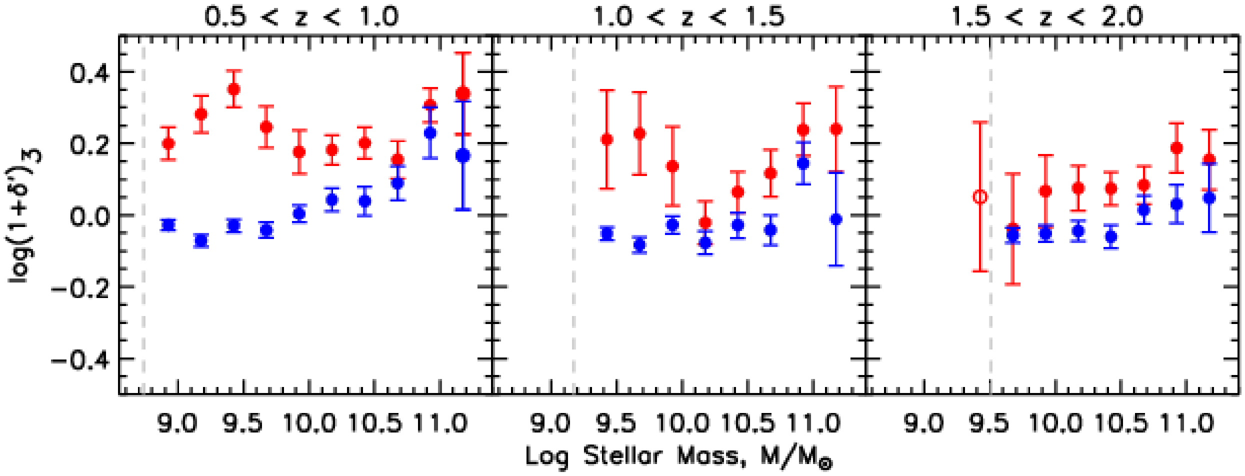

Figure 4.7: Average overdensity versus stellar mass for quiescent and star-forming galaxies.

Average overdensity versus stellar mass for quiescent galaxies (red circles) and star-forming galaxies (blue circles) in 0.25 dex mass bins. The mass-completeness at each redshift bin is shown as the vertical dashed line. The error bars are the standard deviation of the mean. Even at fixed mass, the quiescent galaxies tend to have higher overdensities than the star-forming galaxies. Reprinted with permission from "Effect of local environment and stellar mass on galaxy quenching and morphology at $0.5 < z < 2.0$" by Kawinwanichakij et al., 2017. The Astrophysical Journal, Volume 847, Issue 2, article id. 134 pp. 21, Copyright 2017.

4.5.3 Environmental and Stellar Mass Quenching Efficiencies

To quantify environment and stellar mass in quenching the star-formation activity in galaxies, we follow the approach of Peng et al. (2010) (which is similar to methods of van den Bosch et al., 2008; Quadri et al., 2012; Kovač et al., 2014; Lin et al., 2014). We define the environmental quenching efficiency, $\varepsilon_{\rm env}$, as the fraction of galaxies at a given stellar mass, M, that are quenched in excess of those in the lowest-density environment (presumably these are galaxies that would be forming stars in the lowest-density environments, but have had their star-formation truncated due to some physical process related to the environment). The environmental quenching efficiency is then

$$\varepsilon_{\rm env}(\delta, \delta_0, M) = \frac{f_q(\delta, M) - f_q(\delta_0, M)}{1 - f_q(\delta_0, M)}, \tag{4.4}$$

where f_q is the quiescent fraction for galaxies with stellar mass M and overdensity, δ. δ_0 is the overdensity of the low-density reference environment, where we choose $\delta_0 = \delta_{25}$, i.e., the overdensity demarcating the lowest 25th percentile of the overdensity distribution (see Figure 4.2). We note, however, that we are parameterizing non-environmental quenching with stellar mass because it correlates with other quantities associated with (stellar) mass quenching such as central stellar mass and black hole mass (e.g., Woo et al., 2013, 2015; Zolotov et al., 2015; Terrazas et al., 2016; Tacchella et al., 2016b,a; Woo et al., 2017)

For galaxies with $\delta \leq \delta_{25}$ our definition of $\varepsilon_{\rm env}$ explicitly assumes that the environment quenching is negligible (i.e.,$\varepsilon_{\rm env}(\delta < \delta_0) \approx 0$) for all stellar masses. This is a reasonable assumption as there is no apparent evolution in the shape of the quiescent galaxy stellar mass function in low-density environments over the redshift and stellar mass range considered here (Papovich et al., 2018), as would be expected if galaxy quenching correlates only with stellar mass. For the remainder of this chapter we will also denote the (stellar mass dependent) quiescent fraction of galaxies in the lowest and highest-density quartiles as $f_q(\delta_{25}, M)$ and $f_q(\delta_{75}, M)$, respectively.

Similarly, we define the (stellar) mass quenching efficiency $\varepsilon_{\rm mass}$ as the fraction of galaxies at a fixed overdensity, $\log(1 + \delta)$, that are quenched compared to the star-forming fraction at low masses. Specifically we define the mass quenching efficiency to be,

$$\varepsilon_{\rm mass}(M, M_0, \delta) = \frac{f_q(\delta, M) - f_q(\delta, M_0)}{1 - f_q(\delta, M_0)}, \tag{4.5}$$

where in practice we take the reference mass M_0 to be the stellar mass at the completeness limit for a given redshift, and we compute mass quenching efficiency for galaxies with $\delta < \delta_{75}$.

4.5.4 Dependence of Quenching Efficiencies on Stellar Mass and Redshift

Figure 4.8 compares the strength of the environmental quenching and (stellar) mass quenching efficiencies as a function of stellar mass for galaxies in the highest density environments ($\delta \geq \delta_{75}$). At all redshifts, the (stellar) mass quenching efficiency increases with stellar mass. At $1 < z < 1.5$ and $1.5 < z < 2$, the magnitude of environmental quenching efficiency is on par with the (stellar) mass quenching efficiency: in the highest density environments roughly half of all galaxies are quenched by the environment.

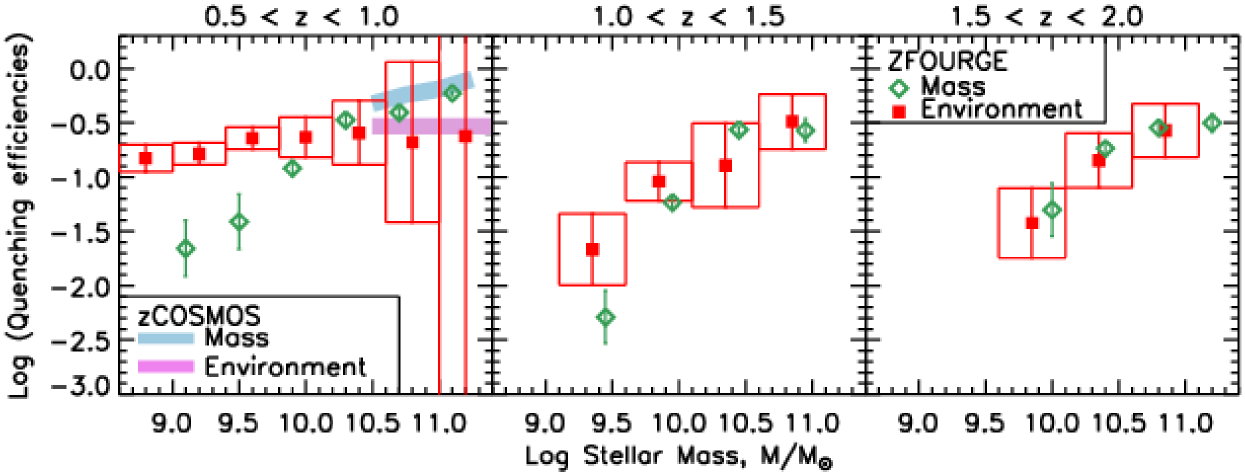

Figure 4.8: The relative strength of environmental and mass quenching efficiency.

The environmental quenching efficiency (red squares) and (stellar) mass quenching efficiency (green diamond) versus stellar mass in three different redshift bins. The environmental quenching efficiencies shown here correspond to the highest overdensity quartiles, $\varepsilon_{\rm env}(\delta = \delta_{75}, \delta_0, M)$. The box widths show the stellar mass binning, and the box heights (and error bars) indicate 1σ Poisson uncertainties. The purple and light blue rectangles show the environmental and (stellar) mass quenching efficiencies, respectively, measured in zCOSMOS at $0.3 < z < 0.6$ (Peng et al., 2010). Some error bars are smaller than the size of the data points. The data points are slightly offset for clarity. Reprinted with permission from “Effect of local environment and stellar mass on galaxy quenching and morphology at $0.5 < z < 2.0$" by Kawinwanichakij et al., 2017. The Astrophysical Journal, Volume 847, Issue 2, article id. 134 pp. 21, Copyright 2017.

At lower redshifts, $0.5 < z < 1$, the evolution of environmental quenching efficiency is strongest for lower mass galaxies. For example, in the mass range, $8.8 < \log(M/M_\odot) < 10$, $\varepsilon_{\rm env}$ increases from <10% at $z > 1$ to ∼30% at $z < 1$. Moreover, at these redshifts the environmental quenching efficiency dominates over (stellar) mass quenching efficiency for these lower mass galaxies (in the highest density environments). Therefore, in the highest density environments the majority of quiescent lower-mass galaxies have been quenched by environmental processes rather than by other processes (see also Hogg et al., 2003; van den Bosch et al., 2008; Quadri et al., 2012). Comparing the magnitudes of the environmental and (stellar) mass quenching efficiencies gives an estimate of the effect, which is of order $\varepsilon_{\rm env}/\varepsilon_{\rm mass} > 5$ for galaxies with $\log(M/M_\odot) = 8.8 - 9.8$: i.e., the environment accounts for the quenching of 5 out of 6 galaxies in this mass range.

Figure 4.8 also shows that at $0.5 < z < 1.0$, the environmental quenching efficiency appears to be nearly independent of stellar mass. At $z > 1$, the environmental quenching efficiency shows a clearer dependence on stellar mass: more massive galaxies experience stronger environmental quenching. This persists at least to $z \simeq 2$ for galaxies with $\log(M/M_{\odot}) > 9.8$.

We explore the evolution with redshift of both the environmental quenching efficiency and the mass quenching efficiency for galaxies in three stellar mass bins: $9.5 < \log(M/\mathrm{M}_{\odot}) < 9.8$, $9.8 < \log(M/\mathrm{M}_{\odot}) < 10.2$, and $\log(M/\mathrm{M}_{\odot}) > 10.2$ in Figure 4.9. At lower redshifts, $0.5 < z < 1$, the environmental quenching efficiency of galaxies at all masses is ≈0.3. This is generally consistent with that measured with the same (relatively higher) stellar mass at $0.3 < z < 0.6$ from zCOSMOS (Peng et al., 2010). However, this "constant" quenching efficiency is a coincidence of epoch. At higher redshifts the environmental quenching efficiency of low-mass galaxies decreases and is very low ($\lesssim 5\%$) at $z > 1.5$, while for more massive galaxies it remains roughly constant (or possibly slightly declining) out to $z \sim 2$. The evolution of the environmental quenching efficiency depends both on redshift and stellar mass, and its effects are not separable from stellar mass at higher redshift.

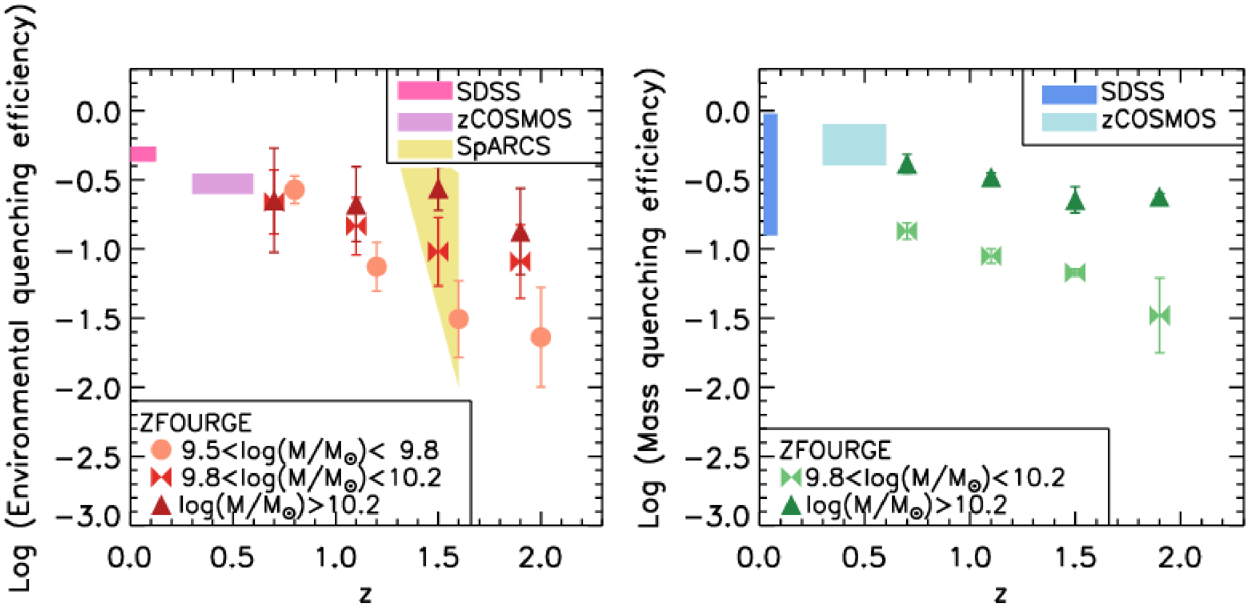

Figure 4.9: The redshift evolution of environment and mass quenching efficiency.

The redshift evolution of the environmental quenching efficiency, $\varepsilon_{\rm env}$ of galaxies in the highest overdensities ($\delta > \delta_{75}$; Equation 4.4; Left panel) and (stellar) mass quenching efficiency ($\varepsilon_{\rm mass}$; Equation 4.5; Right Panel). The different symbols denote different bins of stellar mass, as labeled. The error bars indicate 1σ uncertainties based on Poisson statistics. In the left panel, the pink and purple rectangles show the environmental quenching efficiency of galaxies with $9.0 < \log(M/{\rm M}_{\odot}) < 11.0$ at $0.02 < z < 0.085$ from SDSS and of galaxies with $10.2 < \log(M/{\rm M}_{\odot}) < 11.0$ at $0.3 < z < 0.6$ from zCOSMOS, respectively (Peng et al., 2010). The yellow-shaded region shows measurements for galaxy clusters at $0.87 < z < 1.63$ with $\log(M/{\rm M}_{\odot}) > 10.3$ from the Spitzer Adaptation of the Red-Sequence Cluster Survey (SpARCS) (Nantais et al., 2017). In the right panel, the filled rectangles show the (stellar) mass quenching efficiency of galaxies with $9.0 < \log(M/{\rm M}_{\odot}) < 11.0$ at $0.02 < z < 0.085$ from SDSS and of galaxies with $10.2 < \log(M/{\rm M}_{\odot}) < 11.0$ at $0.3 < z < 0.6$ from zCOSMOS, as labeled (Peng et al., 2010). Reprinted with permission from “Effect of local environment and stellar mass on galaxy quenching and morphology at $0.5 < z < 2.0$" by Kawinwanichakij et al., 2017. The Astrophysical Journal, Volume 847, Issue 2, article id. 134 pp. 21, Copyright 2017.

Comparing to the literature, the environmental quenching efficiency we derive at $1 < z < 1.5$ is modestly lower than that derived for a sample of spectroscopically confirmed galaxy clusters at $0.87 < z < 1.63$ with $\log(M/\mathrm{M}_{\odot}) > 10.3$ from the Spitzer Adaptation of the Red-Sequence Cluster Survey (SpARCS) (Nantais et al., 2017). However, this may be expected as the SpARCS sample includes very rich clusters at these redshifts, which include galaxies in even higher overdensities than the galaxies in our highest density environments in ZFOURGE. Our result of increasing quiescent fractions in high-density environments implies that the strength of environment quenching efficiency increases with overdensity, it is very reasonable that this efficiency is even higher in the rich environments of galaxy clusters.

Figure 4.9 also shows that the strength of (stellar) mass quenching efficiency increases with increasing stellar mass and decreasing redshift. This is consistent with the overall decrease in star-formation activity in galaxies at later cosmic times (e.g., Madau & Dickinson, 2014).

4.6 Discussion

4.6.1 On the Environmental Impact on Quenching

Our main result is that there is strong evidence for both (stellar) mass quenching and environmental quenching for galaxies to high redshift. For massive galaxies, $\log(M/M_{\odot}) > 10.2$, environmental quenching is evident, and nearly unchanging (or slowly declining), over the redshift range of our sample, $0.5 < z < 2$. For lower mass galaxies the environmental quenching efficiency evolves strongly with redshift, at least to $\log(M/M_{\odot}) = 9.5$, where our data are complete. For such lower-mass galaxies, the environmental quenching declines by roughly an order of magnitude from $z = 0.5$ to 2. At our lower redshift range, $0.5 < z < 1.0$, the environmental quenching efficiency dominates over the (stellar) mass quenching efficiency by a factor of >5:1 for galaxies with $\log(M/M_{\odot}) = 8.8 - 9.8$ (Figure 4.8). Therefore the majority of low-mass quiescent galaxies are quenched by their environment (Hogg et al., 2003; Quadri et al., 2012). Our result here is consistent with Geha et al. (2012) who found that number of quiescent low-mass galaxies with $7 < \log(M/M_{\odot}) < 9$ in the field is very low ($< 0.06\%$), demonstrating that star-formation of low-mass galaxies ($\log(M/M_{\odot}) < 9$) are suppressed by being nearby more massive galaxies (although see Geha et al., 2017). In addition, our results are in excellent agreement with recent study by Guo et al. (2017), who used CANDELS data to measure distance from low-mass galaxies to the nearest massive neighbor galaxies. They found that environmental quenching is dominant quenching mechanism for galaxies with $\log(M/M_{\odot}) < 9.5$ out to $z \sim 1$. At higher redshift, Guo et al. (2017) observed minimal environmental quenching for low-mass galaxies, which is consistent with our finding here, but our observation with ZFOURGE survey provides us sufficient statistics and accurate environment measurement (due to the precise photometric redshifts) to strengthen this result.

We note that at $0.5 < z < 1.0$, even in low-density environments, the fraction of massive quiescent galaxies with stellar mass $\log(M/\mathrm{M}_{\odot}) \gtrsim 10.8$ are comparable to those in high-density environment. The observation of quiescent galaxies in voids (low-density environment) has been reported by Croton et al. (2005). Croton & Farrar (2008) further compared luminosity function of void galaxies in the 2dF Galaxy Redshift Survey to those from a galaxy formation model built on the Millennium simulation. These authors demonstrated that a population of quiescent galaxies in low-density environments will arise naturally due to a combination of a shift in the halo mass function in low-density environments and an environment independent star-formation suppression mechanism efficient above a critical halo mass of $M_{\mathrm{vir}} \sim 10^{12.5}\mathrm{M}_{\odot}$ (radio-mode AGN).

Some hint of the quenching mechanism comes from the timescales and the evolution in the quenching efficiency. The lack of significant environmental quenching of low-mass galaxies at $z > 1$ suggests that the quenching timescale is at least 3–5 Gyr (corresponding to the lookback time from $z = 1$ to an infall epoch of $z =$ 3 to 6). This is consistent with quenching times from other studies of environmental processes (e.g., Peng et al., 2010; Tinker & Wetzel, 2010; Quadri et al., 2012; Slater & Bell, 2014; Peng et al., 2015; Wetzel et al., 2015; Darvish et al., 2016; Fossati et al., 2017; Guo et al., 2017). Several recent studies (e.g., Fillingham et al., 2015; Peng et al., 2015; Davies et al., 2016) argue that environmental quenching for galaxies with $\log(M/M_{\odot}) = 8.0-10.0$ are primarily driven by starvation because quenching timescales and cold gas depletion timescales are comparable. For more massive galaxies, $\log(M/M_{\odot}) \gtrsim 10$, the quenching timescale could be shorter, given that we see higher environmental quenching efficiency for these galaxies even in our highest redshift bin, $1.5 < z < 2.5$. This suggests a mass-dependent quenching mechanism, such as “overconsumption” (McGee et al., 2014), which arises as more massive (star-forming) galaxies have shorter gas-depletion times (which we discuss more below). Our results support these findings, but with the additional requirement (also discussed below) that the quenching process also transform the morphologies of the quenching galaxies.

The environmental processes driving the quenching must occur in environments with overdensities comparable to that of our high-density quartile. The ZFOURGE fields contain some massive groups (Fossati et al., 2017), but no massive, virialized clusters given the cosmological volume contained by the ZFOURGE/CANDELS fields. Furthermore, our overdensity estimator based on the third nearest neighbor distance measurements are primarily sensitive to group-sized scales (Muldrew et al., 2012). Therefore the environmental quenching efficiency we measure pertains to physical mechanisms within such environments, and not necessarily to more massive clusters, which may have even stronger environmental quenching efficiency. In addition, even though we do not separate our galaxy sample into central and satellite galaxies in this study, we note that if environmental effects are specific to satellite galaxies, the observed trend here would be even stronger (see Fossati et al., 2017).

4.6.2 On the Lack of Environmental Impact on Morphology

One way to constrain the cause or causes of the environmental quenching is to test if they also affect the morphological structures of the quenched galaxies. Previous studies have demonstrated a relation between galaxy morphology and star-formation activity, quenched fractions, and implied gas fractions (e.g., Franx et al., 2008; Wuyts et al., 2011; Bell et al., 2012; Papovich et al., 2015), and quenching is driven by the processes that change morphology and grow black holes (e.g., Dekel & Burkert, 2014; Zolotov et al., 2015; Woo et al., 2015; Terrazas et al., 2016) (non-environmental effects which we refer to as “(stellar) mass quenching" in this study).

In contrast, quenching from environmental processes manifests in different ways. One null hypothesis is that environmental quenching has no effect on galaxy morphology. If this is true, then it would suggest that quiescent galaxies in high density environments (which are affected by quenching processes that correlate with stellar mass and environment; Figure 4.8) would have different morphologies than quiescent galaxies in low density environments (which are affected only by mass quenching); instead, their morphologies would be more similar to the star-forming population in dense environments. We test this hypothesis here by comparing the morphological distributions of quiescent and star-forming galaxies in our different environments.

We begin by showing the number of galaxies as functions of stellar mass and projected local density (environment) at $0.5 < z < 1.0$, $1.0 < z < 1.5$, and $1.5 < z < 2.0$ as a function of both $\log(1+\delta')_3$ and $\log(M/\mathrm{M}_\odot)$ in Figure 4.10 (top panels). We then show the quiescent fraction of galaxies at the same redshift ranges as a function of both $\log(1+\delta')_3$ and $\log(M/\mathrm{M}_\odot)$ in Figure 4.10 (middle panels). We observe both environmental quenching and mass quenching out to $z \sim 2.0$ — the quiescent fraction of galaxies increases with both stellar mass and overdensity as we have shown earlier.

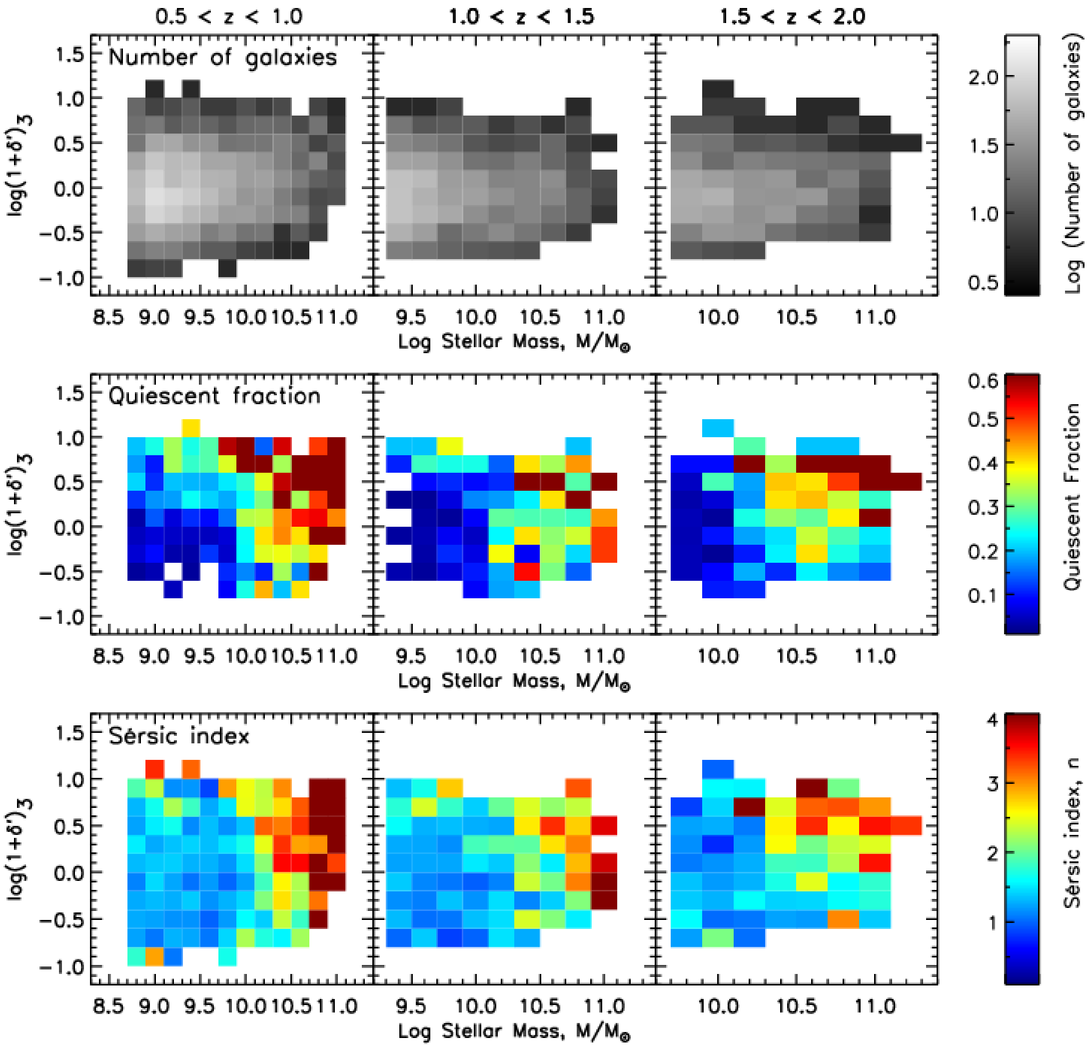

Figure 4.10: Number of galaxies, quiescent fraction, and Sérsic index of galaxies as functions of stellar mass and overdensity.

Top: number of galaxies as functions of stellar mass and projected local density (environment) in three redshift bins (from left to right). The number of galaxies is determined in a bin of 0.2 dex in both $\log(M/\mathrm{M}_{\odot})$ and $\log(1+\delta')$. In each panel the color-scaling indicates the number of galaxies (as indicated by the color bar); note that the range of the abscissa changes in each panel to include only galaxies down to the stellar mass completeness in each redshift bin. ***Middle:*** quiescent fraction of galaxies as functions of stellar mass and projected local density in three redshift bins (from left to right). The quiescent fraction of galaxies is determined in a bin of 0.2 dex in both $\log(M/\mathrm{M}_{\odot})$ and $\log(1+\delta')$. In each panel the color-scaling indicates the quiescent fraction (as indicated by the color bar). ***Bottom:*** the median Sérsic index of galaxies as functions of stellar mass and projected local density for the same redshift bins as in the top panels. The median Sérsic index of galaxies is determined in a bin of 0.2 dex in both $\log(M/\mathrm{M}_{\odot})$ and $\log(1+\delta')$ as in the top three panels. In each panel the color-scaling indicates the median Sérsic index (as indicated by the color bar). Reprinted with permission from "Effect of local environment and stellar mass on galaxy quenching and morphology at $0.5 < z < 2.0$" by Kawinwanichakij et al., 2017. The Astrophysical Journal, Volume 847, Issue 2, article id. 134 pp. 21, Copyright 2017.

The middle panel of Figure 4.10 also shows that for massive galaxies with $\log(M/\mathrm{M}_{\odot}) > 10$ the contour of "constant color" (quiescent fraction) go from nearly vertical at low redshift to nearly horizontal (the high density regions) at high redshift, demonstrating that we get that 50% of quenching comes from mass quenching and 50% from environmental quenching, even at $z \sim 2$ (in the high density regions). This finding is consistent with what we have shown in Figure 4.8.

The bottom panels of Figure 4.10 show the median Sérsic index of galaxies at $0.5 < z < 1.0$, $1.0 < z < 1.5$, and $1.5 < z < 2.0$ as a function of stellar mass ($\log(M/\mathrm{M}_{\odot})$) and environment ($\log(1 + \delta')_3$). We find that the distribution of the median Sérsic index closely resembles that of quiescent fractions of galaxies as shown in the top panels – as in previous work (see references above). In this work we see that these quantities closely track each other remarkably well across the all masses, environments and redshifts we probe (this can be seen visually in Figure 4.10). The similarity of the quiescent fraction and Sérsic index distributions is consistent with a picture in which (stellar) mass quenching is reflecting quenching processes that are more directly correlated with morphology, such as bulge-building/compacting mechanisms (e.g., Lang et al., 2014; Zolotov et al., 2015; Tacchella et al., 2016b,a; Terrazas et al., 2016; Woo et al., 2015, 2017).

In addition, it is interesting that quiescence and concentrated morphology (Sérsic index) go together even at high redshift ($z > 1.5$) and for the environmental quenching, indicating that only particular galaxies are susceptible to environmental quenching, and those are galaxies which already having high Sérsic index. These galaxies have time to make it into dense environments, or they collapsed early and have concentrated morphologies. At low redshift it is different, environment affects galaxy star-formation is independent of their properties.

There are some indications of deviations from this. As a function of environmental density, for lower mass galaxies with $\log(M/\mathrm{M}_{\odot}) < 10.2$ there is some indication that the change in quiescent fraction is faster than the change in galaxy Sérsic index (at fixed stellar mass), and this exists at all redshifts. Figure 4.11 shows the ratio of quiescent fraction to the median Sérsic index of galaxies (f_q/n) in 0.2 dex bins of projected local density. At low masses ($\log(M/\mathrm{M}_{\odot}) < 10.2$; top panels) the plots show that the ratio of f_q/n is roughly constant for densities, $\log(1+\delta')_3 \lesssim 0$, at all redshifts, but that the ratio increases at higher overdensity. This is caused by a faster increase in the quiescent fraction while the median Sérsic index remains roughly constant (or increases slower) as a function of projected local density ($\log(1+\delta')_3$) out to $z \sim 2$, at least for these low-mass galaxies (this is evident by a close inspection of Figure 4.10). Our finding here is consistent with Weinmann et al. (2009) who demonstrated that satellite-specific processes mildly enhance concentration of galaxies once they become satellites. This may be taken as some evidence that these low-mass galaxies retain some memory of the morphology of their star-forming progenitors. However, as we discuss below, once galaxies quench (even as a result of their environment), some process also transforms galaxy morphologies on fast time scales as the distributions of the morphological and structural parameters of quiescent galaxies in high and low densities appear highly similar (see Figure 4.12).

In contrast, for more massive galaxies ($\log(M/\mathrm{M}_{\odot}) > 10.2$; bottom panels of Figure 4.11) there is no evidence that the ratio of quiescent fraction to the median Sérsic index of these galaxies increases with environmental density. It is also interesting that there are more quiescent high mass galaxies in dense environments. They already came in with high Sérsic index, providing tentative evidence for a morphological version of the pre-processing – the processes that make galaxies concentrated have happened already.

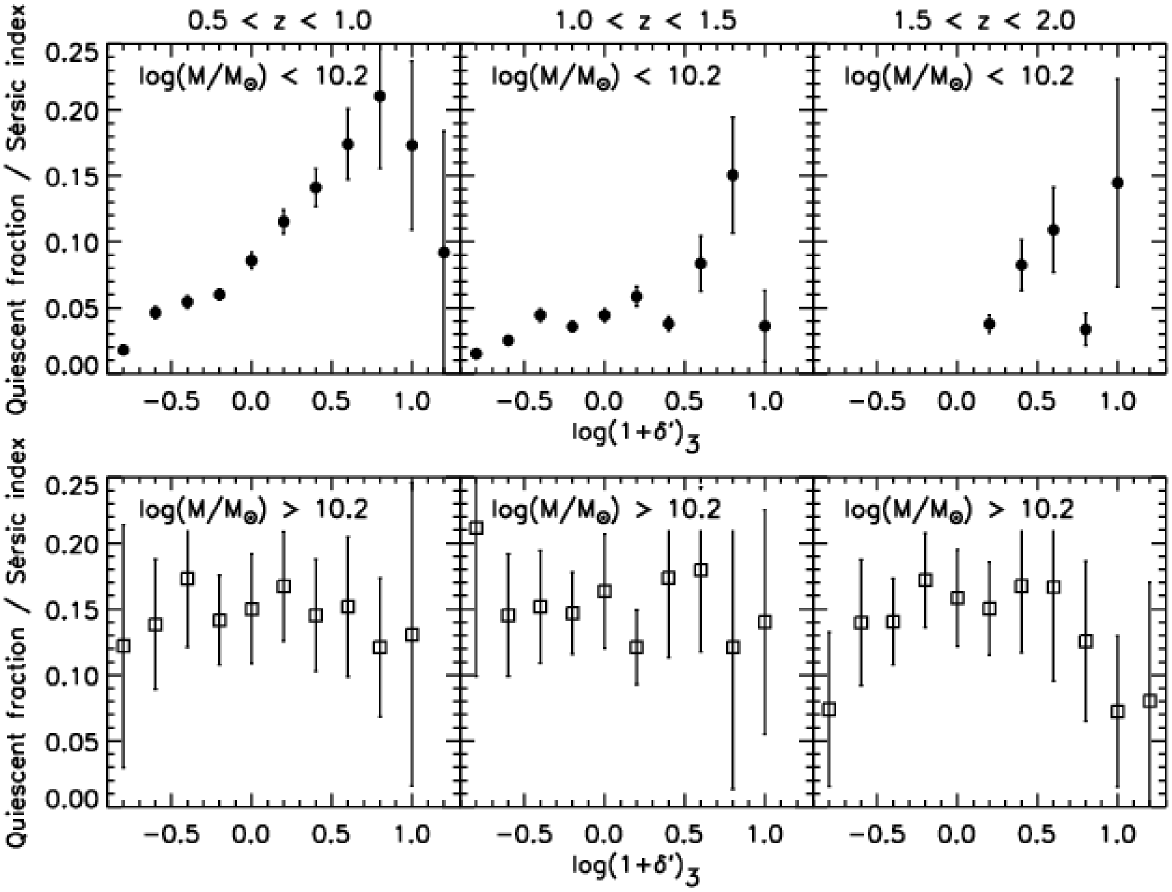

Figure 4.11: The ratio of quiescent fraction to the median Sérsic index of galaxies.

Top: the ratio of quiescent fraction to the median Sérsic index of galaxies (f_q/n) versus the projected local density (environment) in three redshift bins (from left to right) for $\log(M/\mathrm{M}_{\odot}) < 10.2$ galaxies with stellar mass down to the mass completeness limit in each redshift range. Both quiescent fractions and median Sérsic index of galaxies are determined in a bin of 0.2 dex in $\log(1+\delta')$ as in Figure 4.10. The error bars indicate 1σ uncertainties based on Poisson statistics. ***Bottom:*** same as the top panels but for the more massive galaxies ($\log(M/\mathrm{M}_{\odot}) > 10.2$). Reprinted with permission from "Effect of local environment and stellar mass on galaxy quenching and morphology at $0.5 < z < 2.0$" by Kawinwanichakij et al., 2017. The Astrophysical Journal, Volume 847, Issue 2, article id. 134 pp. 21, Copyright 2017.

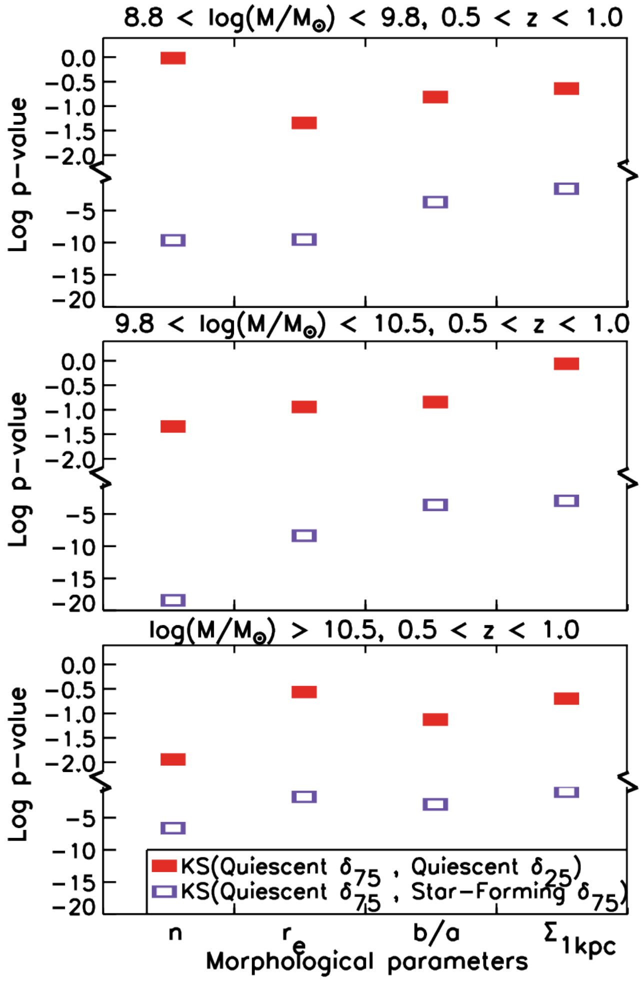

Figure 4.12: The p-values from the K-S tests comparing the distributions of four different morphological parameters.

The p-values (i.e., likelihoods that the samples have the same parent distribution) from the K-S tests comparing the distributions of four different morphological parameters – Sérsic index (n), effective radius (r_e), axis ratio (b/a), and stellar mass surface density in inner 1 kpc ($\Sigma_{\rm 1kpc}$) – for subsamples of quiescent and star-forming galaxies in different environments. The top, middle, and bottom panels show different bins of stellar mass for galaxies at $0.5 < z < 1.0$ (as labeled; these are typical – we do not show higher redshift bins, but they show similar results). Comparing star-forming and quiescent galaxies in high-density environments (open purple rectangles), in all cases the p-values ($\lesssim 10^{-3}$) indicate that we can reject the hypothesis that their morphologies are drawn from the same parent distribution. Performing similar analysis by comparing quiescent galaxies in the highest-density environments to those in the lowest-density environments (filled red rectangles), the p-values indicate that both populations are drawn from the same parent distribution (all p-values are >0.05), except for the effective radius distributions of low-mass quiescent galaxies and Sérsic index distributions of high-mass quiescent galaxies, but the p-values are only 0.02 (see Section 4.3.4 and Section 4.6.2 for the discusssion) Reprinted with permission from “Effect of local environment and stellar mass on galaxy quenching and morphology at $0.5 < z < 2.0$" by Kawinwanichakij et al., 2017. The Astrophysical Journal, Volume 847, Issue 2, article id. 134 pp. 21, Copyright 2017.

We have compared the morphological properties of the galaxy populations using the cumulative distributions of Sérsic index (n), effective radius (r_e), axis ratio (b/a) (using values from van der Wel et al., 2012), and stellar mass surface density in inner 1 kpc ($\Sigma_{\rm 1kpc}$) for quiescent and star-forming galaxies in the highest and lowest density environments, using the measurements described in Appendix B. At all redshifts and stellar masses in our sample, the quiescent galaxies have higher Sérsic indices, smaller effective radii, higher axis ratios, and higher mass surface densities than star-forming galaxies (Figure B.3), in agreement with previous studies both in the local Universe (e.g., Bell, 2008; Fang et al., 2013; Omand et al., 2014) and at high redshift (e.g., van Dokkum et al., 2011; Wuyts et al., 2011; Cheung et al., 2012; Bell et al., 2012; Szomoru et al., 2012; Barro et al., 2013; Lang et al., 2014; Barro et al., 2017).

Turning to the environmental dependence, we also find that quiescent galaxies in high density environments have different structural parameters than star-forming galaxies in the same environments. This would not be expected if a significant portion of quiescent galaxies in high density environments were recently quenched and retained the morphologies of star-forming galaxies. This is true for all subsamples in stellar mass and redshift that we probe, ($8.5 < \log(M/\mathrm{M}_{\odot}) < 11.0$ and $0.5 < z < 2.0$). Figure 4.12 shows a summary of the p-values from K–S tests comparing the distributions of quiescent galaxies in the highest density quartile to those of star-forming galaxies in the highest density quartile at $0.5 < z < 1.0$, and Appendix B.2 shows the cumulative distributions of the morphological parameters that we tested (Sérsic indexes, effective radii, axis ratios, stellar mass surface densities) for galaxies at the same redshift. We do not show the higher redshift bins, but we find the same results in all bins of mass and redshift. In all cases the p-values are $\ll 10^{-2}$. In other words, we can reject the hypothesis that their morphologies are drawn from the same parent distribution.

Similarly, there is no evidence (or at best, weak evidence) that quiescent galaxies in high-density environments have different morphologies than quiescent galaxies in low-density environments at any stellar mass or redshift, except at $0.5 < z < 1.0$. At this low redshift we find tentative evidence that low-mass quiescent galaxies ($8.8 < \log(M/\mathrm{M}_{\odot}) < 9.8$) in high-density environment have larger effective radius than their counterparts in low-density environment, and high-mass quiescent galaxies ($\log(M/\mathrm{M}_{\odot}) > 10.5$) have higher Sérsic index than their counterparts in low-density environment. However,the p-values of these are only 0.02 (equivalent to $\sim 2\sigma$ significance under the assumption of a Gaussian distribution). Figure 4.12 shows a summary of the p-values from K–S tests comparing the distributions of quiescent galaxies in the highest density quartile to those in the lowest density quartile at $0.5 < z < 1.0$. In all cases, we are unable to reject the hypothesis that the morphological distributions are the same (p-values $> 10^{-1.3}$).

Our results that the morphologies of neither quiescent nor star-forming galaxies depend on environment are generally consistent with previous studies, with some notable exceptions. Some studies have found differences in the sizes and Sérsic indexes of galaxies in (lower-density) field and (higher-density) environments at high redshift, but this has mostly been restricted to comparisons between the field and clusters. Papovich et al. (2012) and Bassett et al. (2013) study the structural and morphological properties of galaxies in a $z = 1.62$ proto-cluster and compare those with the field galaxies at the same stellar mass and redshift. Both studies show that the cluster quiescent galaxies have larger average effective sizes compared to field galaxies at fixed mass (see also Cooper et al., 2012; Zirm et al., 2012; Lani et al., 2013; Delaye et al., 2014). In addition, Bassett et al. (2013) found that quiescent cluster galaxies have smaller Sérsic indices compared to the field galaxies (but this was driven by several quiescent galaxies on the edge of the cluster that may be a rare population of recently quenched star-forming galaxies), whereas the star-forming galaxies in both cluster and field show no difference in their morphologies.

On the other hand, Newman et al. (2014) do not detect a significant difference between the mass-radius relation of the quiescent galaxies in the cores of clusters (within $R_{\mathrm{proj}} < 1$ pMpc) and quiescent field galaxies at $z \sim 1.8$. Recently, Allen et al. (2016) studied the dependence of the mass-size relation on environment using field and cluster galaxies at $z \sim 1$. The cluster haloes of their sample are on the order of $10^{13}\mathrm{M}_{\odot}$, which are comparable to group-sized environments we probe here. Allen et al. ruled out a size difference of quiescent field galaxies and quiescent cluster galaxies. Similarly, they also showed that the Sérsic indexes of field quiescent galaxies and cluster quiescent galaxies are consistent. Our results are also consistent with Woo et al. (2017), who compared the specific SFR-$\Sigma_{\rm 1kpc}$ relation for field and satellite galaxies from SDSS with stellar mass $\log(M/{\rm M}_{\odot}) = 9.75 - 11.0$, and find that, in a given stellar mass bin, quiescent galaxies have higher $\Sigma_{\rm 1kpc}$ relative to star-forming galaxies by $\sim 0.2 - 0.3$ dex regardless of being field or satellite galaxies. Therefore, our results add to the growing body of literature that the environment at most weakly affects the morphologies of galaxies when matched in mass, star-formation activity, and redshift.

The lack of evidence for any environmental dependence of the morphological parameters of star-forming or quiescent galaxies has important consequences for the physical effects that drives environmental quenching. Over the mass and redshift ranges considered here, quiescent galaxies even in high-density environments have very different morphological properties than star-forming galaxies at that epoch, and thus do not appear simply as recently-quenched star-forming galaxies. The implication is that the environmental quenching process transforms galaxy morphologies, and it must do so on timescales comparable to the quenching process.

However, it is important to keep in mind the following caveats. We perform the analysis using morphologies as traced by light (“light"-weighted morphology), which may lead to different morphologies as traced by stellar mass (“stellar mass"-weighted morphology Fang et al., 2013). Second, galaxies grow in size with time, but once galaxies is quenched, it stops growing in size at some earlier time. As a result, the quiescent galaxies necessary need to be smaller than star-forming galaxies at a given stellar mass and epoch. Based on this argument, Lilly & Carollo (2016) demonstrated that a high degree of environmental transformation might not be needed if one keeps track of morphologies of the progenitor of quiescent galaxies, and links mild environmental processes such as stripping of galaxy outer part, disk fading, or removal of dust to reproduce to observed quiescent morphology.

4.6.3 What processes could be driving environmental quenching?

The fact that the environmental quenching efficiency evolves with redshift and (at higher redshift) on stellar mass implies that the quenching mechanism itself is correlated with those quantities (namely time and galaxy stellar mass). This observation is consistent with the "overconsumption" model (McGee et al., 2014), where the environmental quenching time depends on the stellar mass of the satellite. In this model cosmological accretion of gas is halted once a galaxy becomes a satellite of a larger halo, and the decline in star-formation in satellites is then due to the exhaustion of a gas reservoir through star formation and outflows ("starvation"). The timescale on which the galaxy quenches is equal to the total gas available at the point of accretion, divided by the gas consumption rate.

Given the strong correlation between SFR and stellar mass (e.g., Tomczak et al., 2016), more massive star-forming galaxies have shorter gas-depletion timescales. In the overconsumption model, McGee et al. (2014) predict that delay times should depend both on galaxy stellar mass and redshift. Using this model, Balogh et al. (2016) showed that the high SFRs of massive galaxies ($\log(M/\mathrm{M}_{\odot}) \sim 10.5$) in their sample of groups and clusters at high redshift, $0.8 < z < 1.2$, lead to short delay times at $z \sim 1$, consistent with the quenching timescale of at least 3–5 Gyr. This is consistent with the lack of significant environmental quenching of low-mass galaxies at $z > 1$ which we observed here. In addition, McGee et al. argue that, given the strong redshift evolution of star-formation rate, the quenching timescales should be shorter at $z > 1.5$ and is possible even with moderate outflow rates.

Nevertheless, the overconsumption model by itself does not account for the differences in the morphological distributions of the galaxies in our study. Qualitatively, in its simplest form, the overconsumption model predicts no morphological evolution of star-formation galaxies (galaxies simply exhaust their gas supply and retain the morphological appearance at infall modulo affects of disk fading, see discussion in Section 4.6.4 below). Therefore, while overconsumption can mainly account for environmental quenching of a galaxy at high redshift ($z \gtrsim 1$) after it becomes a satellite, alone it probably cannot account for the lack of observed morphological differences in quiescent galaxies in high and low density environments discussed above.

At lower redshift, as galaxy specific SFRs declines and associated outflow rates decrease, the quenching time predicted from McGee et al. overconsumption becomes long (> 10 Gyr), and other environmental effects that are more closely aligned with dynamical processes in the halo may become more important, and ultimately dominate (Balogh et al., 2016). This may also drive the environmental quenching efficiency to be more constant with stellar mass at later times ($z \lesssim 0.5 - 1$), as is observed here and in previous studies (e.g., Peng et al., 2010; Quadri et al., 2012; Kovač et al., 2014).

At low redshift ($z < 1$), there is still clear evidence that the act of becoming quiescent is accompanied by a change in galaxy structure, and this is true even when environmental processes are responsible for quenching star-formation in galaxies. As we discussed above, the environmental quenching processes at low redshift are more likely driven by dynamical processes. Strangulation — the removal the gas reservoir — is not expected to affect significantly galaxy morphology (see also van den Bosch et al., 2008; Woo et al., 2015). Ram-pressure stripping can remove cold gas from galaxies (e.g., Vollmer et al., 2012; Kenney & Koopmann, 1999; Oosterloo & van Gorkom, 2005; Chung et al., 2007; Sun et al., 2007; Abramson et al., 2011; Kenney et al., 2015), , but again the morphology of a galaxy is not expected to be significantly modified (Weinmann et al., 2006; van den Bosch et al., 2008). Moreover, a hot gaseous halo is requirement for ram-pressure stripping to be effective in satellites (e.g., Larson et al., 1980; Balogh et al., 2000; Kawata & Mulchaey, 2008; McCarthy et al., 2008), so it is not clear that this can be a dominant mechanism in the lower-mass systems that dominate our study.

While several studies argue that ram pressure stripping is likely a rapid quenching mechanism, in groups and interacting pairs it is primarily effective in quenching lower mass galaxies ($\log(M/\mathrm{M}_{\odot}) < 8.0$) (Slater & Bell, 2014; Davies et al., 2015; Weisz et al., 2015; Fillingham et al., 2016) and is a less relevant quenching mechanism for more moderate mass galaxies (Woo et al., 2017, $9.75 < \log M/\mathrm{M}_{\odot} < 10$). Given the stellar mass range of galaxies in our samples, their environmental quenching efficiencies, and expected range of group–halo masses (e.g., Fossati et al., 2017), these processes (by themselves) seem unlikely to dominate the overall environmental trends that we observe.

4.6.4 What processes could be driving the environmental morphological transformation?

It may be that multiple environmental processes are at work to quench star-forming galaxies, while others transform their morphologies. One candidate for environmental processes that would affect galaxy morphologies are mergers and interactions (similar to "merging quenching", Peng et al., 2010), which are expected to be more frequent in denser environments at both $z = 0$ and higher redshifts (Fakhouri & Ma, 2009). Each merger and interaction can build up the density in the inner kiloparsec of a galaxy (Lake et al., 1998). Such interactions are also shown to be more frequent for higher mass galaxies out to $z = 2.5$ (Xu et al., 2012; Man et al., 2016), where the interactions could increase gas consumption, redistribute angular momentum, and form spheroids.

Frequent galaxy-galaxy encounters also lead to strong tidal torques, which could drive material to galaxy centers, fuel starbursts, build bulges, (e.g., Sobral et al., 2011), and can also lead to disk stripping. These could be combined with disk fading, which enhances the relative importance of the bulge and shifts galaxy morphology toward being more bulge-dominated (higher Sérsic index and higher $\Sigma_{\rm 1kpc}$) (e.g., Carollo et al., 2013, 2016). To test for disk fading requires morphological measurements weighted by stellar mass (rather than weighted by luminosity, which they are at present). For this, we require spatially resolved optical-near-IR structures in galaxies, which will be possible through forthcoming observations with JWST. A higher rate of (minor) mergers has been invoked to explain the accelerated morphological evolution in galaxies in higher density environments (e.g, at $z \sim 1.6$, Papovich et al., 2012; Rudnick et al., 2012; Lotz et al., 2013), and this could explain the weak evidence that massive quiescent galaxies in the highest density environments have increased Sérsic indexes compared to massive quiescent galaxies in low density environments (based on the p-values, Figure 4.12 and Appendix B). While these processes act on galaxies over a range of redshift, they also have the ability to transform galaxy morphologies once they become satellites and would help to explain the structural differences in quiescent and star-forming galaxies in different environments.

To summarize, dense galaxy regions are complex environments, and our results suggest that there are multiple processes at work. The redshift and stellar mass evolution of the environmental quenching efficiency favors models where the gas supply is truncated as galaxies become satellites (e.g., starvation), combined with stellar mass dependent star-formation and outflows (e.g., overconsumption). This must be combined with processes such as more frequent interactions and mergers that are prevalent in denser environments and are capable of transforming galaxy morphologies. These processes would naturally connect the quenching timescale with the morphological transformation timescale, which is required to explain the data. This leads to the prediction that massive galaxies in denser environments have more tidal features than those in less dense environments. Again, forthcoming observations with JWST will provide deeper imaging to test our prediction.

5. AN APPLICATION OF MULTI-BAND FORCED PHOTOMETRY TO DARK ENERGY CAMERA CATALOG FOR THE SHELA SURVEY

5.1 Synopsis

In this chapter we apply *The Tractor* image modeling code to improve upon existing multi-band photometry for the *Spitzer*/HETDEX Exploratory Large-Area (SHELA) survey. SHELA covers $\sim 24\ \mathrm{deg}^2$ of the Sloan Digital Sky Survey (SDSS) "Stripe82" region with seven bandpasses spanning a wavelength range of 0.35 to 0.45 μm. To accomplish this, we are using *The Tractor* to perform forced photometry to measure 3.6 and 4.5 μm fluxes for all objects within our DECam catalog. This technique employs prior measurements of source positions and surface brightness profiles from a high-resolution band from DECam/SHELA survey to model and fit the fluxes of the source in the lower-resolution band and allows one to take advantage of a higher resolution image to model source crowding, and derives optimal "colors" for sources down to the detection limit of higher resolution image. We discuss our implementation of *The Tractor* riz-band selected $ugriz$-band DECam catalogs that reach a 5σ depth of $\sim$ 24.5 AB mag and cover $17.5\ \mathrm{deg}^2$ of the overall SHELA field. Our new multi-band source catalogs offer a number of advantages over traditional position-matched catalog, including (1) consistent source cross-identification between bands, (2) deblending of sources that are clearly resolved in the fiducial bands ($ugriz$-band DECam) but but blended in the lower resolution *Spitzer*/IRAC bands, (3) detecting extremely faint sources that fall below the IRAC detection threshold, and (4) an improvement in the photometric redshift accuracy as evidenced by decreasing in bias and outlier fraction compared to spectroscopic redshifts. Therefore, forced photometry using *The Tractor* provides a means of improving the accuracy of multi-band extragalactic surveys, enabling a broad range of studies of the galaxy evolution. We will extend our application of this technique to the full SHELA footprint in the future.

5.2 Background Information

Spitzer/HETDEX Exploratory Large-Area (SHELA) survey is a wide-field ($\sim 24\ \mathrm{deg}^2$) field in the Sloan Digital Sky Survey (SDSS) Stripe 82 field (Annis et al., 2014) and covers a portion of the footprint of the Hobber Eberly Telescope Dark Energy eXperiment (HETDEX, Hill et al. 2008. The SHELA field contains a large amount of ground-based imaging, including the deep $ugriz$ data from the Dark Energy Camera (DECam) imaging program (Wold et al. 2018, in preparation), $K-$band data from the NEWFIRM instrument (Stevans et al. 2018, in preparation) plus archival J, K_s-bands data from VISTA-CFHT Stripe 82 Survey (VICS82) (Geach et al., 2017). Also, the SHELA field contains deep *Spitzer*/IRAC imaging at 3.6 and 4.5 μm. The large SHELA field covers nearly $0.5\ \mathrm{Gpc}^3$ in cosmological volume at both moderate redshifts, $0.5 < z < 2.0$, and at high redshifts, $0.2 < z < 3.5$. All of these will provide accurate photometric redshift and stellar mass measurements and enable a broad range of scientific studies, including the relationship between structure formation, galaxy stellar mass, halo mass, AGN, and environmental effects over $0.5 < z < 3.5$.

The basis of the scientific success of surveys such as SHELA lies in the construction of robust multi-band source catalogs. Papovich et al. (2016) presented the reduced *Spitzer*/IRAC imaging at 3.6 and 4.5 μm and source catalogs for the *Spitzer*/HETDEX Exploratory Large-Area (SHELA) survey. Papovich et al. used an aperture photometry approach with the SExtractor software package (Bertin & Arnouts, 1996) to measure 3.6 and 4.5 μm photometry. Our ancillary data contains ground-based near-infrared and optical imaging at higher spatial resolution ($0\farcs27$) compared to the IRAC 3.6 and 4.5μm imaging ($0\farcs8$). To construct a mixed-resolution, multi-band catalogs of the ancillary data, one could perform positional cross-matching between individual source for each band within a predefined search radius. A disadvantage of this technique for SHELA is that sources that clearly resolved in the higher resolution, ground-based DECam bands may appear “blended” together as a single source in the *Spitzer*/IRAC imaging. If this is not properly accounted for, this will lead to incorrect source cross-identification between bands and potentially less accurate flux and photometric redshift measurements.

Motivated by the need for robust multi-band source catalogs, we apply *The Tractor* image modeling code to improve upon existing multi-band photometry for the *Spitzer*/HETDEX Exploratory Large-Area (SHELA) survey.We present new multi-band forced photometry incorporating the $ugriz$-band Dark Energy Camera (DECam) plus 3.6 and 4.5 μm IRAC catalogs. In Section 5.3 we describe our application of forced photometry using *The Tractor*. In Section 5.4, we compare the IRAC 3.6 and 4.5 μm fluxes from our new multi-band forced photometric catalogs with the original IRAC catalog constructed using original SHELA IRAC catalog (Papovich et al., 2016), constructed using traditional positional matching between bands. In Section 5.4.3 we demonstrate the utility of the new multi-band photometric catalog by estimating photometric redshift and quantify the bias and outliers by comparing with spectroscopic redshifts. In Section 5.4.4 and 5.4.5, we describe the estimation of rest-frame color and stellar mass, respectively. Unless otherwise noted, we give all magnitudes in the AB magnitude system ($m_{\rm AB} = 23.9 - 2.5 \log_{10} f_\nu$, with f_ν in units of μJy).

5.3 Method: Spitzer/IRAC Forced Photometry with *The Tractor*

5.3.1 Input Catalog and Image Calibration Parameters

We begin our source modeling procedure by selecting the fiducial band, high-resolution model of each source. We use the fluxes and shape parameters, including semi-major axis (a), position angle, and axis ratio (b/a), measured in our DECam detection image because the detection image combines the information of all sources in the five optical band images.

Second, we supply *The Tractor* with the input image of SHELA IRAC 3.6 and 4.5 μm images (Papovich et al., 2016) with corresponding image calibration information, including rms maps (noise model), the empirical IRAC point response function (PRFs), and image astrometric information (WCS).

5.3.2 Surface Brightness Profile Modeling

Broadly speaking, *The Tractor* proceeds by rendering a model of galaxy or a point source convolved with the IRAC PRF at each IRAC band and then performs a linear least-square fit for source fluxes such that the sum of source fluxes is closest to the actual image pixels, with respect to the noise model. Finally, the Tractor provides the measurement IRAC flux of each DECam source with the lowest reduced chi squared value (χ^2_{red}).

In practice, we extract an IRAC 3.6 and 4.5 μm image cutouts at the location of each DECam source. We select the cutout size of $20'' \times 20''$. This cutout size represents a trade-off between minimizing computational costs related to larger cutout sizes and ensuring that the sources lie well within the cutout extent.

For each DECam source, we measure its IRAC fluxes with three brightness profiles: a point source profile, an exponential profile (equivalent to a Sérsic profile with $n = 1$), and a deVaucouleurs profile (equivalent to a Sérsic profile with $n = 4$). In our final output catalog, we report optimized IRAC fluxes resulting in the lowest reduced chi squared (χ^2_{red}) value, and we also report the model corresponding to the optimized photometry.

To avoid unphysical results due to optimizing too many sources parameters (i.e., source positions, shapes, and brightness) and the presence of crowded neighboring sources or bright and extended nearby sources, we perform *The Tractor* forced photometry twice for each DECam source of interest. We begin with identifying and masking out bright and extended DECam sources located within $20''$ from a source of interest. For the first optimization, we exclude the source of interest and other sources within $4''$ aperture radius from the modeling.[1] We simultaneously model all other neighboring sources located at distance $> 4''$ within the cutout by holding all image calibration parameters, positions, and surface brightness profile shapes of neighboring sources fixed except for their brightnesses, which are allowed to be optimized.

We then subtract the resulting modeled image cutout of neighboring sources from the IRAC image cutout, and we therefore left with the image of the source of interest and its neighboring sources located within $4''$ aperture radius.

For the second optimization, we run *The Tractor* on IRAC "neighboring sources subtracted"

---

[1] The light profile of these neighboring sources located within $4''$ aperture radius could potentially blend with that of a source of interest, and therefore we simultaneously fit these neighboring sources and a source of interest during the second optimization.

cutout (resulting from the first optimization as described above) by holding all image calibration parameters fixed and allow source position, brightness, and effective radius (for an exponential profile or a deVaucouleurs profile) for the source of interest to be optimized. We allow the position of the source of interest to be varied within 1 arcsecond relative to the input source position from DECam catalog. In addition, if the modeled effective radius output from *The Tractor* are unphysical (i.e., negative value), we then rerun *The Tractor* by fixing the effective radius to the input effective radius from DECam catalog. Examples of the original multi-band images, models, χ^2 maps for a blended IRAC source and a non-blended, faint IRAC source for which *The Tractor* has produced improved IRAC photometry are shown in Figure 5.1. In particular, the example of the faint source is for an object that is undetected in the original SHELA IRAC catalog. Even in this case the Tractor provides an estimate for the IRAC flux density and uncertainty. These examples demonstrate the ability of our forced photometry to detect extremely faint sources that fall below the detection threshold and sources known to be blended in the original SHELA IRAC catalog. These are the primary motivations for performing forced photometry with *The Tractor*.

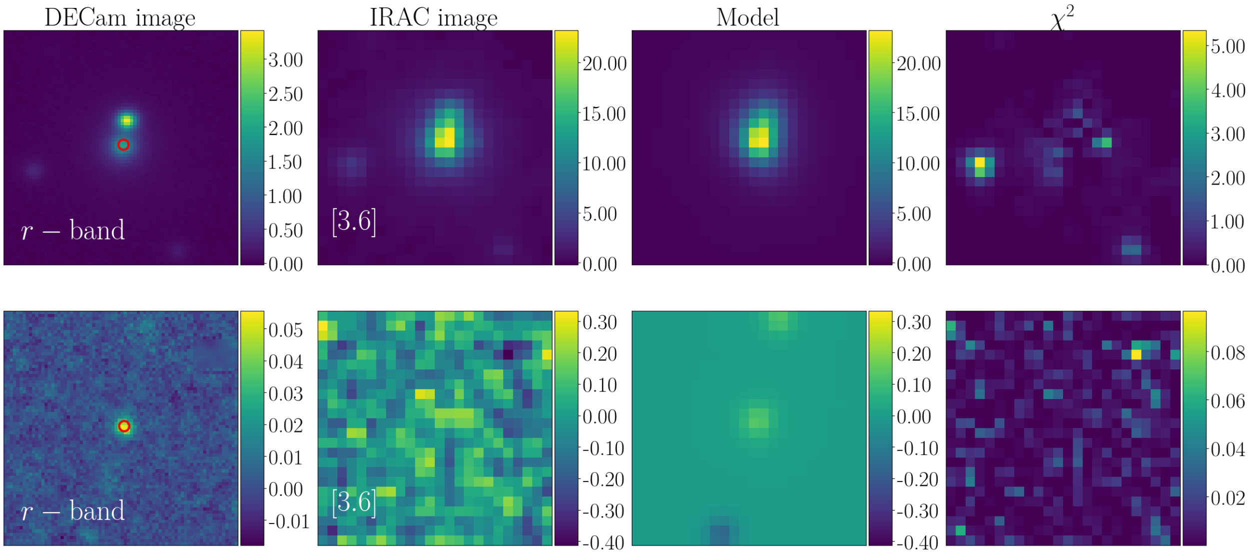

Figure 5.1: Example of our forced photometry procedure for blended and faint IRAC sources.

Top: example of our forced photometry procedure for a source that is clearly blended in the IRAC 3.6μm image but resolved in the DECam image (for this source, $r-$band). The cutout dimensions are $20'' \times 20''$ and the source was modeled using a deVaucouleurs profile. The first two columns show the original images in DECam $r-$band and IRAC 3.6 μm band, respectively. The third column shows the source model convolved with the PRF of each IRAC band, and the fourth column shows the χ^2 maps. The colorbar units are μJy. We indicate a DECam source whose its IRAC photometry is measured as red circle symbol in the the first column. ***Bottom:*** example of a source with no blending issues that is much fainter than the example shown in the top row. The source was modeled using an exponential profile. We emphasize that this faint source with measurements based on our DECam-selected forced photometry were not detected in the original SHELA IRAC SExtractor catalog.

5.4 Results

We find that about 47% of the sources in the DECam-selected forced photometry catalogs are best modeled by spatially resolved surface brightness profiles (see Section 5.3.2). Of the resolved sources, the majority are best modeled by an exponential profile ($\sim 61\%$) rather than a deVaucouleurs profile ($\sim 39\%$).

To compare *The Tractor* forced photometry with the existing SHELA IRAC photometry, we make a catalog of DECam-sources which are cross-matched with SHELA IRAC catalog within a search radius of $3''$ (1,076,210 objects in total). We identify blended sources in IRAC based on the presence of a nearby source in the DECam catalog within $4''$ (about twice the angular resolution of the IRAC data), whereas sources lacking neighbors in DECam within $4''$ are free of blending issues in IRAC. Based on these criteria, we expect at least 35% of the total sources in DECam input catalog will be blended in the 3.6 and 4.5 μm IRAC data. This high fraction of blended sources in IRAC is one of the primary motivations for performing forced photometry with *The Tractor*.

In Figure 5.2, we show a comparison between the source magnitudes from *The Tractor* forced photometry and the original IRAC photometry measured in $6''$-diameter aperture, corrected to total fluxes (Papovich et al., 2016). We find that our forced photometry is typically in good agreement with the SHELA IRAC magnitudes though some scatter is apparent, particularly for blended sources. The scatter is reduced when we restrict the comparison to isolated sources that lack a neighbor within $4''$. For sources with the IRAC the aperture-corrected magnitudes brighter than 22 AB mag, the median offsets between the Tractor and the IRAC the aperture-corrected magnitudes are -0.12, -0.06, -0.45 for all, not blended, and blended sources, respectively. We expect that the larger offset and scatter for blended sources are mainly due to the ability of our *The Tractor* force photometry procedure to de-blending those sources. The other contributing factors to the scatters could be spatial PSF variations, inaccurately matched sources in DECam and IRAC catalogs, and issues with the photometry from the original catalogs.

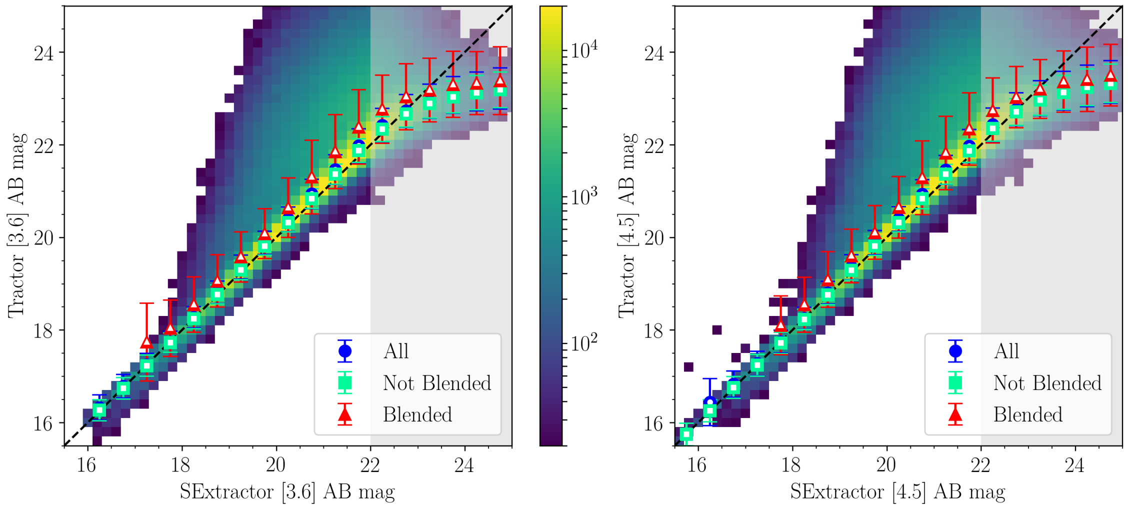

Figure 5.2: The comparison between *The Tractor* and original IRAC photometry

We compare *The Tractor* and original IRAC photometry measured in 6″-diameter aperture, corrected to total fluxes. The color scale represents the density of points for all sources matched between DECam catalogs and IRAC SExtractor catalog (Papovich et al., 2016). Data points with error bars show median Tractor IRAC magnitudes and corresponding standard deviation from median absolute deviations in bins of original IRAC magnitudes for all sources (blue circles), not blended sources (green squares), and blended sources (red triangles). Blended sources in IRAC is identified based on the presence of a nearby source in the DECam catalog within 4″. Sources lacking neighbors in DECam within 4″ are free of blending issues in IRAC. The dashed line shows the one-to-one correspondence between *The Tractor* and original catalog magnitudes. The grey-shaded region highlights the parameter space below 80% completeness limit (22.0 AB mag).

5.4.1 Error Estimates

The Tractor outputs error on each optimized parameter, including source brightness. To ensure that *The Tractor* outputs photometric error consistent with those from the existing SHELA IRAC photometric catalog (Papovich et al., 2016), we generate the rms map for *The Tractor* forced photometry procedure by taking IRAC 3.6 or 4.5 μm weight map and scaling C in a $C/\sqrt{(\text{weight map})}$ image such that the median photometric error output from *The Tractor* are roughly matched with those measured in 6″-diameter aperture, corrected to total. As a result, we find $C = 0.265$ and 0.287 as scaling factors for our in 3.6 or 4.5 μm rms images ($C/\sqrt{(\text{weight map})}$), respectively. Finally, we add the Tractor photometric error in quadrature with an additional error $\sigma_{\rm sys} = 0.05$ mag to account for the median offset between the Tractor and the the aperture-corrected magnitudes for non-blended sources. The total photometric error $\sigma_{i,c}$ on each DECam source i in IRAC channel c is then given by,

$$\sigma_{i,c}^2 = \sigma_{i,c,\rm forced\ phot}^2 + (0.921\sigma_{\rm sys} \times F_{i,c,\rm forced\ phot})^2 \tag{5.1}$$

where $F_{i,c,\rm forced\ phot}$ and $\sigma_{i,c,\rm forced\ phot}$ are the flux density and its error measured from *The Tractor* forced photometry procedure.

5.4.2 Caveats

We emphasize that improved photometry of blended IRAC sources can only be achieved if the blended objects are well resolved in the DECam catalog. We also note that the accuracy of our photometry with *The Tractor* will be reduced for highly complex and extended sources that are not well described by an exponential galaxy profile or a deVaucouleurs model. These sources can be identified by comparing the Tractor fluxes with those from the existing SHELA IRAC photometric catalog (Papovich et al., 2016) and looking for outliers.

5.4.3 Photometric Redshifts

We use the photometric code EAZY (Brammer et al., 2008) to estimate photometric redshifts to demonstrate the utility of our multi-band SHELA catalog. We require measured objects to have measured fluxes at least in 5 bands. As discussed in Wold et al. 2018 (in prep.), we find that the completeness and purity of our DECam catalog is improved by excluding magnitudes with internal SExtractor flags > 3 and external SExtractor flags > 0. For the DECam $ugriz$ photometry we use FLUX_AUTO fluxes from SExtractor. In addition to use DECam $ugriz$ and IRAC [3.6] and [4.5] μm fluxes from *The Tractor* forced photometry. We obtain J and K-band fluxes from VISTA-CFHT Stripe 82 Survey (VICS82) (Geach et al., 2017) which is limited to $K_s < 21.4$ AB mag (80% complete)[2]

---

[2] We perform a positional cross-matching of each source in the DECam catalog to that of VICS82 catalog within a $3''$ search radius. We note that in the future work will focus on utilizing *the Tractor* to provide a more sophisticated DECam$+J+K+$IRAC catalog.

We then utilized EAZY's option to apply a K-band magnitude prior. As described in Muzzin et al. (2013), we performed a calibration run fixing EAZY's z_{photo} to the known SDSS z_{spec} to make small ($\lesssim 2\%$) zero-point offsets to our $ugirz$-band catalog. We demonstrate the quality of our derived photometric redshifts (EAZY's z_{peak} parameter[3]) by comparing our dataset to the available SDSS spectroscopic sample at $z < 1.0$ in Figure 5.3. We find a that the median $\Delta z = z_{\text{photo}} - z_{\text{spec}}$ is 0.001 and the normalized median absolute deviation, defined as:

$$\sigma_{NMAD} = 1.48 \times median\left(\left|\frac{\Delta z - median(\Delta z)}{1 + z_{\text{spec}}}\right|\right), \tag{5.2}$$

is 0.04 with 0.3% of sources found to be 5σ outliers. We find that our photometric results are comparable to those reported in the EAZY test fields (Brammer et al., 2008).

We note that in the near future HETDEX will allow us to extend this analysis out to $z = 3.5$ by providing spectroscopic redshifts for a sample of $N \sim 200{,}000$ galaxies at both $z < 0.5$ and $1.9 < z < 3.5$. We plan to incorporate HETDEX spectroscopic redshifts to improve our photometric redshift measurements.

---

[3] This parameter corresponds to the peak probability of the P(z) function, and is considered the best z_{photo} estimate (Muzzin et al., 2013).

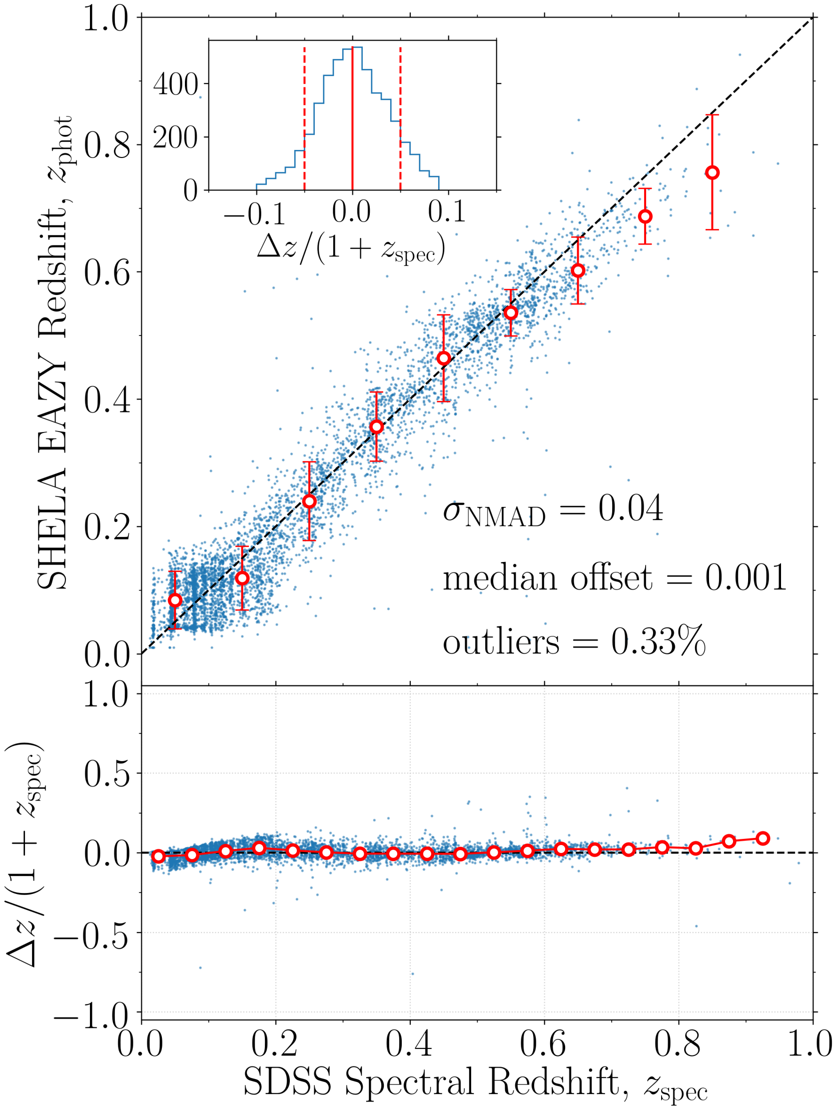

Figure 5.3: SDSS spectroscopic redshifts verses our SHELA photometric redshifts.

Comparison between our SHELA photometric redshifts ($z_{\rm phot}$) and spectroscopic redshift ($z_{\rm spec}$) from SDSS DR12. We derived the photometric redshifts using EAZY code (Brammer et al., 2008) with nine bands photometry: DECam $ugriz$, VISTA J, K_s, and IRAC 3.6 and 4.5 μm DECam+J + K+IRAC catalog. We use forced photometry technique to measure IRAC 3.6 or 4.5 μm photometry for each source in the SHELA/DECam catalog. The σ_{NMAD} denotes 1.48 times the median absolute deviation of the different between $z_{\rm spec}$ and $z_{\rm phot}$ (Δz), normalized to the $1 + z_{\rm spec}$. The percentage of outlier corresponds to the fraction of sources with $\Delta z/(1 + z_{\rm spec})$ exceeding 5σ.

5.4.4 Rest-Frame Colors

We are motivated by Martin et al. (2007) and also Wyder et al. (2007) who have demonstrated that UV-optical color-magnitude diagram, particularly $NUV-r$ vs. M_r can separate red sequences from blue sequences. Our z-band (5σ at 24.6 AB mag) and IRAC [3.6] μm are deep enough for deriving rest-frame $NUV-g$ color and robust stellar mass. We therefore use the rest-frame$NUV-g$ color vs. stellar mass diagram to classify galaxies into quiescent and star-forming. After we estimate photometric redshift for all objects in the DECam photometric catalog, we use EAZY to interpolate the input SED to obtain the rest-frame $NUV-g$ color for each galaxy.

5.4.5 Stellar Mass Estimates

We use nine bands photometry from (DECam $ugriz$, VISTA J, Ks, and IRAC 3.6 and 4.5 μm) to derive stellar mass by fitting Bruzual & Charlot (2003) models with *FAST* (Kriek et al., 2009), assuming Chabrier (2003) initial mass function, exponentially declining star formation histories with timescale τ, fixed solar metallicity and a dust law as described in Calzetti et al. (2000). For each source the redshift is fixed to the photometric redshift ($z_{\rm peak}$) derived with EAZY. We limit dust extinction to $0 \leq A_V \leq 4$, age to $7.5 \leq \log_{10}(\rm age) \leq 10.1$ Gyr and τ to $7 \leq \tau \leq 11$ Gyr.

In the next chapter, we also estimate stellar masses using the Bayesian *iSEDfit* package presented in Moustakas et al. (2013), *iSEDfit*, based on the same photometric data set (DECam $ugriz$, VISTA J, K_s, and IRAC 3.6 and 4.5 μm) and study the systematic offsets that arise when we use different priors of star formation history and stellar population synthesis models.

We estimate mass completeness limit from a stellar population synthesis model obtained from EzGal (Mancone & Gonzalez, 2012). Specifically, we consider a single stellar population synthesis model (SSP) following a Chabrier (2003) initial mass function of solar metallicity formed at a formation redshift (z_f) of 4. In Figure 5.4 we show the distribution of galaxy stellar mass as function of redshift, and the mass completeness limits estimated using the limiting DECam/z-band magnitude of 24.4 AB mag, the limiting VISTA/K_s-band magnitude of 21.4 AB mag, and the limiting IRAC/[3.6] magnitude of 22.0 AB mag (80$\%$ complete).

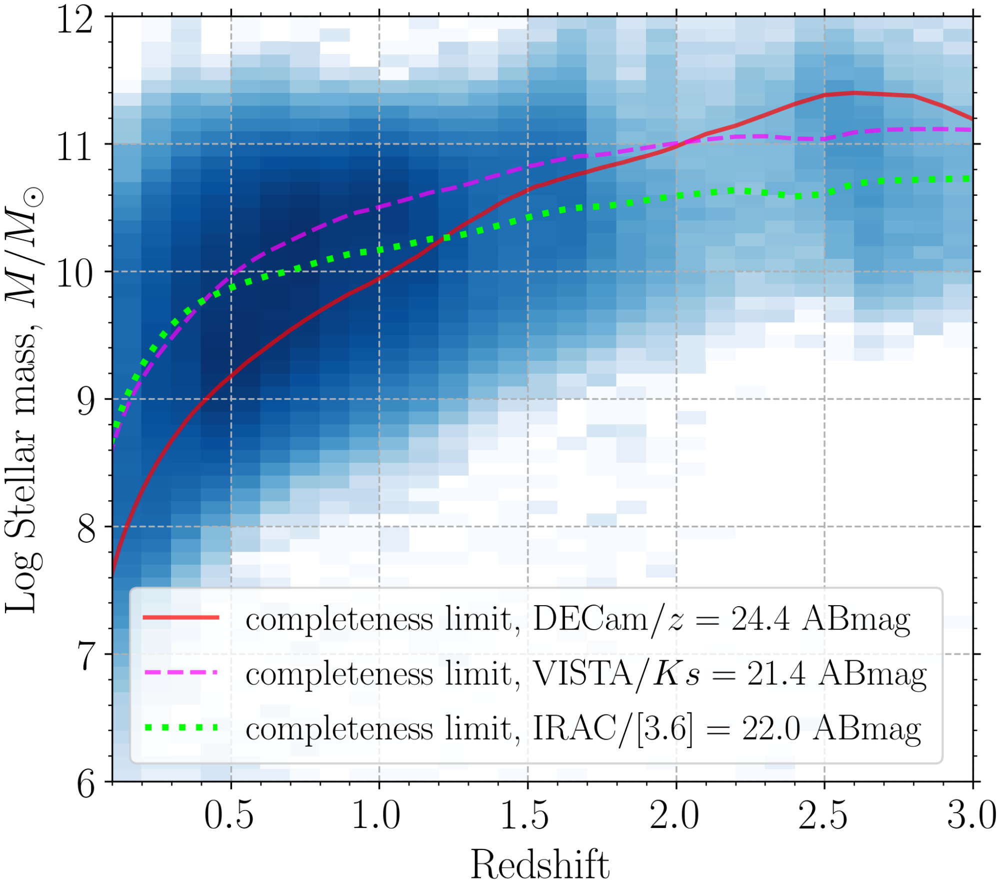

Figure 5.4: Galaxy stellar mass as function of redshift for DECam/SHELA sample

Distribution of stellar mass derived by fitting Bruzual & Charlot (2003) models with *FAST* (Kriek et al., 2009) as function of redshift. The colorscale indicates the density in each bin of stellar mass and redshift (0.1 dex). The solid red line indicates the mass completeness limit determined from passively evolving single stellar population synthesis (SSP) with a formation redshift $z_f = 4$ when using limiting DECam/z-band magnitude of 24.4 AB mag (80% complete). The dashed magenta line indicates the mass completeness limit determined from SSP with $z_f = 4$ when using a limiting VISTA/K_s-band magnitude of 21.4 AB mag (80% complete). The dotted green line indicates the mass completeness limit determined from SSP with $z_f = 4$ when using a limiting IRAC/[3.6] magnitude of 22.0 AB mag (80% complete).

6. DECam/SHELA: A LACK OF GROWTH AMONG MASSIVE GALAXIES

6.1 Synopsis

In this chapter we study number density evolution of galaxies at the highest masses using imaging in nine photometric bands over 17.5 deg^2 in the *Spitzer*/HETDEX Exploratory Large-Area Survey (SHELA) within the footprint of the SDSS Stripe82. The large area and moderate depth of our survey drastically reduces the statistical uncertainties due to Poissonian error and cosmic variance. After accounting for a number of potential systematic errors, including the effects of scatter in stellar mass, we measure galaxy stellar mass functions over $0.3 < z < 1.0$ down to $\log(M_*/M_\odot) = 10.5$. We detect no growth in the typical stellar mass of massive galaxies over this redshift range with an uncertainty of 12%. This confidence interval is dominated by uncertainties in the assumed star formation history and stellar population synthesis models for stellar mass estimations. We divide our sample into star-forming or quiescent galaxies based on the degree of star formation as determined from our SED fitting. We do not detect evolution ($\lesssim 0.1$ dex) in the characteristic stellar mass determined from the stellar mass function of massive quiescent galaxies even after accounting for the systematic uncertainty and the random error in stellar mass measurement. If the mass assembly of massive galaxies at late times are dominated by minor mergers, our observed lack of evolution in stellar mass function of massive galaxies indicating a balance between build-up of stellar mass through mergers and mass loss due to stellar evolution process. Our observation provides the upper limit on mass growth by merging over this redshift range to be $\sim 48\%$ (~ 0.17 dex).

6.2 Introduction

One of the major feature of the cold dark matter dominated universe is the hierarchical structure-formation, by which increasingly larger dark matter halos are formed through the assembly of smaller one. As galaxies reside in these halos, they trace the underlying dark matter distribution, and therefore we expect these galaxies to undergo hierarchical growth as well (e.g., White & Rees, 1978; Blumenthal et al., 1984; White & Frenk, 1991; Lacey & Cole, 1993; Springel et al., 2005).

It is generally argued that the formation of massive galaxies follows "two-phase" formation scenario (e.g., Oser et al., 2010, 2012; Wellons et al., 2015). According to this scenario, galaxies form a compact cores through an early rapid phase of dissipational in situ star formation at $2 \lesssim z \lesssim 6$ (Kereš et al., 2005; Dekel et al., 2009; Oser et al., 2010) and/or gas-rich mergers (Weinzirl et al., 2011; Wellons et al., 2015). The subsequent evolution is dominated by assembly of stellar halos by dissipationless minor (dry) mergers (e.g., Khochfar & Silk, 2006; Naab et al., 2006; Oser et al., 2010, 2012; Johansson et al., 2012; Hilz et al., 2013). This two-phase formation scenario provides explanation for observed growth in effective radii (e.g., Newman et al., 2012; van der Wel et al., 2014) and stellar halos of massive galaxies (e.g., Szomoru et al., 2012; Patel et al., 2013; Huang et al., 2018).

Both numerical simulations (e.g., Oser et al., 2010; Wellons et al., 2015) and semi-analytic models (SAM; e.g., Lee & Yi, 2013, 2017) generally show that the fraction of accreted stars through mergers increase with total galaxy stellar mass or halo mass (e.g., Lackner et al., 2012; Cooper et al., 2013; Rodriguez-Gomez et al., 2016; Qu et al., 2017; Pillepich et al., 2018). For instance, with hydrodynamical simulations, Naab et al. (2009) showed that since $z = 1$ to $z = 0$ galaxies have grown by 25% in mass and in size by gas-poor (dry) mergers. Recently, Qu et al. (2017) analyzed the mass assembly of central galaxies in the EAGLE cosmological simulation and find that $\sim 20\%$ of stellar mass of present day massive galaxies ($> 10^{11} M_{\odot}$) are built up through mergers. These implied growth should reflect in evolving typical mass in stellar mass function (SMF) from $z \sim 1$ to the present day (e.g., Conroy & Wechsler, 2009; Mutch et al., 2013; Moster et al., 2013; Behroozi et al., 2013; Rodríguez-Puebla et al., 2017).

Previous observational works on galaxy stellar mass function were mostly based on deep galaxy surveys (e.g., Pozzetti et al., 2007; Drory et al., 2009; Brammer et al., 2011; Moustakas et al., 2013; Tomczak et al., 2014) These studies provide the global view on the evolution of stellar mass assembly over the wide range of redshift and mass. While the different studies do not necessarily agree with each other, it has been consistently demonstrated that since $z \sim 1$ most massive galaxies have undergone less evolution than less massive ones, revealing a faster stellar mass assembly for the most massive systems (e.g., Fontana et al., 2006; Pozzetti et al., 2007; Moustakas et al., 2013). However, given their small angular coverage, these surveys are particularly subject to the statistical variance (i.e., cosmic variance) at low redshift, and imaging survey with large cosmic volume is crucial for probing very rare galaxy population at the high-mass end of the exponentially declining stellar mass function.

Early attempts utilize ten of square degrees surveys to minimize the contribution from cosmic variance and focus on the evolution of high-mass galaxies. Matsuoka & Kawara (2010) presented the first analysis of the massive galaxies with $M_* > 10^{11}M_\odot$ out to $z = 1$ drawn from $55\ \mathrm{deg}^2$ of the UKIDSS Large Area Survey K-band images on the SDSS southern equatorial stripe, and they find the massive galaxies with $M_* > 10^{11.0-11.5}M_\odot$ and $M_* > 10^{11.5-12.0}M_\odot$ experience rapid growth in the number density since $z = 1$ by a factor of 3 and 10, respectively. Moutard et al. (2016) analyzed evolution of the galaxy stellar mass function at $0.2 < z < 1.5$ using $K_s < 22-$selected, photometric redshift-based sample over $\sim 22.4\ \mathrm{deg}^2$ of the footprint of the VIPERS spectroscopic survey. The authors provided an evidence of increasing in the number density of massive galaxies with $M_* > 10^{11.5}M_\odot$ by a factor ~ 2 from $z \sim 1$ to $z \sim 0.3$. Even though both Matsuoka & Kawara (2010); Moutard et al. (2016) generally detected growth in the number density of massive galaxies; however, there is inconsistency concerning the amplitude of the evolution in the number density

This discrepancy highlights the challenges of probing the high-mass end of the SMF and raises concerns about other systematic uncertainties, including those caused by the assumption in the modeling of the galaxy spectral energy distribution (SED) such as model templates, initial mass function, metallicity, and dust content. This could significantly contribute to the total error budget, and consequently affects the robustness of the detected evolution of galaxy stellar mass function (Marchesini et al., 2009). To address this issue, recent study by Bundy et al. (2017) exploited of the Stripe 82 Massive Galaxy Catalog (S82-MGC) to construct a mass-limited sample at $0.3 <$

$z < 0.65$ that is complete to $M_* > 10^{11.3} M_\odot$, over a large area of $139\ \mathrm{deg}^2$. After accounting for both random and systematic uncertainty, they measured galaxy stellar mass function and reported no evolution in the typical stellar mass over the redshift range they probed.

The purpose of this work is to utilizing the 17.5 deg^2 *Spitzer*/HETDEX Exploratory Large-Area Survey (SHELA) survey dataset to probe stellar mass function, particularly for massive galaxies with $\log(M_*/M_\odot) > 10.5$ over $0.3 < z < 1.0$. Motivated by the recent study by Bundy et al. (2017), we account for potential systematic uncertainties, including the assumptions in modeling SED and random error in the stellar mass. After accounting for systematic uncertainties arising from differences in star-formation histories and stellar population synthesis models, we find no redshift evolution ($\lesssim 0.1$ dex) in the the characteristic stellar mass, (M^*) from $z = 1.0$ to $z = 0.3$

A plan of this chapter is as follows. We begin Section 6.3 by summarizing how we build our sample from nine photometric bands spanning optical to mid-infrared wavelength. We describe the various estimates of stellar mass in Section 6.4. In Section 6.5 we discuss potential biases in derived mass function for large samples, including the impact of the scatter in stellar masses. We present our results in Section 6.6. In Section 6.7 we discuss the significance of our results as well as comparisons to other works. Finally, we provide summary in Chapter 7. Throughout this chapter, we use the AB magnitude system and adopt a standard cosmology with $H_0 = 70\ h_{70} \mathrm{km\ s^{-1}\ Mpc^{-1}}$, $\Omega_M = 0.3$, and $\Omega_\Lambda = 0.7$.

6.3 Data description

6.3.1 The Dark Energy Camera $ugriz$ photometry

We presented the full details of measurements of IRAC photometry for the Dark Energy Camera catalog for the SHELA Survey in Wold et al. 2018, in prep. The SHELA dataset includes deep (22.6 AB mag, 50% complete) 3.6 and 4.5 μm imaging from *Spitzer*/IRAC (Papovich et al., 2016) and $ugriz$ imaging from the Dark Energy Camera over 17.5 deg^2 (DECam; Wold et al. 2018, in prep).

6.3.2 *Spitzer*/IRAC Photometry

We apply the *Tractor* image modeling code (Lang et al., 2016b,a) to perform "forced photometry" and measure 3.6 and 4.5 μm photometry for each source in the DECam/SHELA catalog. The full details of how we construct this mixed-resolution multiband catalog of DECam $ugriz+$ *Spitzer*/IRAC 3.6 and 4.5 μm are presented in Chapter 5.

6.3.3 The VISTA J and K_s photometry

In addition, SHELA field falls within SDSS Stripe82. We therefore include in our analysis the VISTA J and K_s photometry from the VISTA-CFHT Stripe 82 Survey (VICS82; Geach et al. (2017)) to better constrain stellar masses. For this work, we cross-match all DECam/SHELA galaxies within $3''$ of the VISTA J and K_s-band data. Future work will focus on utilizing forced photometry technique with *Tractor* code to provide more sophisticated DECam$+J+K_s+$IRAC multiwavelength catalog.

The VISTA J and K_s photometry from the VICS82 Survey covered $\sim 70\%$ of the total SHELA survey area. The near-infrared waveband is more sensitive for probing older stellar population, which typically dominated the stellar mass content of galaxies, and we have tested that including the J and K_s photometry in SED fitting significantly improve our stellar mass measurements. We therefore exclude $\sim 30\%$ of galaxies which do not have flux measurements in the VISTA bands from our sample.

6.4 Stellar Mass Estimates

In this section, we present a set of stellar mass (M_*) estimated based on nine bands photometric data set (DECam $ugriz$, VISTA J, K_s, and IRAC 3.6 and 4.5 μm) and study the systematic offsets that arise when we use different priors of star formation history and stellar population synthesis models. In Section 6.6, we will show how the offsets in M_* translate into systematics in the recovered stellar mass functions.

For the following analysis, we adopt the stellar mass completeness limit derived using the limiting VISTA/Ks-band magnitude of 21.4 AB mag (80$\%$ complete) because we include the

VISTA bands into our SEDs fitting procedure. We present the full details of the stellar mass completeness estimation in Chapter 5 (Figure 5.4).

6.4.1 Stellar Mass Estimate from *FAST*

We use the stellar masses for our SHELA sample by fitting Bruzual & Charlot 2003 models with *FAST* (Kriek et al., 2009) (see Chapter 5). We assume Chabrier (2003) initial mass function, exponentially declining star formation histories with timescale τ, fixed solar metallicity and a dust law as described in Calzetti et al. (2000). We denote stellar mass estimated using *FAST* based on Bruzual & Charlot (2003) model as $M_{*,\mathrm{FAST}}^{\mathrm{BC03}}$.

6.4.2 Stellar Mass Estimates from *iSEDfit*

We also estimate M_* ($M_{*,\mathrm{iSED}}$) using the Bayesian *iSEDfit* package presented in Moustakas et al. (2013). *iSEDfit* code performs a refined grid search of the posterior distributions of stellar mass and enable priors with nonflat probability distributions. In addition, *iSEDfit* code provides stellar mass estimates from multiple stellar population synthesis models, including Flexible Stellar Population Synthesis (FSPS Conroy & Gunn, 2010a,b), Bruzual & Charlot 2003, and Maraston 2005 models. We summarize the key aspects of *iSEDfit* code below.

The basic set of *iSEDfit* priors is based only a set (randomly generated for each run of *iSEDfit*) of 10,000 declining exponential models. The parameters for each *iSEDfit* model vary independently, and it is therefore good at sampling the range of each prior. We adopt fiducial prior parameters for $M_{*,\mathrm{iSED}}$ from Moustakas et al. (2013). In brief, we allow the *iSEDfit* age t (time for the onset of star formation) of each model to range with equal probability between $0.1 - 13$ Gyr. We draw the exponential τ from the the linear range $0.1 - 5$ Gyr. We assume a uniform prior on stellar metallicity Z in the range of $0.004 - 0.03$. For the stellar masses based on Bruzual & Charlot 2003 and FSPS (Conroy & Gunn, 2010a,b) models, we assume Chabrier 2003 initial mass function. For the stellar masses based on Maraston 2005 model, we assume Kroupa 2001 initial mass function. Finally, we adopt the time-dependent attenuation curve of Charlot & Fall (2000), in which stellar populations older than 10 Myr are attenuated by a factor of μ times less than younger stellar populations. As in Moustakas et al. (2013), we draw μ from an order four Gamma distribution that range from zero to unity centered on a typical value $\langle\mu\rangle = 0.3$.

The $M_{*,\mathrm{iSED}}$ estimates additionally include a prescription for bursts. Following the similar study by Bundy et al. (2017), we add stochastic bursts randomly to the star formation histories (SFHs). For every 2 Gyr interval over the lifetime of a given model, the cumulative probability that a burst occurs is $P_{\mathrm{burst}} = 0.2$. Each burst's SFH is in the form of Gaussian as a function of time, with an amplitude of F_b, defined as the total amount of stellar mass formed in the burst divided by the underlying mass of the smooth SFH at the burst's peak time. The F_b is drawn from the range of 0.03-4.0. The allowed burst duration ranges from 0.03 to 0.3 Gyr.

In Table 6.1, we list several $M_{*,\mathrm{iSED}}$ runs we performed. We discuss the impact of the resulting stellar mass estimates (M_*) on the derived mass function in Section 6.6.

6.4.3 The Comparison Between Stellar Mass Estimates from *iSEDfit* and *FAST*

In Figure 6.1, we track the difference between stellar masses estimated using *iSEDfit* and *FAST*, based on the same photometric data set but different priors of star formation history and stellar population synthesis models. We find that the median offset between the stellar mass estimated from both SED fitting codes are $\sim 0.13 - 0.27$ dex, with the scatter of $\sim 0.17 - 0.22$. These differences are more evident for lower-mass galaxies.

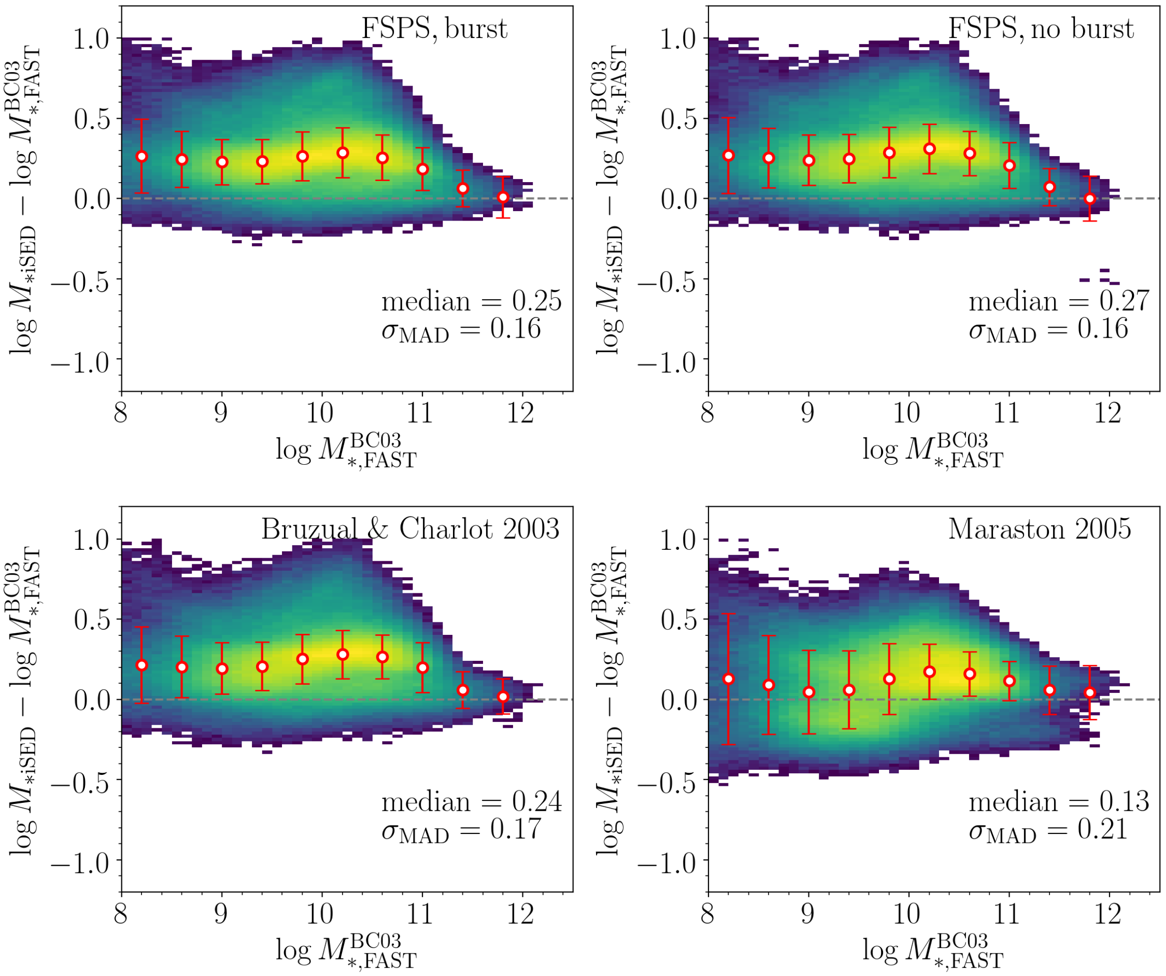

Figure 6.1: Comparison of stellar masses derived using *iSEDfit* vs. stellar masses derived from *FAST*

Comparison of M_* derived using *iSEDfit* with different SFH prior assumptions and stellar population synthesis model vs. stellar masses derived from *FAST* based on Bruzual & Charlot 2003 model, assuming fixed solar metalicity. The σ_{MAD} denotes 1.48 times the median absolute deviation of the different between stellar masses derived using *iSEDfit* and stellar masses derived from *FAST*.

Table 6.1: Stellar mass estimates

Name	Models	Main Priors	Bursts
$M_{*,\mathrm{FAST}}^{\mathrm{BC03}}$	Bruzual & Charlot 2003	Fixed solar metallicity (Chapter 5)	none
$M_{*,\mathrm{iSED}}^{\mathrm{FSPS,\ burst}}$	FSPS (Conroy & Gunn, 2010a)	PRIMUS (Moustakas et al., 2013)	$P_{\mathrm{burst}} = 0.2$
$M_{*,\mathrm{iSED}}^{\mathrm{FSPS,\ no\ burst}}$	FSPS (Conroy & Gunn, 2010a)	PRIMUS (Moustakas et al., 2013)	none
$M_{*,\mathrm{iSED}}^{\mathrm{BC03}}$	Bruzual & Charlot 2003	PRIMUS (Moustakas et al., 2013)	none
$M_{*,\mathrm{iSED}}^{\mathrm{Ma05}}$	Maraston 2005	PRIMUS (Moustakas et al., 2013)	none

6.5 Methods: Galaxy Stellar Mass Function

Random errors in the stellar mass estimates (M_*) introduce Eddington bias in the derived galaxy stellar mass functions due to the steep decline in the number of galaxies at the massive end. Because there are many more intrinsically lower-mass galaxies subject to random M_* errors, the contamination from these lower-mass galaxies scattering upward outweighs the downscattering of the higher-mass galaxies. As a result, the scatter in M_* inflates the observed galaxy stellar mass function at the high-mass end. The bias in the stellar mass estimates is expected to evolve with redshift because of the decreasing in signal-to-noise ration with increasing redshift. The observed evolution of the galaxy stellar mass function could be biased by not accounting for the Eddington bias (e.g., Fontanot et al., 2009; Moster et al., 2013).

We account for a varying Eddington bias by assuming an intrinsic shape of a galaxy stellar mass function and forward-model the data while accounting for the estimated stellar mass uncertainty. To do that, we first assume a double Schechter function (Baldry et al., 2008) of the form

$$\phi(M_*) = (\ln 10)\exp\left[-\frac{M_*}{M^*}\right] \times \left\{\phi_1 10^{(\alpha_1+1)(\log M_* - \log M^*)} + \phi_2 10^{(\alpha_2+1)(\log M_* - \log M^*)}\right\}, \quad (6.1)$$

where $\alpha_2 < \alpha_1$ and the second term dominates at the low-mass end. We refer to "knee" or characteristic stellar mass of the stellar mass function as M^*, which marks the stellar mass above which the stellar mass function declines exponentially.

We generate Monte Carlo realizations of this function that sample various parameters ranges as described below. We add scatter in stellar mass estimates drawn from a Gaussian distribution with the width of the distribution equals to the 1σ uncertainty stellar mass arising from SED fitting, $\sigma_{M_*}(\log M_*, z)$, which is stellar mass- and redshift-dependent quantity.

We do not constrain the normalization ϕ_1 and ϕ_2 of the double Schechter function. Instead, we define the parameters $\lambda_{\rm mix}$ and $1 - \lambda_{\rm mix}$ to indicate the relation between of the first term and the second term of the double Schechter form, respectively. We then evaluate the normalization factor of the the stellar mass function of mock sample $\phi(M_{*,\rm mock})$ such that the comoving number density of mock galaxies n_{mock}

$$n_{\mathrm{mock}} = C \int_{\log M_{*\mathrm{min}}}^{\log M_{*\mathrm{max}}} \phi_{\mathrm{mock}}(M_*) d \log M_*, \tag{6.2}$$

equal to the observed comoving number density of SHELA galaxies, n_{SHELA}. We then bin the mock samples identically to the data. Finally, we constrain the input parameters by comparing the mock stellar mass functions with the observed one in an iterative approach.

6.6 Results

6.6.1 Assumption-averaged Estimate of the Stellar Mass Function

We define the "assumption-averaged" stellar mass function from the average[1] of results from five different sets of M_* estimates: $M_{*,\mathrm{FAST}}^{\mathrm{BC03}}$ (Bruzual & Charlot 2003 models, assuming fixed solar metallicity), $M_{*,\mathrm{iSED}}^{\mathrm{FSPS,burst}}$ (FSPS with bursts; Conroy & Gunn 2010a,b), $M_{*,\mathrm{iSED}}^{\mathrm{FSPS,no\ burst}}$ (FSPS, no bursts), $M_{*,\mathrm{iSED}}^{\mathrm{BC03}}$ (Bruzual & Charlot 2003 model, no bursts), and $M_{*,\mathrm{iSED}}^{\mathrm{Ma05}}$ (Maraston 2005 model, no bursts). These five estimates encompass the range of M_* values obtained by adopting currently uncertain priors. The assumption-averaged result represents a compromise among differing approaches.

In Figure 6.2, we show the observed galaxy stellar mass function in each redshift bin defined as $z = [0.3, 0.4], [0.4, 0.5], [0.5, 0.6], [0.6, 0.7], [0.7, 0.8], [0.8, 0.9], [0.9, 1.0]$ with shaded regions corresponding to the Poisson errors. We indicate the stellar mass completeness limit of $\log M_*/M_\odot = 10.5$ at $z = 1.0$ with vertical dotted line. We present number of galaxy sample and the corresponding stellar mass completeness at each redshift bin in Table 6.2.

We further perform forward-modeling the observed galaxy stellar mass function in each redshift bin to account for Poisson errors and uncertainties in stellar mass estimates arising from SED fitting (σ_{M_*}). We assume these uncertainties to be Gaussian and add in quadrature for a given bin of redshift and stellar mass.

---

[1] In practice, we compute the average number density by binning concatenated array of five different sets of M_* estimates and dividing by five times the corresponding volume of each redshift slice.

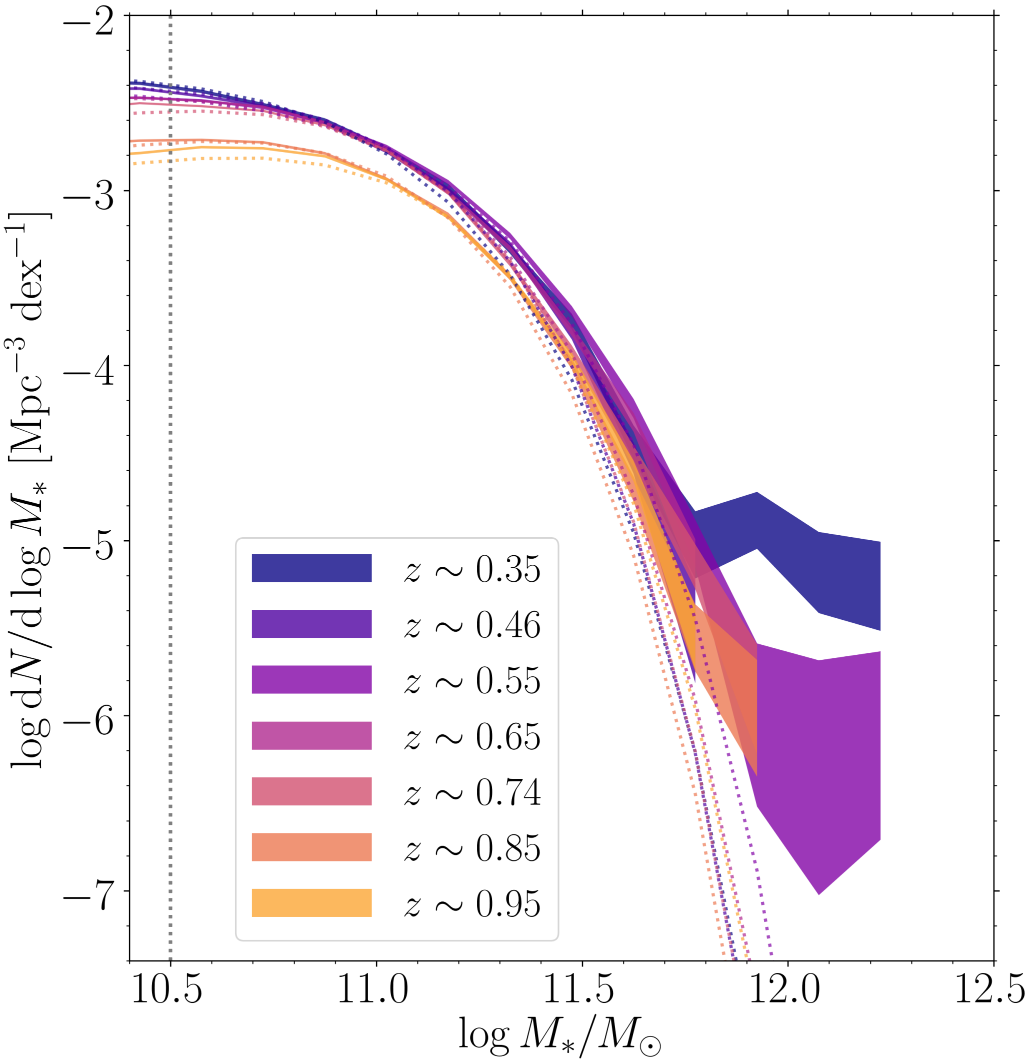

Figure 6.2: Assumption-averaged estimated of SHELA galaxy stellar mass function at $0.3 < z < 1.0$.

Stellar mass functions (SMF) estimated from combining five separate stellar mass estimators using different assumptions in star formation history and stellar population synthesis models: $M_{*,\mathrm{FAST}}^{\mathrm{BC03}}$ (Bruzual & Charlot 2003 models, assuming fixed solar metallicity), $M_{*,\mathrm{iSED}}^{\mathrm{FSPS,burst}}$ (FSPS with bursts; Conroy & Gunn 2010a,b), $M_{*,\mathrm{iSED}}^{\mathrm{FSPS,no\ burst}}$ (FSPS, no bursts), $M_{*,\mathrm{iSED}}^{\mathrm{BC03}}$ (Bruzual & Charlot 2003 model, no bursts), and $M_{*,\mathrm{iSED}}^{\mathrm{Ma05}}$ (Maraston 2005 model, no bursts). Shaded regions indicate Poisson error. The estimated stellar mass completeness is indicated by a vertical dotted line at $\log M_*/M_\odot = 10.50$. Forward modeling results, which aim to account for (and thereby remove) biases caused by scatter in stellar mass measurement, are shown as dotted curves. The intrinsic models from forward modeling can vary from run to run with a scatter consistent with the error bars indicated on the raw SMFs because the modeling involves random draws from estimated error distribution of stellar mass measurement. We detect no ($\lesssim 0.1$ dex) redshift evolution at the high-mass end ($\log M_*/M_\odot > 11.0$) of the SMF over $0.3 < z < 1.0$.

For the modeling, we assume the double Schechter form described in Section 6.5 (Equation 6.1). We allow M^*, α_1, α_2, and $\lambda_{\rm mix}$ to vary. We present the intrinsic stellar mass function shape parameters from forward modeling in Table 6.2.

In Figure 6.2, we also show a set of intrinsic fitted stellar mass function where the scatter in stellar mass measurement has been accounted for as dotted lines with redshift-dependent colors. The intrinsic models can vary from run to run with a scatter consistent with the error bars indicated on the observed stellar mass functions because the forward-modeling involves random draws from estimated error distributions of stellar masses (σ_{M_*}).

To quantify the observed (lacked of) evolution in the SMF, we first present the evolution of characteristic stellar mass (M^*) resulting from the forward-modeling of the assumption-average mass function (Figure 6.3). Within the systematic uncertainty due to the different stellar mass estimators, we detect no redshift evolution in the typical stellar mass ($\lesssim 0.1$ dex) from $z = 1.0$ to $z = 0.3$ for massive galaxies with $\log M_*/M_\odot > 11.0$ even after accounting for the bias caused by random errors in stellar mass measurement (i.e., Eddington bias).

Second, we derive the cumulative number density of galaxies with stellar mass greater than $10^{11}\ M_\odot$ by integrating the intrinsic stellar mass function inferred from the forward modeling,

$$n(> 10^{11}\ M_\odot) = \int_{10^{11}\ M_\odot}^{10^{12.5}\ M_\odot} \phi(M_*) dM_*. \tag{6.3}$$

We note that the cumulative number density is less sensitive to the degeneracy between the characteristic stellar mass M^* and other derived Schechter parameters. In Figure 6.3 we plot the cumulative number density of galaxies with stellar mass greater than $10^{11}\ M_\odot$.

Table 6.2: Intrinsic mass function shape parameters from forward modeling

Redshift	N_{gal}	$\log(M_{limit}/M_\odot)$	$\log(\phi_1/\mathrm{Mpc}^{-3}\mathrm{dex}^{-1})$	$\log(\phi_2/\mathrm{Mpc}^{-3}\mathrm{dex})$	$\log(M^*/M_\odot)$	α_1	α_2
$[0.3, 0.4]$	16114	9.74	-2.10	-3.05	$10.76^{+0.04}_{-0.03}$	-0.60 ± 0.17	-1.45 ± 0.10
$[0.4, 0.5]$	21928	9.96	-2.21	-2.58	$10.72^{+0.02}_{-0.01}$	-0.12 ± 0.08	-1.25 ± 0.08
$[0.5, 0.6]$	23336	10.12	-2.22	-2.82	$10.85^{+0.02}_{-0.02}$	-0.50 ± 0.08	-1.30 ± 0.08
$[0.6, 0.7]$	24810	10.24	-2.27	-3.22	$10.78^{+0.01}_{-0.03}$	-0.45 ± 0.05	-1.25 ± 0.08
$[0.7, 0.8]$	23992	10.35	-2.36	-3.32	$10.72^{+0.02}_{-0.06}$	-0.15 ± 0.17	-1.25 ± 0.08
$[0.8, 0.9]$	16219	10.44	-2.54	-3.50	$10.70^{+0.03}_{-0.02}$	-0.02 ± 0.08	-1.25 ± 0.08
$[0.9, 1.0]$	15700	10.50	-2.63	-3.58	$10.76^{+0.04}_{-0.02}$	-0.05 ± 0.12	-1.25 ± 0.08

N_{gal} denotes the number of galaxies with stellar mass between $M_{limit} < M_*/M_\odot < 10^{12.5}$ at a given redshift bin. The error reported here for each of the derived Schechter parameters is from the forward modeling fits to the assumption-averaged stellar mass functions.

To better compare the relative evolutionary trend, we normalized the cumulative number density of galaxy with mass $\log M_*/M_\odot > 11.0$ at each redshift bin to that at $z = 0.3$ (Figure 6.4). The assumption-average mass function suggests no more than a $\lesssim 0.1$ dex increase in the cumulative number density of these massive galaxies over $z = 1.0$ to $z = 0.3$. In the following section, we further explore the impact of the difference in star formation history priors and stellar population synthesis models on the stellar mass functions and their redshift evolution.

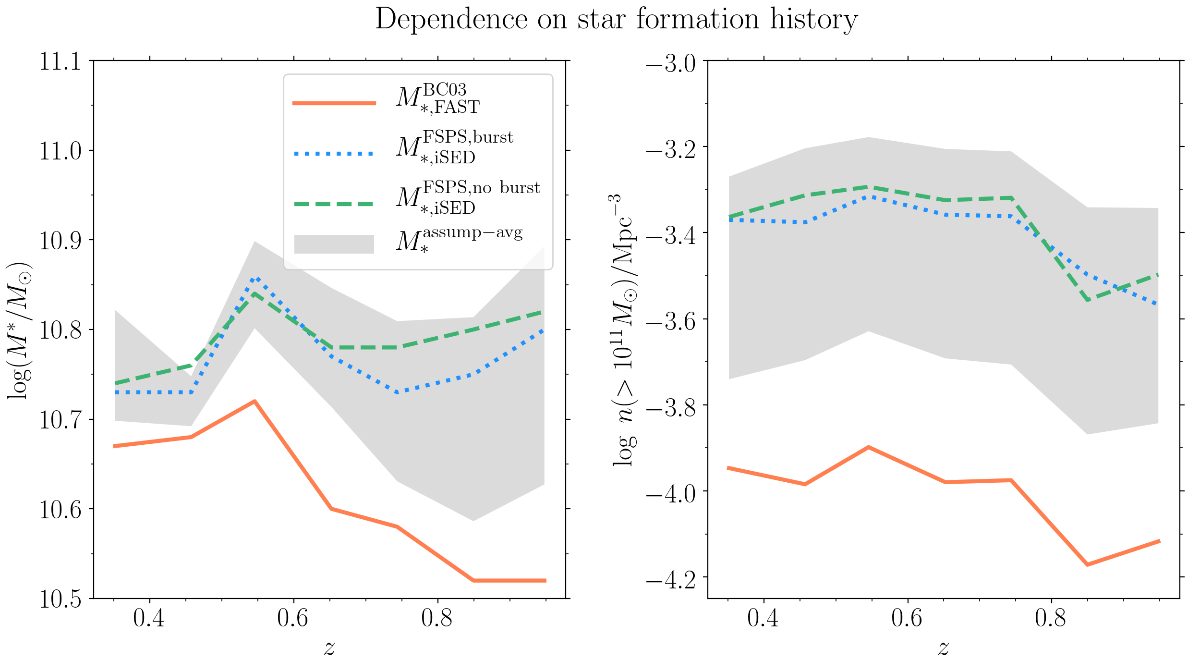

Figure 6.3: The evolution of galaxy stellar mass functions derived using three M_* estimators with different SFH prior assumptions.

Left: the redshift evolution of the characteristic stellar mass (M^*) of galaxy stellar mass function (SMF) resulting from the forward-modeled SMF for three M_* estimates as indicated in each plot. ***Right:*** the redshift evolution of the cumulative comoving space density of galaxies more massive than $10^{11}\ M_\odot$ resulting from integrating each of the forward-modeled stellar mass function. In each panel, the grey shaded region show the result from the assumption-averaged stellar mass function (Figure 6.2) and the 1σ confidence region over all five M_* estimators we use to compute the assumption-averaged SMF. We find that the individual evolutionary trends are generally consistent with one another at the $\pm 1\sigma$ level, except for the stellar mass derived using the $M_{*,\mathrm{FAST}}^{\mathrm{BC03}}$ assuming Bruzual & Charlot 2003 model with fixed solar metallicity, which exhibits an increase in the characteristic stellar mass by ~ 0.2 dex and a lower overall number density over the redshift range. Given the systematic uncertainty due to the different stellar mass estimators, we detect no redshift evolution in either the typical stellar mass (M^*) or the cumulative number density of massive galaxies ($> 10^{11}\ M_\odot$) from $z = 1.0$ to $z = 0.3$ even after accounting for the bias caused by random errors in stellar mass measurement.

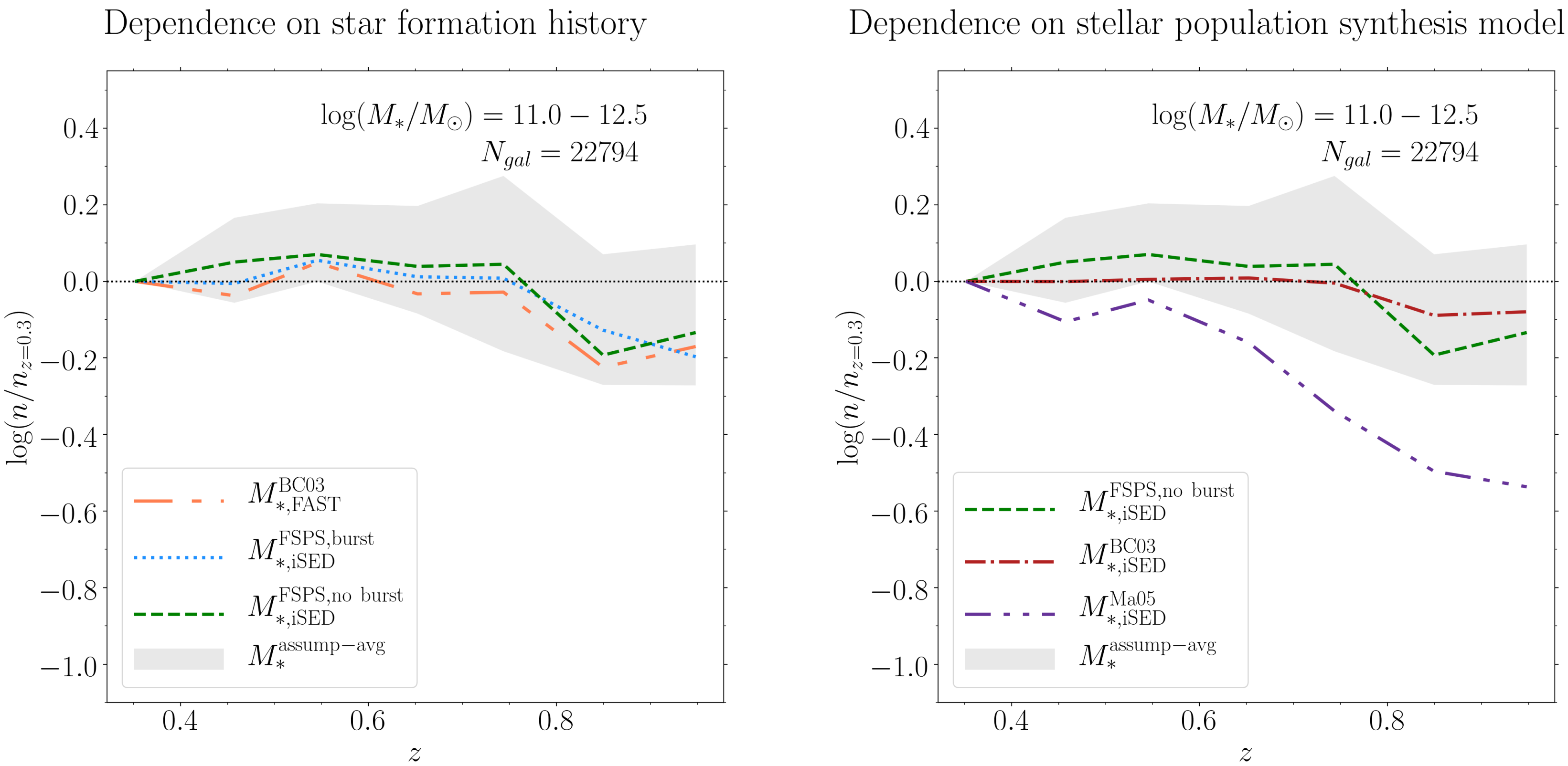
Dependence on star formation history

Dependence on stellar population synthesis model

Figure 6.4: Evolution of number density of galaxies more massive than 10^{11} $M_\odot$ vs. redshift

Left: the redshift evolution of the number density for galaxies more massive than 10^{11} $M_\odot$ resulting from the forward-model fits of the stellar mass functions with different assumptions in star formation history (SFH). Each relation has been normalized by the number density at $z = 0.3$ to compare the relative evolutionary trend. The grey shaded region shows the result from the assumption-averaged stellar mass function (Figure 6.2) and the 1σ confidence region over all five M_* estimators we use to compute the assumption-averaged SMF. ***Right:*** similar to the left panel but for a set of different stellar population synthesis (SPS) models. The individual evolutionary trends are generally consistent with one another at the $\pm 1\sigma$ level, except for the stellar mass derived using Maraston 2005 model without bursts ($M_{*,\mathrm{iSED}}^{\mathrm{Ma05}}$), which exhibits an increase in the number density of massive galaxies with decreasing redshift ($\lesssim 0.5$ dex). Overall, given the systematic uncertainty due to the different assumptions in SFH and SPS models, we detect no evolution ($\sim 11\%$) in the cumulative number density of galaxies more massive than 10^{11} $M_\odot$ at a given redshift relative to those at $z = 0.3$.

6.6.2 Dependence on Star Formation History Priors

In the previous section, we derive galaxy stellar mass functions by averaging all different sets of M_* measurements that include different assumptions on the star formation history (SFH) and stellar synthesis models. Within the systematic uncertainty due to the different stellar mass estimators, we detect no redshift evolution in either the characteristic stellar mass (M^*) or the cumulative number density of massive galaxies ($\log(M_*/M_\odot) > 11$) over $0.3 < z < 1.0$ even after accounting for the Eddington bias. In this section, we further investigate mass functions derived using specific sets of M_* measurements.

In Figure 6.5, we show galaxy stellar mass functions derived using three M_* estimators with different SFH prior assumptions: $M_{*,\mathrm{FAST}}^{\mathrm{BC03}}$, $M_{*,\mathrm{iSED}}^{\mathrm{FSPS,\ burst}}$, $M_{*,\mathrm{iSED}}^{\mathrm{FSPS,\ no\ burst}}$. The stellar mass function based on $M_{*,\mathrm{FAST}}^{\mathrm{BC03}}$, assuming fixed solar metallicity, exhibits a ~ 0.2 dex increase in characteristic mass (Figure 6.3). The trend is milder for the stellar mass derived from ***iSEDfit***, based on FSPS and including bursts ($M_{*,\mathrm{iSED}}^{\mathrm{FSPS,burst}}$) and based on FSPS but no bursts are allowed ($M_{*,\mathrm{iSED}}^{\mathrm{FSPS,no\ burst}}$).

In Figure 6.4 we show the comoving number density of massive galaxies ($> 10^{11}M_\odot$) normalized to that at $z = 0.3$. Over $0.3 < z < 1.0$, the normalized comoving number density of massive galaxies for each SFH prior is generally consistent within $\pm1\sigma$ level ($\sim 0.02-0.1$ dex; Figure 6.4). While we leave a detailed investigation of the role of specific prior in star formation history, we conclude that the number density of galaxies more massive than 10^{11} $M_\odot$ does not evolve since $z = 1.0$ to $z = 0.3$, at least among the sets of SFH priors adopted in this study.

6.6.3 Dependence on Stellar Population Synthesis Models

In Figure 6.6 we evaluate how three choices for the stellar population models underlying M_* estimates from ***iSEDfit*** impact the derived stellar mass functions, and constraints on the growth of massive galaxies. In all cases, we compare models without bursts. We show again the FSPS $M_{*,\mathrm{iSED}}^{\mathrm{FSPS,no\ burst}}$ stellar mass function in the left panel. We show the stellar mass functions based on Bruzual & Charlot 2003 masses ($M_{*,\mathrm{iSED}}^{\mathrm{BC03}}$, middle panel) and Maraston 2005 masses ($M_{*,\mathrm{iSED}}^{\mathrm{Ma05}}$, right panel). The different stellar population synthesis models lead to different trends in terms of

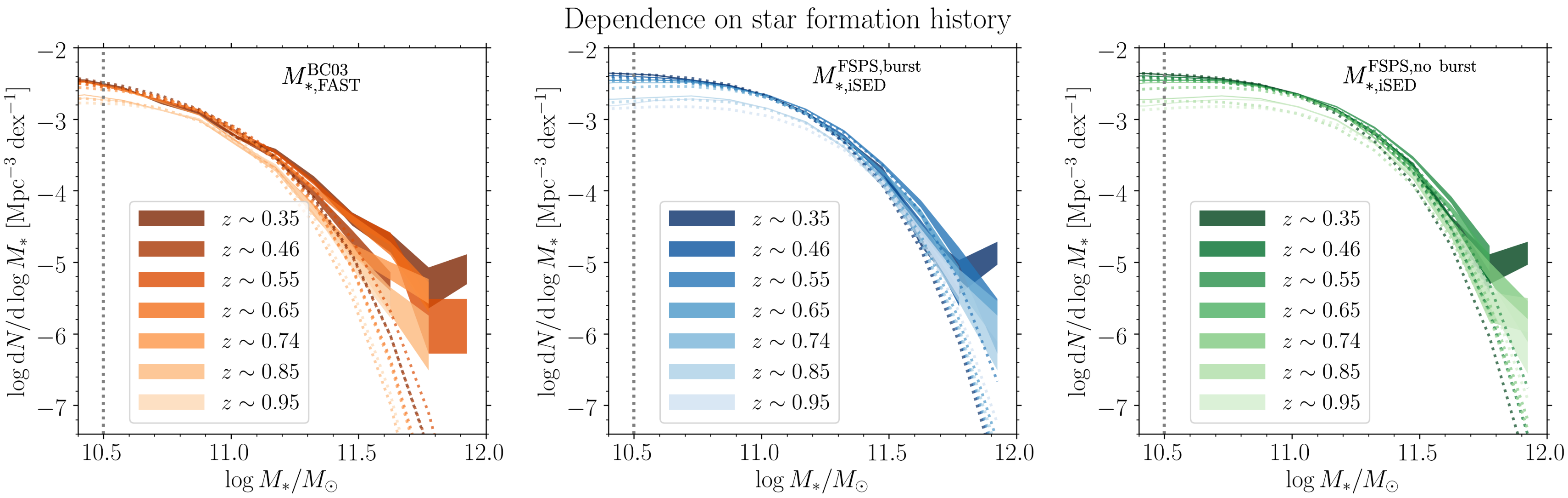

Figure 6.5: Stellar mass functions obtained using three M_* estimators with different assumptions in star formation history (SFH).

The left panel correspond to stellar mass estimates from *FAST* assuming Bruzual & Charlot 2003 model with fixed solar metallicity ($M_{*,\mathrm{FAST}}^{\mathrm{BC03}}$). The resulting mass function suggests no more than a $\lesssim 0.2$ dex increase in the average number density of massive galaxies (at fixed stellar mass) over the redshift range plotted. The trend is milder for the stellar mass derived from *iSEDfit*, based on FSPS and including bursts ($M_{*,\mathrm{iSED}}^{\mathrm{FSPS,burst}}$; middle panel) and based on FSPS but no bursts are allowed ($M_{*,\mathrm{iSED}}^{\mathrm{FSPS,no\ burst}}$; right panel). Forward-modeling results, which aim to account for (and thereby remove) biases caused by errors in the stellar mass, are shown as dotted curves in each panel.

the redshift of evolution of both characteristic mass (M^{*}) of stellar mass function and comoving number density of galaxies with stellar mass $> 10^{11} M_{\odot}$.

The stellar mass function based on Maraston 2005 masses ($M_{*,\mathrm{iSED}}^{\mathrm{Ma05}}$) exhibits a ~ 0.3 dex increase in characteristic mass (Figure 6.7). The trend is milder for the stellar mass derived from *iSEDfit*, based on Bruzual & Charlot 2003 masses ($M_{*,\mathrm{iSED}}^{\mathrm{BC03}}$) and based on FSPS but no bursts are allowed ($M_{*,\mathrm{iSED}}^{\mathrm{FSPS,no\ burst}}$).

We derive the cumulative number density of massive galaxies ($> 10^{11} M_{\odot}$) normalized to that at $z = 0.3$ for each stellar population synthesis model (Figure 6.4). At $z < 0.8$ we find almost no evolution in the cumulative number density of massive galaxies with stellar mass $> 10^{11} M_{\odot}$ based on two mass estimates from *iSEDfit*: Bruzual & Charlot 2003 and FSPS (without bursts). On the other hand, we find 0.5 dex increase in the number density of massive galaxies based on Maraston (2005) masses.

Again, a detailed investigation of the role of specific stellar population synthesis model is beyond the scope of this work, and we conclude from Figure 6.4 (right panel) that systematic uncertainties arising from the choice of stellar population synthesis model contribute 0.1-0.3 dex to the error budget in the growth of the characteristic stellar mass of massive galaxies, which we determined from the combined assumption-average mass function. In addition, at least among the set of stellar mass estimates used here, the difference in stellar population synthesis models are more important than priors on the star formation history in inferring conclusions about the average growth rate in the massive galaxy population.

6.6.4 Dependence on Galaxy Stellar Mass

We further quantify the evolution in the stellar mass function based on different SFH prior in various stellar mass bins. In Figure 6.8, we plot versus redshift the number density of galaxies in four mass bins with stellar mass between $10^{10.4} - 10^{12.5}\ M_{\odot}$ at each redshift bin normalized to those at $z = 0.3$. Figure 6.8 and Figure 6.9, we show the evolutionary trend for a set of different priors in star formation history (SFH) and a set of different stellar population synthesis (SPS) models, respectively.

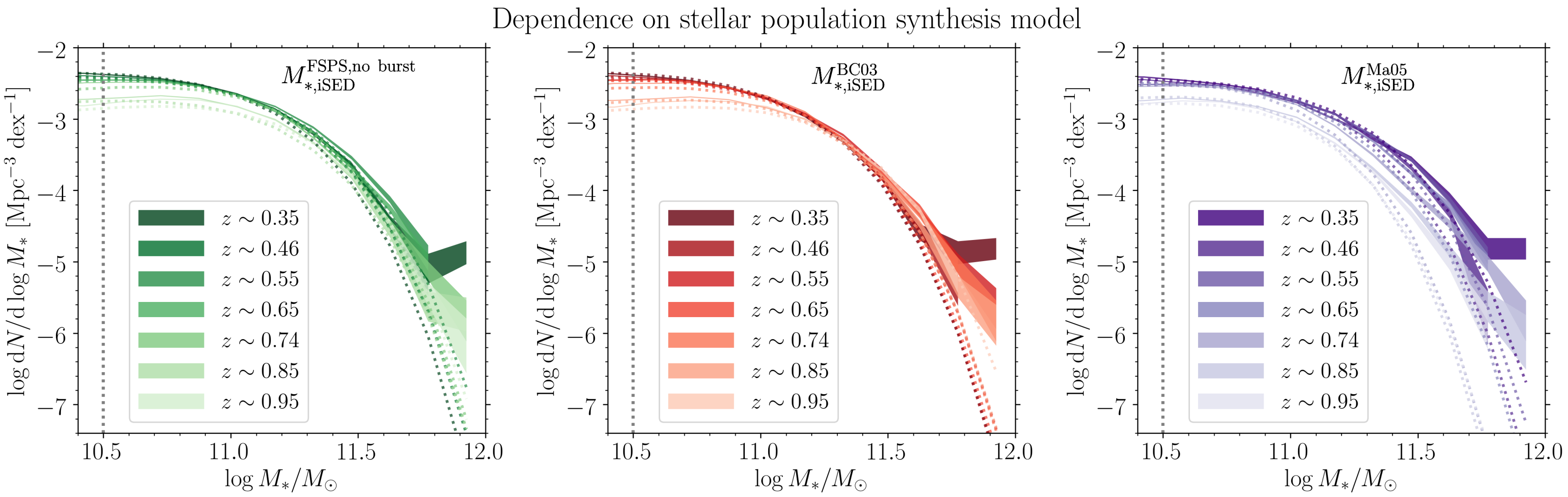

Figure 6.6: Stellar mass functions obtained using three M_* estimators with different stellar population synthesis models.

All panels use the stellar masses estimated from *iSEDfit*, based on the same SFH priors and without bursts. We compare $M_{*,\mathrm{iSED}}^{\mathrm{FSPS,no\ burst}}$ (left panel), $M_{*,\mathrm{iSED}}^{\mathrm{BC03}}$ (middle panel), $M_{*,\mathrm{iSED}}^{\mathrm{Ma05}}$ (right panel). Forward-modeling results, which aim to account for (and thereby remove) biases caused by errors in the stellar mass, are shown as dotted curves in each panel.

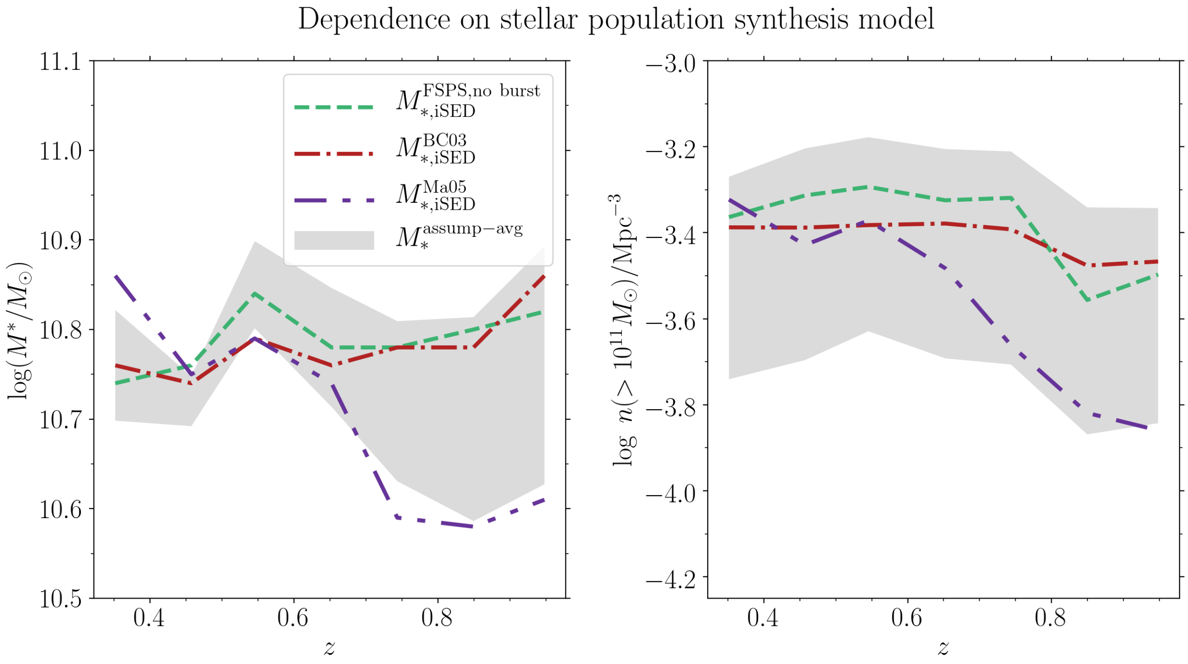

Figure 6.7: The evolution of galaxy stellar mass functions derived using three M_* estimators with different stellar population synthesis models.

Left: the redshift evolution of the characteristic stellar mass (M^*) of galaxy stellar mass function resulting from the forward-modeled SMF for three estimators M_* with different stellar population synthesis models. ***Right:*** the redshift evolution of the cumulative comoving space density of galaxies more massive than $10^{11}\ M_{\odot}$ resulting from the forward-modeled SMF for three estimators M_*. In each panel, the grey shaded region shows the result from the assumption-averaged stellar mass function (Figure 6.2) and the 1σ confidence region over all five M_* estimators we use to compute the assumption-averaged SMF.

The number density of galaxies in all four mass bins does not appear to change significantly over the range of redshift we probe where our sample is complete in stellar mass. In each stellar mass bin, the individual evolutionary trends are consistent with one another at the $\pm 1\sigma$ level regardless of the the choice of SFH priors and stellar popular synthesis models (Figure 6.8 and Figure 6.9).

For the lowest-mass galaxy sample ($10^{10.4} - 10^{10.7}\ M_{\odot}$), we find a $\lesssim 0.15$ dex increase in the number density from $z = 1.0$ to $z = 0.3$. Galaxies with stellar mass between $10^{10.7} - 10^{11.3}\ M_{\odot}$, at $z = 1.0$ to $z = 0.8$, the number density of galaxies exhibits ~ 0.2 dex growth, with no evidence for additional growth in number density from $z = 0.8$ to $z = 0.3$.

For the most massive galaxy sample ($10^{11.3} - 10^{12.5}$ $M_{\odot}$), there is a weak evidence of $\sim$ 0.25 dex increasing in the number density from $z = 1.0$ to $z = 0.5$. However, given the large uncertainty in our data, mainly driven by the stellar mass estimates using $M_{*,\mathrm{FAST}}^{\mathrm{BC03}}$ with Bruzual & Charlot 2003 model assuming solar metallicity and $M_{*,\mathrm{iSED}}^{\mathrm{Ma05}}$ with Maraston 2005 model (no burst), we do not interpret this trend of increasing in the number density of the most massive galaxies ($10^{11.3} - 10^{12.5}$ $M_{\odot}$) to be meaningful.

Overall, regardless of the choice of SFH priors and stellar popular synthesis models used in this study, there is no evidence for evolution in the number density of massive galaxies with stellar mass of $10^{10.7} - 10^{12.5}$ $M_{\odot}$, from $z = 0.8$ to $z = 0.3$.

In addition, the higher relative number density of the lowest-mass systems ($10^{10.4} - 10^{10.7}$ $M_{\odot}$) compared to those of more massive galaxies could also be hints of mass assembly downsizing – the preferred site of star formation activity has migrated from massive systems at high redshift to low mass systems at low redshift, usually referred to as the downsizing effect (Cowie et al., 1996; Juneau et al., 2005). This finding is qualitatively consistent with previous studies (e.g., Fontana et al., 2006; Pozzetti et al., 2007, 2010; Bundy et al., 2017).

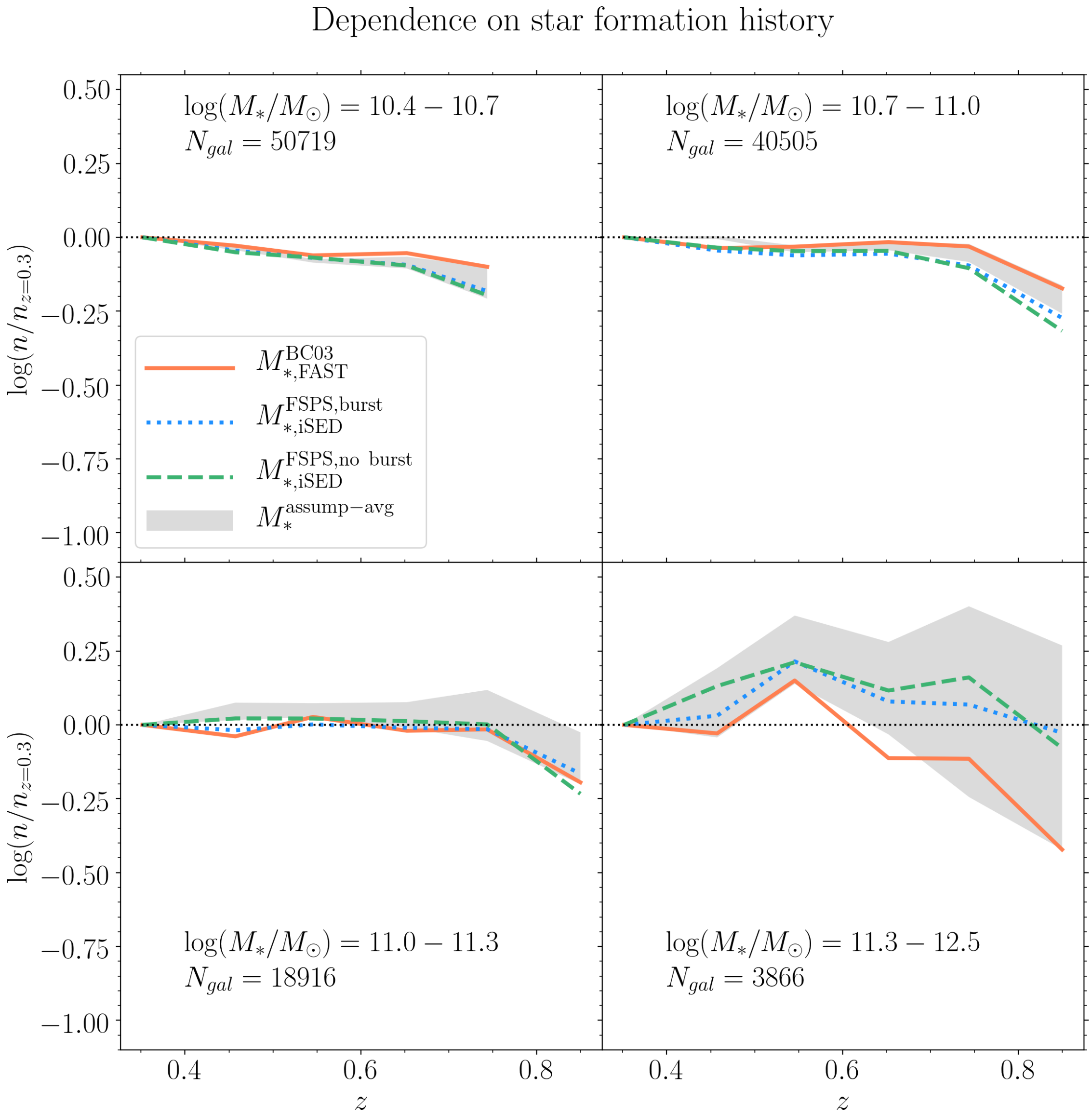

Figure 6.8: The relative number density of galaxies in four bins of stellar mass between $10^{10.4} - 10^{12.5}$ $M_\odot$ based on different assumptions in star formation history vs. redshift.

For each stellar mass estimate based on different assumptions in SFH, we show the redshift evolution of the relative number density of galaxies with stellar mass ranging from $10^{10.4} - 10^{10.8}$ $M_\odot$ (top left), $10^{10.7} - 10^{11.0}$ $M_\odot$ (top right), $10^{11.0} - 10^{11.3}$ $M_\odot$ (bottom left) and $10^{11.3} - 10^{12.5}$ $M_\odot$ (bottom right). Each relation has been normalized by the number density at $z \sim 0.3$. In each panel, the grey shaded region shows the result from the assumption-averaged stellar mass function (Figure 6.2) and the 1σ confidence region over all five M_* estimators we use to compute the assumption-averaged SMF. At each stellar mass bin, the individual evolutionary trends are generally consistent with one another at the $\pm 1\sigma$ level. For the lowest-mass galaxy sample ($10^{10.4} - 10^{10.7}$ $M_\odot$), we find a $\sim 40\%$ increasing in the number density from $z = 1.0$ to $z = 0.3$. The number density of more massive galaxies with stellar mass of $10^{10.7} - 10^{12.5}$ $M_\odot$ does not significantly change since $z = 0.8$ to $z = 0.3$.

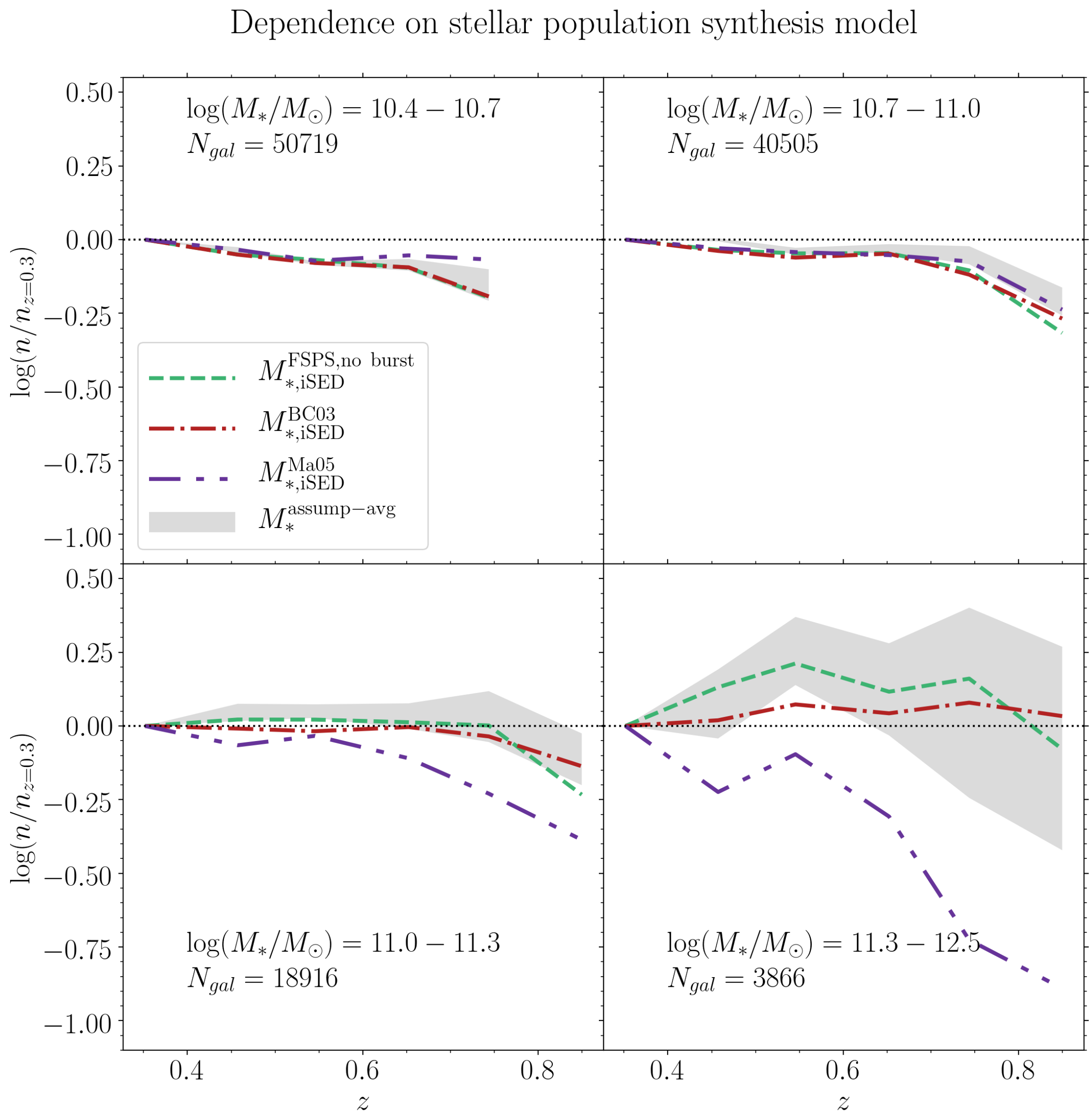

Figure 6.9: The relative number density of galaxies in four bins of stellar mass between $10^{10.4} - 10^{12.5}$ $M_\odot$ based on different stellar population synthesis models vs. redshift.

For each stellar mass estimate based on different stellar population synthesis models, we show the redshift evolution of the relative number density of galaxies with stellar mass ranging from $10^{10.4} - 10^{10.8}$ $M_\odot$ (top left), $10^{10.7} - 10^{11.0}$ $M_\odot$ (top right), $10^{11.0} - 10^{11.3}$ $M_\odot$ (bottom right) and $10^{11.3} - 10^{12.5}$ $M_\odot$ (bottom left). Each relation has been normalized by the number density at $z \sim 0.3$. In each panel, the grey shaded region show the result from the assumption-averaged stellar mass function (Figure 6.2) and the 1σ confidence region over all five M_* estimators we use to compute the assumption-averaged SMF. At each stellar mass bin, the individual evolutionary trends are generally consistent with one another at the $\pm 1\sigma$ level. However, for massive galaxies with $\log(M_*/M_\odot) > 11.0$, the stellar mass derived using Maraston 2005 model without bursts ($M_{*,\mathrm{iSED}}^{\mathrm{Ma05}}$), exhibits a steeper increase in the number density of massive galaxies with decreasing redshift.

6.6.5 Dependence on Galaxy Star Formation Activity

In the previous sections we measured the evolution of the SMF for the global population of galaxies from $z = 0.3 - 1.0$. We found no significant change in both the characteristic stellar mass and the cumulative number density of galaxies more massive than $10^{11}\ M_{\odot}$. There is evolution at lower stellar masses. One explanation for this different growth is that a higher fraction of the lower mass galaxies are still star-forming (and therefore the number density of galaxies at fixed stellar mass grows with time). We therefore explore the evolution in the stellar mass function for galaxies that are star-forming and those that are quiescent. To make this classification, we use median of the star formation rate (SFR) posteriors reported by *iSEDfit*, and compute the specific star formation rate (sSFR). We divide sample into quiescent and star forming galaxies using the sSFR threshold of $\mathrm{sSFR} = 10^{-10}\ \mathrm{yr}^{-1}$ (Bezanson et al., 2018).

In Figure 6.10, we show the assumption-averaged estimate of galaxy stellar mass functions for quiescent and star forming galaxies, and our forward modeling result. For quiescent galaxies, we do not detect growth ($\lesssim\ 0.1$ dex) in the typical stellar mass at fixed number density since $z = 1.0$ to $z = 0.3$ for massive quiescent galaxies with stellar mass $\gtrsim 10^{11}\ M_{\odot}$. For star forming population, we find moderate growth of $\sim\ 0.2$ dex in the typical stellar mass from $z = 1.0$ to $z = 0.4$ overall stellar mass range.

Figure 6.10 also shows that, over $0.3 < z < 1.0$, we find that the population of massive galaxies ($\log M_*/M_{\odot} > 11$) are dominated by quiescent population. We expect some mass loss from stellar evolution, and that needs to be balanced by mass growth, presumably from mergers. In the next section, we discuss the implication of our finding on the rate mass growth for these massive galaxies through merging.

6.7 Discussion

6.7.1 On the Lack of Evolution of Stellar Mass Function of Massive Galaxies

The most significant systematic errors we have studied so far are the redshift-dependent biases in stellar mass estimates under different assumptions for both star formation history and stellar

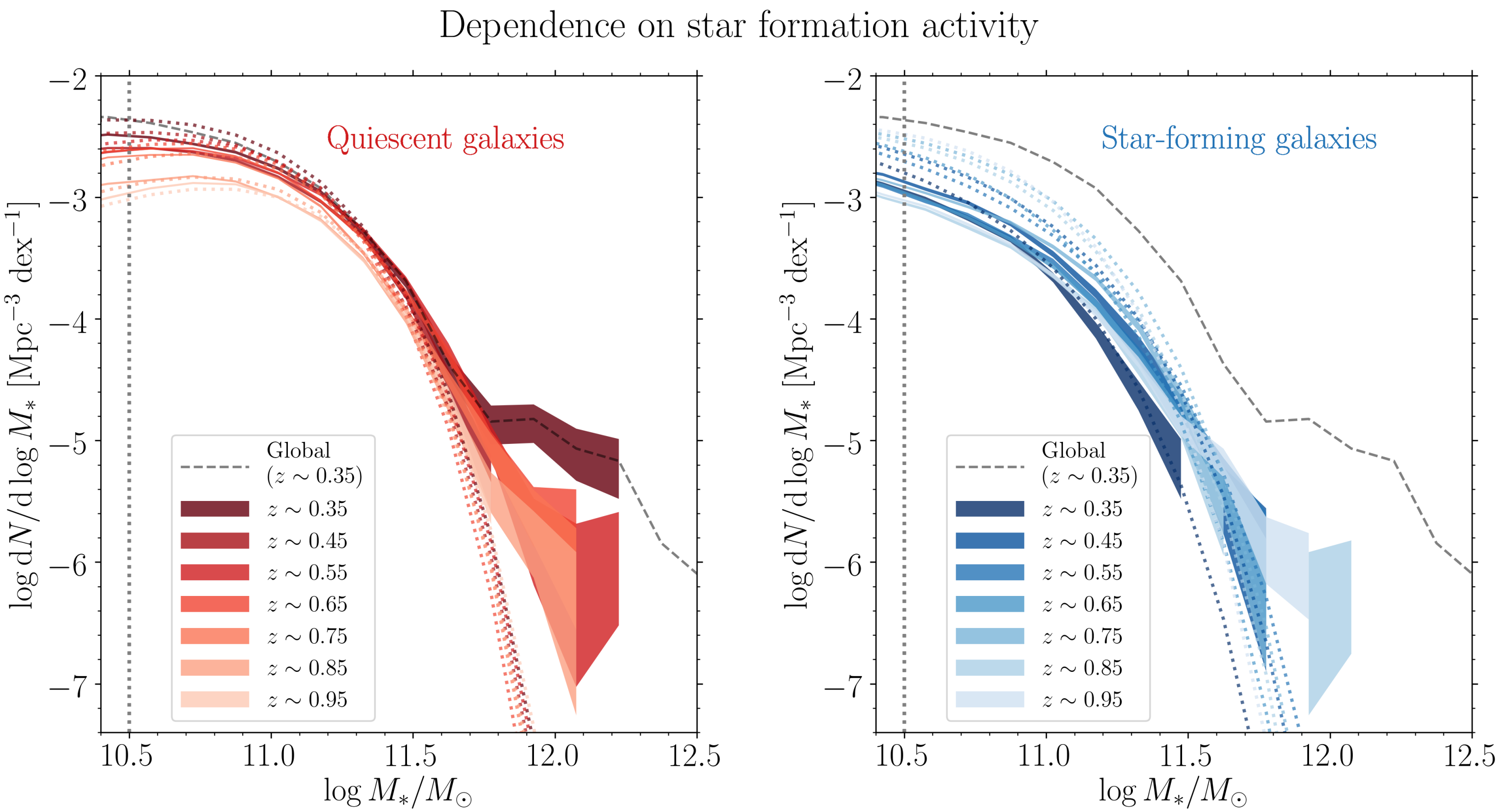

Figure 6.10: Assumption-averaged estimated of SHELA galaxy stellar mass function with different star formation activity.

The assumption-average stellar mass functions estimated from combining five stellar mass estimators: $M_{*,\mathrm{FAST}}^{\mathrm{BC03}}$ (Bruzual & Charlot 2003 model, assuming solar metallicity), $M_{*,\mathrm{iSED}}^{\mathrm{FSPS,burst}}$ (FSPS with bursts; Conroy & Gunn 2010a,b), $M_{*,\mathrm{iSED}}^{\mathrm{FSPS,no\ burst}}$ (FSPS, no bursts), $M_{*,\mathrm{iSED}}^{\mathrm{BC03}}$ (Bruzual & Charlot 2003 models, no bursts), and $M_{*,\mathrm{iSED}}^{\mathrm{Ma05}}$ (Maraston 2005 models, no bursts) for quiescent (left panel) and star formation galaxies (right panel). Shaded regions indicate Poisson error. The estimated stellar mass completeness is indicated by a vertical dotted line at $\log M_*/M_\odot = 10.5$. Forward-modeling results, which aim to account for (and thereby remove) biases caused by scatter of stellar mass measurement, are shown as dotted curves. The population of massive galaxies ($\gtrsim 10^{11}\ M_\odot$) are dominated by quiescent galaxies, which exhibits no growth ($\lesssim 0.1$ dex) in the typical stellar mass at fixed number density since $z = 1.0$ to $z = 0.3$. In contrast, the star-forming population shows moderate growth of ~ 0.2 dex in the typical stellar mass over the same redshift range.

population synthesis models. Of the five different M_* we combine in our assumption-averaged mass functions, the $M_{*,\mathrm{FAST}}^{\mathrm{BC03}}$ assuming Bruzual & Charlot 2003 with fixed solar metallicity (used alone) indicates an increase in the characteristic stellar mass by ~ 0.2 dex over the redshift range. The $M_{*,\mathrm{iSED}}^{\mathrm{Ma05}}$ assuming Maraston 2005 model indicates even larger mass growth (~ 0.3 dex). On the other hand, the $M_{*,\mathrm{iSED}}^{\mathrm{FSPS,burst}}$ and the $M_{*,\mathrm{iSED}}^{\mathrm{FSPS,no\ burst}}$, and $M_{*,\mathrm{iSED}}^{\mathrm{BC03}}$ indicates no evolution in the typical stellar mass. Therefore, when we average the results from the different stellar mass estimates, we take the scatter as an estimate on the systematic uncertainty, which is about 0.05 dex. With that, our analysis is consistent with no growth (at < 0.1 dex) in the typical stellar mass of massive galaxies over $0.3 < z < 1.0$, with an systematic uncertainty of about 12% arising from differences in stellar mass measurements (and the systematic uncertainty dominates).

According to the two-phase formation scenario for the formation of massive galaxies (e.g., Oser et al., 2010, 2012), the mass assembly of massive galaxies at late times are dominated by minor mergers (e.g., Hilz et al., 2013; Oogi & Habe, 2013; Bédorf & Portegies Zwart, 2013; Laporte et al., 2013). We also expect some mass loss of quiescent galaxies from stellar evolutionary processes. The lack of observed evolution in the SMF of massive galaxies indicating a balance between build-up of stellar mass through mergers and mass loss due to stellar evolution process.

We can estimate the rate at which these massive galaxies grow by mergers at this late epoch. To estimate the fraction of the stellar mass created via star formation that will be lost due to stellar evolution processes, we follow the approach by Moster et al. (2013). We employ the following formula of the fraction of mass lost, $f_{\mathrm{loss}}(t)$ by a stellar evolution with an age t, resulting from parametrizing the mass loss of a stellar population with a Chabrier (2003) initial mass function as developed by Bruzual & Charlot (2003)

$$f_{\mathrm{loss}}(t) = 0.05 \ln \left(\frac{t + 3 \times 10^5 \mathrm{year}}{3 \times 10^5 \mathrm{year}} \right) \tag{6.4}$$

For example, this relation implies that 40% of stellar mass is lost within 1 Gyr and 50% within 10 Gyr. The redshift range probed in this study of $0.3 < z < 1.0$ corresponds to $t = 4.3$ Gyr and $f_{\text{loss}}(t) = 48\%$. Therefore, the amount of mass loss is expected to be 48%. For mergers to balance this mass loss, then the upper limit on the amount of mass growth from mergers is also 48% ($\simeq 0.17$ dex).

6.7.2 Comparison to Other Studies

Our estimate of mass growth by mergers is in good agreement with a study by van Dokkum et al. (2010) who used stacking analysis to study the mass growth of massive galaxies with a constant number density of 2×10^{-4} Mpc^{-3}, corresponding to galaxy with stellar mass of $3 \times 10^{10}\ M_{\odot}$. At $0.6 < z < 0.1$, van Dokkum et al. found ~ 0.1 dex mass growth for massive galaxies. In addition, Marchesini et al. (2014) used the UltraVISTA catalogs to investigate the evolution of the progenitors of local ultra-massive galaxies ($\log(M_*/M_{\odot}) \approx 11.8$; UMGs). They selected the progenitors with the semi-empirical approach using abundance matching, and found a growth in stellar mass of $0.27^{+0.08}_{-0.12}$ from $z = 1$ to $z = 0$ after including the scatter in the progenitor's number density in the error budget. Marchesini et al. also found that the half of the assembled stellar mass of local UMGs are primarily by merging over this redshift range. Our infer stellar mass growth and that of Marchesini et al. (2014) is consistent within the uncertainty.

Ownsworth et al. (2014) presented a study on the stellar mass growth of the progenitors of massive galaxies with $M_* = 10^{11.24} M_{\odot}$ at $z = 0.3$, and showed that the progenitors of these massive galaxies grow by a factor of 2 (~ 0.3 dex) in total stellar mass since $z = 1.0$. They also found that, on average, major and minor mergers account for the mass assembled to galaxies at $z = 0.3$ by $\sim 17\%$ and $\sim 34\%$, respectively. The slightly discrepancy between our inferred mass growth by mergers and that from the Ownsworth et al. (2014) and might be probably arising from the SED-modeling assumptions and the correction for the Eddington bias.

Our finding can be directly compared with the recent study by Bundy et al. (2017), who followed a similar analysis as we have here. Bundy et al. (2017) detected no growth (with an uncertainty of 9%) in the typical stellar mass of massive galaxies ($\log(M^*/M_{\odot}) > 11.3$) from $z = 0.65$ to $z = 0.3$ in S82-MGC. Our analysis is consistent with that of Bundy et al., and we extend this to hold for galaxies to higher redshift $z < 1$ and lower stellar masses ($\log(M^*/M_{\odot}) = 10.5$).

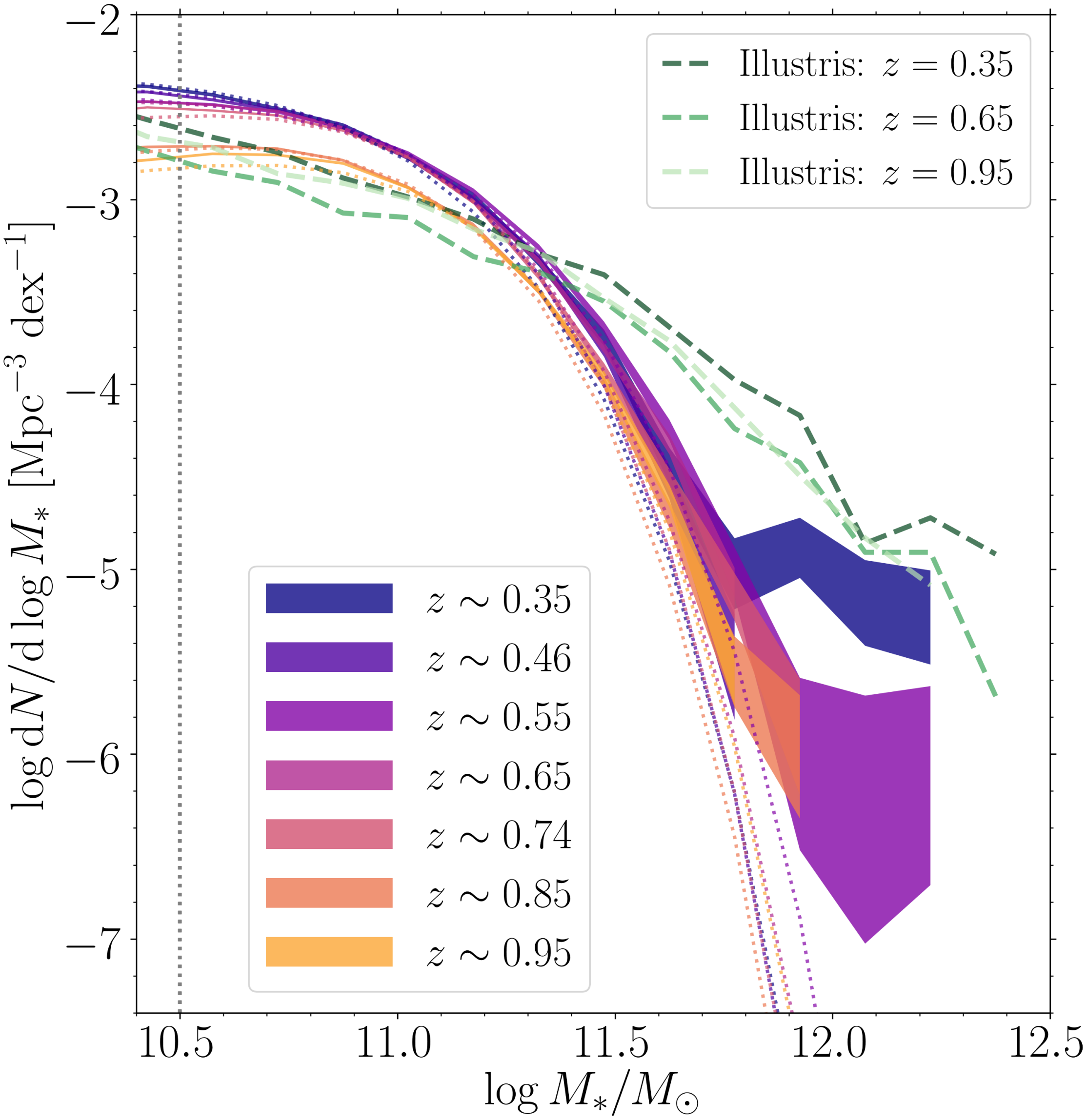

Figure 6.11: The comparison of stellar mass functions from the Illustris, a cosmological hydrodynamical simulation and our observational results.

The comparison between stellar mass functions for galaxies from the Illustris simulation (green dashed curves) and from our SHELA galaxy sample. We reproduce our assumption-averaged stellar mass function results from Figure 6.2, with shaded regions indicating the raw number densities and associated error ranges and the dotted lines representing the forward-model fitting results after accounting for measurement scatter. The Illustris simulation predicts ~ 0.2 dex growth in stellar mass at fixed number density, which we do not observe based on the assumption-averaged SMF. Global offsets in either the typical stellar mass (M_*) or the normalization of the SMF from the simulation and observation are expected (see discussion in Bundy et al., 2017), and we are particularly interested in the internal redshift evolution.

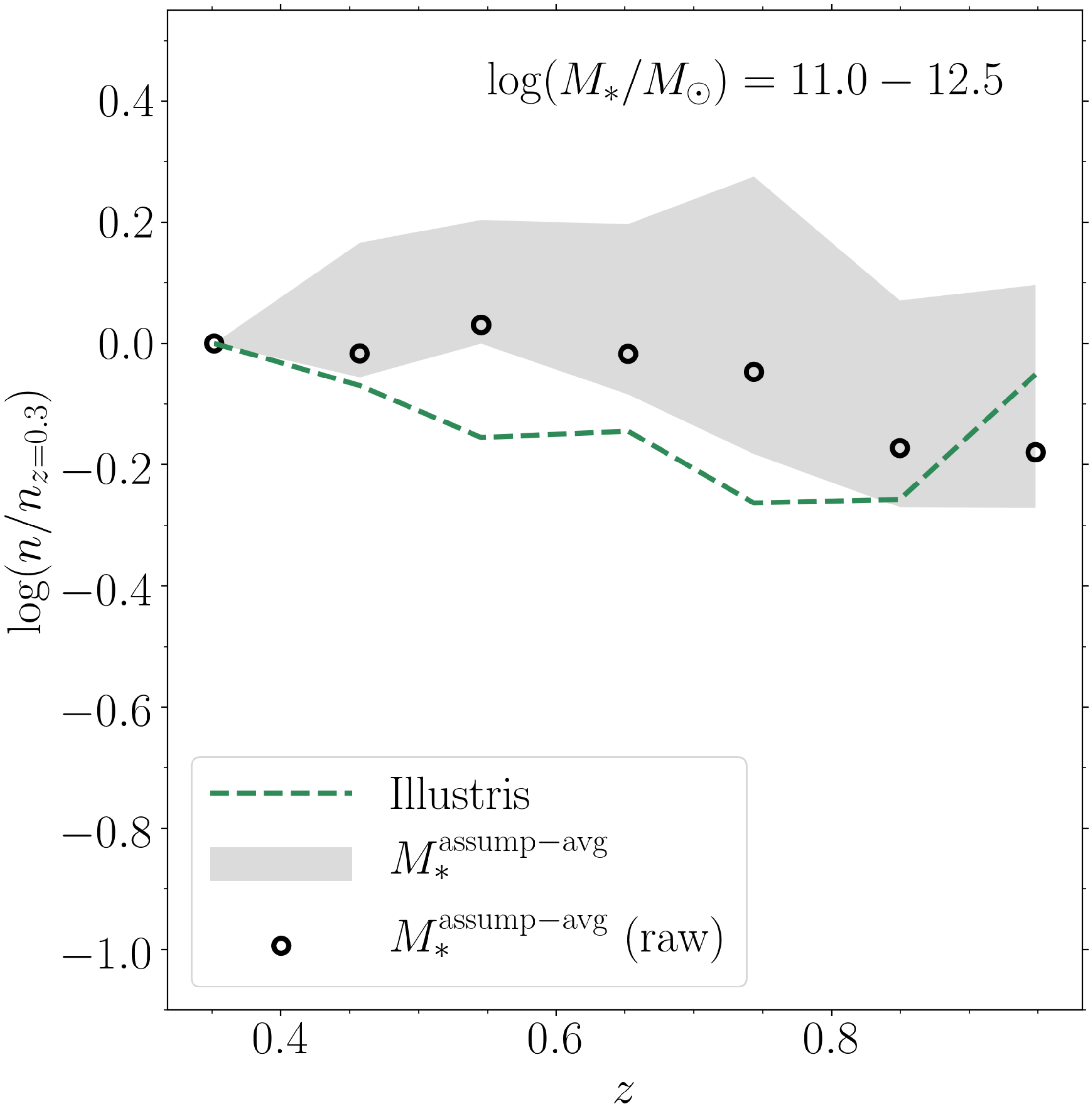

Figure 6.12: The comparison of the relative number density from the Illustris, a cosmological hydrodynamical simulation and our observational results.

The comparison between the relative number density of galaxies from the Illustris simulation (green dashed line), from the forward-model fits of the assumption-average stellar mass functions (gray shaded region), and from the raw mass functions (black open circles). Each relation has been normalized by the number density at $z \sim 0.3$ as shown in Figure 6.4. The grey shaded region shows the result from the assumption-averaged stellar mass function (Figure 6.2) and the 1σ confidence region over all five M_* estimators we use to compute the assumption-averaged SMF. The Illustris simulation predicts 0.2 dex growth in the number density from $z = 0.8$ to $z = 0.3$, which we do not observe based on the assumption-averaged SMF.

Moutard et al. (2016) presented an analysis on the evolution of the stellar mass function from redshift $z = 0.2$ to $z = 1.5$ of a $K_s < 22$-selected sample, and over an effective area of ~ 22.4 deg^2, similar to our study here. They also used the forward modeling approach to account for scatter in stellar mass measurement. Moutard et al. showed that the number density of the most massive galaxies ($\log(M_*/M_\odot > 11.5$) increases by a factor of ~ 2 from $z \sim 1$ to z 0.3. They also demonstrated that the quiescent population largely dominates of massive galaxies population since $z \sim 1$, and in agreement with our result here that the massive galaxies assemble their stellar masses through mergers.

Finally, our result of lack of evolution ($\sim 11\%$) in the cumulative number density of galaxies more massive than $M_* > 10^{11}$ $M_\odot$ since $z = 1$ to $z = 0.3$ is in agreement with the result of Moustakas et al. (2013), who find a $\lesssim 10\%$ change in the number density of all $M_* > 10^{11}$ $M_\odot$ galaxies since $z \approx 1$, based on the 5.5 deg^2 PRIsm MUlti-object Survey (PRIMUS Coil et al., 2011). It is interesting that when Moustakas et al. (2013) divided their sample into quiescent and star-forming galaixes, they found that above $\sim 10^{11} M_\odot$, the number density of quiescent galaxies change relatively little since $z = 1$, and the most significant evolutionary trends for star formatin galaxies occurs above $\sim 10^{11} M_\odot$. Again, this is in agreement with our finding.

6.7.3 Comparison to Theoretical Predictions

We present a comparison of the SHELA stellar mass functions to theoretical results from the Illustris, the recent cosmological hydrodynamical simulation, in Figure 6.11. We reproduce from Figure 6.2 the raw number counts from the assumption-averaged SHELA mass function with associated error bars indicated by shaded regions, as well as fits from forward modeling the raw results. For a comparison to the Illustris simulation results, we obtain the stellar assembly catalog for the Illustris-1 simulation (Rodriguez-Gomez et al., 2015, 2016). This stellar assembly catalog contains information about the stellar assembly of all galaxies across all snapshots. We use the total stellar mass of the galaxy in each snapshot corresponding to $z = 0.35, 0.65, 0.95$, and construct stellar mass function as we do for our SHELA mass function. We note that the global offsets in either the typical stellar mass (M_*) or the normalization of the SMF from the simulation and observation are expected (see discussion in Bundy et al., 2017), and we are particularly interested in the internal redshift evolution.

To better compare the SMF from the Illustris simulation with our SHELA SMF in terms of the evolution of number density of massive galaxies, we also compute the number density of galaxies with mass of $10^{11.0} - 10^{12.5}\ M_\odot$ at each redshift and normalize to that at $z = 0.3$ (Figure 6.12). For SHELA sample, we show the relative number density computed from both the forward-modeling fitted to the assumption-average SMF and raw number density without forward modeling. The Illustris simulation predicts a $\sim 20\%$ increasing in the number density of galaxies at these masses from redshift $z \sim 0.95$, which are not detected in our data (based on the assumption-average SMF).

7. SUMMARY AND CONCLUSIONS

In this thesis, I have contributed to the body of knowledge on the properties of galaxies across broad range of environments and cosmic time. I addressed several outstanding questions in the field: (1) How properties of host galaxies (such as stellar mass and star formation activity) are related to the mass of their dark matter halos at $1 < z < 3$? (2) How satellite quenching depends on the star formation activity of the central galaxies? (3) How galactic star formation activity depend on environment and stellar mass over $0.5 < z < 1.0$? and (4) Is there any evolution in the stellar mass of massive galaxies over $0.3 < z < 1.0$? and what does this mean for galaxy growth through the mergers of satellites? These questions were the focus of this thesis, and I summarize below the results of each chapter.

7.1 The Distribution of Satellites around Massive Galaxies at $1 < z < 3$

First, in Chapter 2 I have studied the statistical distribution of satellites around star-forming and quiescent central galaxies at $1 < z < 3$ using imaging from ZFOURGE and CANDELS. The deep near-IR data allow me to select satellites down to $\log(M/\mathrm{M}_{\odot}) > 9$ at $z < 3$. The results from this chapter can be summarized as follows.

I found that the projected radial number density of satellites around centrals with stellar mass $\log(M/\mathrm{M}_{\odot}) > 10.48$ is consistent with a projected NFW profile.

Furthermore, I found that the number density of satellites significantly depends on the stellar mass of the central galaxies. The most massive central galaxies ($\log(M/\mathrm{M}_{\odot}) > 10.78$) have $\sim$ 1.6 times the number of satellites within 100 kpc compared to intermediate mass centrals ($10.48 < \log(M_{\mathrm{c}}/\mathrm{M}_{\odot}) < 10.78$), which is significant at $\simeq 1.9\sigma$.

For the most massive galaxies, $\log(M/\mathrm{M}_{\odot}) > 10.78$, quiescent centrals have ~ 2 times the number of satellites within 100 kpc compared to star-forming centrals (significant at $\simeq 3.1\sigma$). This excess persists at 2.7 sigma significance even when I account for differences in the centrals' stellar mass distributions. In contrast, I found no statistical difference in the satellite distributions of less-massive quiescent and star-forming centrals, $10.48 < \log(M/\mathrm{M}_{\odot}) < 10.78$.

I interpreted the number density of satellites in my data using the semi-analytic model of Guo et al. (2011) from the lightcone made available by Henriques et al. (2012). I found that quiescent galaxies in the model also have more satellites than star-forming galaxies of similar stellar mass. By matching the halo masses of the star-forming and quiescent samples, I demonstrate that the difference in satellite content in the simulation is due almost entirely to differences in halo mass. I interpret this as evidence that the differences in satellite content observed in the data is driven by a difference in halo mass, and conclude that — at stellar masses $\log(M/\mathrm{M}_{\odot}) > 10.78$ — the halos that host quiescent galaxies are ~ 0.3 dex more massive than the halo that host star-forming galaxies.

In addition, I used a simple model to investigate the relationship between quenching and halo mass, which roughly reproduces the observed quenched fractions and the differences in halo mass between star-forming and quenched galaxies in the two stellar mass bins. The model suggests a scenario where galaxies have some probability of being quenched over roughly two decades in halo mass, $\log(M_h/\mathrm{M}_{\odot}) \sim 11 - 13.5$, where the probability increases with mass. This wide mass range suggests that, while halo mass quenching may be an important mechanism at $1 < z < 3$, halo mass is not the only factor driving quiescence. It remains unclear why some central galaxies in relatively massive halos can keep forming stars.

7.2 Satellite Quenching and Galactic Conformity at $0.3 < z < 2.5$

Second, Chapter 3 I have studied the quiescent fraction ($f_{q,sat}$) and quenching efficiency ($\epsilon_{q,sat}$) of satellites around star-forming and quiescent central galaxies with $\log(M_{\mathrm{cen}}/\mathrm{M}_{\odot}) > 10.5$ at $0.3 < z < 2.5$. I use data from three different deep near-IR surveys ZFOURGE/CANDELS, UDS, and UltraVISTA that span different ranges of depth and area in order to achieve significant volume at lower redshifts as well as sufficient depth for high redshift measurements. The deep near-IR data allow us to select satellites down to $\log(M/\mathrm{M}_{\odot}) > 9.3$ at $z < 2.5$. The results from this chapter can be summarized as follows.

I found that satellite galaxies, $9.3 < \log(M_{\mathrm{sat}}/\mathrm{M}_{\odot}) < 10.2$ at $0.3 < z < 2.5$ are more quenched compared to mass-matched samples of field galaxies.

Galactic conformity exists at $0.3 < z < 2.5$: while the satellites of star-forming central galaxies are quenched in excess of field galaxies, the satellites of quiescent centrals are quenched at an even higher rate. There is a strong conformity signal at $0.6 < z < 0.9$ (4.5σ) and at $0.9 < z < 1.6$ (3.5σ), whereas the conformity in the lowest and highest redshifts bins, $0.3 < z < 0.6$ and $1.6 < z < 2.5$, is less significant. This may be a real physical effect, or may be due to insufficient statistics. Regardless, conformity is not a recent effect, but has been present for a significant fraction of the age of the universe — conformity may even be as old as satellite-quenching itself.

A comparison between the quenching efficiency of intermediate-mass centrals ($10.5 < \log(M_{\rm cen}/{\rm M}_{\odot}) < 10.8$) and high-mass centrals ($\log(M_{\rm cen}/{\rm M}_{\odot}) > 10.8$) indicates that satellite quenching depends on the stellar mass of the central, in that satellites around more massive centrals have a higher quenching efficiency. This appears to be true for both star-forming and quiescent centrals.

The existence of galactic conformity is observed for both low mass ($9.3 < \log(M_{\rm sat}/{\rm M}_{\odot}) < 9.8$) and high mass satellites ($9.8 < \log(M_{\rm sat}/{\rm M}_{\odot}) < 10.2$) around centrals of all masses and redshifts (with the possible exception of the highest mass satellites at the highest redshifts $1.6 < z < 2.5$, and the lowest mass satellites at the lowest redshifts $0.3 < z < 0.6$, where the statistics are poorer). There is no significant evidence that satellite quenching depends on the stellar mass of the satellites.

Furthermore, I tested if galactic conformity is due to a difference in the typical halo mass of star-forming and quiescent centrals by selecting star-forming centrals with ~ 0.2 dex higher stellar mass. This difference should be enough to eliminate any difference in halo mass between my quiescent and star-forming samples. From this test I found that the difference in halo mass can explain most of the conformity signal in the ZFOURGE data. However, there still remains evidence for conformity, particularly at $0.6 < z < 0.9$. This suggests that satellite quenching is connected to the star-formation properties of the central, beyond the mass of the halo.

While halo mass may be a significant (even dominant) driver of conformity, it does not appear to explain all of the conformity signal. I have discussed other physical effects that may account for the existence and evolution of the conformity signal, including hot gas halos, feedback effects, halo assembly history, and large-scale environment – and I have discussed some of the issues involved with these explanations.

7.3 Effect of local environment and stellar mass on galaxy quenching and morphology at $0.5 < z < 2.0$

Third, Chapter 4 I have studied how the local environmental density affects star-formation activity in galaxies using a mass-complete sample to $\log(M/\mathrm{M}_{\odot}) > 8.8 - 9.5$ from deep near-IR ZFOURGE survey at $z = 0.5 - 2.0$. I measured galaxy overdensities using a Bayesian-motivated estimate of the distance to the third nearest neighbor, where the precise photometric redshifts from ZFOURGE ($\sigma_z/(1+z) \lesssim 0.02$) allow me to measure accurately the galaxies in the highest and lowest density environments. I then studied the redshift evolution and stellar mass dependence of the quiescent fraction, environmental quenching efficiency, and (stellar) mass quenching efficiency. The results from this chapter can be summarized as follows.

The quiescent fraction of galaxies increases in denser environments (greater overdensity). This star-formation-density relation can be traced to at least to $z \sim 2.0$, and for galaxies with $\log(M/\mathrm{M}_{\odot}) > 9.5$. I showed that the star-formation-density relation is not simply the result of a mass-density relation combined with a mass-star-formation relation: even at fixed mass, there is a higher quiescent fraction of galaxies in denser environments, although the significance of this effect is weaker at $z > 1.5$.

Both the environmental quenching efficiency and the (stellar) efficiency evolve with redshift. I observed minimal environmental effects at $z \gtrsim 1.5$ ($\lesssim 5\%$) for low-mass galaxies ($\log(M/\mathrm{M}_{\odot}) < 9.5$), but the strength of environmental quenching increases at later times, eventually dominating over the mass quenching process, particularly at these lower stellar masses.

For more massive galaxies ($\log(M/\mathrm{M}_{\odot}) > 9.5$), the environmental quenching efficiency is already significant at high redshift: at $z \sim 2$ it is already $\sim 30\%$ in the highest densities and remains roughly constant as a function of redshift to $z \sim 0$. For these massive galaxies, (stellar) mass quenching and environmental quenching are comparable in high-density environments.

The environmental quenching efficiency depends on stellar mass at high redshift, $z > 1$, and *the effects of (stellar) mass quenching and environmental quenching are not separable*. The environmental quenching mechanisms, particularly for lower-mass galaxies, may be fundamentally different at low and high redshift. At high redshift, the (stellar) mass-dependence of environmental quenching is qualitatively consistent with a decline in star-formation due to the exhaustion of a gas reservoir through star formation and outflows in the absence of cosmological accretion (overconsumption). On the other hand, this overconsumption process is less efficient at low redshift, suggesting that external gas stripping process like strangulation may become more important.

Furthermore, the distribution of galaxy morphology as a function of galaxy star-formation activity shows no strong dependence (or at most a weak dependence) on environment. I found the established relation between star formation and morphology such that quiescent galaxies have higher Sérsic indices, smaller effective radii, higher axis ratios, and higher mass surface density than mass-matched samples of star-forming galaxies. I do not detect any strong environmental effect on the morphologies of quiescent galaxies (and similarly for star-forming galaxies). There is the weakest of evidence that at $0.5 < z < 1.0$ in the highest density environments quiescent massive galaxies have larger Sérsic indexes and quiescent lower-mass galaxies have larger effective radii than mass-matched quiescent galaxies in low density environments, but the evidence is minimal ($\approx 1.5 - 2\sigma$), and these conclusions are tentative.

In addition, the morphologies suggest that environmental quenching must also transform galaxy morphologies such that there is no observable difference with galaxies in the field. This is true even for lowest-mass galaxies ($\log(M/\mathrm{M}_{\odot}) = 8.8$) where I expect approximately all such quiescent galaxies to be quenched by their environment. Therefore, the environmental process responsible for quenching the galaxies also transforms their morphologies such that they no longer share the same parent distribution as mass-matched star-forming galaxies.

Finally, I argued that the redshift evolution of the mass and environmental quenching favors models that combine "starvation" (as galaxies become satellites in larger mass halos) with the exhaustion of a gas reservoir through star-formation and outflows (“overconsumption”). These models must be combined with additional processes such as galaxy interactions, tidal stripping, and disk fading to account for the morphological differences between the quenched and star-forming low-mass galaxy populations

7.4 An Application of Multi-band Forced Photometry to Dark Energy Camera Catalog for the SHELA Survey

Fourth, Chapter 5 I constructed a robust multi-band photometric catalog of the $ugriz$-band from Dark Energy Camera (DECam) plus 3.6 and 4.5 μm from *Spitzer*/IRAC for the *Spitzer*/HETDEX Exploratory Large-Area (SHELA) survey. Rather than performing cross-matching between the individual source in DECam catalog with SHELA IRAC catalog (Papovich et al., 2016), I improved upon the existing multi-band catalog of DECam $ugriz$ + Spitzer/IRAC 3.6 and 4.5 μm bands by performing a “forced photometry” with *The Tractor* image modeling code (Lang et al., 2016a,b). This technique employs prior measurements of source positions and surface brightness profiles from a high-resolution band to model and fit the fluxes of the source in the remaining bands. I specifically used *The Tractor* to optimize the likelihood for the photometric properties of DECam sources in each of IRAC 3.6 and 4.5 μm bands given initial information on the source obtained from DECam catalog and IRAC image parameters. I found that use of *The Tractor* led to the following key advantages compared to position-matched multi-band photometry.

I modeled the surface brightness profile of each source in a fiducial, high-resolution DECam band and perform forced photometry with *The Tractor*. This allows me to de-blend these objects in the *Spitzer*/IRAC images and more accurately measure 3.6 and 4.5 μm fluxes. This is naturally lead to more accurate source cross-identification. I demonstrated these improvements by estimating the lower limit of 35$\%$ of the total sources in the DECam input catalog, which will be blended in the 3.6 and 4.5μm IRAC data.

I compared the 3.6 and 4.5μm of source magnitudes from *The Tractor* forced photometry and the original IRAC photometry measured in $6''$-diameter aperture, corrected to total fluxes (Papovich et al., 2016). I found that my forced photometry is typically in good agreement though some scatter is apparent, particularly for blended sources. The scatter is reduced when I restrict the comparison to isolated sources that lack a neighbor within $4''$. For blended sources with the IRAC the aperture-corrected magnitudes brighter than 22 AB mag, I expect that the large median offset (0.45 AB mag) and scatter between the forced photometry and the IRAC the aperture-corrected magnitudes are mainly due to the ability of *The Tractor* force photometry procedure to de-blending those sources. The other contributing factors to the scatters could be spatial PSF variations, inaccurately matched sources in DECam and IRAC catalogs, and issues with the photometry from the original catalogs.

I demonstrated the utility of the multi-band photometric catalog by estimating photometric redshifts. In addition to the $ugriz$-band Dark Energy Camera (DECam) plus 3.6 and 4.5 μm IRAC catalogs, I incorporate J and K-band fluxes from VISTA-CFHT Stripe 82 Survey (VICS82) (Geach et al., 2017) for this purpose. Based on comparisons between the photometric redshifts and spectroscopic redshift from SDSS at $z < 1.0$, I found that the Tractor multi-band photometry lead to accurate photometric redshift, with $\sigma_z/(1+z) \sim 0.04$ with only 0.3% of sources found to be 5σ outliers. In the near future HETDEX will enable this analysis out to $z = 3.5$ by providing spectroscopic redshifts for a sample of $N \sim 200{,}000$ galaxies at both $z < 0.5$ and $1.9 < z < 3.5$. I plan to incorporate HETDEX spectroscopic redshifts to improve the photometric redshift measurements at higher redshift.

Finally, motivated by the photometric redshift accuracy, I used the galaxy spectral energy distribution (SED) fitting code to measure rest-frame color and stellar mass of galaxies. The stellar mass completeness limit is $M_* > 10^{10.5} M_\odot$ at $z < 1.0$. I demonstrated the utility of these derived galaxy properties by measure galaxy stellar mass function and quantify the building up of stellar mass for these massive galaxy population in Chapter 6.

7.5 A Lack of Growth among Massive Galaxies

Finally, in Chapter 6 I have exploited optical to mid-infrared photometric catalog over 17.5 $\deg^2$ in the *Spitzer*/HETDEX Exploratory Large-Area Survey (SHELA) to measure the galaxy stellar mass function in six redshift bins from $z = 0.3$ to $z = 1.0$ down to $\log(M_*/M_\odot) =$

10.5. The large area and moderate depth of the SHELA survey drastically reduces the statistical uncertainties due to Poissonian error and cosmic variance.The results from this chapter can be summarized as follows.

I performed forward modeling to account for random and systematic error in stellar mass estimates and investigate their effects on the derived mass functions. I combined M_* estimates that adopt a range of currently uncertain prior assumptions in star formation history and stellar population synthesis. Even though the recent simulation predict ~ 0.2 dex growth in M_*, I do not detect evolution ($\lesssim 0.1$ dex) in both typical stellar mass and the cumulative number density of massive galaxies ($> 10^{11.0}$ $M_\odot$) over $0.3 < z < 1.0$ with the the uncertainty of 12%. This confidence interval is dominated by uncertainties in the assumed star formation history and stellar population synthesis models for stellar mass estimations.

Among those considered here, the largest contribution to this uncertainty are biases in M_* estimates arising from different stellar population synthesis models.

Finally, I divided the galaxy sample into subsamples of quiescent and star-forming galaxies based on their specific SFRs. I do not detect evolution ($\lesssim 0.1$ dex) in the characteristic stellar mass determined from the stellar mass function of massive quiescent galaxies even after accounting for the systematic uncertainty and the random error in M_* measurement. If the mass assembly of massive galaxies at late times are dominated by minor mergers, the observed lack of evolution in SMF of massive galaxies indicating a balance between building-up of stellar mass through mergers and mass loss due to stellar evolution process. My observation provides the upper limit on mass growth by merging over this redshift range to be $\sim 48\%$ (~ 0.17 dex).

7.6 Future work

Much of the work presented in this dissertation involved the environmental effects on galaxy star formation and assembly. Additionally, I have demonstrated that the forced photometry using *The Tractor* offers a means of improving the accuracy of multi-band extragalactic survey designed for galaxy evolution studies. In this section, I describe my plan to use the multi-band forced photometry for the SHELA survey to study the effects of environment on galaxy evolution.

7.6.1 The Environmental Effects on Galaxy Evolution with DECam/SHELA

The impact of environment on the assembly and quenching of galaxy star-formation is poorly known, and the strength of environmental effects and even the physical processes themselves may evolve with redshift (e.g., McGee et al., 2014; Nantais et al., 2017). The critical epoch is $z \gtrsim 0.9$, where the clusters and groups are in the process of collapsing (Muldrew et al., 2015). Also, Figure 4.8 in Chapter 4 shows that at $z \sim 1$ is the epoch when environmental processes are becoming dominant (e.g., Peng et al., 2010; Kovač et al., 2014; Balogh et al., 2016; Nantais et al., 2017). Nearly all previous studies relied on cluster samples selected using heterogeneous methods (and ranging from rich clusters to low-mass groups), and compared results to “field” populations studied using different datasets, often with highly inhomogeneous wavelength coverage and depth. Here, I discuss some preliminary work to identify galaxy cluster candidates at $0.6 < z < 1.2$ by adapting the redMaPPer, a cluster finding algorithm (Rykoff et al., 2014) to SHELA survey, highly homogeneous imaging survey combining deep DECam ($ugriz$), NEWFIRM (K), and IRAC (3.6, 4.5μm) imaging in a 24 deg^2 region of the HETDEX/SDSS Stripe82 field. The main scientific goal is to study the build-up of the star-forming and quenched (red sequence) galaxy population as a function of mass and environment (from rich clusters to groups and to the field).

The redMaPPer algorithm identifies galaxy overdensity by making use of the increases in the contrast between cluster, which is mainly made up of old, red galaxies, and background galaxies in color space. In addition, I will utilize the “stellar bump sequence” (SBS) presented by Muzzin et al. (2013) (see also Papovich, 2008) to identify galaxy clusters. This SBS identified candidate overdensities using $[3.6] - [4.5]$ color with an additional $z - [3.6]$ color cut. Muzzin et al. (2013) demonstrated that this $z - [3.6]$ color cut effectively eliminates foreground galaxies at $0.2 < z < 0.4$. Figure 7.1 I show DECam gi and *Spitzer*/IRAC 3.6 color image of four cluster candidates from my preliminary analysis. Then in Figure 7.2 I show an observed $[3.6] - [4.5]$ color as a function of $[3.6]$ magnitude of galaxies in a $5' \times 5'$ region around each candidate redMaPPer clusters at $0.6 < z < 1.2$.

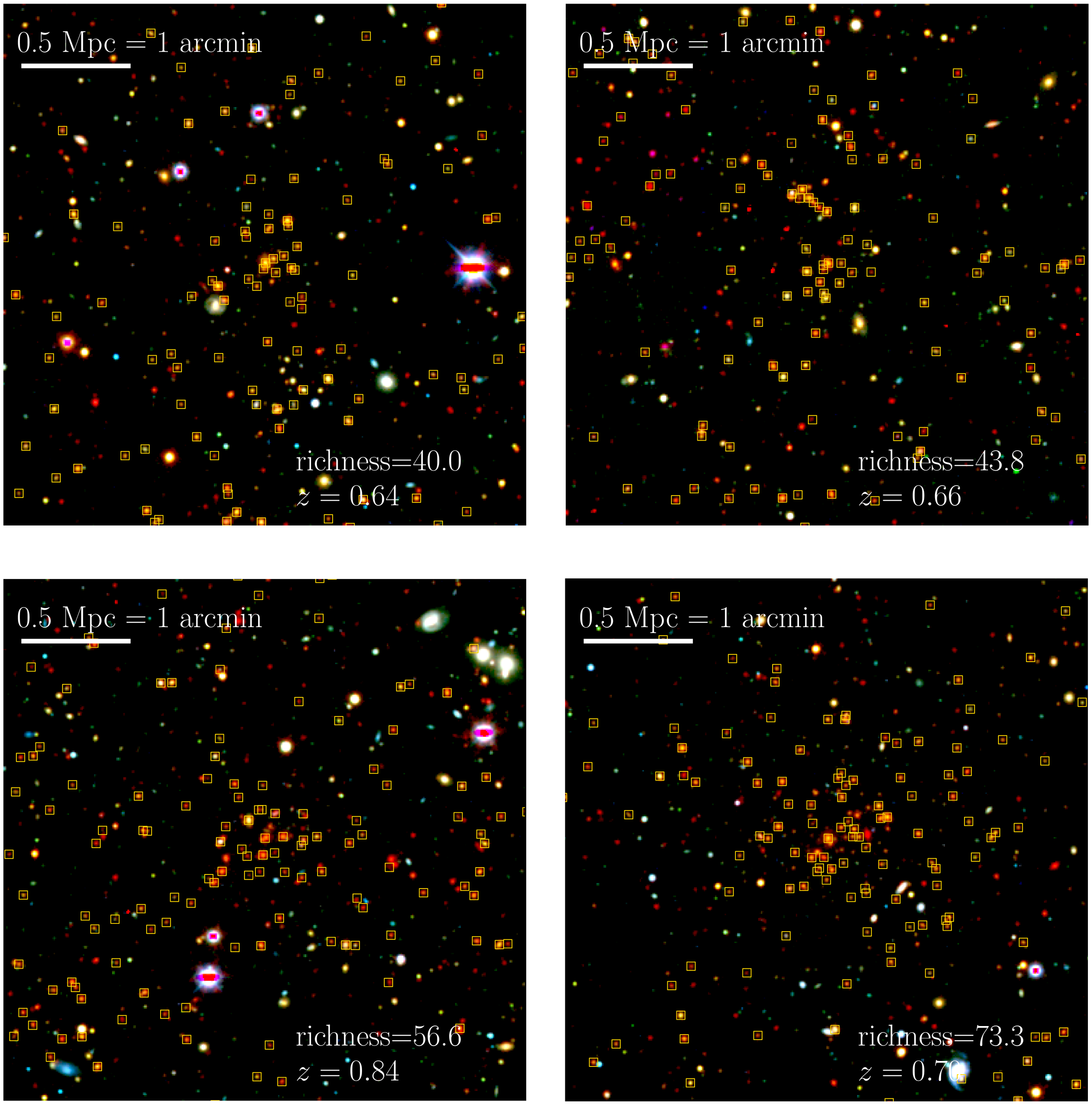

Figure 7.1: DECam gi and Spitzer $[3.6]$ color images of four cluster candidates from the preliminary analysis.

In each panel, the yellow squares show objects with $[3.6] - [4.5]$ colors consistent with the redshift and richness (λ), defined as the sum of the membership probability of every member galaxy in the cluster (Rykoff et al., 2012), of the galaxy overdensity as labeled. These four cluster candidates have at least one brightest cluster galaxy, with other galaxies spread out over several Mpc.

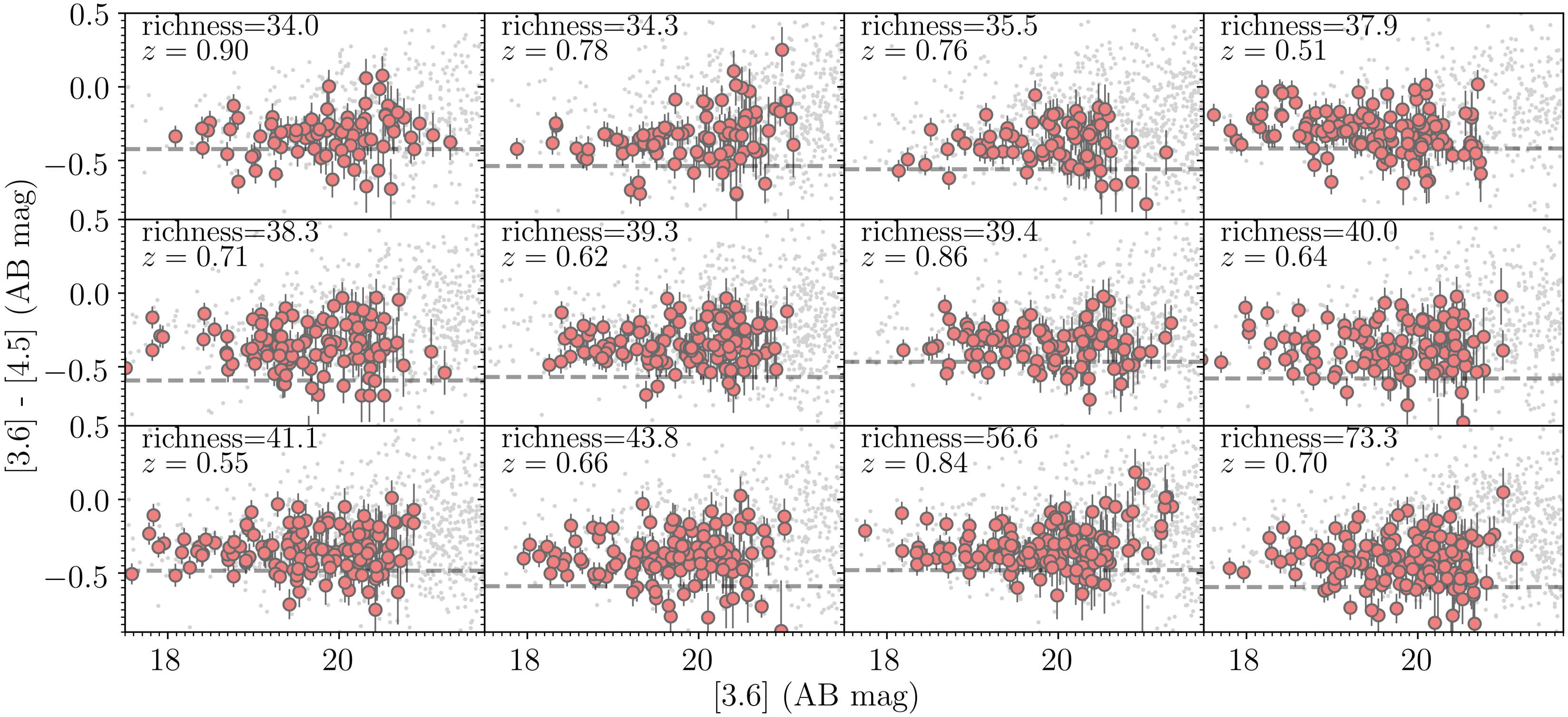

Figure 7.2: Observed $[3.6] - [4.5]$ color as a function of $[3.6]$ magnitude of galaxies in a $5' \times 5'$ region around candidate redMaPPer clusters at $0.6 < z < 1.2$ from the preliminary analysis.

In each panel the small points show all galaxies in the pointing. The red-filled circles show galaxies with $[3.6] - [4.5]$ color consistent with the galaxy overdensity (this is the "IRAC color sequence" for these colors). The redshift and cluster richness of the overdensity are listed in each panel, and the dashed lines show the $[3.6] - [4.5]$ color corresponding to this redshift. The small circles represents field galaxies at other with photometric redshifts in the range $0.6 < z < 1.2$, but not part of the overdensities.

Second, I plan to explore the effect of environments on galaxy quenching by estimating quiescent fraction of galaxies in field and in redMaPPer clusters. I will first use the rest-frame $NUV - g$ color vs. stellar mass diagram to classify galaxies into quiescent and star-forming, as described in Chapter 5 and compute the quiescent fraction of galaxies in fields – galaxies which are not identified as a member of any redMaPPer cluster $f_{q,\text{field}}$ – and the quiescent faction of galaxies in redMaPPer clusters, $f_{q,\text{field}}$. I will derive quiescent fractions (and quenching efficiency) using galaxies with stellar mass down to the stellar mass completeness limit at each redshift bin ($\log(M/M_{\odot}) = 9.6$ at $0.6 < z < 0.8$ and $\log(M/M_{\odot}) = 10.2$ at $0.8 < z < 1.2$). In Figure 7.3 I show quiescent fraction of galaxies in field and clusters in two redshift bins, $0.6 < z < 0.8$ and $0.8 < z < 1.2$ from my preliminary analysis of the redMaPPer cluster catalog. The fraction of quiescent galaxies in fields is roughly constant at $\sim 30\%$ over $0.6 < z < 1.2$, whereas the fraction of quiescent galaxies in redMaPPer clusters weakly evolve with redshift such that f_q increases from 32% at $0.8 < z < 1.2$ to 36% at $0.6 < z < 0.8$.

In addition to the fraction of quiescent galaxies, I also plan to study the differences in quiescent fractions of galaxies in redMaPPer clusters and galaxies in fields. This difference, normalized by the star-forming fraction of the field galaxies, gives a direct estimate of the fraction of cluster galaxies than have been quenched in excess of the quenched field galaxy population. Figure 7.3 shows the quenching efficiency of redMaPPer cluster galaxies at $0.6 < z < 0.8$ and $0.8 < z < 1.2$. The quenching efficiency of galaxies in redMaPPer clusters weakly evolve with redshift such that ϵ_{q} increases from 3% at $0.8 < z < 1.2$ to 10% at $0.6 < z < 0.8$.

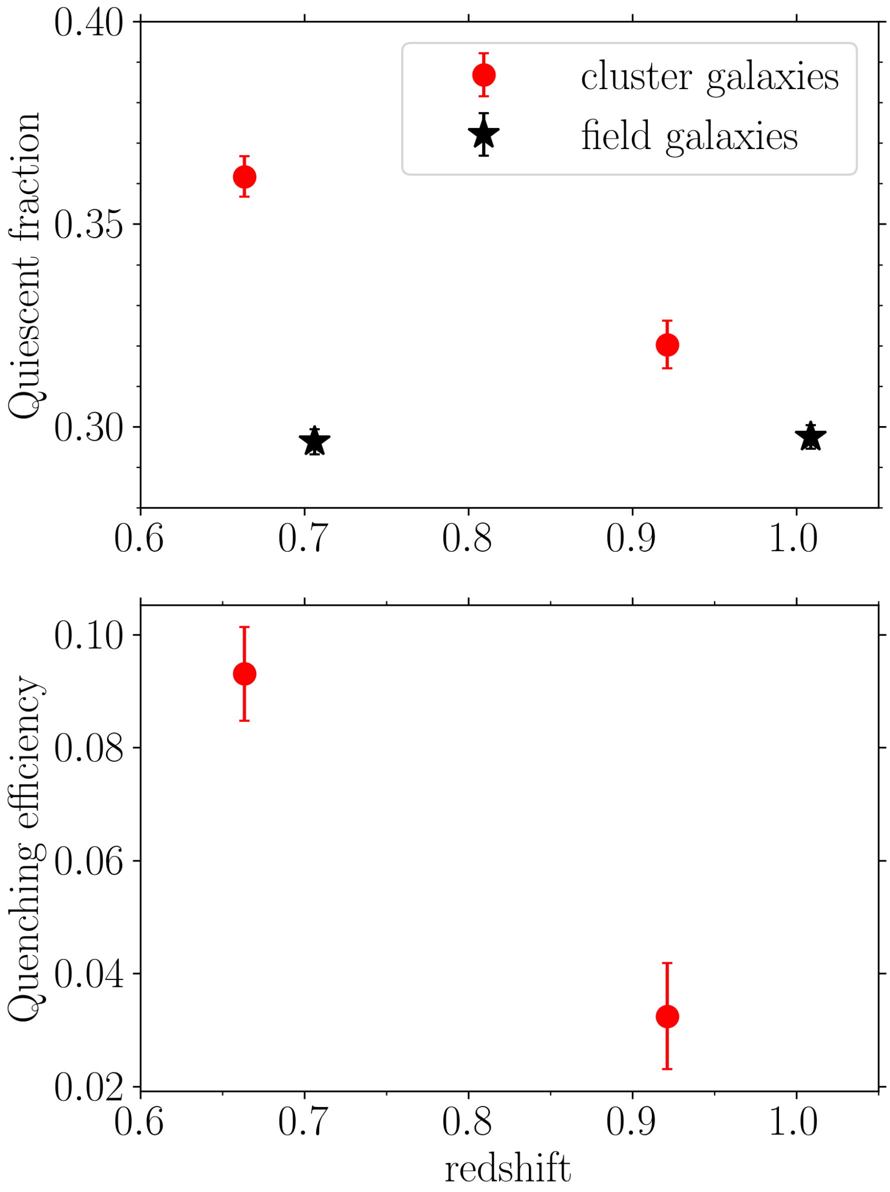

Figure 7.3: Quiescent fraction and quenching efficiency of galaxies as a function of redshift for galaxies in fields and redMaPPer clusters from the preliminary analysis.

Top: the quiescent fraction of galaxies as a function of redshift for galaxies in fields (stars) and redMaPPer clusters (circles) at two redshift bins ($0.6 < z < 0.8$ and $0.8 < z < 1.2$). The quiescent fraction of galaxies in redMaPPer clusters increases toward low redshift, whereas those of field galaxies stay roughly constant with redshift. ***Bottom:*** the quenching efficiency of galaxies in redMaPPer clusters defined as the excess quenching of galaxies in redMaPPer clusters relative to those in fields at fixed stellar mass. I derive quiescent fractions and quenching efficiency using galaxies with stellar mass down to the stellar mass completeness limit at each redshift bin ($\log(M/M_{\odot}) = 9.6$ at $0.6 < z < 0.8$ and $\log(M/M_{\odot}) = 10.2$ at $0.8 < z < 1.2$). The quenching efficiency significantly increases toward lower redshift.

7.6.2 The Two-point Correlation Function

As part of my future work, I plan to estimate the cluster masses using the redMaPPer galaxy cluster richness. I plan to calibrate this using the angular correlation function, $w(\theta)$, which is the probability of finding a companion object in a solid angle $d\Omega$ at an angular separation θ in excess of a random distribution. Figure 7.4 shows the estimates of angular correlation functions, spatial correlation function, and bias of redMaPPer clusters with richness (λ) above 10 and 15 at two redshift bins, $0.6 < z < 0.8$ and $0.8 < z < 1.2$.

Finally, in Figure 7.5 I show the relation between redMaPPer cluster richness and minimum halo mass, bias, and correlation lengths from my preliminary analysis of the redMaPPer cluster catalog. The inferred minimum halo mass of redMaPPer clusters increases of cluster richness as I expected. The redMaPPer cluster sample with cluster richness of $10 < \lambda < 80$ corresponds to the dark matter halo mass of $10^{12} - 10^{14.5}\ h^{-1}M_{\odot}$ at $0.6 < z < 0.8$ and $10^{13.4} - 10^{15.5}\ h^{-1}M_{\odot}$ at $0.8 < z < 1.2$. Figure 7.5 also shows that, on average, these candidate redMaPPer clusters at higher redshift correspond to more massive dark matter halo masses than those of clusters at lower redshift at a given cluster richness bin.

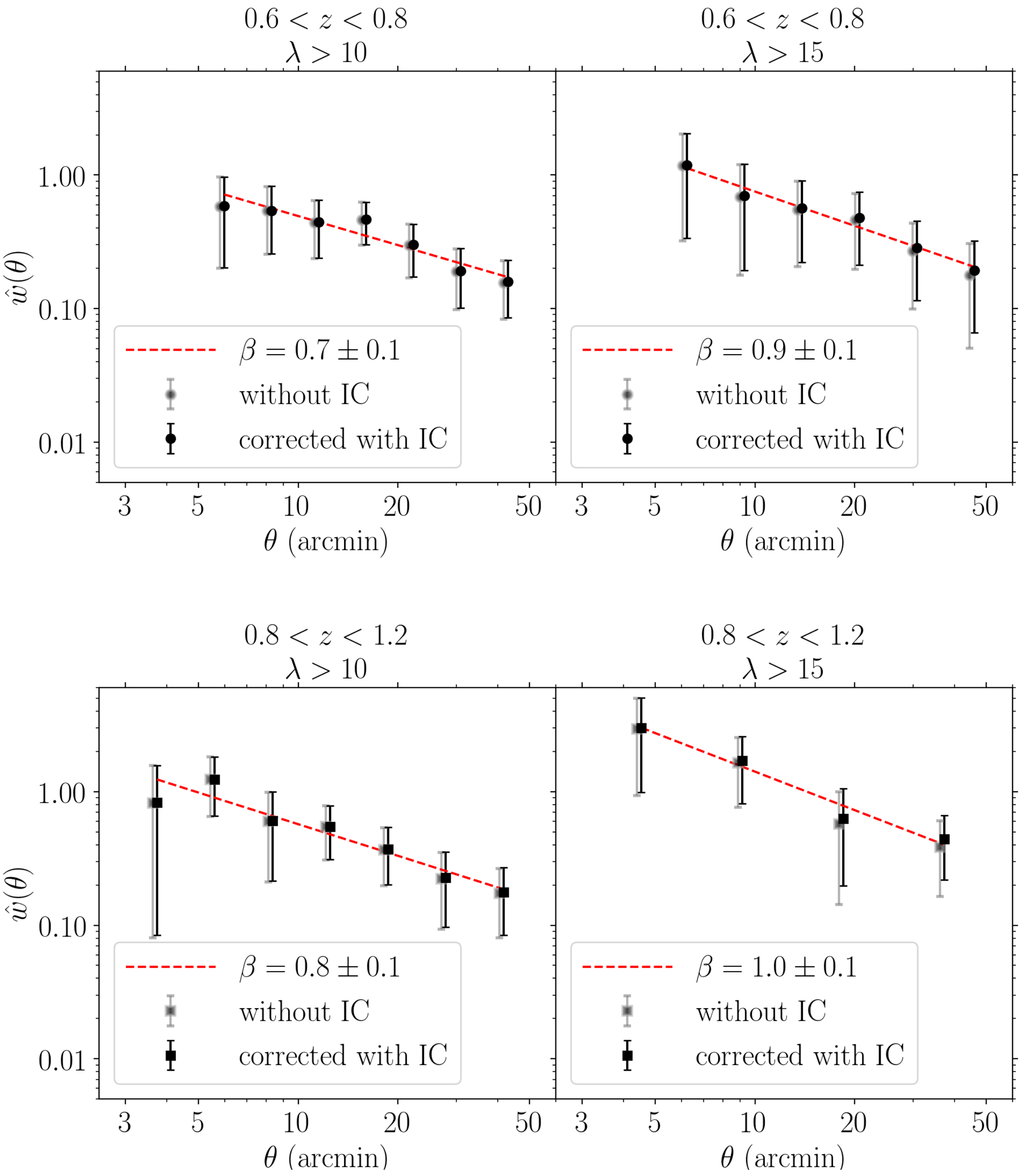

Figure 7.4: Measurements of angular correlation function for candidate redMaPPer clusters at $0.6 < z < 0.8$ from the preliminary analysis.

Top: Angular correlation function for candidate redMaPPer clusters at $0.6 < z < 0.8$ (circle symbol) in SHELA field in each cluster richness bin ($\lambda > 10$; left and $\lambda > 15$; right). The open symbols show the raw angular correlation function without the correction from the integral constraint ($IC = 0$). The filled symbols show the measured angular correlation function derived assuming that $w(\theta) = A_w\theta^{-\beta}$, with both β and A_w are free parameters and has been corrected with the integral constraint. The data point points are shifted slightly along the abscissa for clarity. The dash lines show the fit to filled data points. ***Bottom:*** same as the top panels but for candidate redMaPPer clusters at $0.8 < z < 1.2$.

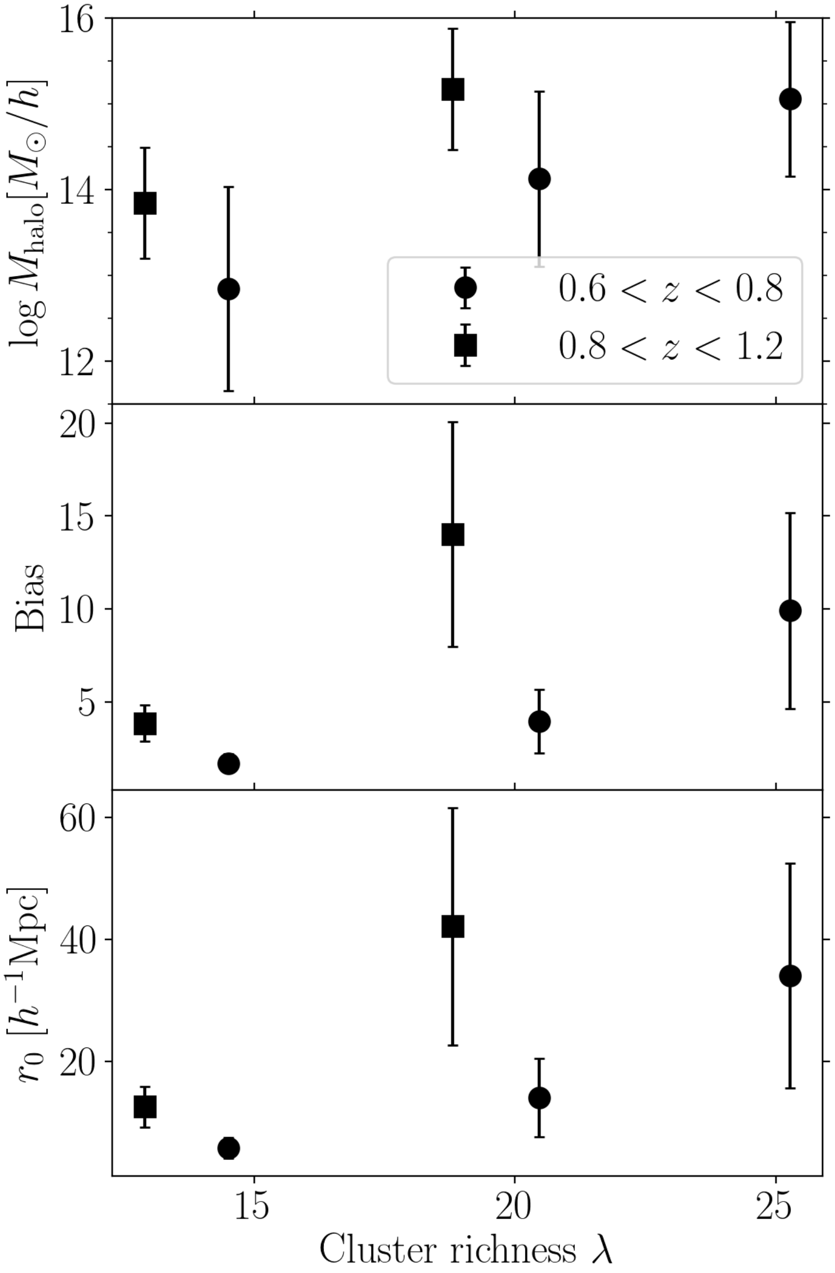

Figure 7.5: Redshift evolution of the inferred halo mass, linear halo bias, and correlation length of the candidate redMaPPer clusters

Top: the inferred halo mass of redMaPPer clusters as a function of median cluster richness at $0.6 < z < 0.8$ (circle) and at $0.8 < z < 1.2$ (square). ***Middle:*** the linear bias of redMaPPer clusters as a function of median cluster richness. ***Bottom:*** the correlation length of the candidate redMaPPer clusters as a function of median cluster richness. The inferred minimum halo mass of redMaPPer clusters increases of cluster richness. The candidate redMaPPer cluster sample with cluster richness of $10 < \lambda < 80$ corresponds to the dark matter halo mass of $10^{12} - 10^{14.5}$ $h^{-1}M_\odot$ at $0.6 < z < 0.8$ and $10^{13.4} - 10^{15.5}$ $h^{-1}M_\odot$ at $0.8 < z < 1.2$.

To summarize, I presented the preliminary analysis of the candidate redMaPPer clusters at $0.6 < z < 1.2$ for the SHELA survey. First, I estimate quiescent fraction of galaxies in field and in the candidate redMaPPer clusters and find that the fraction of quiescent galaxies in fields is roughly constant at $\sim 30\%$ over $0.6 < z < 1.2$. In contrast, the fraction of quiescent galaxies in candidate redMaPPer clusters weakly evolve with redshift such that f_q increases from 32% at $0.8 < z < 1.2$ to 36% at $0.6 < z < 0.8$.

In addition, the preliminary analysis of angular clustering of the candidate redMaPPer clusters shows that their halo mass increases with cluster richness. The redMaPPer clusters with richness of $10 < \lambda < 80$ corresponds to the dark matter halo larger than $10^{12} - 10^{14.5}\ h^{-1}M_{\odot}$ at $0.6 < z < 0.8$ and $10^{13.4} - 10^{15.5}\ h^{-1}M_{\odot}$ at $0.8 < z < 1.2$.

As part of my future work, I will continue to study the impact of environment on the assembly and quenching of galaxy star-formation through measuring the galaxy stellar mass functions for galaxies in field and in the redMaPPer clusters. Then I will separate the galaxy sample into quiescent and star-forming galaxies and measure the stellar mass functions of these subsamples in different environments (field vs. clusters). Finally, I will use the redMaPPer richness-mass relation calibrated using the angular clustering measurement to transform the redMaPPer cluster richness into halo mass for all redMaPPer clusters, and then estimate the stellar-to-halo mass relation as a function of redshift. This measurement is the key to understand the efficiency of converting baryons into stars (for a recent review see Wechsler & Tinker, 2018).

REFERENCES

Abadi, M. G., Moore, B., & Bower, R. G. 1999, MNRAS, 308, 947

Abramson, A., Kenney, J. D. P., Crowl, H. H., et al. 2011, AJ, 141, 164

Allen, R. J., Kacprzak, G. G., Glazebrook, K., et al. 2016, ApJ, 826, 60

Annis, J., Soares-Santos, M., Strauss, M. A., et al. 2014, ApJ, 794, 120

Baldry, I. K., Balogh, M. L., Bower, R. G., et al. 2006, MNRAS, 373, 469

Baldry, I. K., Glazebrook, K., Brinkmann, J., et al. 2004, ApJ, 600, 681

Baldry, I. K., Glazebrook, K., & Driver, S. P. 2008, MNRAS, 388, 945

Balogh, M., Eke, V., Miller, C., et al. 2004a, MNRAS, 348, 1355

Balogh, M. L., Baldry, I. K., Nichol, R., et al. 2004b, ApJ, 615, L101

Balogh, M. L., Morris, S. L., Yee, H. K. C., Carlberg, R. G., & Ellingson, E. 1997, ApJ, 488, L75

—. 1999, ApJ, 527, 54

Balogh, M. L., Navarro, J. F., & Morris, S. L. 2000, ApJ, 540, 113

Balogh, M. L., McGee, S. L., Mok, A., et al. 2016, MNRAS, 456, 4364

Barro, G., Faber, S. M., Pérez-González, P. G., et al. 2013, ApJ, 765, 104

Barro, G., Faber, S. M., Koo, D. C., et al. 2017, ApJ, 840, 47

Bartelmann, M. 1996, A&A, 313, 697

Bassett, R., Papovich, C., Lotz, J. M., et al. 2013, ApJ, 770, 58

Bédorf, J., & Portegies Zwart, S. 2013, MNRAS, 431, 767

Behroozi, P. S., Conroy, C., & Wechsler, R. H. 2010, ApJ, 717, 379

Behroozi, P. S., Wechsler, R. H., & Conroy, C. 2013, ApJ, 770, 57

Bell, E. F. 2008, ApJ, 682, 355

Bell, E. F., Wolf, C., Meisenheimer, K., et al. 2004, ApJ, 608, 752

Bell, E. F., van der Wel, A., Papovich, C., et al. 2012, ApJ, 753, 167

Bertin, E., & Arnouts, S. 1996, A&AS, 117, 393

Bezanson, R., van Dokkum, P. G., Tal, T., et al. 2009, ApJ, 697, 1290

Bezanson, R., van der Wel, A., Pacifici, C., et al. 2018, ApJ, 858, 60

Birnboim, Y., & Dekel, A. 2003, MNRAS, 345, 349

Birnboim, Y., Dekel, A., & Neistein, E. 2007, MNRAS, 380, 339

Blanton, M. R. 2006, ApJ, 648, 268

Blanton, M. R., & Moustakas, J. 2009, ARA&A, 47, 159

Blumenthal, G. R., Faber, S. M., Primack, J. R., & Rees, M. J. 1984, Nature, 311, 517

Bower, R. G., Benson, A. J., Malbon, R., et al. 2006, MNRAS, 370, 645

Brammer, G. B., van Dokkum, P. G., & Coppi, P. 2008, ApJ, 686, 1503

Brammer, G. B., Whitaker, K. E., van Dokkum, P. G., et al. 2011, ApJ, 739, 24

Bray, A. D., Pillepich, A., Sales, L. V., et al. 2016, MNRAS, 455, 185

Bruzual, G., & Charlot, S. 2003, MNRAS, 344, 1000

Buitrago, F., Trujillo, I., Curtis-Lake, E., et al. 2017, MNRAS, 466, 4888

Bullock, J. S. 2010, ArXiv e-prints, arXiv:1009.4505

Bullock, J. S., Kolatt, T. S., Sigad, Y., et al. 2001, MNRAS, 321, 559

Bundy, K., Leauthaud, A., Saito, S., et al. 2017, ApJ, 851, 34

Calzetti, D., Armus, L., Bohlin, R. C., et al. 2000, ApJ, 533, 682

Campbell, D., van den Bosch, F. C., Hearin, A., et al. 2015, MNRAS, 452, 444

Capak, P., Aussel, H., Ajiki, M., et al. 2007, ApJS, 172, 99

Carollo, C. M., Bschorr, T. J., Renzini, A., et al. 2013, ApJ, 773, 112

Carollo, C. M., Cibinel, A., Lilly, S. J., et al. 2016, ApJ, 818, 180

Cattaneo, A., Dekel, A., Devriendt, J., Guiderdoni, B., & Blaizot, J. 2006, MNRAS, 370, 1651

Chabrier, G. 2003, PASP, 115, 763

Charlot, S., & Fall, S. M. 2000, ApJ, 539, 718

Chen, J., Kravtsov, A. V., Prada, F., et al. 2006, ApJ, 647, 86

Cheung, E., Faber, S. M., Koo, D. C., et al. 2012, ApJ, 760, 131

Chung, A., van Gorkom, J. H., Kenney, J. D. P., & Vollmer, B. 2007, ApJ, 659, L115

Churchill, C. W., Nielsen, N. M., Kacprzak, G. G., & Trujillo-Gomez, S. 2013, ApJ, 763, L42

Chuter, R. W., Almaini, O., Hartley, W. G., et al. 2011, MNRAS, 413, 1678

Cimatti, A., Daddi, E., Mignoli, M., et al. 2002, A&A, 381, L68

Coil, A. L., Blanton, M. R., Burles, S. M., et al. 2011, ApJ, 741, 8

Conroy, C., & Gunn, J. E. 2010a, FSPS: Flexible Stellar Population Synthesis, Astrophysics Source Code Library, ascl:1010.043

—. 2010b, ApJ, 712, 833

Conroy, C., & Wechsler, R. H. 2009, ApJ, 696, 620

Cooper, A. P., D'Souza, R., Kauffmann, G., et al. 2013, MNRAS, 434, 3348

Cooper, M. C., Newman, J. A., Madgwick, D. S., et al. 2005, ApJ, 634, 833

Cooper, M. C., Newman, J. A., Coil, A. L., et al. 2007, MNRAS, 376, 1445

Cooper, M. C., Coil, A. L., Gerke, B. F., et al. 2010, MNRAS, 409, 337

Cooper, M. C., Griffith, R. L., Newman, J. A., et al. 2012, MNRAS, 419, 3018

Cowan, N. B., & Ivezić, Ž. 2008, ApJ, 674, L13

Cowie, L. L., Songaila, A., Hu, E. M., & Cohen, J. G. 1996, AJ, 112, 839

Croton, D. J., & Farrar, G. R. 2008, MNRAS, 386, 2285

Croton, D. J., Gao, L., & White, S. D. M. 2007, MNRAS, 374, 1303

Croton, D. J., Farrar, G. R., Norberg, P., et al. 2005, MNRAS, 356, 1155

Croton, D. J., Springel, V., White, S. D. M., et al. 2006, MNRAS, 365, 11

Cucciati, O., Iovino, A., Marinoni, C., et al. 2006, A&A, 458, 39

Cucciati, O., Iovino, A., Kovač, K., et al. 2010, A&A, 524, A2

Darvish, B., Mobasher, B., Sobral, D., et al. 2016, ApJ, 825, 113

Davies, L. J. M., Robotham, A. S. G., Driver, S. P., et al. 2015, MNRAS, 452, 616

—. 2016, MNRAS, 455, 4013

Davis, M., & Geller, M. J. 1976, ApJ, 208, 13

De Lucia, G., Weinmann, S., Poggianti, B. M., Aragón-Salamanca, A., & Zaritsky, D. 2012, MNRAS, 423, 1277

Dekel, A., & Birnboim, Y. 2006, MNRAS, 368, 2

—. 2008, MNRAS, 383, 119

Dekel, A., & Burkert, A. 2014, MNRAS, 438, 1870

Dekel, A., Sari, R., & Ceverino, D. 2009, ApJ, 703, 785

Dekel, A., & Silk, J. 1986, ApJ, 303, 39

Delaye, L., Huertas-Company, M., Mei, S., et al. 2014, MNRAS, 441, 203

Dressler, A. 1980, ApJ, 236, 351

Drory, N., Bundy, K., Leauthaud, A., et al. 2009, ApJ, 707, 1595

Eisenhardt, P. R. M., Brodwin, M., Gonzalez, A. H., et al. 2008, ApJ, 684, 905

Fakhouri, O., & Ma, C.-P. 2009, MNRAS, 394, 1825

Fang, J. J., Faber, S. M., Koo, D. C., & Dekel, A. 2013, ApJ, 776, 63

Farouki, R., & Shapiro, S. L. 1981, ApJ, 243, 32

Feigelson, E. D., & Babu, G. J. 2012, Modern Statistical Methods for Astronomy

Feldmann, R., & Mayer, L. 2015, MNRAS, 446, 1939

Fillingham, S. P., Cooper, M. C., Pace, A. B., et al. 2016, MNRAS, 463, 1916

Fillingham, S. P., Cooper, M. C., Wheeler, C., et al. 2015, MNRAS, 454, 2039

Finn, R. A., Balogh, M. L., Zaritsky, D., Miller, C. J., & Nichol, R. C. 2008, ApJ, 679, 279

Fioc, M., & Rocca-Volmerange, B. 1997, A&A, 326, 950

Fontana, A., Salimbeni, S., Grazian, A., et al. 2006, A&A, 459, 745

Fontanot, F., De Lucia, G., Monaco, P., Somerville, R. S., & Santini, P. 2009, MNRAS, 397, 1776

Forrest, B., Tran, K.-V. H., Broussard, A., et al. 2017, ApJ, 838, L12

Fossati, M., Wilman, D. J., Mendel, J. T., et al. 2017, ApJ, 835, 153

Franx, M., van Dokkum, P. G., Förster Schreiber, N. M., et al. 2008, ApJ, 688, 770

Gabor, J. M., & Davé, R. 2012, MNRAS, 427, 1816

—. 2015, MNRAS, 447, 374

Gabor, J. M., Davé, R., Oppenheimer, B. D., & Finlator, K. 2011, MNRAS, 417, 2676

Gao, L., Springel, V., & White, S. D. M. 2005, MNRAS, 363, L66

Gavazzi, R., Treu, T., Rhodes, J. D., et al. 2007, ApJ, 667, 176

Geach, J. E., Lin, Y.-T., Makler, M., et al. 2017, ApJS, 231, 7

Geha, M., Blanton, M. R., Yan, R., & Tinker, J. L. 2012, ApJ, 757, 85

Geha, M., Wechsler, R. H., Mao, Y.-Y., et al. 2017, ApJ, 847, 4

Giacconi, R., Zirm, A., Wang, J., et al. 2002, ApJS, 139, 369

Granato, G. L., De Zotti, G., Silva, L., Bressan, A., & Danese, L. 2004, ApJ, 600, 580

Greene, J. E., Murphy, J. D., Comerford, J. M., Gebhardt, K., & Adams, J. J. 2012, ApJ, 750, 32

Greene, J. E., Murphy, J. D., Graves, G. J., et al. 2013, ApJ, 776, 64

Grogin, N. A., Kocevski, D. D., Faber, S. M., et al. 2011, ApJS, 197, 35

Gunn, J. E., & Gott, III, J. R. 1972, ApJ, 176, 1

Guo, Q., White, S., Boylan-Kolchin, M., et al. 2011, MNRAS, 413, 101

Guo, Y., Bell, E. F., Lu, Y., et al. 2017, ApJ, 841, L22

Haines, C. P., Pereira, M. J., Smith, G. P., et al. 2013, ApJ, 775, 126

Hartley, W. G., Conselice, C. J., Mortlock, A., Foucaud, S., & Simpson, C. 2015, MNRAS, 451, 1613

Hartley, W. G., Almaini, O., Cirasuolo, M., et al. 2010, MNRAS, 407, 1212

Hartley, W. G., Almaini, O., Mortlock, A., et al. 2013, MNRAS, 431, 3045

Hatfield, P. W., & Jarvis, M. J. 2017, MNRAS, 472, 3570

Hearin, A. P., Behroozi, P. S., & van den Bosch, F. C. 2016, MNRAS, 461, 2135

Hearin, A. P., & Watson, D. F. 2013, MNRAS, 435, 1313

Henriques, B. M. B., White, S. D. M., Lemson, G., et al. 2012, MNRAS, 421, 2904

Henriques, B. M. B., White, S. D. M., Thomas, P. A., et al. 2015, MNRAS, 451, 2663

Hill, G. J., Gebhardt, K., Komatsu, E., et al. 2008, in Astronomical Society of the Pacific Conference Series, Vol. 399, Panoramic Views of Galaxy Formation and Evolution, ed. T. Kodama, T. Yamada, & K. Aoki, 115

Hilz, M., Naab, T., & Ostriker, J. P. 2013, MNRAS, 429, 2924

Hogg, D. W., Blanton, M. R., Eisenstein, D. J., et al. 2003, ApJ, 585, L5

Hogg, D. W., Blanton, M. R., Brinchmann, J., et al. 2004, ApJ, 601, L29

Hopkins, P. F., Bundy, K., Hernquist, L., Wuyts, S., & Cox, T. J. 2010, MNRAS, 401, 1099

Hopkins, P. F., Hernquist, L., Cox, T. J., et al. 2006, ApJS, 163, 1

Huang, S., Ho, L. C., Peng, C. Y., Li, Z.-Y., & Barth, A. J. 2013, ApJ, 768, L28

Huang, S., Leauthaud, A., Greene, J. E., et al. 2018, MNRAS, 475, 3348

Ivezić, Ž., Vivas, A. K., Lupton, R. H., & Zinn, R. 2005, AJ, 129, 1096

Jian, H.-Y., Lin, L., Oguri, M., et al. 2018, PASJ, 70, S23

Johansson, P. H., Naab, T., & Ostriker, J. P. 2009, ApJ, 697, L38

—. 2012, ApJ, 754, 115

Juneau, S., Glazebrook, K., Crampton, D., et al. 2005, ApJ, 619, L135

Kauffmann, G. 2015, MNRAS, 454, 1840

Kauffmann, G., Li, C., & Heckman, T. M. 2010, MNRAS, 409, 491

Kauffmann, G., Li, C., Zhang, W., & Weinmann, S. 2013, MNRAS, 430, 1447

Kauffmann, G., White, S. D. M., Heckman, T. M., et al. 2004, MNRAS, 353, 713

Kauffmann, G., Heckman, T. M., White, S. D. M., et al. 2003, MNRAS, 341, 54

Kawata, D., & Mulchaey, J. S. 2008, ApJ, 672, L103

Kawinwanichakij, L., Papovich, C., Quadri, R. F., et al. 2014, ApJ, 792, 103

Kawinwanichakij, L., Quadri, R. F., Papovich, C., et al. 2016, ApJ, 817, 9

Kawinwanichakij, L., Papovich, C., Quadri, R. F., et al. 2017, ApJ, 847, 134

Kenney, J. D. P., Abramson, A., & Bravo-Alfaro, H. 2015, AJ, 150, 59

Kenney, J. D. P., & Koopmann, R. A. 1999, AJ, 117, 181

Kereš, D., Katz, N., Weinberg, D. H., & Davé, R. 2005, MNRAS, 363, 2

Khochfar, S., & Silk, J. 2006, ApJ, 648, L21

Klypin, A. A., Trujillo-Gomez, S., & Primack, J. 2011, ApJ, 740, 102

Knobel, C., Lilly, S. J., Woo, J., & Kovač, K. 2015, ApJ, 800, 24

Koekemoer, A. M., Faber, S. M., Ferguson, H. C., et al. 2011, ApJS, 197, 36

Koester, B. P., McKay, T. A., Annis, J., et al. 2007, ApJ, 660, 221

Kovač, K., Lilly, S. J., Knobel, C., et al. 2010, ApJ, 718, 86

—. 2014, MNRAS, 438, 717

Kriek, M., van Dokkum, P. G., Labbé, I., et al. 2009, ApJ, 700, 221

Kroupa, P. 2001, MNRAS, 322, 231

Lacey, C., & Cole, S. 1993, MNRAS, 262, 627

Lackner, C. N., Cen, R., Ostriker, J. P., & Joung, M. R. 2012, MNRAS, 425, 641

Lake, G., Katz, N., & Moore, B. 1998, ApJ, 495, 152

Lang, D., Hogg, D. W., & Mykytyn, D. 2016a, The Tractor: Probabilistic astronomical source detection and measurement, Astrophysics Source Code Library, ascl:1604.008

Lang, D., Hogg, D. W., & Schlegel, D. J. 2016b, AJ, 151, 36

Lang, P., Wuyts, S., Somerville, R. S., et al. 2014, ApJ, 788, 11

Lani, C., Almaini, O., Hartley, W. G., et al. 2013, MNRAS, 435, 207

Laporte, C. F. P., White, S. D. M., Naab, T., & Gao, L. 2013, MNRAS, 435, 901

Larson, R. B. 1974, MNRAS, 169, 229

Larson, R. B., Tinsley, B. M., & Caldwell, C. N. 1980, ApJ, 237, 692

Lawrence, A., Warren, S. J., Almaini, O., et al. 2007, MNRAS, 379, 1599

Lee, J., & Yi, S. K. 2013, ApJ, 766, 38

—. 2017, ApJ, 836, 161

Lee, S.-K., Im, M., Kim, J.-W., et al. 2015, ApJ, 810, 90

Li, C., Kauffmann, G., Jing, Y. P., et al. 2006, MNRAS, 368, 21

Lilly, S. J., & Carollo, C. M. 2016, ApJ, 833, 1

Lin, L., Jian, H.-Y., Foucaud, S., et al. 2014, ApJ, 782, 33

Lotz, J. M., Papovich, C., Faber, S. M., et al. 2013, ApJ, 773, 154

Lu, Y., Wechsler, R. H., Somerville, R. S., et al. 2014, ApJ, 795, 123

Madau, P., & Dickinson, M. 2014, ARA&A, 52, 415

Madore, B. F., Freedman, W. L., & Bothun, G. D. 2004, ApJ, 607, 810

Man, A. W. S., Zirm, A. W., & Toft, S. 2016, ApJ, 830, 89

Mancone, C., & Gonzalez, A. 2012, EzGal: A Flexible Interface for Stellar Population Synthesis

Models, Astrophysics Source Code Library, ascl:1208.021

Mandelbaum, R., Seljak, U., Kauffmann, G., Hirata, C. M., & Brinkmann, J. 2006, MNRAS, 368, 715

Mann, H. B., & Whitney, D. R. 1947, Ann. Math. Statist., 18, 50

Maraston, C. 2005, MNRAS, 362, 799

Marchesini, D., van Dokkum, P. G., Förster Schreiber, N. M., et al. 2009, ApJ, 701, 1765

Marchesini, D., Muzzin, A., Stefanon, M., et al. 2014, ApJ, 794, 65

Markwardt, C. B. 2009, in Astronomical Society of the Pacific Conference Series, Vol. 411, Astronomical Data Analysis Software and Systems XVIII, ed. D. A. Bohlender, D. Durand, & P. Dowler, 251

Martig, M., Bournaud, F., Teyssier, R., & Dekel, A. 2009, ApJ, 707, 250

Martin, D. C., Wyder, T. K., Schiminovich, D., et al. 2007, ApJS, 173, 342

Masjedi, M., Hogg, D. W., Cool, R. J., et al. 2006, ApJ, 644, 54

Matsuoka, Y., & Kawara, K. 2010, MNRAS, 405, 100

McCarthy, I. G., Frenk, C. S., Font, A. S., et al. 2008, MNRAS, 383, 593

McCracken, H. J., Milvang-Jensen, B., Dunlop, J., et al. 2012, A&A, 544, A156

McGee, S. L., Balogh, M. L., Wilman, D. J., et al. 2011, MNRAS, 413, 996

McGee, S. L., Bower, R. G., & Balogh, M. L. 2014, MNRAS, 442, L105

McLure, R. J., Pearce, H. J., Dunlop, J. S., et al. 2013, MNRAS, 428, 1088

Moore, B., Katz, N., Lake, G., Dressler, A., & Oemler, A. 1996, Nature, 379, 613

More, S., van den Bosch, F. C., Cacciato, M., et al. 2011, MNRAS, 410, 210

Morishita, T., Abramson, L. E., Treu, T., et al. 2017, ApJ, 835, 254

Moster, B. P., Naab, T., & White, S. D. M. 2013, MNRAS, 428, 3121

Moustakas, J., Coil, A. L., Aird, J., et al. 2013, ApJ, 767, 50

Moutard, T., Arnouts, S., Ilbert, O., et al. 2016, A&A, 590, A103

Muldrew, S. I., Hatch, N. A., & Cooke, E. A. 2015, MNRAS, 452, 2528

Muldrew, S. I., Croton, D. J., Skibba, R. A., et al. 2012, MNRAS, 419, 2670

Mutch, S. J., Croton, D. J., & Poole, G. B. 2013, MNRAS, 435, 2445

Muzzin, A., Wilson, G., Yee, H. K. C., et al. 2012, ApJ, 746, 188

Muzzin, A., Marchesini, D., Stefanon, M., et al. 2013, ApJS, 206, 8

Naab, T., Johansson, P. H., & Ostriker, J. P. 2009, ApJ, 699, L178

Naab, T., Johansson, P. H., Ostriker, J. P., & Efstathiou, G. 2007, ApJ, 658, 710

Naab, T., Khochfar, S., & Burkert, A. 2006, ApJ, 636, L81

Nanayakkara, T., Glazebrook, K., Kacprzak, G. G., et al. 2016, ApJ, 828, 21

Nantais, J. B., Muzzin, A., van der Burg, R. F. J., et al. 2017, MNRAS, 465, L104

Newman, A. B., Ellis, R. S., Andreon, S., et al. 2014, ApJ, 788, 51

Newman, A. B., Ellis, R. S., Bundy, K., & Treu, T. 2012, ApJ, 746, 162

Nierenberg, A. M., Auger, M. W., Treu, T., Marshall, P. J., & Fassnacht, C. D. 2011, ApJ, 731, 44

Nierenberg, A. M., Auger, M. W., Treu, T., et al. 2012, ApJ, 752, 99

Noeske, K. G., Weiner, B. J., Faber, S. M., et al. 2007, ApJ, 660, L43

Oemler, Jr., A. 1974, ApJ, 194, 1

Oguri, M. 2014, MNRAS, 444, 147

Omand, C. M. B., Balogh, M. L., & Poggianti, B. M. 2014, MNRAS, 440, 843

Oogi, T., & Habe, A. 2013, MNRAS, 428, 641

Oosterloo, T., & van Gorkom, J. 2005, A&A, 437, L19

Oser, L., Naab, T., Ostriker, J. P., & Johansson, P. H. 2012, ApJ, 744, 63

Oser, L., Ostriker, J. P., Naab, T., Johansson, P. H., & Burkert, A. 2010, ApJ, 725, 2312

Ownsworth, J. R., Conselice, C. J., Mortlock, A., et al. 2014, MNRAS, 445, 2198

Papovich, C. 2008, ApJ, 676, 206

Papovich, C., Moustakas, L. A., Dickinson, M., et al. 2006, ApJ, 640, 92

Papovich, C., Bassett, R., Lotz, J. M., et al. 2012, ApJ, 750, 93

Papovich, C., Labbé, I., Quadri, R., et al. 2015, ApJ, 803, 26

Papovich, C., Shipley, H. V., Mehrtens, N., et al. 2016, ApJS, 224, 28

Papovich, C., Kawinwanichakij, L., Quadri, R. F., et al. 2018, ApJ, 854, 30

Paranjape, A., Kovač, K., Hartley, W. G., & Pahwa, I. 2015, MNRAS, 454, 3030

Patel, S. G., Holden, B. P., Kelson, D. D., et al. 2012, ApJ, 748, L27

Patel, S. G., van Dokkum, P. G., Franx, M., et al. 2013, ApJ, 766, 15

Peng, Y., Maiolino, R., & Cochrane, R. 2015, Nature, 521, 192

Peng, Y.-j., Lilly, S. J., Renzini, A., & Carollo, M. 2012, ApJ, 757, 4

Peng, Y.-j., Lilly, S. J., Kovač, K., et al. 2010, ApJ, 721, 193

Phillips, J. I., Wheeler, C., Boylan-Kolchin, M., et al. 2014, MNRAS, 437, 1930

Phillips, J. I., Wheeler, C., Cooper, M. C., et al. 2015, MNRAS, 447, 698

Pillepich, A., Nelson, D., Hernquist, L., et al. 2018, MNRAS, 475, 648

Pozzetti, L., Bolzonella, M., Lamareille, F., et al. 2007, A&A, 474, 443

Pozzetti, L., Bolzonella, M., Zucca, E., et al. 2010, A&A, 523, A13

Qu, Y., Helly, J. C., Bower, R. G., et al. 2017, MNRAS, 464, 1659

Quadri, R. F., & Williams, R. J. 2010, ApJ, 725, 794

Quadri, R. F., Williams, R. J., Franx, M., & Hildebrandt, H. 2012, ApJ, 744, 88

Quadri, R. F., Williams, R. J., Lee, K.-S., et al. 2008, ApJ, 685, L1

Read, J. I., Wilkinson, M. I., Evans, N. W., Gilmore, G., & Kleyna, J. T. 2006, MNRAS, 366, 429

Rees, M. J., & Ostriker, J. P. 1977, MNRAS, 179, 541

Rodriguez-Gomez, V., Genel, S., Vogelsberger, M., et al. 2015, MNRAS, 449, 49

Rodriguez-Gomez, V., Pillepich, A., Sales, L. V., et al. 2016, MNRAS, 458, 2371

Rodríguez-Puebla, A., Primack, J. R., Avila-Reese, V., & Faber, S. M. 2017, MNRAS, 470, 651

Ross, A. J., & Brunner, R. J. 2009, MNRAS, 399, 878

Rozo, E., Rykoff, E., Koester, B., et al. 2011, ApJ, 740, 53

Rozo, E., Rykoff, E. S., Evrard, A., et al. 2009a, ApJ, 699, 768

Rozo, E., Rykoff, E. S., Koester, B. P., et al. 2009b, ApJ, 703, 601

Rudnick, G. H., Tran, K.-V., Papovich, C., Momcheva, I., & Willmer, C. 2012, ApJ, 755, 14

Rykoff, E. S., Koester, B. P., Rozo, E., et al. 2012, ApJ, 746, 178

Rykoff, E. S., Rozo, E., Busha, M. T., et al. 2014, ApJ, 785, 104

Rykoff, E. S., Rozo, E., Hollowood, D., et al. 2016, ApJS, 224, 1

Schawinski, K., Urry, C. M., Simmons, B. D., et al. 2014, MNRAS, 440, 889

Scoville, N., Aussel, H., Brusa, M., et al. 2007, ApJS, 172, 1

Slater, C. T., & Bell, E. F. 2014, ApJ, 792, 141

Sobral, D., Best, P. N., Smail, I., et al. 2011, MNRAS, 411, 675

Somerville, R. S., & Davé, R. 2015, ARA&A, 53, 51

Somerville, R. S., Hopkins, P. F., Cox, T. J., Robertson, B. E., & Hernquist, L. 2008, MNRAS, 391, 481

Speagle, J. S., Steinhardt, C. L., Capak, P. L., & Silverman, J. D. 2014, ApJS, 214, 15

Spitler, L. R., Labbé, I., Glazebrook, K., et al. 2012, ApJ, 748, L21

Spitler, L. R., Straatman, C. M. S., Labbé, I., et al. 2014, ApJ, 787, L36

Springel, V., Di Matteo, T., & Hernquist, L. 2005, MNRAS, 361, 776

Springel, V., White, S. D. M., Tormen, G., & Kauffmann, G. 2001, MNRAS, 328, 726

Straatman, C. M. S., Labbé, I., Spitler, L. R., et al. 2014, ApJ, 783, L14

Straatman, C. M. S., Spitler, L. R., Quadri, R. F., et al. 2016, ApJ, 830, 51

Strateva, I., Ivezić, Ž., Knapp, G. R., et al. 2001, AJ, 122, 1861

Sun, M., Donahue, M., & Voit, G. M. 2007, ApJ, 671, 190

Szomoru, D., Franx, M., & van Dokkum, P. G. 2012, ApJ, 749, 121

Tacchella, S., Dekel, A., Carollo, C. M., et al. 2016a, MNRAS, 458, 242

—. 2016b, MNRAS, 457, 2790

Tal, T., van Dokkum, P. G., Franx, M., et al. 2013, ApJ, 769, 31

Tal, T., Wake, D. A., & van Dokkum, P. G. 2012, ApJ, 751, L5

Tal, T., Dekel, A., Oesch, P., et al. 2014, ApJ, 789, 164

Taylor, E. N., Franx, M., Glazebrook, K., et al. 2010, ApJ, 720, 723

Terrazas, B. A., Bell, E. F., Henriques, B. M. B., et al. 2016, ApJ, 830, L12

Tilvi, V., Papovich, C., Tran, K.-V. H., et al. 2013, ApJ, 768, 56

Tinker, J. L., Conroy, C., Norberg, P., et al. 2008, ApJ, 686, 53

Tinker, J. L., & Wetzel, A. R. 2010, ApJ, 719, 88

Tomczak, A. R., Quadri, R. F., Tran, K.-V. H., et al. 2014, ApJ, 783, 85

—. 2016, ApJ, 817, 118

Tran, K.-V. H., Papovich, C., Saintonge, A., et al. 2010, ApJ, 719, L126

Tumlinson, J., Thom, C., Werk, J. K., et al. 2011, Science, 334, 948

Vader, J. P., & Sandage, A. 1991, ApJ, 379, L1

van de Voort, F., Schaye, J., Booth, C. M., Haas, M. R., & Dalla Vecchia, C. 2011, MNRAS, 414, 2458

van den Bosch, F. C., Aquino, D., Yang, X., et al. 2008, MNRAS, 387, 79

van der Wel, A., Bell, E. F., Häussler, B., et al. 2012, ApJS, 203, 24

van der Wel, A., Franx, M., van Dokkum, P. G., et al. 2014, ApJ, 788, 28

van Dokkum, P. G., Whitaker, K. E., Brammer, G., et al. 2010, ApJ, 709, 1018

van Dokkum, P. G., Brammer, G., Fumagalli, M., et al. 2011, ApJ, 743, L15

van Dokkum, P. G., Bezanson, R., van der Wel, A., et al. 2014, ApJ, 791, 45

Vollmer, B., Soida, M., Braine, J., et al. 2012, A&A, 537, A143

Wake, D. A., Sheth, R. K., Nichol, R. C., et al. 2008, MNRAS, 387, 1045

Wang, W., Sales, L. V., Henriques, B. M. B., & White, S. D. M. 2014, MNRAS, 442, 1363

Wang, W., & White, S. D. M. 2012, MNRAS, 424, 2574

Watson, D. F., Berlind, A. A., McBride, C. K., Hogg, D. W., & Jiang, T. 2012, ApJ, 749, 83

Wechsler, R. H., & Tinker, J. L. 2018, ArXiv e-prints, arXiv:1804.03097

Wechsler, R. H., Zentner, A. R., Bullock, J. S., Kravtsov, A. V., & Allgood, B. 2006, ApJ, 652, 71

Weinmann, S. M., Kauffmann, G., van den Bosch, F. C., et al. 2009, MNRAS, 394, 1213

Weinmann, S. M., Kauffmann, G., von der Linden, A., & De Lucia, G. 2010, MNRAS, 406, 2249

Weinmann, S. M., van den Bosch, F. C., Yang, X., & Mo, H. J. 2006, MNRAS, 366, 2

Weinzirl, T., Jogee, S., Conselice, C. J., et al. 2011, ApJ, 743, 87

Weisz, D. R., Dolphin, A. E., Skillman, E. D., et al. 2015, ApJ, 804, 136

Wellons, S., Torrey, P., Ma, C.-P., et al. 2015, MNRAS, 449, 361

Wetzel, A. R., Tinker, J. L., Conroy, C., & van den Bosch, F. C. 2013, MNRAS, 432, 336

Wetzel, A. R., Tollerud, E. J., & Weisz, D. R. 2015, ApJ, 808, L27

Whitaker, K. E., Labbé, I., van Dokkum, P. G., et al. 2011, ApJ, 735, 86

Whitaker, K. E., Bezanson, R., van Dokkum, P. G., et al. 2017, ApJ, 838, 19

White, S. D. M., & Frenk, C. S. 1991, ApJ, 379, 52

White, S. D. M., & Rees, M. J. 1978, MNRAS, 183, 341

Williams, R. J., Quadri, R. F., Franx, M., van Dokkum, P., & Labbé, I. 2009, ApJ, 691, 1879

Woo, J., Carollo, C. M., Faber, S. M., Dekel, A., & Tacchella, S. 2017, MNRAS, 464, 1077

Woo, J., Dekel, A., Faber, S. M., & Koo, D. C. 2015, MNRAS, 448, 237

Woo, J., Dekel, A., Faber, S. M., et al. 2013, MNRAS, 428, 3306

Wuyts, S., Förster Schreiber, N. M., van der Wel, A., et al. 2011, ApJ, 742, 96

Wyder, T. K., Martin, D. C., Schiminovich, D., et al. 2007, ApJS, 173, 293

Xu, C. K., Zhao, Y., Scoville, N., et al. 2012, ApJ, 747, 85

Yang, X., Mo, H. J., van den Bosch, F. C., et al. 2007, ApJ, 671, 153

Yuan, T., Nanayakkara, T., Kacprzak, G. G., et al. 2014, ApJ, 795, L20

Zehavi, I., Blanton, M. R., Frieman, J. A., et al. 2002, ApJ, 571, 172

Zheng, Z., Berlind, A. A., Weinberg, D. H., et al. 2005, ApJ, 633, 791

Zirm, A. W., Toft, S., & Tanaka, M. 2012, ApJ, 744, 181

Zolotov, A., Dekel, A., Mandelker, N., et al. 2015, MNRAS, 450, 2327

APPENDIX A

APPENDICES OF CHAPTER 3

A.1 The Dependence of Satellite Quenching on the Aperture Size

The comparison of satellite galaxy quenching and galactic conformity in the literature is complicated because different studies use a wide range of aperture sizes within which to identify satellites (e.g., Wang & White, 2012; Tal et al., 2014; Phillips et al., 2014, 2015; Hartley et al., 2015). The primary results in this study are based on a 300 ckpc aperture, but in this appendix we show how the use of different aperture sizes affects the quenching efficiencies.

We recomputed the quenching efficiencies of satellites for the central and star-forming galaxy samples in each redshift bin using different aperture sizes, including both comoving and physical aperture radii: 200 ckpc, 300 ckpc, 500 ckpc, 200 pkpc, 300 pkpc, and 500 pkpc. The results are shown in Figure A.1 and are tabulated in Table A.1.

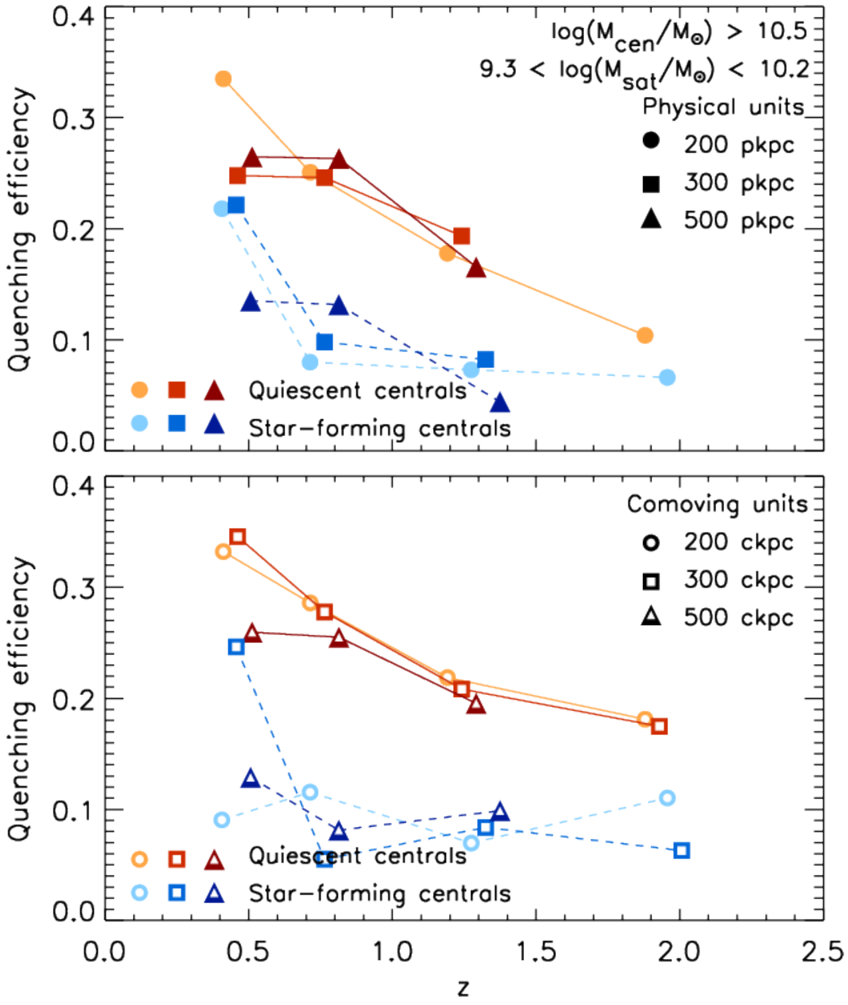

Figure A.1: Effects of aperture sizes on the evolution of the satellite quenching efficiency

The satellite quenching efficiency as a function of redshift and central galaxy type, where the satellites are identified within different aperture sizes around the central galaxies. The satellites have stellar mass $9.3 < \log(M_{\rm sat}/{\rm M}_\odot) < 10.2$ and the central galaxies have $\log(M_{\rm cen}/{\rm M}_\odot) > 10.5$. The top and bottom panels show the results in apertures that have fixed radii in physical and comoving units, respectively. (In the highest redshift bin, $1.6 < z < 2.5$ the 300 pkpc, 500 pkpc,and 500 ckpc probe a significant portion of the image: at $z \sim 2$, 500 pkpc corresponds to $0'.5$, making the measurements intractable, and we do not include them here.) There is no strong dependence on the strength of the quenching efficiency with the choice of aperture radius, with the possible exception of the $0.3 < z < 0.6$ bin. Uncertainties have been suppressed for clarity. Reprinted with permission from “Satellite Quenching and Galactic Conformity at $0.3 < z < 2.5$" by Kawinwanichakij et al., 2016. The Astrophysical Journal, Volume 817, Issue 1, article id. 9 pp. 19, Copyright 2016.

The observed conformity signal does not depend strongly on the choice of aperture. At redshifts $0.6 < z < 2.5$ there is no significant dependence on the quenching efficiency on aperture. The biggest difference is apparent in our lowest redshift bin, $0.3 < z < 0.6$, where we see that the quenching efficiency of satellites of star-forming galaxies can be reduced, thereby increasing the strength of galactic conformity. However, these are still within the errors (see Figure 7 and Table A.1).

Table A.1: Quiescent fractions ($f_{\rm q}$) and quenching efficiency ($\epsilon_{\rm q}$) of satellites of quiescent and star-forming centrals measured in different apertures size. Reprinted with permission from “Satellite Quenching and Galactic Conformity at $0.3 < z < 2.5$" by Kawinwanichakij et al., 2016. The Astrophysical Journal, Volume 817, Issue 1, article id. 9 pp. 19, Copyright 2016.

Stellar Mass Range	Redshift Range	Aperture size	$f_{\rm q,Quiescent}$	$f_{\rm q,Star-forming}$	$\epsilon_{\rm q,Quiescent}$	$\epsilon_{\rm q,Star-forming}$
Central mass: $\log(M_{\rm cen}/{\rm M}_{\odot}) > 10.5$						
Satellite mass: $\log(M_{\rm sat}/{\rm M}_{\odot}) = 9.3 - 10.2$	$0.3 < z < 0.6$	200 ckpc	0.43	0.23	0.33	0.09
		300 ckpc	0.45 ± 0.04	0.35 ± 0.07	0.35 ± 0.05	0.25 ± 0.09
		500 ckpc	0.37	0.26	0.26	0.13
		200 pkpc	0.43	0.33	0.34	0.22
		300 pkpc	0.36	0.33	0.25	0.22
		500 pkpc	0.37	0.26	0.26	0.14
	$0.6 < z < 0.9$	200 ckpc	0.40	0.25	0.29	0.12
		300 ckpc	0.44 ± 0.02	0.16 ± 0.03	0.33 ± 0.03	-0.02 ± 0.03
		500 ckpc	0.37	0.22	0.25	0.08
		200 pkpc	0.36	0.21	0.25	0.08
		300 pkpc	0.36	0.22	0.25	0.10
		500 pkpc	0.37	0.26	0.26	0.13
	$0.9 < z < 1.6$	200 ckpc	0.31	0.18	0.22	0.07
		300 ckpc	0.30 ± 0.02	0.18 ± 0.02	0.22 ± 0.02	0.08 ± 0.02
		500 ckpc	0.29	0.20	0.20	0.10
		200 pkpc	0.27	0.18	0.18	0.07
		300 pkpc	0.29	0.19	0.19	0.08
		500 pkpc	0.26	0.16	0.17	0.04
	$1.6 < z < 2.5$	200 ckpc	0.23	0.17	0.18	0.11
		300 ckpc	0.22 ± 0.03	0.12 ± 0.03	0.17 ± 0.04	0.06 ± 0.03
		200 pkpc	0.16	0.12	0.10	0.07
		300 pkpc	0.10	0.11	0.04	0.05

The uncertainties of quiescent fractions and quenching efficiencies of satellites measured in aperture radii of 200 ckpc, 500 ckpc, 200 pkpc, 300 pkpc, and 500 pkpc are not shown and are assumed to be the same as the uncertainties measured in 300 ckpc aperture radius.

APPENDIX B

APPENDICES OF CHAPTER 4

B.1 Measuring Galaxy Overdensities with Photometric Redshifts

In this work we use a variation of the distance to the 3NN as a measure of the galaxy environment. We derive the 3NN from the ZFOURGE photometric redshifts and here we quantify how well the overdensity derived from the 3NN reproduces the true overdensity as measured in spectroscopic redshift surveys.

We use a mock galaxy catalog based on the semi-analytic model from Henriques et al. (2015), which is the Munich galaxy formation model updated to the Plank first-year cosmology. Henriques et al. modify the treatment of baryonic processes to address problems regarding the overabundance of low-mass galaxies and quiescent galaxies. For our purposes the details of galaxy formation and feedback in the mock are less important than the actual redshifts (which include both the cosmological expansion and peculiar velocity). We take all galaxies in the mock down to the stellar mass limit of our ZFOURGE survey at every redshift. We then perturb the redshift from the mock catalog by a random number selected from a normal distribution with σ_z equal to the uncertainty of the ZFOURGE photometric redshift ($\sigma_z = 0.01 - 0.02(1+z)$, depending on the galaxy mass and magnitude, see Straatman et al., 2016).

We then calculate the distance to the Nth nearest neighbor, with N=1, 2, 3, . . . , 7 in two ways. First, we use the "true" redshifts from the mock (which include the peculiar velocity) to measure the distance to the nearest neighbor within a cylindrical volume of length (in the radial dimension) corresponding to $\Delta v = \pm 2100\,\mathrm{km\,s^{-1}}$, which serves as an estimate of the density measured in a spectroscopic survey. We then repeat the measurement, but using the perturbed redshifts as an estimate of the density measured by a ZFOURGE-like photometric redshift survey.

We then compute two estimates of the local surface density of galaxies derived from the Nth nearest neighbor, first with the standard method, $\Sigma_N = N(\pi d_N^2)^{-1}$, where d_N is the distance to the

Nth nearest neighbor. Second, we use the Bayesian estimate of the local surface density derived to the Nth nearest neighbor, Σ'_N, which uses the density information of the distances to all neighbors $\leq N$ (Ivezić et al., 2005; Cowan & Ivezić, 2008) defined in Equation 4.3 above. From both estimates of the local surface density, we compute the overdensity, $(1 + \delta)_N$, using Equation 4.2 above.

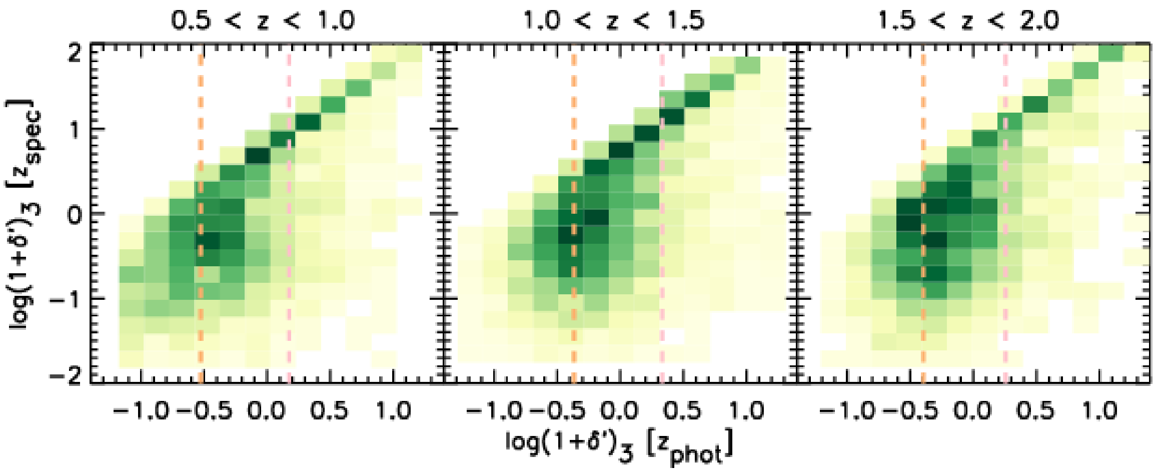

Figure B.1: Comparison of environmental density measured using photometric and spectroscopic redshifts

Simulated density measurements based on photometric redshifts $(\log(1 + \delta')_{N=3}\ [z_{\rm phot}];\ \Delta z = 0.02(1 + z))$ versus measurements based on spectroscopic redshifts $(\log(1 + \delta')_{N=3}\ [z_{\rm spec}];\ \Delta v = 2100$ km/s) for the Bayesian N=3 (3rd nearest neighbor [3NN]) in three redshift ranges. The black data points and error bars indicate the median values and 1σ ranges of $\log(1 + \delta')_{N=3}[z_{\rm spec}]$ calculated in bins of $\log(1 + \delta')_{N=3}[z_{\rm phot}]$. The orange and pink vertical dashed lines indicate the lowest and top quartiles (the 25th and 75th percentiles of $\log(1+\delta')_{N=3}[z_{\rm phot}]$ distribution), which we used to specify low- and high-density environments. There is a strong correlation between both density measurements – at all redshifts galaxies identified in the highest (lowest) density quartiles using photometric redshifts with this precision recover those galaxies in the highest (lowest) density quartiles as defined using spectroscopic redshifts. Reprinted with permission from “Effect of local environment and stellar mass on galaxy quenching and morphology at $0.5 < z < 2.0$" by Kawinwanichakij et al., 2017. The Astrophysical Journal, Volume 847, Issue 2, article id. 134 pp. 21, Copyright 2017.

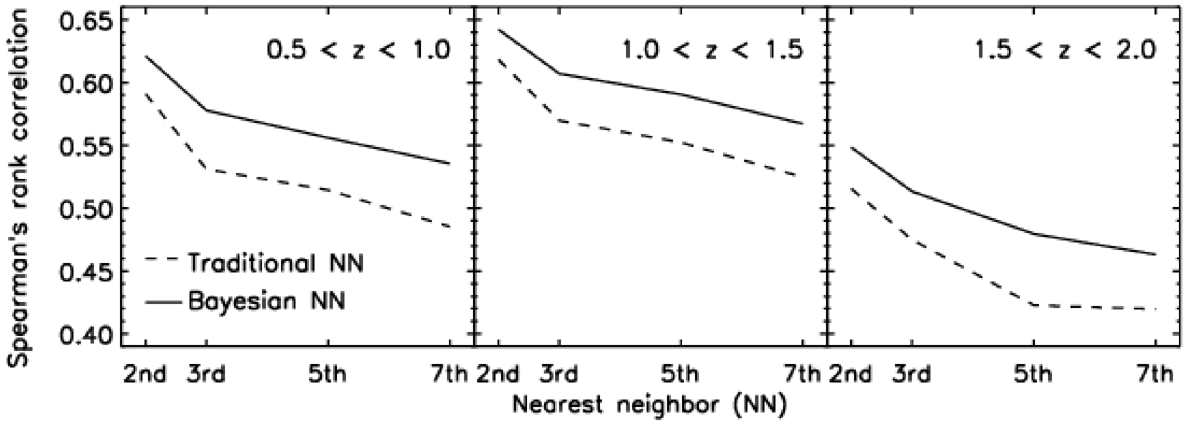

Figure B.2: Spearman's rank correlation coefficient between photometric environment measurements and spectroscopic environment measurements

Spearman's rank correlation coefficient between photometric environment measurements and spectroscopic environment measurements as a function of the Nth nearest neighbors with $N = 2, 3, 5, 7$ for mock galaxy sample at $0.5 < z < 1.0$ (left), $1.0 < z < 1.5$ (middle), and $1.5 < z < 2.0$ (right). The Bayesian and traditional Nth nearest neighbors are shown as solid and dash lines, respectively. Reprinted with permission from "Effect of local environment and stellar mass on galaxy quenching and morphology at $0.5 < z < 2.0$" by Kawinwanichakij et al., 2017. The Astrophysical Journal, Volume 847, Issue 2, article id. 134 pp. 21, Copyright 2017.

For convenience, we define $\log(1+\delta')_N[z_{\rm phot}]$ as the density measured for galaxies in the mock using the ZFOURGE-like photometric redshift uncertainties. We also define $\log(1 + \delta\ ')_N[z_{\rm spec}]$ as the density measured in the mock using "true" redshifts (which include the cosmological and peculiar redshift in the mock). Figure B.1 shows the overdensities for the Bayesian 3NN for the mock catalog, $\log(1+\delta')_{N=3}[z_{\rm spec}]$, compared to the those derived from the photometric redshifts, $\log(1+\delta')_{N=3}[z_{\rm phot}]$. The relations are clearly correlated, with galaxies at low and high overdensity in the spectroscopic survey generally displaying low and high overdensity when measured in the ZFOURGE–like survey. However, there are clear examples of mismatch, for example there is a tail of objects with low overdensity, as defined in the spectroscopic-quality data, that have measured high overdensity in the ZFOURGE–like data. This tail is caused by redshift errors and chance projections of unassociated objects along the line of sight, and is consistent with the findings of Cooper et al. (2005) that photometric redshifts can wash out structure.

To quantify the accuracy of the overdensity as measured by the ZFOURGE-like dataset, we first measured the Spearman's rank correlation coefficient for the overdensities measured in the spectroscopic-like and ZFOURGE-like datasets for the overdenstiy calculated using the $N = 2$, 3, 5, 7th nearest neighbor, for the standard and Bayesian methods described above. Figure B.2 shows the correlation coefficients as a function of N for the mock galaxies. We find that for all redshift bins from $z = 0.5$ to 2.0, the Bayesian density estimators have higher Spearman's rank correlation relative to the traditional nearest neighbors regardless of number of nearest neighbors, indicating that the Bayesian density estimator is better correlated with the spectroscopic density estimator relative to the standard Nth nearest neighbors. The two-sided significance (p–value) of the Spearman's rank correlation for all three redshift bins are $< 3 \times 10^7$ ($> 5\sigma$), implying very strong correlation. Second, we find that the correlation increases with lower Nth nearest neighbors.

Second, we computed the completeness and contamination in low- and high-density environments derived using the ZFOURGE-like mock survey. Our goal is to derive robust samples of galaxies in low-density (high-density) environments that are relatively "pure" in that they have a low contamination fraction of galaxies in high-density (low-density) environments misclassified by our method. Specifically, we will define samples of galaxies in high density and low density environments based on the ranked quartiles (where we define galaxies in the top density quartile as "high density" and those in the bottom density quartile as "low density".

Selecting galaxies in the top (highest) density quartile in $\log(1 + \delta')_N$ $[z_{\rm phot}]$, using the 3NN (N=3) we recover >60% of galaxies that are also in the top density quartile in $\log(1 + \delta')_N$ $[z_{\rm spec}]$ (see Figure B.1; the completeness declines for higher values of N). Of the galaxies in the top density quartile in $\log(1 + \delta')_N$ $[z_{\rm spec}]$ that we miss, more than half are in the next (3rd) quartile in $\log(1 + \delta')_N$ $[z_{\rm phot}]$. More importantly, the contamination is low. The fraction of galaxies in our top density quartile in $\log(1 + \delta')_N$ $[z_{\rm phot}]$ that are actually in the lowest or 2nd-lowest density quartiles in $\log(1 + \delta')_N$ $[z_{\rm spec}]$ is <20% (using N=3, i.e., the 3NN; the contamination increases for larger choices of N and also increases when using the non-Bayesian estimator for the nearest-neighbor distance). This is acceptable as our goal is to identify a relatively pure sample of galaxies in high density environments, which we achieve. In other words, we loose about one-third of galaxies that should be in our top density quartile, but the majority (>80%) of galaxies in our top density quartile are truly in high density environments as measured by $\log(1+\delta')_N\ [z_{\rm spec}]$) (i.e., there is a low incidence of chance alignments of galaxies in projection compared to real, physically associated galaxies).

Selecting galaxies in the bottom (lowest) density quartile in $\log(1+\delta')_N\ [z_{\rm phot}]$, we recover only $\sim$50% of galaxies that are also in the lowest density quartile in $\log(1+\delta')_N\ [z_{\rm spec}]$ for N=3 (see Figure B.1). (As for galaxies in high density environments, we find the completeness decreases for higher N and when using the non-Bayesian estimator for the nearest neighbor distance). The sample of galaxies in the lowest density quartile measured by $\log(1+\delta')_N\ [z_{\rm phot}]$ is very pure in that it contains almost no contamination of galaxies in high density environments in $\log(1+\delta')_N\ [z_{\rm spec}]$ (see Figure B.1): we find the contamination of sources that are in (from the spectroscopic redshift survey) the highest density or 2nd highest density quartile is 15% (the contamination again increases for larger values of N and when using the non-Bayesian estimator for the nearest neighbor distance). Again, this is acceptable as it says that the majority (85%) of galaxies identified in our lowest density quartile in $\log(1+\delta')_N\ [z_{\rm phot}]$ are in low density environments.

Taking the information about the correlation coefficients, completeness, and contamination together, this provides justification that the overdensity derived from the Bayesian 3NN density estimator accurately recovers galaxies accurately in high and low densities with a strong correlation between measured density and true density. We also choose the N=3rd nearest neighbor as it allows higher completeness and lower contamination (see above). A further advantage of using the 3NN as a density indicator is that it has also been shown to provide a faithful measure of the local environmental on scales of galaxy and galaxy group halos, which is appropriate for our study here (Muldrew et al., 2012). Therefore, we adopt the Bayesian 3NN as our density measure for the study here.

B.2 Structural Morphological Parameters

In our analysis, we study the morphological differences between quiescent and star-forming galaxies in different environments and as a function of stellar mass. The majority of galaxies in our sample fall within the CANDELS coverage from HST/WFC3, with effective semi-major axis, a_{eff}, and Sérsic index, n, measured by van der Wel et al. (2012) using the HST/WFC3 F160W (H_{160})–band imaging. We cross–matched the sources in our catalog with those of van der Wel et al.. We further define the circularized effective radius as $r_{\text{eff}} = a_{\text{eff}}\sqrt{q}$, where a_{eff} is the effective semi-major axis and $q = b/a$ is the ratio of the semi-minor to semi-major axis. We also consider correlations with the stellar-mass surface density within the inner 1 kpc, Σ_{1kpc}. We calculate Σ_{1kpc} following the procedure described by Bezanson et al. (2009) and Whitaker et al. (2017) using the galaxies' best-fit Sérsic indexes (n) and circularized effective radii (r_{eff}). In brief, we assume isotropic spherical galaxies with surface luminosity profiles following the Sérsic profile to perform an Abel Transform to deproject the circularized, three-dimensional light profile:

$$\rho\left(\frac{r}{r_e}\right) = \frac{b_n}{\pi}\frac{I_o}{r_e}\left(\frac{r}{r_e}\right)^{1/n-1}\int_1^{\infty}\frac{\exp[-b_n(r/r_e)^{1/n}t]}{\sqrt{t^{2n}-1}}dt \tag{B.1}$$

We convert the total luminosity to total stellar mass, assuming that mass follows the light, and there are no strong color gradients. We follow van Dokkum et al. (2014) by applying a small correction to these stellar masses to take into account the different between the total magnitude in the photometric catalog and the total magnitude implied by Sérsic fit (see Taylor et al., 2010). Finally, we calculate the stellar mass surface density in inner 1 kpc by numerically integrating the following equation

$$\Sigma_{\text{1kpc}} = \frac{\int_0^{1\text{ kpc}}\rho(r)r^2dr}{\int_0^{\infty}\rho(r)r^2dr}\frac{L_{\text{model}}}{L_{\text{phot}}}\frac{M_{\text{phot}}}{\frac{4}{3}(1\text{ kpc})^3} \tag{B.2}$$

where M_{phot} is the stellar mass of the galaxy from the ZFOURGE catalogs, L_{phot} is the total, aperture-corrected luminosity from the ZFOURGE catalogs in the bandpass corresponding to the Sérsic profile measurement (H_{160}), and L_{model} is the total luminosity as measured from integrating the best-fit Sérsic profile.

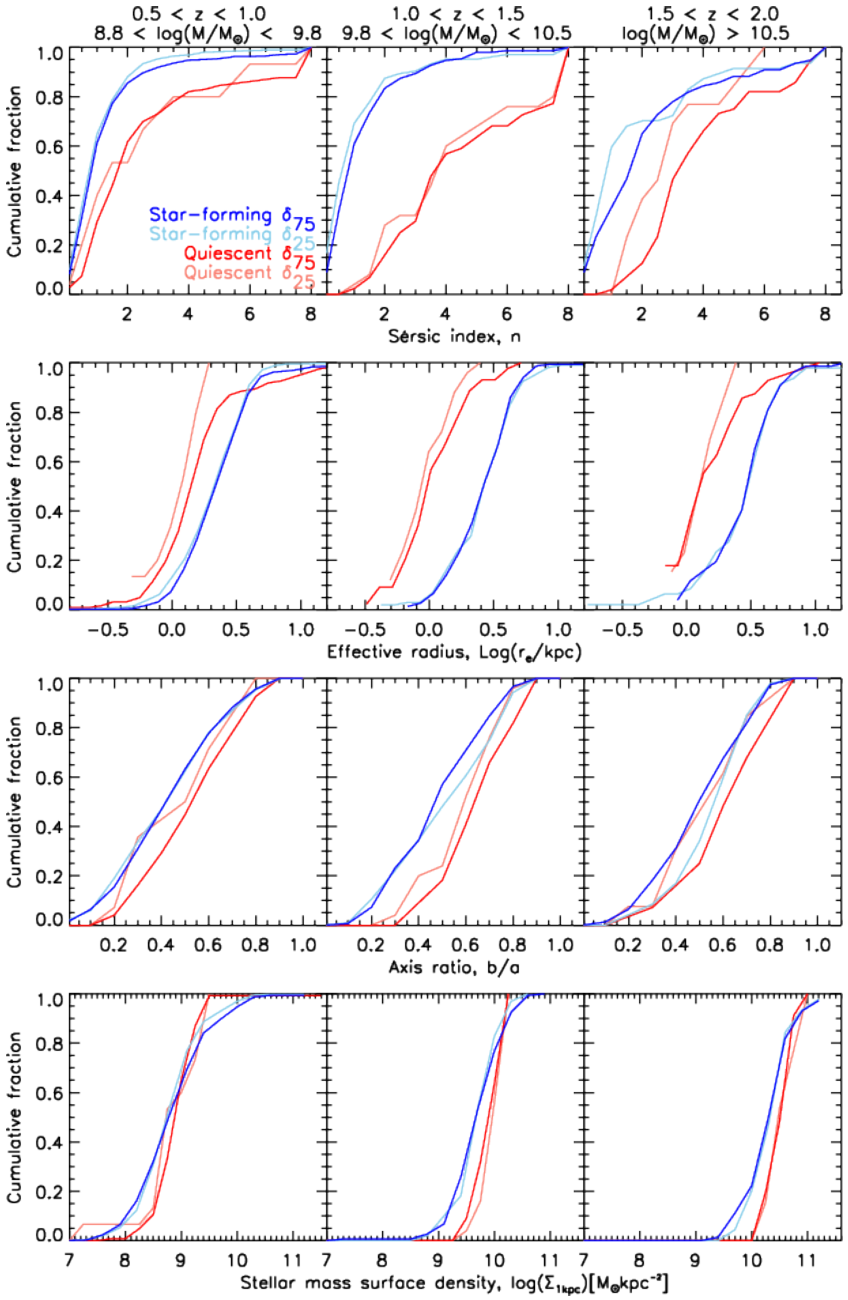

Figure B.3: Comparison of morphological parameters of galaxies in different environments

The cumulative distribution of Sérsic index (top row), effective radius (second row), axis ratio (third row), and stellar mass surface density in inner 1 kpc (bottom row) for quiescent galaxies in the lowest-density quartile (δ_{25}; light-red), quiescent galaxies in the highest-density quartile (δ_{75}; red), star-forming galaxies in the lowest-density quartile (δ_{25}; light blue), and star-forming galaxies in the highest-density quartile (δ_{75}; blue) in three redshift and stellar mass ranges. There is no significant evidence for a difference in distributions of any of the four morphological parameters between quiescent (and star-forming) galaxies in low- and high-density environment. Reprinted with permission from "Effect of local environment and stellar mass on galaxy quenching and morphology at $0.5 < z < 2.0$" by Kawinwanichakij et al., 2017. The Astrophysical Journal, Volume 847, Issue 2, article id. 134 pp. 21, Copyright 2017.

Figure B.3 shows the cumulative distributions of Sérsic index (n), effective radius (r_e), axis ratio (b/a), and stellar mass surface density in inner 1 kpc ($\Sigma_{\rm 1kpc}$) for quiescent galaxies and star-forming galaxies in the lowest and highest overdensity quartiles for representative redshift and stellar mass bins. In all cases, we find that there is no statistical difference in the distributions of quiescent galaxies in high density environments and quiescent galaxies in low density environments. Similarly, we find that the morphology distributions of star-forming galaxies and quiescent galaxies in the highest density regions are dissimilar (therefore, quiescent galaxies in high density regions do not have the morphologies of (recently quenched) star-forming galaxies. We use these distributions in Section 4.6.2 (see also Figure 4.12). Note that we do not show all combinations of redshift and stellar mass bins in the figures, but we find the same results in all bins of mass and redshift.